Upper mantle structure using P wave data from an east African array station

Richard W. Blackhouse

UPPER MANTLE STRUCTURE USING P WAVE DATA FROM AN EAST AFRICAN ARRAY STATION

by

Richard W. Backhouse

A thesis submitted for the degree of

Doctor of Philosophy

in the

University of Durham.

Graduate Society, November 1972.

ABSTRACT

A seismic array of ten short period seismometers has been set up at Kaptagat, 10 km west of the Elgeyo escarpment in Kenya, by the Durham University Geology Department. This study concerns the analysis of teleseismic arrivals.

The method of onset time analysis is used to calculate values of $dT/d\Delta$ and azimuth of approach for 34 events from epicentral distances of 18 - 99°. Large systematic variations in slowness and azimuth are observed as a function of the great circle azimuth to the epicentre. These are similar to those found at other arrays but are of unusually high amplitude. From consideration of onset time residuals and the velocities of regional earthquake arrivals at Kaptagat it appears that these effects are not caused by variations in near-surface structure or by errors in the array geometry. An explanation is developed in terms of sharply dipping interfaces beneath the array, and the preferred model is of a mantle low velocity zone with sloping boundaries underneath the Gregory Rift. This anomalous zone attenuates rapidly westward to sink below mantle material typical of the stable areas of Africa.

P-wave delay times are measured relative to Bulawayo for 78 events in the distance range 24 - 99°. Substantial values confirm the presence of a considerable low velocity body beneath the array and the absence of large variations with azimuth implies ultra-low velocities with relatively moderate dips on the zone boundaries.

A reinterpretation of Rayleigh wave phase and group velocities for the AAE-NAI path is made and found to be compatible

with the top of the low velocity mantle material sinking eastward from the Gregory Rift underneath normal shield-type topmost mantle.

Although the model derived is probably not continuous throughout the East African rift system, the upper mantle structure beneath the Gregory Rift is similar to that suggested to exist below oceanic ridges.

ACKNOWLEDGEMENTS

I should like to thank Professor M. H. P. Bott for the opportunity to work in the Department of Geology, and the Natural Environment Research Council for a research studentship.

I would also like to thank Dr. R. E. Long for supervision and encouragement throughout my research and for invaluable criticism of this work.

I am grateful to the staff of U.K.A.E.A. Blacknest, in particular Mr. P. W. Burton, for advice and assistance. The ISC, Edinburgh, kindly provided listings of earthquake arrival times at Bulawayo.

Many of my colleagues in the Durham Geology Department deserve acknowledgement for their help, in particular Dr. K. Sundaralingam, Mr. A. K. Goodacre, and Mr. L. Arnold. Special thanks are due to Mr. P. K. H. Maguire, not only for the use of unpublished results from the Kaptagat array, but also for help with day-to-day problems.

CONTENTS

CHAPTER 1.

THE EAST AFRICAN RIFT SYSTEM

1.1. General Geology

The East African rift system extends for about 4000 km., beginning at the junction of the Gulf of Aden and the Red Sea, stretching southward and bifurcating south of Ethiopia to form the Western and Eastern Rifts (Fig.1.). These two features converge towards Lake Malawi and the system peters out around the Limpopo River area, although it has been suggested from seismicity studies that rifting may reach as far as 24°S (Fairhead and Girdler, 1969). Rifting is not continuous along the whole length but although variations in its pattern are common, it generally consists of grabens 30 - 70 km. in width, mainly of Tertiary or later age. However, in places, a very similar fault pattern of late Karroo or Jurassic Age is seen, and there is correlation between the latest dominant faulting and Precambrian structural trends (Dixey, 1956). This suggests that movement occurred along lines of weakness resulting from previous orogenic periods, but it seems unlikely that the persistence of Precambrian stress systems caused the major structures of Tertiary or later age, as the older trends followed by the rift faults belong to orogenic belts of widely varying ages and structures of differing kinds (King, 1970).

Faulting, which is particularly intense within the rifts, is predominantly normal with dips generally 55 - 70°. Rifts are bordered by en echelon rather than single large faults, and reverse faulting is very rare. Along the length of the rift system there is

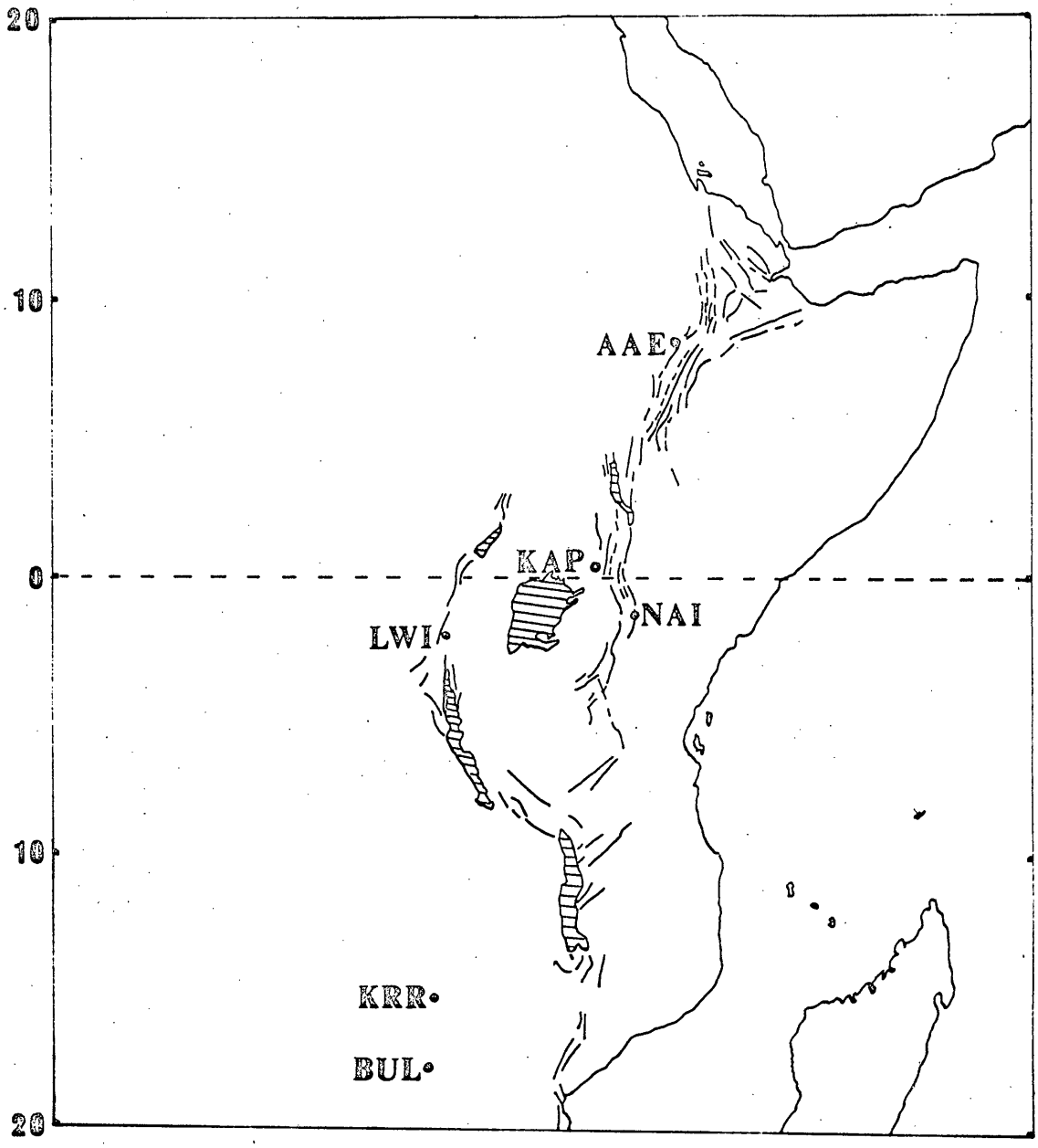

Fig.1. Map of East Africa showing major faults and Kaptagat (KAP), Kariba (KRR) and WWSSN seismic stations.

great variation in the altitude of the plateaux and valleys, but the overall displacements seem to be of the same general order and this, taken with the uniformity in width of the rift valleys, is perhaps indicative of the crustal thickness and principal stresses being of comparable magnitude over much of East Africa (King, 1970).

In many places the size of the actual displacement has been obscured by infilling of the rift valleys with sediments and volcanics. The original drainage pattern in Uganda and northern Tanzania was towards the Atlantic with the watershed along the line of the Eastern Rift, resulting in greater sedimentation in the Western Rift which is also extensively occupied by lakes. This drainage pattern has since been changed, partly as a result of the considerable volcanic activity. This volcanism is one of the most striking features of the whole rift system and although there are correlations between rifting and periods of eruption, both tectonic and compositional relationships are still not clearly resolved. Marked differences in lava type exist along the system with much smaller changes across the rifts. As a simplification, the rift system has a preponderance of alkaline salic rocks with carbonatite most conspicuous outside the rift zones. In Ethiopia, lava tends to be less alkalic than elsewhere and this also holds for areas of general volcanism when compared with isolated neighbouring centres (Harris, 1969; Bailey, 1964).

1.2. The Kenya Rift

The Kenya Rift is a downfaulted belt roughly bisecting the uplifted area of the Kenya Dome, an elliptical feature some 1000 km. across. Northward around Lake Rudolf the rift zone becomes ill-defined as faulting splays out and only a narrow axial trough continues into the main Ethiopian Rift. Similarly the main structure

continues southward into northern Tanzania until faulting forms a broad zone of tilted blocks.

Centrally the rift largely resembles a classic graben, 60 - 70 km. wide, with dense sub-parallel faulting withinthe rift zone, individual displacements varying from metres to thousands of metres. As well as subsidence of the floor, uplift of the rift shoulders has occurred, this rise towards the flanks being accentuated by extensive plateau lava flows which often reach 2 - 3 km. above sea level. The volcanic rocks associated with the Kenya Rift Valley show great variety but two main genetic series are distinguishable: one strongly alkaline and nepheline-rich (melanephelinite-nephelinite) and the second mildly alkaline with modal nepheline (alkali-basalt-trachybasalt-trachyte-soda rhyolite). All rocks are alkaline and usually soda-rich with some intermediate trends of more or less alkaline rocks, although such as plateau phonolites show great uniformity. Eruptions are from central volcanoes of different sizes as well as from multi-centre and fissure sources.

1.3. Evolution of the Kenya Rift

Studies of Miocene and late Pliocene erosion surfaces (Baker and Wohlenberg, 1971), faunal evidence from sediments and isotopic age dates (King and Chapman, 1972), allow delineation of the main phases of Tertiary rifting and accompanying volcanism. In early Miocene times, upwarping of the Kenya-Uganda border area and down-flexing of the Turkhana depression immediately pre-dated the beginning of volcanism with alkali basalts erupted from central fissure sources in northern Kenya. A broad domal uplift of central Kenya of about 300 metres in the late Miocene formed a site for massive fissure phonolite eruptions from as early as 16 m.y., but generally within

the range 12 - 13.5 m.y.ago and nephelinites and phonolites built central volcanoes west of the rift (Elgon, Kisingiri, Tinderet). At the culmination of this uplift rift faulting developed extensively and basalt lava was erupted along the whole length of the trough.

In late Pliocene and early Pleistocene times, voluminous plateau trachytes and moderate to weak undersaturated lavas formed central volcanoes east of the rift (Longonot, Menengai, Kenya) coinciding with the last and largest uplift of about 1400 metres (Baker and Wohlenberg, 1971). In general terms tectonic and volcanic events, beginning in mid-Tertiary in the northern part of the rift, have progressed southward. In addition, the earliest and latest volcanics occur respectively on the western and eastern flanks of the rift with a trend from undersaturated towards oversaturated types with the passage of time.

1.4. Seismicity of East Africa

The seismic activity of the rift system forms a continuation of the zone of shallow seismicity associated with the Mid-Atlantic Ridge and extending around southern Africa and beneath the Indian Ocean and the Gulf of Aden (Rothé, 1954; Girdler, 1964a). However, whereas earthquake epicentres along oceanic ridges are largely confined to a narrow belt less than 50 km. wide, those in East Africa exhibit a much greater scatter, which is also seen elsewhere in continental areas (Sykes and Landisman, 1964). Much of the activity can be related to different branches of the rift system, with the Western Rift seemingly the most active large section. Studies using data from networks of stations show that epicentres within this region are generally associated with rift structures except for

a large group west of Lake Kivu (Sutton and Berg, 1956; De Bremaecker, 1959; Wohlenberg, 1970; Sykes and Landisman, 1964). Wohlenberg (1970) studied focal depths for events in the Western Rift area and found all reliable determinations gave values of less than 40 km.

In contrast to the western branch of the system, the Eastern Rift in Kenya shows little or no teleseismic activity and Wohlenberg (1970) could locate no earthquakes of magnitude $\geq$ 4.0 within the Rift between 1°S 36°E and Lake Rudolf for the period 1957 - 1964. Activity around the Eastern Rift in this area is largely confined to the Kavirondo and Speke Gulf Rifts and the rifting in northern Tanzania. Microseismicity is also very low in the north of Kenya but increases southward, being restricted to the rift floor and border faults with no detectable activity on the flanks (Tobin, Ward and Drake, 1969; Molnar and Aggarwal, 1971). As in Iceland (Ward, Palmason and Drake, 1969) where microearthquakes correlate with major thermal events, the high detection rates in southern Kenya coincide well with steam jets and hot springs. Thus local and microseismicity results in the Kenya Rift seem to indicate a different state of stress from that beneath the Western Rift (Gill, 1972), and perhaps a low strength lithosphere below the Eastern Rift, (Fairhead and Girdler, 1971).

Earthquake mechanism data in eastern and southern Africa reveal dip-slip and strike-slip faulting. It is possible that no simple stress system could produce the observed variation of fault directions (De Bremaecker, 1959), but Fairhead and Girdler (1971) conclude that the data are consistent with an WNW-ESE stress field. In general the data are consistent with normal faulting in the rift

system. (Banghar and Sykes, 1969).

1.5. Structure from Seismic Studies

Except for the rift zones, Africa seems to have a structure similar to that within stable shield areas. Gumper and Pomeroy (1970) studied surface wave and body wave data and derived a model for the crust and upper mantle beneath Africa chiefly from Rayleigh wave phase and group velocities in the period range 10 - 63 seconds. This, the AFRIC model (Table 1), is a modification of the CANSD model of Brune and Dorman (1963) for the Canadian Shield and the similarities between the two indicate that the velocities found for Africa are not substantially different from those associated with other shield regions. The body wave travel-time studies give velocities for P_n of 8.06 km/sec. and for S_n of 4.55 - 4.72 km/sec. These values are determined for more varied paths than were used in the dispersion work and are lower than corresponding velocities for the Canadian Shield and for the Western Transvaal, where velocities for P_n and S_n of 8.27 km/sec and 4.73 - 4.83 km/sec respectively have been found from travel-time work (Willmore, Hales and Gane, 1952; Gane, Atkins, Sellschop and Seligman, 1956). This values does not, however, seem typical of the rest of Africa; for instance, the Eastern Transvaal, where the P_n phase has a velocity of 7.96 km/sec. (Hales and Sachs, 1959), lower than those to the west.

Bloch, Hales and Landisman (1969) studied the crust of southern Africa in more detail from short period Rayleigh and Love wave dispersion data for the paths Pretoria-Bulawayo and Kariba-Pretoria (Table 2). They also found that over a longer period range that phase and group velocities are similar to, or slightly lower than those for most shield areas.

TABLE 1

AFRIC MODEL. Gumper and Pomeroy (1970)

H (km)	V_p (km/sec)	V_s (km/sec)	ρ (gm/cc)
7.0	5.90	3.35	2.70
10.5	6.15	3.55	2.80
18.7	6.60	3.72	2.85
80.0	8.05	4.63	3.30
100.0	8.20	4.78	3.44
100.0	8.30	4.65	3.53
80.0	8.70	4.85	3.70
	9.20	5.25	3.76

TABLE 2

MODEL SASD - 2 Bloch, Hales and Landisman (1969)

H (km)	V_p (km/sec)	V_s (km/sec)	ρ (gm/cc)
8.0	5.7	3.50	2.70
12.0	6.2	3.64	2.90
8.0	6.7	3.84	2.95
8.0	6.9	3.97	3.00
9.0	7.3	4.24	3.20
25.0	8.1	4.67	3.30
	8.3	4.80	3.37

Bonjer, Fuchs and Wohlenberg (1970) determined crustal response ratios by spectral analysis of long-period body waves from two Hindu Kush earthquakes observed at stations Addis Abbaba (AAE), Nairobi (NAI) and Lwiro (LWI) - see Fig.1. The data were found to be consistent with crustal thicknesses of 39 km, 43 km and 35 km beneath AAE, NAI and LWI respectively. The preferred models had an upper crustal layer of velocity 6.0 km/sec. and an intermediate layer of velocity 6.7 km/sec. (Fig.2.). Sundaralingam (1971) studied the propagation of Rayleigh waves across the rift system and found that the dispersion curves tended to merge with that for the AFRIC model at short periods, which indicates some crustal uniformity throughout Africa. However, at longer periods, lower phase and group velocities than for AFRIC suggest anomalously low upper mantle velocities beneath the Rift. As this effect is most pronounced for the path Addis Abbaba (AAE) to Nairobi (NAI)(Fig.3.), it is concluded that the main anomaly extends along the eastern branch of the rift system, although some mantle anomaly probably exists below the Western Rift.

The existence of such a low velocity zone is confirmed by P-wave delay time measurements (Table 3). Large positive delays are observed at Nairobi and Addis Abbaba and a smaller positive value at Lwiro. These are measured relative to Bulawayo and so provide a measure of the divergence of the structure beneath the Rift from that similar to shield areas. These results are in broad agreement with those from other arrival time studies (Fairhead and Girdler, 1971; Griffiths et al, 1971). In addition, Gumper and Pomeroy (1970), in their study of body waves found that the S_n phase failed to propagate across most of the rift zone and suggested that this was due

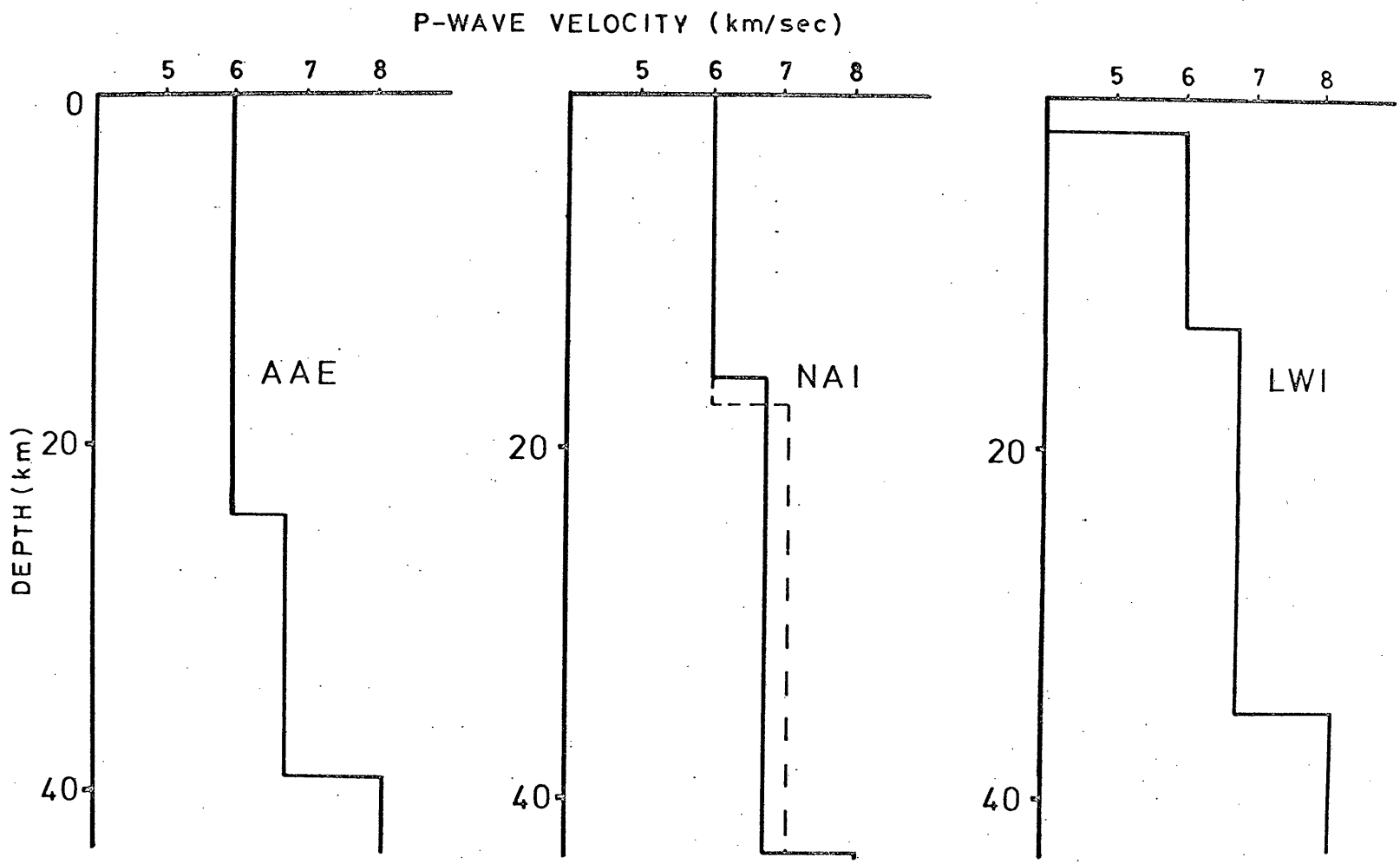

Fig.2. P wave models for the crust beneath Addis Abbaba, Nairobi, and Lwiro from spectral analysis of body waves (Bonjer, Fuchs and Wohlenberg, 1970).

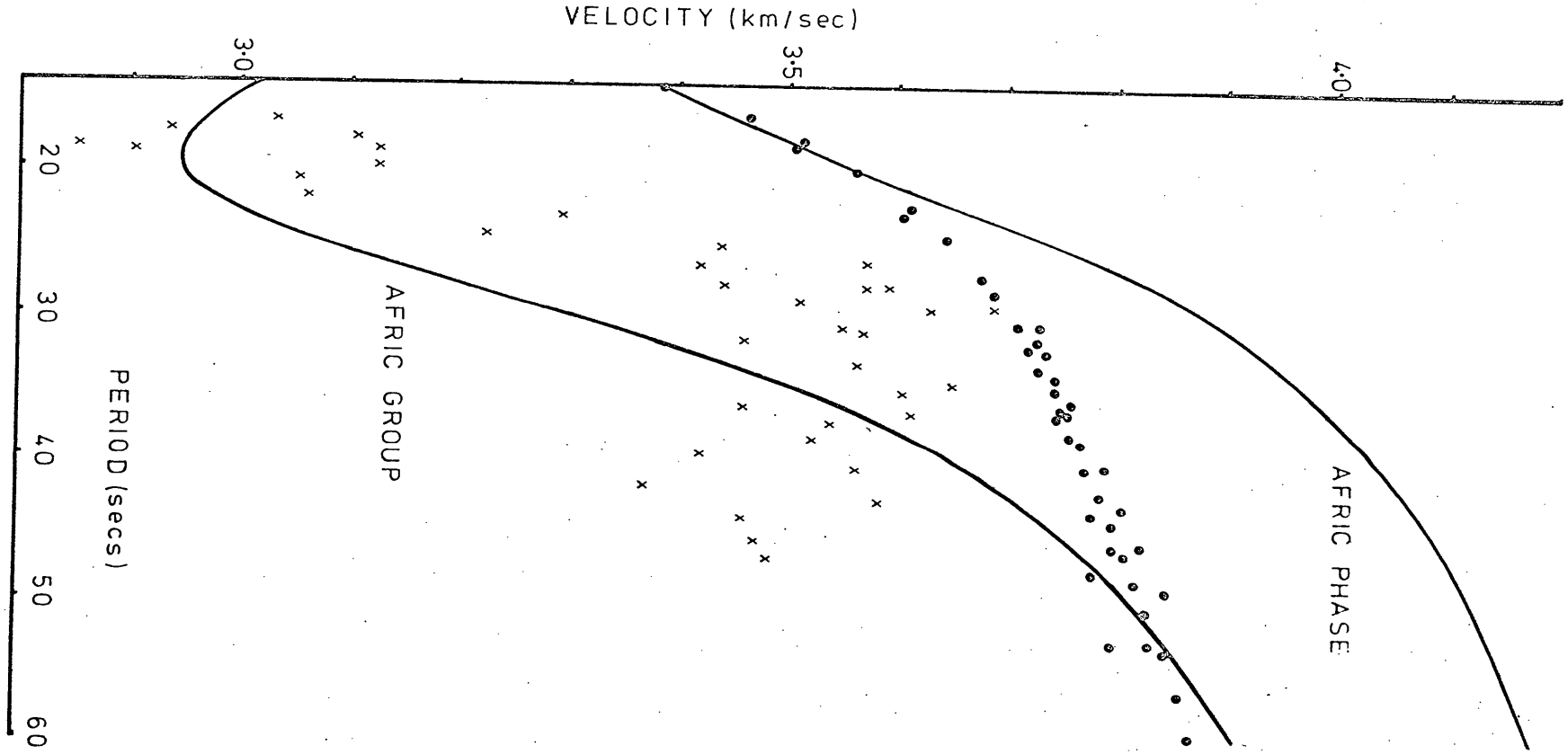

Fig.3. Observed Rayleigh wave phase (dots) and group velocities (crosses) for the AAE-NAI path (Sundaralingam, 1971) with computed dispersion curves for AFRIC model of Gumper and Pomeroy (1970).

TABLE 3

P-WAVE DELAY TIMES RELATIVE TO BULAWAYO

Sundaralingam (1971)

Addis Abbaba, AAE	2.7 ± 0.3 secs
Nairobi, NAI	2.3 ± 0.3 secs
Lwiro, LWI	1.1 ± 0.3 secs

Errors are 95% confidence limits.

to 'a gap in the lithosphere'. Griffiths et al (1971) set up a seismic refraction line within the Gregory Rift to further define the axial structure. The results show a 20 km thick layer of P-wave velocity 6.4 km/sec overlying a layer of velocity 7.5 km/sec (Fig.4.), giving a similar structure to that found in Iceland (Båth, 1960; Bott, 1965). Gravity interpretation (Khan and Mansfield, 1971) suggests that the 7.5 km/sec body thins away from the rift indicating modification of the crust (Fig.5.). A similar interpretation to that for the Gregory Rift refraction line could be given to results from the Western Rift (Dopp, 1964) where a refractor of velocity 6.7 - 6.82 km/sec. was observed at depths 17 - 33 km underneath a layer of velocity 5.57 km/sec. However, it is more likely that the former represents a crustal layer with probably a low velocity mantle layer beneath (Wohlenberg, 1970).

1.6. Gravity and other Geophysical Studies

The East African Plateau is characterised by a broad negative Bouguer anomaly which generally increases in magnitude over the rift valleys. The Plateau is approximately in isostatic equilibrium, but Bullard (1936) found negative isostatic anomalies over several rifts as great as - 100 mgals. The major negative anomaly has a wavelength of several hundred kilometres and must be caused by a mass distribution at depth, while the existence of isostatic equilibrium indicates that the mass effect of the Plateau block is compensated at depth by a relative mass deficiency (Sowerbutts, 1969). Hence the cause of the Bouguer anomalies is probably a body of low density material at the base of the lithosphere, which extends underneath the Plateau areas and is nearer the surface beneath individual rifts. Additional contributions come from low density rift volcanics and sediments (Searle, 1970).

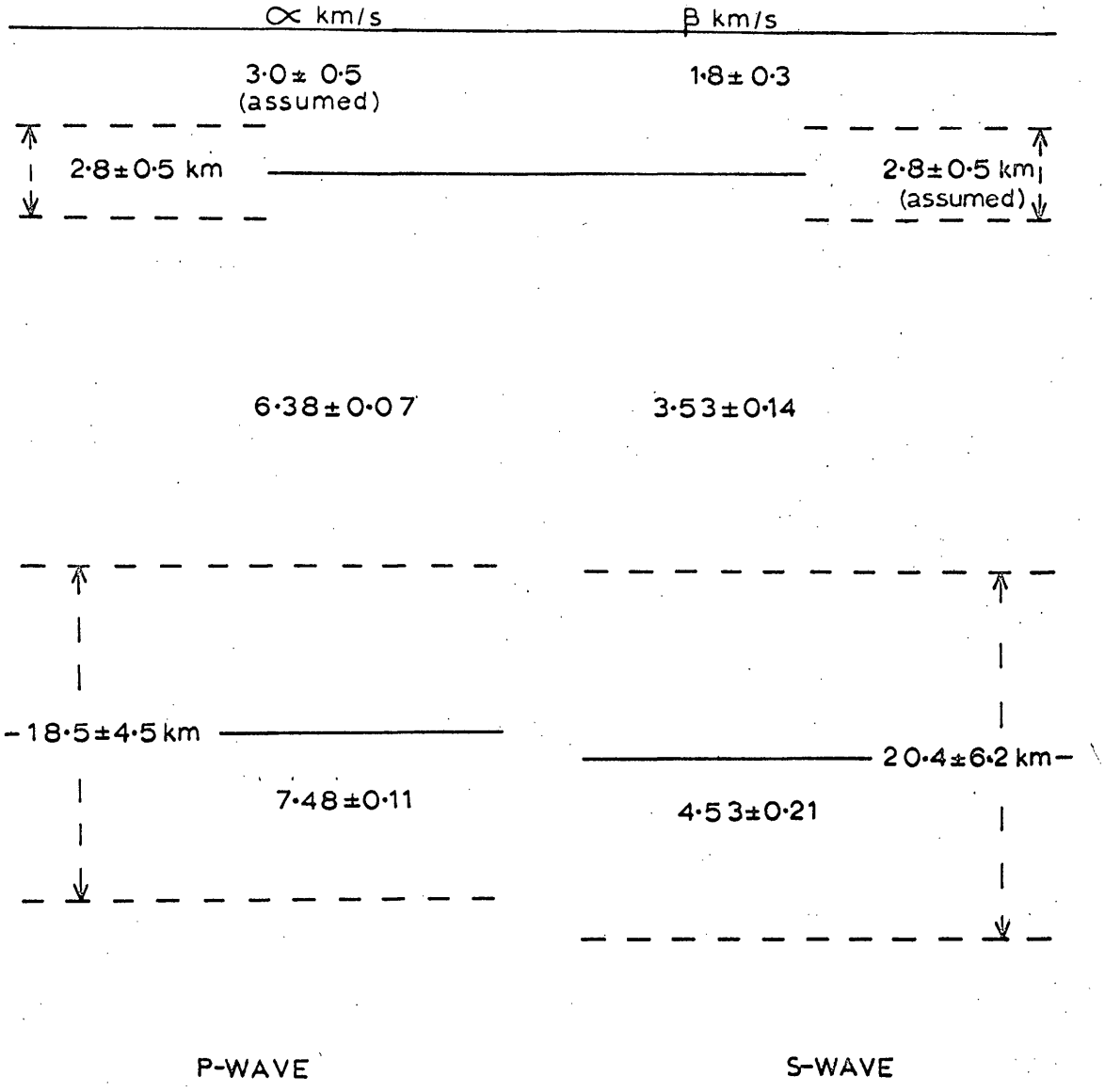

INTERPRETATION OF REFRACTION LINE IN KENYA RIFT
GRIFFITHS et al., 1968

Fig.4.

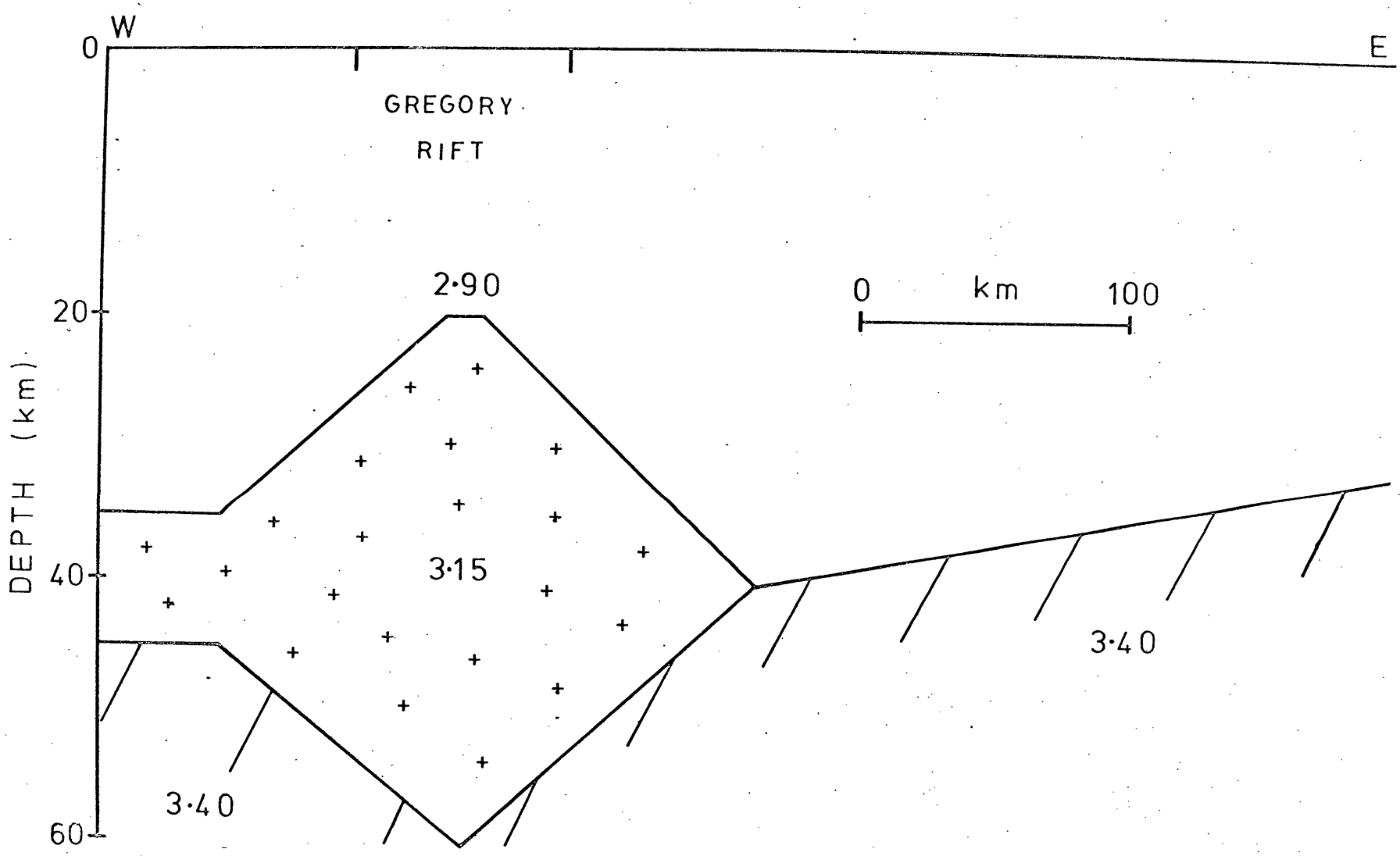

Fig.5. Crust and upper mantle model from a gravity line crossing the Gregory Rift (Khan and Mansfield, 1971). Densities are in gm/cc.

Studies of the Kenya Rift Valley have shown a small wavelength positive anomaly superimposed on the much broader negative. This is 40 - 100 km wide with a magnitude of about 30 - 60 mgals and is generally centred about the rift axis. Using the seismic controls provided by Griffiths et al (1971), Khan and Mansfield (1971) interpreted this anomaly from an east-west profile at 1° N and postulated a diamond-shaped body reaching to within 20 km of the surface (Fig.5.). The gradients of the positive anomaly indicate that the upper surface of the body cannot be more than 20 km from the surface but other workers prefer a model with a mantle-derived body coming within1 or 2 km of the rift valley floor in places. Baker and Wohlenberg (1971), from gravity measurements ENE and WSW of Menengai, explained the positive peak by an intra-crustal body of specific gravity contrast + 0.15, the top of which is 10 km wide and 1.5 km below sea level under the centre of the rift. Similar interpretations have yielded wider intrusions in the range 16 - 28 km (Searle, 1971).

The presence of this intrusive zone within the crust, presumably derived from a partially molten body centred beneath the rift, is supported by Quaternary grid faulting and the proliferation of steam jets and fumaroles within the rift valley (Searle, 1971). The grid faulting marks the trend of the positive anomaly more closely than Tertiary faults bounding the rift and probably the grid faulting and geothermal activity both occur where the crust is thinnest. Microearthquakes show a similar pattern except in northern Kenya, where such activity dies out.

No comparable axial positive Bouguer anomaly has been found over the Western Rift, and this, taken with volcanic evidence (Illies, 1969) suggests that the Western Rift is in a less advanced state of development than the Gregory Rift.

Heat flow measurements are sparse in East Africa. However, Von Herzen and Vacquier (1967) made several such observations in Lake Malawi, and found strong regional variations. In the north and south of the lake, the mean values are 0.54 μcal.cm.$^{-2}$sec.$^{-1}$ and 0.70 μcal.cm.$^{-2}$sec.$^{-1}$, lower than the world average but similar to those found in South African shield areas. In the central part of the lake, an abnormally high mean value of 2.30 μcals.cm.$^{-2}$sec.$^{-1}$ may be due to a small shallow magmatic intrusion. The low values, at least those in the north, could also be due to local effects and rapid sedimentation may have lowered the thermal gradient.

1.7. Theories of Rift Formation

It is now generally agreed that the rift system is a tensional feature and not a result of horizontal compression as has been suggested (Bullard, 1936; Willis, 1936). It has been shown by geological observation, gravity interpretation and earthquake mechanism studies that the faults bounding the rifts are normal and not reverse (Gregory, 1921; Girdler, 1964a; Heiskanen and Vening Meinesz, 1958; Sykes and Landisman, 1964; Fairhead, 1968; Fairhead and Girdler, 1971), indicating extension of the crust. A variety of processes have been suggested to account for the formation of the rifts, including crustal doming (Willis, 1936), crustal thinning (Girdler, Fairhead, Searle and Sowerbutts, 1969; Searle, 1970), 'necking' of the crust (Freund, 1966) and subsidence as a result of isostatic forces (Girdler, 1964a). However, since the recent developments in the fields of sea-floor spreading and plate tectonics, most explanations of rift formation have been formulated in terms of these concepts.

The continuous belt of shallow seismicity which passes

through the Indian Ocean, the Gulf of Aden and the Red Sea (Rothé, 1954; Girdler, 1964a; Drake and Girdler, 1964) is taken as the spreading axis between rigid lithospheric plates, where new oceanic material is formed. The Gulf of Aden is underlain by oceanic crust as wide as 200km and seismic, magnetic and gravity interpretation (Girdler, 1958; Vine, 1966; Tramontini and Davies, 1969; Philips, 1970), suggest that the southern Red Sea has some 50 km width of new oceanic crust. This means that Africa and Arabia have moved away since Tertiary times. If the shallow seismicity in East Africa also delineates a spreading centre then a simple model defined by the seismic activity is that of three plates - the Arabian, Nubian and Somalian plates (McKenzie, Davies and Molnar, 1970). The fitting of magnetic lineations and 500-fathom contours within the Gulf of Aden yields a pole of rotation for the Arabian plate relative to the Somalian plate at about 26.5°N 21.5°E with a rotation angle of 7.6° (McKenzie et al, 1970; Le Pichon, 1968). A fit of the coast-lines on either side of the Red Sea north of 15°N gives a pole of rotation for the Nubian-Arabian plate system at 36.5°N 18°E (McKenzie et al, 1970; Fairhead and Girdler, 1970). The poles of opening and rotation angles for the Gulf of Aden and the Red Sea can be combined to place the pole for the Nubian and Somalian plates at 8.5°S 31.0°E with a rotation angle of 1.9°, which necessitiates an opening of the rift of 65 km in northern Ethiopia and 30 km in Kenya. The Arabia-Somalia pole is in general agreement with observed geological features (Gass and Gibson, 1969) but the positions of the other two poles are more contentious. Fitting the Red Sea coastlines contradicts present knowledge of the crust and does not explain the Danakil and Aisha Horsts (Mohr, 1970) and a fit of the 2000-metre depth contours might be more realistic (Freund, 1970). A change in this pole would

alter the position of the Nubia-Somalia pole. The existing position requires separation in northern Ethiopia almost the whole width of the rift (Mohr, 1970) at that latitude and separation in Kenya is incompatible with the structural and gravity interpretation of Baker and Wohlenberg (1971). A wider intrusive body in the rift valley crust such as suggested by Searle (1970, 1970b) would agree with the proposed 30 km separation from plate tectonics, and the trend of the intrusion along the rift axis as deduced from the positive Bouguer anomalies is compatible with the computed relative motion of the two plates about the pole of McKenzie et al (1970). However, the calculation of a reliable pole of rotation for the Nubia-Somalia system may be impossible because of the ambiguities inherent in the positions of the other two Afro-Arabian poles (Al-Chalabi, 1971).

Roberts (1969) suggested that the Nubia-Somalia pole should be at 30°N 47°E with a rate of opening of 0.7 ± 0.3 cm/year/limb, but this implies a separation of 140 km in the north of the rift system and 'impossibly large' spreading further south (Baker, 1969).

Instead of a three-pole system for the Middle East rift zones as a whole, a one or two-pole system may be more likely (Baker, 1969), with left lateral shear along the Eastern Rift (Gass and Gibson, 1969), presumably from movement of the Somalia region in the same direction as Arabia - north-eastwards - but at a slower rate.

Also, it is possible that a single pole applied to East Africa is too much of a simplification (McKenzie et al, 1970) and that if plate tectonics can be applied in regions where spreading is small and slow, then several plates have to be introduced to describe the system. Such complexity would be expected in a

multi-rift zone and is borne out by the diverse pattern of seismicity and structural evidence. Separation in the Kenya Rift, for instance, is probably significantly less at the northern and southern extremities than in central Kenya (Baker and Wohlenberg, 1971). Thus it may be more relevant to think of the Kenya Rift as a physical unit. A connection with the Red Sea and the oceanic ridge system has been established by seismicity and evidence from seismic refraction, surface wave dispersion, P-wave delay times and gravity interpretation shows that there are similarities between the structure beneath the rift system and that beneath some parts of oceanic ridges, such as in Iceland. This has led to the hypothesis that the rift system is an embryonic oceanic ridge (Wilson, 1969; Girdler, 1969; Harris, 1970), but there are geological and petrological problems associated with such a conclusion.

Volcanism in oceanic ridge areas is dominantly basaltic and tholeiitic, occurring with a linear trend and accompanied by high heat flow, transverse faulting and an abundance of dykes (McConnell, 1970; Murray, 1970). Oceanic tholeiitic basalts exist within the Red Sea median trough (Gass, 1970; Harris, 1970; Hutchinson and Gass, 1971), but in East Africa there is a great predominance of alkaline rocks, although there is considerable variation. These rocks are grouped together in large domes such as are found in other continental rift systems (Holmes, 1965; Le Bas, 1971), but without any definite relation between the age of volcanics and the distance from the rift axis. Although the most recent volcanics are generally near the rift axis, there are the young, remote volcanoes of Mt. Elgon and Mt. Kenya (Osmaston, 1971; McConnell, 1970). Transverse faults and dykes are rare and heat flow values would not appear to be as high as those for oceanic ridges (Von Herzen and Vacquier, 1967). A number of other

evolutionary schemes have been suggested.

The coincidence of large topographic domes and volcanism have led to the linking of the two into a pattern of rift development. Bailey (1964) has suggested that the cause of the rifts is upwarping of the crust leading to a relief of pressure and partial melting at the base of the crust and perhaps in the upper mantle, with the production of salic differentiate rock types. These would be formed not by fractional crystallisation, as is widely supposed, but by partial melting of parent crystalline materials such as alkali basalt. This overcomes the problem of the quantity of parent magma required if the East African lavas were produced only by fractional crystallisation (Wright, 1971). However, the proposed mechanism of lateral compression to explain the doming movements (Wright, 1970) is difficult to reconcile with the tensional features observed within the rift system (Le Bas, 1971).

The lack of continuity within the rift system has been taken to indicate that there are a number of independent systems within East Africa. Le Bas (1971) explains the uplift in terms of vertical forces, rather than horizontal compression, resulting from a phase change from a dense to a less dense mineralogical assemblage at depth (Magnitsky and Kalashnikova, 1970) and degassing of the deep upper mantle (Harris, 1969).

Gass (1970), also recognising several regions of doming, assumed that each is a result of localised thermal disturbance involving a discrete portion of the mantle being hotter than its surroundings, resulting in heat and mass transfer (Elder, 1966; Harris, 1970). Partial melting and an increase in volume due to the formation of light high-temperature minerals would cause vertical uplift, but

while still in an early stage of development a low thermal gradient, and hence low heat flow, would mean partial melting at depths of about 60 km to produce alkali basalt magma. This would correspond to the situation in much of the East African rift system, whereas for the Red Sea or the Afro-Arabian Dome (Gass, 1972), continued magma injection through the crust has raised the thermal gradient with the zone of partial melting extending to within 10 km of the surface and favouring the production of tholeiitic basalts (Green, Green and Ringwood, 1967). This does not imply that all such litho-thermal systems develop into sources of ocean floor although the presence of less alkaline rocks in the Ethiopian Rift (Harris, 1969; Mohr, 1963) could mark an intermediate stage, with fractionation in a lower pressure region as the magma rises towards the surface. Also, Mohr (1971) has found in Northern Ethiopia that basalts with tholeiitic affinities are associated with the rift, but alkaline basalts are observed on the rift plateaux, corresponding to their formation at different depths. This change in composition, which probably relates to a lowering of the thermal gradient away from the axis of the structure, has parallels elsewhere; in the Rio Grande Depression (Lipman, 1969) and in oceanic ridge systems (McBirney and Gass, 1967).

CHAPTER 2

THE KAPTAGAT ARRAY STATION

2.1. Introduction

The Seismic Array Station at Kaptagat in western Kenya, (Fig.6.) was set up in August, 1968 by the University of Durham Geology Department as part of an East African Seismic Project. The project objectives were to study the seismicity and the crust and upper mantle structure of East Africa. Surface Wave Dispersion data from permanent WWSSN stations was to provide information about structure on a broad scale, and temporary array stations were installed in regions of particular interest to investigate problems in more detail, using a variety of seismic techniques.

Kaptagat is situated on the Uasin Gishu lava flows, 45 km. north-east of Kapsabet and 10 km west of the Elgeyo Escarpment, which forms the western margin of the Kenya Rift valley. The choice of Kaptagat as an array site allows the monitoring of regional earthquakes from around both the eastern and western branches of the rift system and also from other seismically active regions such as the Kavirondo and Speke Gulf Rifts. In addition to the mapping of seismicity in these areas the array data, including that relevant to distant earthquakes, can be used to study the shallow and deep structure beneath the Kenya Rift and the surrounding plateau areas.

2.2. Geology of the Kaptagat Area

Kaptagat is situated 2.39 km above sea level on the Uasin Gishu plateau (Fig.6), which is characterised by phonolite lavas dipping gently westward. There are two major lava flows (Jennings,

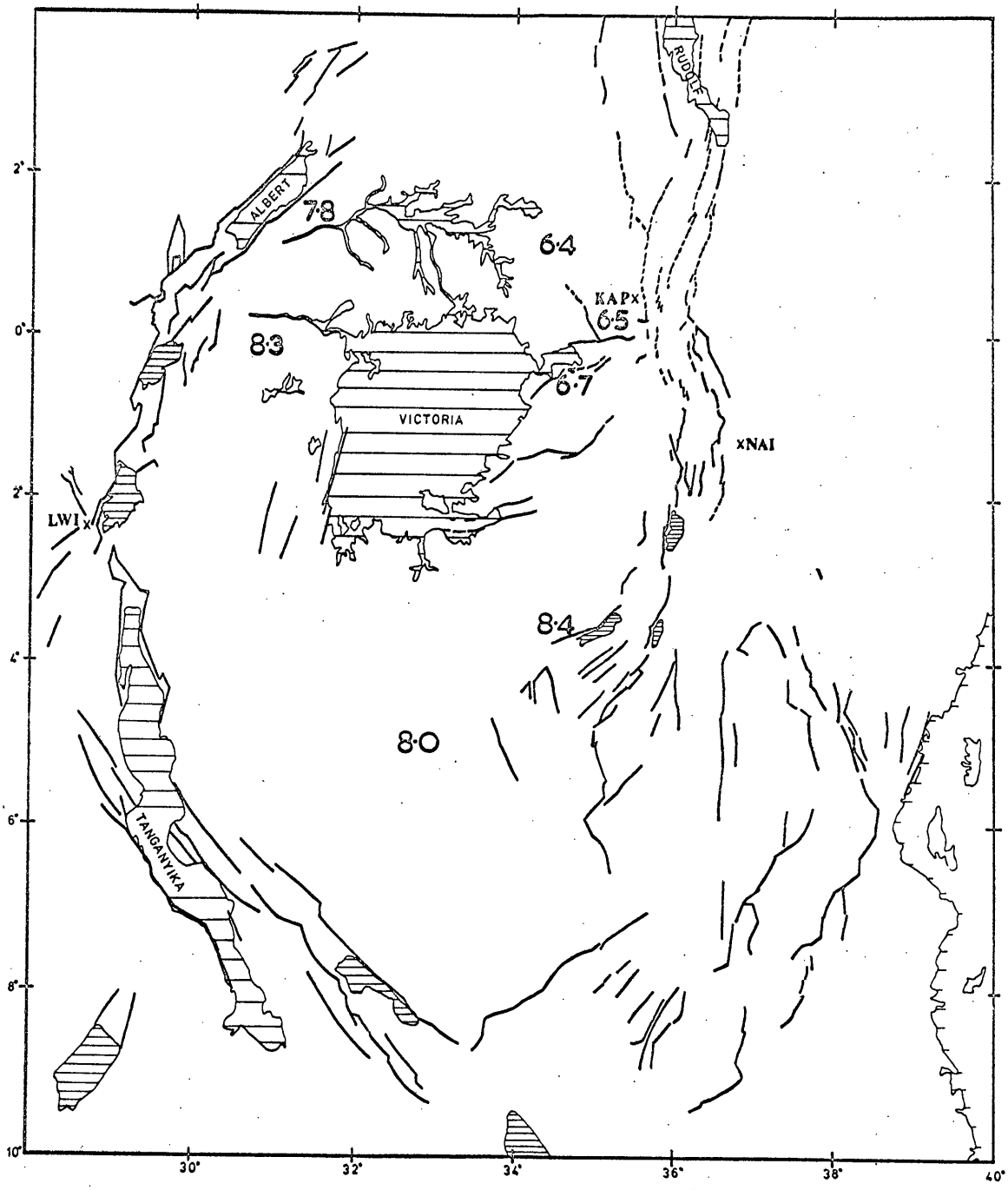

Fig.6. Map of Western and Eastern Rifts showing major faults. Also summaries of P-wave velocities in km/sec for regional earthquake arrivals at Kaptagat (KAP).

1964). The lower Phonolite flow, exposed to the west of Kaptagat and extending further north towards Kitali, is sparsely porphoritic. The Upper Phonolite flow is generally coarser and contains large nepheline and feldspar phenocrysts and overlies the earlier flow immediately east and north of Kaptagat, with a near continuous erosion-scarp at the junction of the two. The Lower Phonolite lies directly on the Precambrian basement system gneisses in the north, although locally there may be a thin intervening pyroclastic layer. The basement gneisses have a regional strike of NNW-SSE with steep dips to the north-east. An estimation of the depth of lava beneath Kaptagat can be obtained from borehole measurements in the area. The only drilling site at which the phonolite was pierced showed that this was at 144 metres, with about 4 metres of soil at the surface. As this site is 15 km south-west of Kaptagat and on the Lower Phonolite flow, this result and those from other sites suggest that there is 150-200 metres of phonolite lava underneath the array station.

The plateau phonolites were erupted in Middle Miocene times after the early periods of major Tertiary uplift, with lava flooding over the rift shoulders and infilling the young rift valley. Isotopic ages for the lava are generally in the range 12 - 13.5 m.y. (King and Chapman, 1972). The rapid and voluminous eruptions of lavas and the presence of phonolitic pyroclastic centres have led to the suggestion that there were a number of central sources within the rift, concealed during later volcanic episodes. However, it is more usual to attribute the flows to fissure sources, probably on the rift shoulders, (Jennings, 1964; Williams, 1970). This is inferred from the gentle dips and the north-south trend of the lava contours, although the presence of fissures has not been confirmed, despite deep erosion of the rift shoulder volcanic succession.

The Kapsabet Plateau Block is defined by faults to the west and south and by the Elgeyo escarpment to the east. To the west, the Nandi fault runs NNW-SSE and can be traced discontinuously from Mt. Elgon, with detailed mapping south-west of Kapsabet showing several faults of similar trend cutting perpendicular to the Nyando escarpment, which forms the northern extension of the Kavirondo Gulf Rift. The Nyando escarpment runs ENE-WSW until obscured by the uppermost lavas of the Tinderet volcano which lies immediately south of the Uasin Gishu phonolites. Further towards the rift escarpment it is inferred from drainage patterns that subsequent movement along the Nyando fault has caused an escarpment trending east-west. This forms the southern boundary of the Kapsabet Plateau. The oldest rocks overlying the Precambrian basement are early Miocene sediments and the differing heights of these beds around the Nyando fault zone show that faulting postdated their deposition.

2.3. Array Siting and Design

In the design and installation of an array of seismometers, several often conflicting considerations have to be balanced to obtain optimum shape and dimensions. A simple arrangement of two perpendicular lines of instruments allows determination of both apparent ground velocity and azimuth of approach for earthquake waves. The choice of array dimensions is controlled partly by the type of arrivals to be studied and the interpretation techniques available. For velocity filtering, for instance, the sharpest response is found to be when the array arms are longer than the signal wavelength but less than five wavelengths (Whiteway, 1965; Birtill and Whiteway, 1965). Obviously, high velocities cannot be accurately determined by a very small array unless exact

measuring methods are employed. On the other hand, with a large array lateral variations in sub-surface geology, if not corrected for, can cause inaccuracies. In addition a large array can often be difficult and expensive to run efficiently.

The Kaptagat array consists of ten Willmore Mk.II short-period seismometers set vertically to two seconds period and arranged in an approximate inverted L-shape (Fig.7.), the yellow (Y) line running east-west and the red (R) line slightly NNE-SSW. With arm dimensions of 4 - 5 km., good velocity filtering response can be obtained for P-waves from regional events of frequency 2 - 5 c/s and with up to sub-Moho velocities. Other methods can be used for analysing the velocities of distant earthquake P arrivals. The instruments are set on phonolite, to ensure good seismic coupling and minimise the effect of any local geological variations. The selection of these sites and of the implied array dimensions also helps to reduce maintenance problems.

The pits were surveyed using a compass and line method and the pit co-ordinates are given relative to a point approximately at the crossover of the two arms (Table 4).

2.4. Recording System

The recording system is substantially the same as that described by Long (1968). Signals from the seismometers are communicated to the recording station by twin field-telephone cable after being amplified and frequency modulated within the seismometer package. At the central station, signals from the ten seismometers and from one long-period instrument are played on to one inch, fourteen track magnetic tape at a speed of 15/160

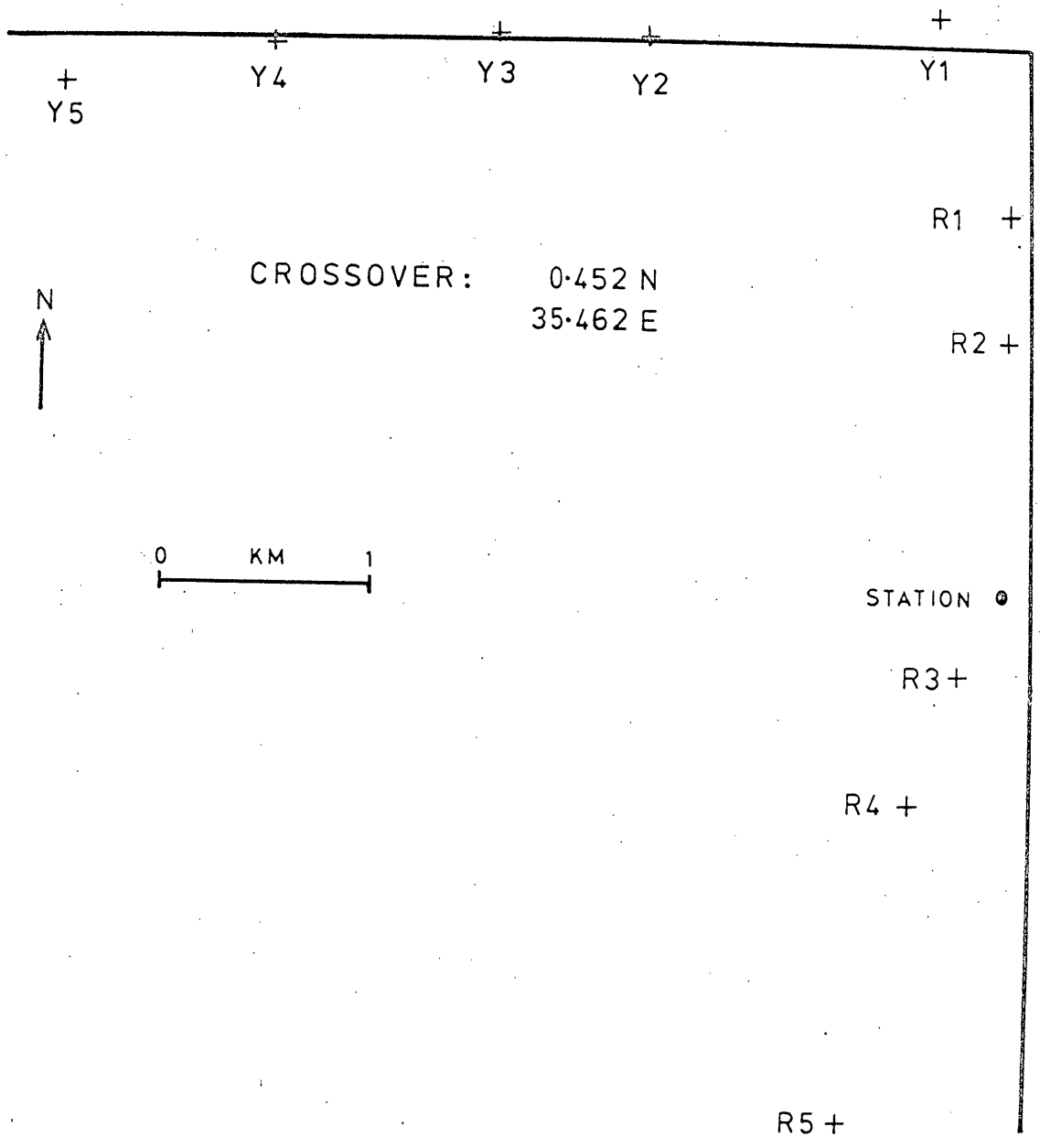

Fig.7. Plan of Kaptagat seismic array with Red (R) and Yellow (Y) lines of seismometers.

TABLE 4

PIT CO-ORDINATES AND ALTITUDES

Pit	x_i(km)	y_i(km)	Estimated Errors (km)	Pit Elevation(metres)
Y1	-0.446	0.166	± 0.0010	0.0
Y2	-1.888	0.003	± 0.015	-30.0
Y3	-2.645	0.025	± 0.030	-50.0
Y4	-3.720	-0.013	± 0.010	-50.0
Y5	-4.750	-0.250	± 0.060	-70.0
R1	-0.098	-0.766	± 0.010	+10.0
R2	-0.114	-1.425	± 0.020	+20.0
R3	-0.365	-3.077	± 0.010	+30.0
R4	-0.663	-3.736	± 0.030	+10.0
R5	-0.925	-5.200	± 0.010	+30.0

in/sec. A binary time code giving the day, hour, minute and seconds is generated by a quartz crystal clock and recorded on the tape, with a radio channel recording Greenwich Mean Time to check the accuracy of the station clock.

To check that the seismometer lines are functioning and also to give amplitude information, calibration pulses can be generated within the seismometer package by remote control from the recording station and then transmitted along the signal line and so on to the tape. The entire system is powered by a single set of twelve 6-volt accumulators at the station, the power being fed down the twin cable that also carries the frequency modulated seismic signal. This arrangement avoids any difficulties that might be incurred with power sources remote from the central station. Each magnetic tape can record continuously for about eleven days.

2.5. Monitoring of Recordings

Playback facilities are available at the Kaptagat recording station and preliminary picking lists are prepared on site giving details of all events recorded. For the purpose of this study, these were used in conjunction with the epicentral information from the Preliminary Determination of Epicentres by the United States National Oceanic and Atmospheric Administration (NOAA) - formerly the U.S. Coast and Geodetic Survey - and the Atomic Weapons Research Establishment GEDESS (Young and Gibbs, 1968) processing of these results to monitor and catalogue all teleseismic events recorded for distances 15° - 99°. For recordings covering the period July 1970 to May 1971, seventy-eight events were selected for arrival time analysis and thirty-four events for the $dT/d\Delta$ study. The criteria used in selection will be discussed in Chapters 3 and 4.

CHAPTER 3

PROCESSING OF THE ARRAY DATA

3.1.1. Measurement of slowness and azimuth

The derivative of the travel-time curve for P-waves is generally denoted by $dT/d\Delta$ or "slowness". This quantity can be estimated using an array of seismometers as the inverse of the phase velocity of a wave crossing the array. If the instruments are arranged in a suitable geometrical pattern, such as two perpendicular intersecting lines, a seismic wave will cross the array with a finite apparent ground velocity and arrive at different seismometers at different times. The apparent velocity vectors can then be determined. There are two main methods that can be used.

One technique is that of velocity filtering, with the outputs of individual seismometers being combined after inserting time delays corresponding to a signal wave of particular velocity and azimuth of approach. These delays can be altered until the maximum correlator response is reached and the inserted delays cancel those incurred at the seismometers by the signal. Other procedures can be used to improve the clarity of a desired signal.

The second technique is that of onset time analysis. The arrival times of the signal at each seismometer are read from playouts of the recorded waveforms and a simple set of equations relating the geometrical co-ordinates and arrival times for each instrument to the signal velocity and azimuth can be solved using

a computer.

The latter method may provide more accurate results than other processing techniques (Mitchell, 1969; Corbishley, 1969). The use of correlator methods generally requires that the array dimensions be at least as great as the signal wavelength for a sharp velocity response using an L-shaped array of instruments, (Whiteway, 1965; Birtill and Whiteway, 1965). For the analysis of teleseismic signals, this would suggest an array of dimensions of the order of 20 km would be necessary for good correlator response. Using onset time analysis with clear early arrivals, it should be possible to read the records to an accuracy of about 0.01 seconds which would give reliable results even with a small array.

3.1.2. Onset Time Analysis

Consider a two-dimensional array of m seismometers at points x_i, y_i, relative to some origin, usually the approximate crossover point of the two arms (Fig.8.). Seismometer i is then at a radial distance R_i from the origin and at azimuth θ_i. If a seismic signal traverses the array in direction OA at azimuth α with velocity V and an assumed plane wavefront, we can derive the following expressions (Carpenter, 1966):-

Apparent velocity of wave along R_i is $\dfrac{V}{\cos(\theta_i - \alpha)}$

Arrival time of wave at x_i, y_i, relative to the origin O is O_i, where:

$$O_i = \frac{-R_i \cos(\theta_i - \alpha)}{V} = \frac{-(x_i \sin\alpha + y_i \cos\alpha)}{V}$$

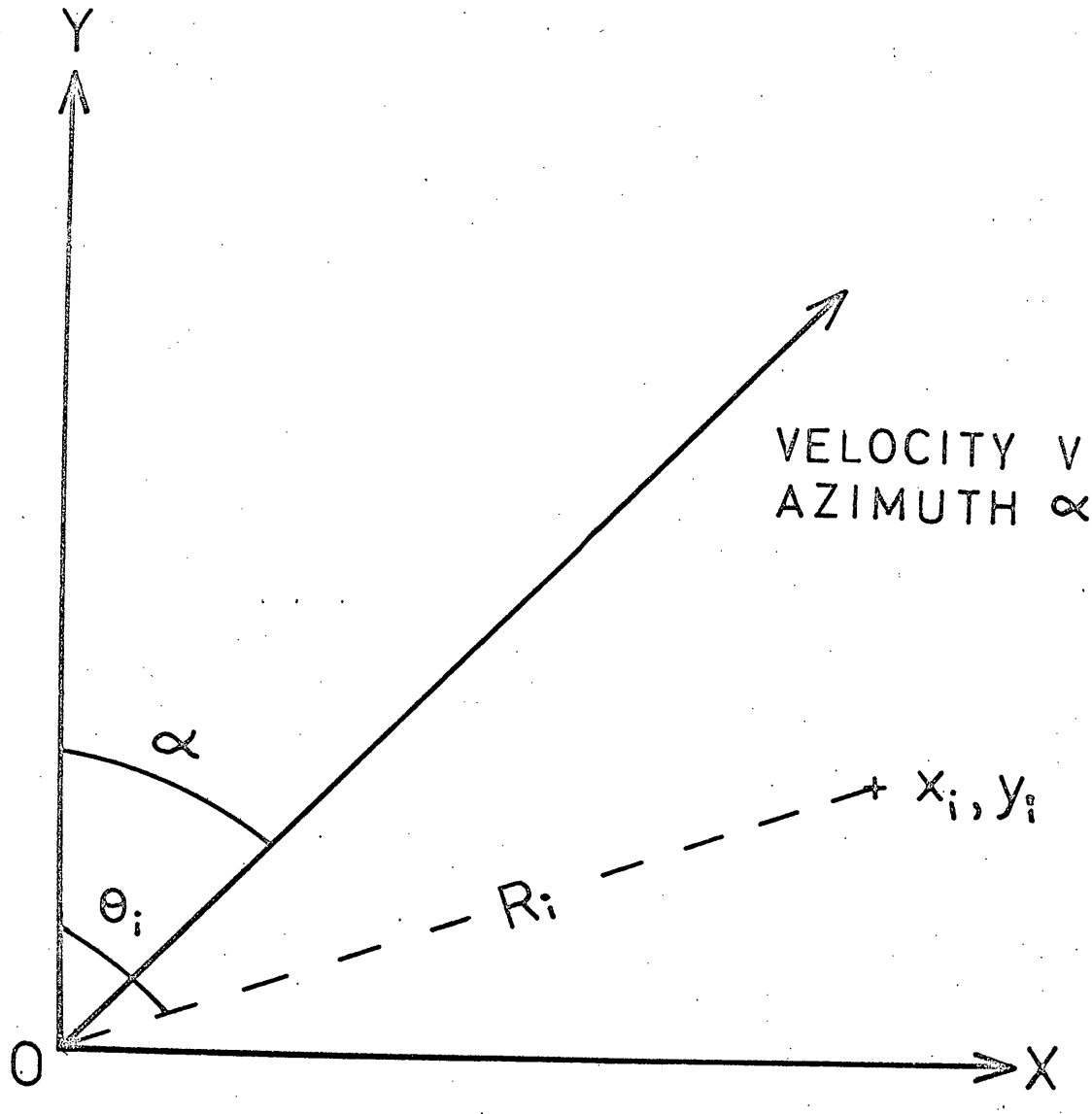

Fig.8. Schematic diagram of a wave crossing an array.

The arrival time relative to an arbitrary zero time, which will normally precede the onsets at x_i, y_i, is given by:

$$t_i = O_i + t_o$$

where t_o is the arrival time at the origin. Therefore,

$$t_i = t_o - \frac{(x_i \sin \alpha + y_i \cos \alpha)}{V} + \varepsilon_i$$

ε_i is the error in the observed arrival time, t_i.
Slowness is the reciprocal of phase velocity and we can write:

$$t_i = C - R_i \cos(\theta_i - \alpha) \cdot \frac{dT}{d\Delta} + \varepsilon_i. \qquad 3(i)$$

Here, $C = t_o$.

With m seismometers working we can observe t_i for i = 1, m and we know x_i, y_i. Therefore we have m equations of condition and three unknowns, C, α and V(or $dT/d\Delta$), so we can solve 3(i) by least squares if ε_i are normally distributed to give C, $\frac{\sin \alpha}{V}$ and $\frac{\cos \alpha}{V}$.

If $S1 = \frac{\sin \alpha}{V}$, $S2 = \frac{\cos \alpha}{V}$, $S3 = C$,

then:

$$\alpha = \tan^{-1}(S1/S2), \quad V = (S1^2 + S2^2)^{-\frac{1}{2}}$$

Hence a value for $dT/d\Delta$ is given by the inverse of V. As t_i is the arrival time relative to an arbitrary origin we can measure onset times for a particular event from any convenient baseline on the playouts. In general, therefore, we can say, for the kth event in our analysis,

$$t_{ik} = C_k - R_i \cos(\theta_i - \alpha_k) \left(\frac{dT}{d\Delta}\right)_k + \varepsilon_{ik} \qquad 3(ii)$$

3.1.3. Method of Least Squares

To estimate the regression coefficients S1, S2 and S3, we solve the equations of condition, 3(ii) by the method of least squares. A matrix inversion method is preferred as it simplifies the calculation of confidence limits to give an estimate of the reliability of the regression coefficients.

A full mathematical treatment of this method is given by Douglas (1967), and this is summarised below.

Given an equation of condition,

$$y_i = x_1 a_{i1} + x_2 a_{i2} + \ldots\ldots x_n a_{in} + \varepsilon_i$$

Then $x_1, x_2 \ldots x_j \ldots x_n$ are the unknowns and $a_{i1} \ldots a_{in}$ are the independent variables. ε_i is the error in y_i.
We have m such equations (i = 1,m) where m > n.

For the best estimate of x_i, $\dfrac{\partial \sum_{i=1}^{m} \varepsilon_i^2}{\partial x_i} = 0.$

This implies:

$$x_1 \sum_{i=1}^{m} (a_{i1})^2 + x_2 \sum_{i=1}^{m} a_{i1}a_{i2} + \ldots x_n \sum_{i=1}^{m} a_{i1}a_{in} = \sum_{i=1}^{m} a_{i1}y_{i1}$$

Similar equations are obtained from equating $\dfrac{\partial \sum_{i=1}^{m} \varepsilon_i^2}{\partial x_j}$ to zero.

using j = 2,n, and multiplying each equation of condition by its own coefficient of x_j and summing coefficients.
These, the normal equations, can be written conveniently in matrix form:

$$\begin{bmatrix} \sum a_{i1}\,a_{i1} & \sum a_{i1}\,a_{i2} & \cdots \sum a_{i1}a_{in} \\ \sum a_{i2}\,a_{i1} & \sum a_{i2}\,a_{i2} & \cdots \sum a_{i2}a_{in} \\ \vdots & & \\ \sum a_{in}\,a_{i1} & \sum a_{in}\,a_{i2} & \cdots \sum a_{in}a_{in} \end{bmatrix} \begin{bmatrix} x_1 \\ x_2 \\ \vdots \\ x_n \end{bmatrix} = \begin{bmatrix} \sum a_{i1}y_1 \\ \sum a_{i2}y_2 \\ \vdots \\ \sum a_{in}y_n \end{bmatrix}$$

Where the summations are for $i = 1, m$.

Symbolically, $Ax = y$ and $x = A^{-1}y$ 3(iii).

Hence we can determine the unknowns by inverting the matrix A. The triangular decomposition method is used with a standard computer subroutine (Douglas, 1967).

3.1.4. Estimation of Confidence Limits

From Section 3.1.3., the regression coefficients can be calculated by solving the normal equations. We can then estimate confidence limits which give a range of possible values for each coefficient. There is then a given probability that the true value of a coefficient lies within these limits. Again, a full mathematical treatment is given elsewhere (Douglas, 1967).

If x_j is the j th unknown, it can be shown that,

$$x_j = \sum_{i=1}^{m} y_i K_{ji}$$

y_i is the dependent variable and K_{ji} a function of the independent variables only. Also, if $V(x_j)$ is the variance of x_j, and σ^2 the variance of y_i (i.e. the variance of errors ε_i), then

$$V(x_j) = \sum_{i=1}^{m} K^2_{ji}\, V(y_i) = \sigma^2 \sum_{i=1}^{m} K^2_{ji}$$

We can evaluate $\sum_{i=1}^{m} K^2_{ji}$ as this is the j th diagonal element

of the inverted matrix A^{-1} in equation 3(iii).

We need to estimate the variance of the errors ε_i, which will be:

$$s^2 = \frac{\sum_{i=1}^{m} (\varepsilon_i^{11})^2}{m - n}$$

ε_i^{11} is obtained by substituting the regression coefficients in the equations of condition.

m - n is the number of degrees of freedom, as we have m equations and n unknowns.

If x_j are normally distributed with variance $s^2 \sum_{i=1}^{m} K^2_{ji}$ the 95% confidence limits are:

$$x_j \pm 1.96 \sqrt{s^2 \sum_{i=1}^{m} K^2_{ji}}$$

This is, however, only true if the number of degrees of freedom is large. If this is not the case, we can say the confidence limits are:

$$x_j \pm t \sqrt{s^2 \sum_{i=1}^{m} K^2_{ji}}$$

Where t is students t and depends on (m - n) but is always greater than 1.96. In particular, with no more than ten seismometers, we can never have more than seven degrees of freedom for each event.

3.1.5. The Data.

Only teleseismic events listed in the NOAA Preliminary Determination of Epicentre bulletins were used for the $dT/d\Delta$ and delay time measurements. Hence both the focal depth and epicentral

co-ordinates are known and the epicentral distance and great circle azimuth can be calculated. Any such listed events likely to have been picked up by the Kaptagat Array were investigated using the preliminary on-site picking lists and the AWRE GEDESS printouts which include extrapolated arrival times at Kaptagat using the Jeffreys-Bullen (1940) travel-time tables and the NOAA epicentres.

Events were used in the $dT/d\Delta$ study only of clear onsets were recorded on at least three seismometers on each arm and, in fact, most of the 34 events analysed were picked up clearly on at least eight instruments.

3.1.6. Reading Onset Times

Because of the small dimensions of the array, a method was needed to measure the relative arrival times of the signal at each seismometer to a few hundredths of a second. Three methods can be used: (1) measuring the relative arrival times of the first peak on each record; (2) measuring the first cross-over point and (3) matching waveforms. Corbishley (1969) studied the accuracy of the three approaches by analysing 22 events from the same area and he found that the lowest repeatable error in measuring the onset times came with (3). This has been used throughout this study.

The waveform matching technique was first used by Evernden (1953) to calculate surface wave velocities across tripartite arrays. It has the advantage that it does not require the recognition of the first motion or crossover and so, at least in principal, signals with fairly emergent onsets could be processed in this way.

The seismometer outputs are recorded on 1" magnetic tape

and were played out, unfiltered, on to paper using a 16-channel Jet Pen Recorder. All ten signal channels were outputted simultaneously with the binary time code. The playout speed was adjusted so that 1 second on the records corresponded to about 52 mm, so that an accuracy of 0.01 seconds could be achieved by reading the records to a few tenths of a millimetre.

The waveform matching method involves, for each event, tracing the waveform of one of the signals on to transparent paper and then matching this curve by eye to every other seismometer output, the relative displacements of the traced curve being measured relative to some baseline drawn on the paper record. All events were played out eight times in this way, with the three unknowns calculated for each of these and then averaged. To allow for any variation in the speed of either the magnetic tape or the Jet Pen Recorder paper, the equivalent length of one second was measured for each playout and the range of values was generally less than 0.01 seconds. In addition, small corrections had to be made for the non-alignment of the Jet Pens. The ink jets are fixed perpendicular to the direction of the trace and a facility is available for generating a calibration pulse simultaneously on the output channels. Any relative displacement of the pens could, if significant, be measured and the onset time readings adjusted by this amount. This calibration was checked as each event was played out.

Corbishley (1969) argued that variations in seismometer characteristics can introduce errors in the onset time analysis method, and concluded that in such a situation impulsive signals should be used and wherever possible this was done.

Lilwall, 1969; Douglas, 1967b; Davies and McKenzie, 1969). Such errors have been interpreted in terms of anisotropy in the upper mantle beneath island arcs (Cleary, 1967) or, in the concepts of plate tectonics, a slab of oceanic material descending into the mantle at the junction of two colliding plates and introducing an azimuthally dependent source term to bias travel time estimates (Davies and McKenzie, 1969). On the other hand, an alternative explanation could be station bias, or the lack of suitable corrections for near-station effects (Douglas and Lilwall, 1968).

The degree to which either or both of these factors influence the results for earthquakes analysed in this study is difficult to asses, and in the absence of any more definitive information, the above figures for the Pacific will be assumed. Hence, the uncertainties in the NOAA data will be taken as 25 km in epicentral coordinates and 50 - 75 in focal depths.

Consider an epicentre E, which is at azimuth ϕ to a station, S, distance Δ away (Fig.9.). Assume the apparent epicentre, E^1 is distance D from the true epicentre. Then the calculated epicentral distance and azimuth have errors $d\Delta$ and $d\phi$ respectively.

From the Sine Theorem for spherical trigonometry,

$$\sin \Phi = \frac{\sin D}{\sin \Delta} \cdot \sin \Theta$$

where Θ is the angle EE^1S.

The maximum value of $d\Phi$ is when $\Theta = 90^\circ$ so that

$$|d\Phi|_{max} = \frac{\sin D}{\sin \Delta}$$

If we take $\Delta = 20^\circ$, and D = 25 km = 0.22°,

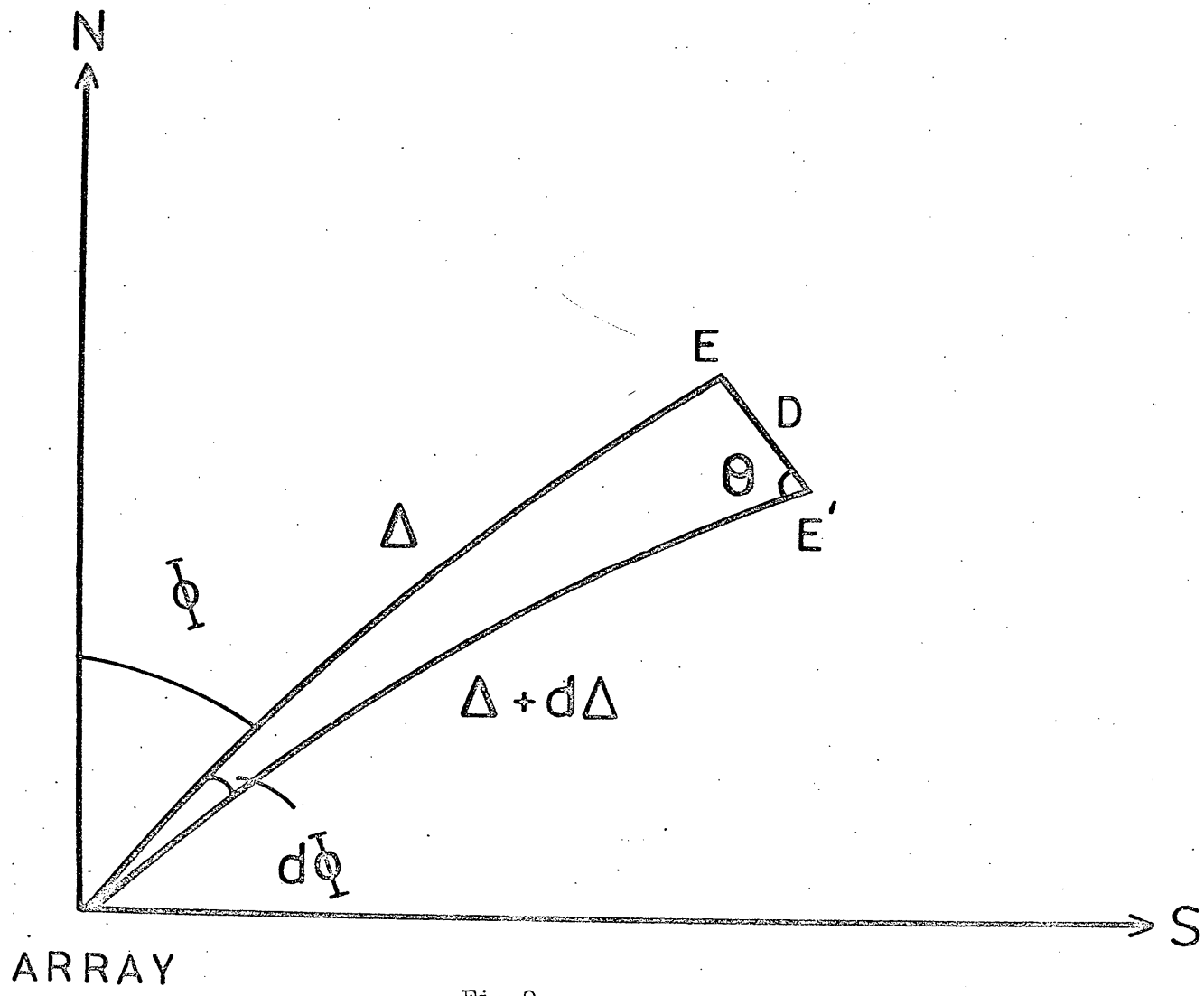

Fig.9.

$$\sin |d\underline{\Phi}|_{max} = 0.7^{\circ}.$$

Therefore for an epicentre at a distance of about 20°, the maximum error in the azimuth to the station will be 0.7°, and the maximum error in epicentral distance is assumed to be 25 kms, corresponding to a deviation in the tabulated (Herrin et al, 1968) values of slowness of 0.1 sec/deg. The error in focal depth of 75 km for a surface focus event will also be about 0.1 sec/deg. These values will be less for more distant earthquakes.

(3). Altitude Corrections

The seismometers are not all at the same altitude, and correction is made for the different distances a signal must travel through near-surface rocks to each instrument.

Assuming we can approximate the signal path to be vertical, then each onset time t_i is corrected to

$$t_i - \frac{(h_i - h_o)}{V_s}$$

h_i, h_o are the heights of the i th seismometers and the reference seismometers respectively. V_s is the subsurface P-wave velocity. All seismometer sites are on phonolite and samples from Kaptagat show a mean density of 2.50 gm/cc. A corresponding value for V_s of 4.5 km/sec is used (Woollard, 1959; Talwani et al, 1959).

(4) Focal Depth Correction.

We know the epicentral co-ordinates for all events as well as their focal depths, so that we can correct for the effects of the latter on $dT/d\Delta$ using the earth structure of Herrin, Tucker

Taggart, Gordon and Lobdell(1968)(Fig.10). Hence we can deduce the corrected values of slowness as expected from Herrin et al's (1968) Seismological Tables.

Assuming this simple structure, the corrected distance CDEL for a focus within the first layer is:

$$CDEL = DEL + H \cdot \tan i \qquad 3(iv)$$

where H is the focal depth, and i can be calculated from the relation $p = R \frac{\sin i}{V}$

R is the radial distance to the focus, V the velocity at this level (Fig.10) and we can take p as $dT/d\Delta$ for distance DEL from Herrin's tables. By simple application of Snell's Law we can extend 3(iv) to cover any focal depth using the same model.

(5) Random Reading Errors

Random errors will occur in reading the records both through variations in the recording and playout systems and also through the observation and measurement of onset times. Although we can correct to a certain extent for the former (Section 3.1.6.), some errors will still remain to affect our estimates of slowness and azimuth.

Assuming the reading errors are independent Gaussian variables with variance σ^2, we also define:

$$[XX] = \frac{1}{m}\sum_{i=1}^{m}(x_i - \bar{x})^2 \qquad [YY] = \frac{1}{m}\sum_{i=1}^{m}(y_i - \bar{y})^2$$

$$[XY] = \frac{1}{m}\sum_{i=1}^{m}(x_i - \bar{x})(y_i - \bar{y})$$

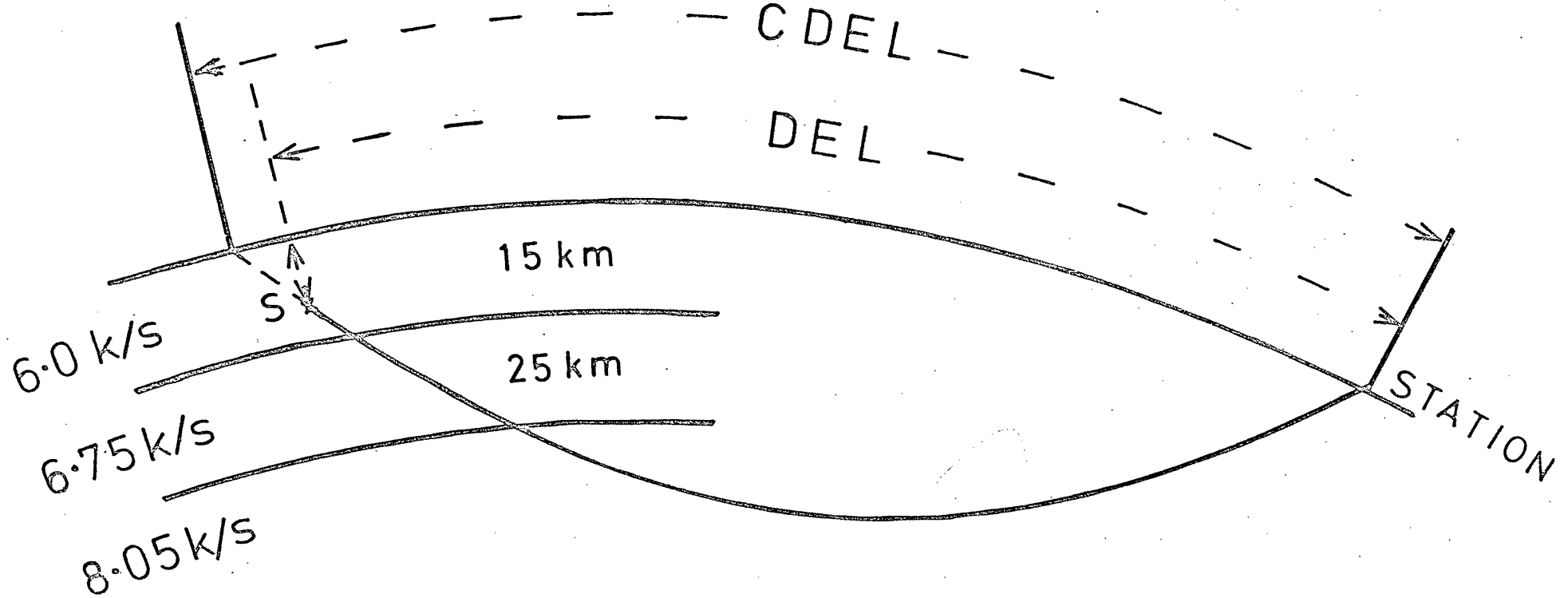

Fig.10. Structure of Herrin, Tucker, Taggart, Gordon, and Lobdell (1968) for correcting epicentral distance for the effect of focal depth.

where x_i and y_i are the co-ordinates of the ith seismometer, where i = 1, m. Then Kelly (1964) has derived the following expressions. The root mean square error in slowness is given by:

$$\frac{\sigma}{\sqrt{mD}}\left[[XX] \cdot \cos^2 A - 2[XY]\sin A \cos A + [YY]\sin^2 A\right]^{\frac{1}{2}}$$

and the root mean square error in azimuth is:

$$S\frac{\sigma}{\sqrt{mD}}\left[[XX] \cdot \sin^2 A + 2[XY]\sin A \cos A + [YY]\cos^2 A\right]^{\frac{1}{2}}$$

where $D = [XX][YY] - [XY]^2$

As the record for each earthquake has been played out several times (Section 3.1.6.), and measurements of onset times made using all playouts, we can estimate σ by calculating the variance of the onset time errors from the multiple readings. The root mean square error averaged over all events is 0.007 seconds, and the corresponding values for the slowness and azimuth errors are shown in Fig.11. These show that for signals from an earthquake at distance $\Delta = 60^\circ$, the random reading errors should not be more than about 0.2 sec/deg.

3.1.8. Discussion of Results

Source parameters for the thirty-four earthquakes used in the onset time analysis are given in Table 5, with the calculated values of $dT/d\Delta$ and azimuth of approach for the Kaptagat array. Error bars are 95% confidence limits. For the purposes of comparison we have assumed that the $dT/d\Delta$ distribution calculated from the travel times of Herrin et al (1968) give "theoretical" values for given distances and that the deviation of the observed travel

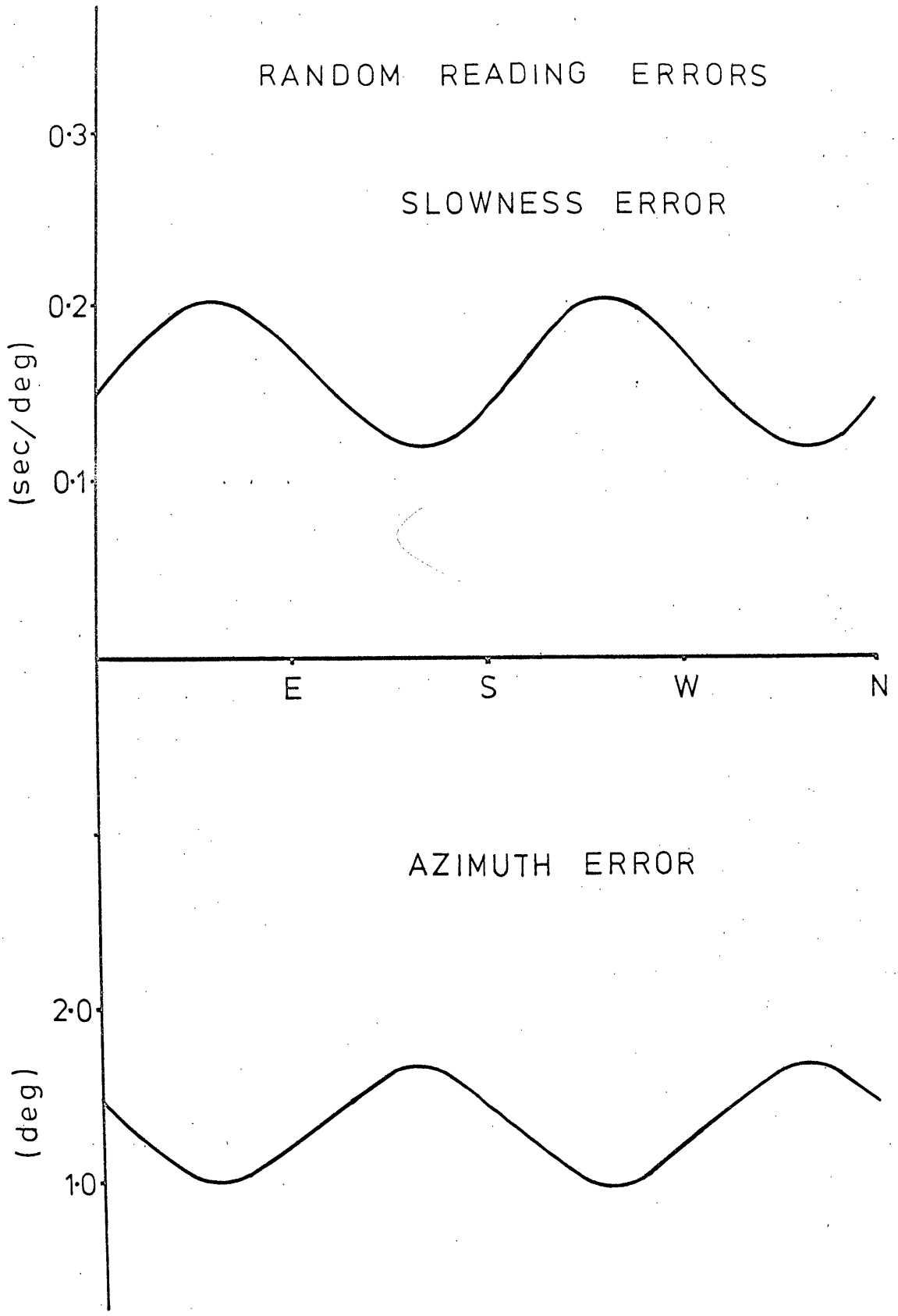

Fig.11. Random reading errors in slowness and azimuth at the Kaptagat array as a function of azimuth for an event from a distance of 60°.

TABLE 5

	EPICENTRAL DATA				MEASURED			MEASURED		
	LAT	LONG	DIST DEG	AZIM DEG	SLOWNESS SEC/DEG	ERROR	ANOMAL	AZIMUT DEGREES	ERROR	ANOMALY
1	75.32	55.15	73.8	5.8	7.56	0.27	1.68	352.7	2.5	-13.1
2	37.82	55.88	41.8	24.5	9.75	1.88	1.58	8.6	6.6	-15.9
3	35.51	58.22	40.9	28.9	10.20	0.64	1.96	17.2	4.4	-11.7
4	49.96	77.76	61.1	29.8	7.78	0.44	1.00	6.3	5.2	-23.5
5	49.82	78.09	61.2	30.0	7.78	0.52	1.00	3.8	5.5	-26.2
6	23.31	55.60	34.0	33.1	13.40	0.90	4.71	27.9	4.1	-5.2
7	36.42	40.07	49.4	38.0	7.72	0.48	0.11	10.4	4.2	-27.6
8	39.94	77.02	54.7	38.8	9.19	0.81	1.92	19.9	4.4	-18.9
9	12.86	48.53	18.2	45.8	11.23	2.14	-0.85	44.6	11.0	-1.2
10	14.83	53.75	23.3	50.8	11.70	1.33	1.86	40.9	6.3	-9.9
11	36.99	136.75	99.7	52.6	4.54	0.49	-0.02	10.3	5.2	-42.3
12	25.71	88.50	57.0	59.3	4.99	0.96	-2.10	30.9	11.5	-28.4
13	26.25	95.13	63.0	60.6	5.53	0.91	-1.13	35.1	9.8	-25.5
14	26.02	95.40	63.2	60.9	5.48	0.56	-1.18	36.2	6.0	-24.7
15	23.76	91.76	59.5	62.5	4.54	1.17	-2.37	46.8	14.5	-15.7
16	22.93	101.03	67.4	65.4	5.40	1.00	-0.96	39.1	11.1	-26.3
17	8.44	57.76	23.8	69.7	9.75	0.65	0.08	60.1	3.5	-9.6
18	19.75	121.33	86.2	70.4	2.65	0.48	-2.22	31.3	11.1	-39.1
19	8.21	58.27	24.2	70.6	9.34	0.53	-0.16	65.9	2.8	-4.7
20	18.63	120.99	85.7	71.5	4.13	0.58	-0.79	33.5	7.4	-38.0
21	18.43	120.88	85.8	71.7	3.89	0.70	-1.03	44.1	10.4	-27.6
22	4.67	97.71	62.4	85.0	3.40	0.38	-3.30	86.1	7.5	1.1
23	4.54	123.02	89.5	85.5	2.77	0.45	-1.94	66.4	10.2	-19.1
24	2.60	97.98	62.6	87.3	4.01	0.34	-2.68	94.3	4.3	7.0
25	1.88	99.16	64.2	88.1	4.12	0.75	-2.50	124.3	9.5	36.2
26	0.94	100.19	65.6	89.2	3.69	0.71	-2.81	84.9	13.2	-4.3
27	-4.33	102.40	67.3	94.9	5.10	0.99	-1.25	85.3	13.2	-9.6
28	-13.69	66.26	33.7	115.9	5.98	0.89	-2.71	113.3	7.0	-2.6
29	-23.49	37.29	24.0	175.8	7.89	0.57	-1.70	172.3	5.2	-3.5
30	-56.01	-27.51	76.2	211.1	7.22	0.61	1.49	238.4	4.5	27.3
31	34.96	13.67	40.1	331.6	9.50	0.55	1.21	325.3	3.6	-6.3
32	43.96	15.96	46.7	340.7	10.90	0.62	3.07	342.6	3.0	1.9
33	74.62	8.41	75.9	352.8	7.36	0.61	1.63	351.0	6.1	-1.8
34	39.03	29.74	38.9	352.9	10.49	1.09	2.13	353.4	6.7	0.5

time derivative from the appropriate tabulated value for an event is its slowness anomaly. Similarly, we can calculate the great circle azimuth of each epicentre from the station from the NOAA data and define the azimuth anomaly for that event as the difference between the observed direction of approach and the great circle azimuth. These slowness and azimuth anomalies are given in Table 5, Fig.12 and Fig.13.

From these it can be seen that the events analysed give rather an uneven angular coverage around the station. The north-east quadrant is well covered with epicentres in the active areas of Southern Europe, Asia and the Far East. However, signals from the west were generally not well recorded during the period of the study, and this, when coupled with the relatively low seismic activity at high magnitudes and suitable distances (except for the Mid-Atlantic Ridge Area) is responsible for a fairly sparse distribution of results from ESE to NNW. Confidence limits on both $dT/d\Delta$ and azimuth are generally substantial, as would be expected for measurements on high velocity signals across a small uncalibrated array. However, some distinct trends can be delineated.

The values of $dT/d\Delta$ show systematic and very pronounced azimuthal variations, which are evident from the anomaly plot. From NW to NNE there are large positive anomalies. That is, the measured slownesses are higher, and the apparent velocities lower, than values for corresponding distances given by Herrin for a mean earth model. On the other hand, between ENE and SE the slowness anomalies are significantly negative. Hence there is a change of sign in the anomaly between about 35° and 60° east of north and another somewhat west of earthquake 29. Despite the uneven distribution of the data,

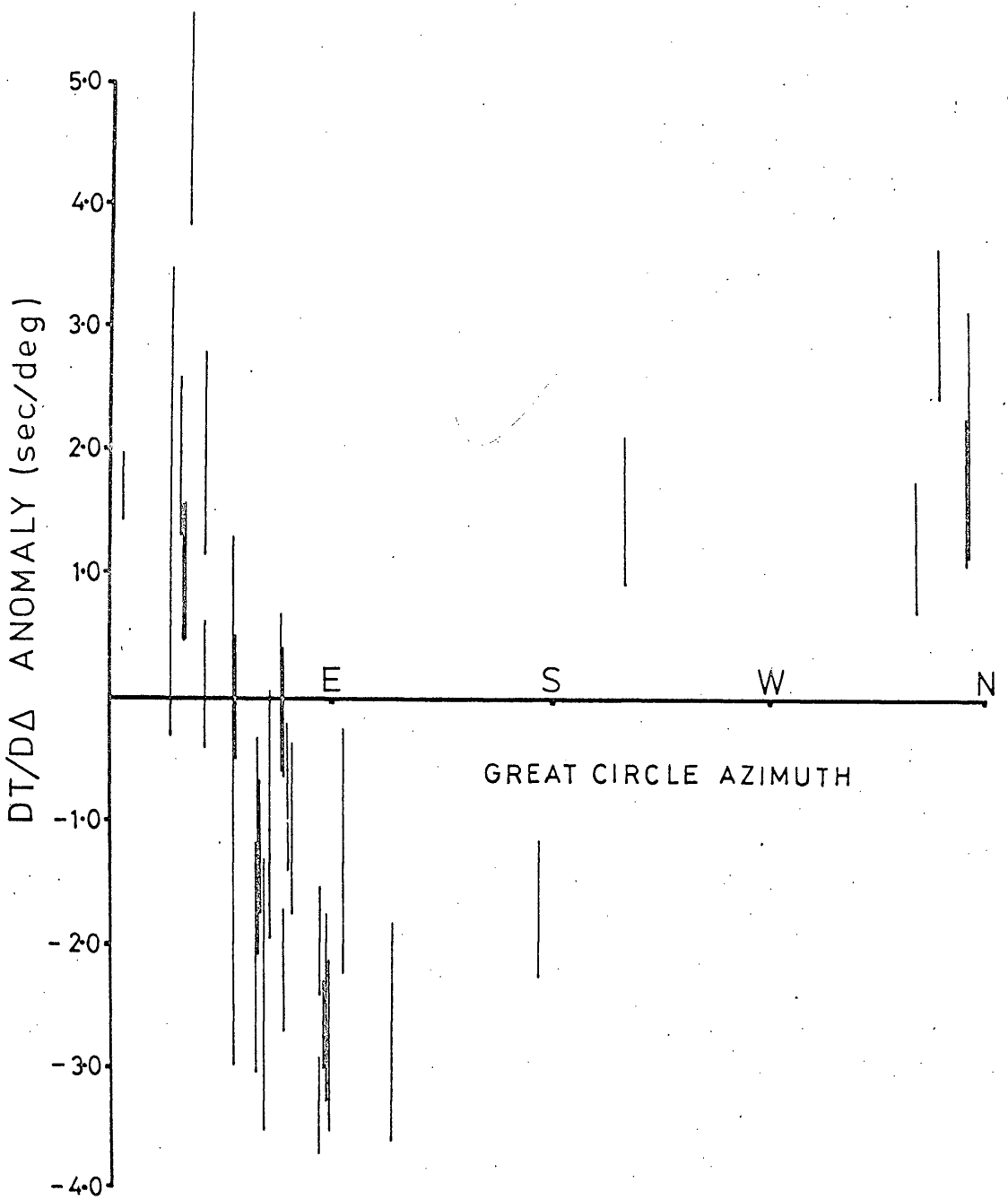

Fig.12. Observed slowness anomaly at Kaptagat. Error bars are 95% confidence limits.

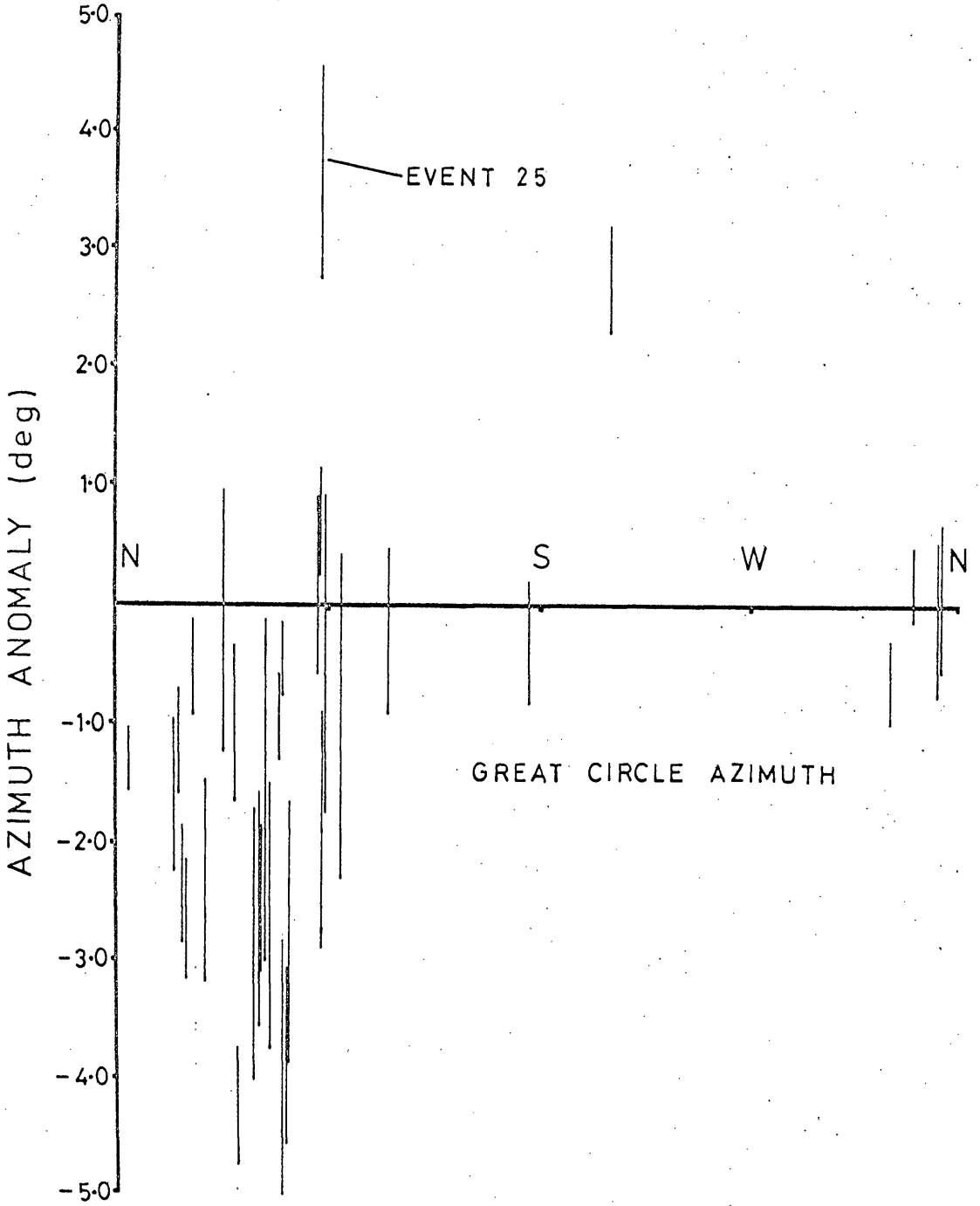

Fig.13. Observed azimuth anomalies at Kaptagat. Error bars are 95% confidence limits.

this suggests that there is a continuous variation in slowness throughout a full circle of azimuths. Although there is scatter for events from similar distances and adjacent epicentres, the positive and negative anomaly peaks are outside the range of the confidence limits.

Fig.12 shows the slowness anomalies for all events, corresponding to signals from different distances. Slowness is, of course, a function of distance and we might expect the anomalies to also show some such dependence. We can consider two small groups of data relevant to epicentres within narrow azimuthal ranges. Events 12 - 21 show anomalies increasing with distance, whereas the smaller group of events 2 - 6 display the opposite variation. Although the data are too few to allow firm conclusions to be drawn, it seems that for large epicentral distances the change in slowness anomaly values with distance is not great compared with the scatter of measurements.

The azimuth anomalies (Fig.13) are also significant although they show greater scatter than the slowness anomalies and a less clearly defined trend. The largest negative values, corresponding to a deviation from the great circle azimuth in an anti-clockwise direction, occur between NE and ENE with changes of sign probably around NNW and between east and south. The anomaly for earthquake 25 is difficult to reconcile with the main body of the data which would predict a negative azimuth deviation. Again considering the two groups of events 2 - 6 and 12 - 21, both show an increase in azimuth anomaly with distance, all the anomalies having the same sign.

Thus, although the variation in the measured azimuths is

less sharp and displays more scatter than that for slownesses, both sets of data show a strong dependence upon the direction of approach to the array. Such systematic changes have been observed at other arrays (Otsuka, 1966a, and 1966b; Niazi, 1966; Greenfield and Sheepard, 1969; Cleary, Wright and Muirhead, 1968). However, the deviations observed at Kaptagat are unusually large.

3.2.1. Analysis of Residuals

Ideally, seismic arrays should be on fairly flat regions that are geologically homogeneous and isotropic. Variations in near-surface structure will cause the speed of seismic arrivals to vary at individual seismometers. Estimates of such effects can be obtained in the following way.

From equation 3(ii) in Section 3.1.2., we can express the onset time residual at the i th seismometer for the k th event as ε_{ik},

$$\varepsilon_{ik} = t_{ik} - C_k + R_i \cdot \cos(\theta_i - \alpha_k) \cdot \left(\frac{dT}{d\Delta}\right)_k \qquad 3(v)$$

However, we can also write $\varepsilon_{ik} = P_i + \varepsilon_{ik}^1$ where P_i is the time correction for the effects of geology underneath the i th instrument, ε_{ik}^1 is the remaining error in t_{ik}.

The values of $(P_i + \varepsilon_{ik}^1)$ for all events studied can be used to define a site correction for each seismometer, which will give information on the structure beneath. This will consist of constant and azimuthally varying terms and can be approximated to a sine curve (Corbishley, 1970) such that

$$P_i + \varepsilon_{ik}^1 = A_i + B_i \sin(Z_k + E_i) + r_{ik} \qquad 3(vi).$$

Z_k is the azimuth of the k th event at the array, and A_i, B_i and E_i are constants for each pit. We can solve this equation by least squares in the presence of errors r_{ik} on $(P_i + \varepsilon_{ik}^{1})$. A better approximation to the onset time residuals would include higher order terms on the right-hand side of 3(vi). However, the additional terms would be small and would complicate any interpretation of the structure beneath the array from these corrections (Corbishley, 1969). In particular, 3(vi) can be taken as an approximate representation of the anomaly associated with a dipping layer underneath the seismometers. The dip at each instrument may be obtained from the phase angle E_i. As $\sin(Z_k + E_i)$ is a maximum when the azimuth Z_k takes the value $(90 - E_i)$, then the pit correction is a maximum when the azimuth is in the direction of dip.

We can compute ε_{ik} for each event by substituting the least squares values of $(dT/d\Delta)_k$, C_k and α_k in the expression for the observed minus the calculated onset times in 3(v). Equation 3(vi) is then solved by least squares for all events and a computer programme has been written for this.

3.2.2. Discussion of Site Corrections.

The site correction terms A_i, B_i and E_i are given in Table 6 with 95% confidence limits, and the onset time residuals ε_{ik} are plotted for each seismometer in Figs. 14 - 18. Superimposed on these graphs are the curves fitted to the residuals.

Site corrections are generally attributed to inhomogeneities in the Earth, but it is not easy to establish which part of the Earth is chiefly responsible. It is assumed here that

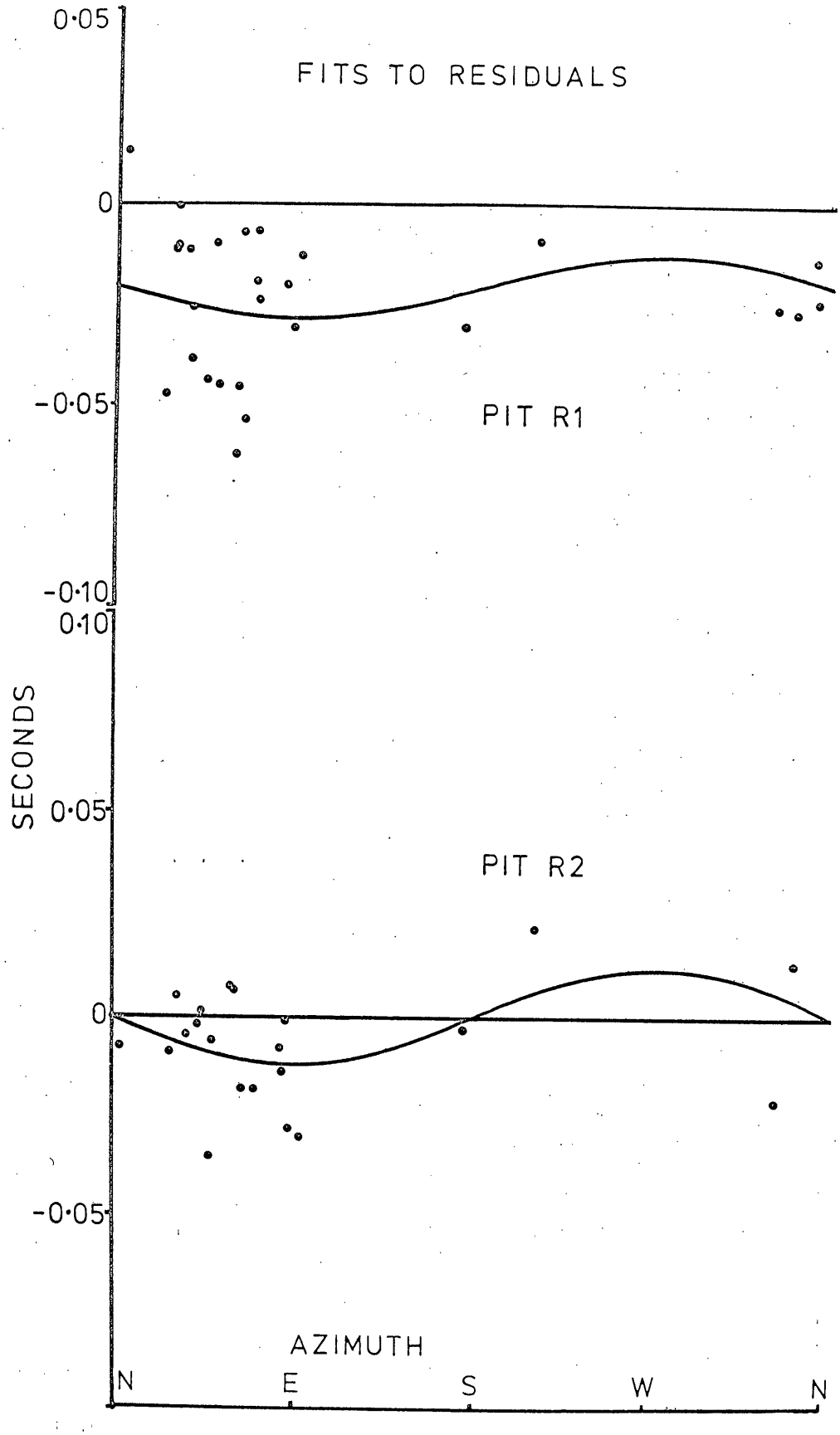

Fig.14. Onset time residuals for seismometers R1 and R2 with fitted sinusoids.

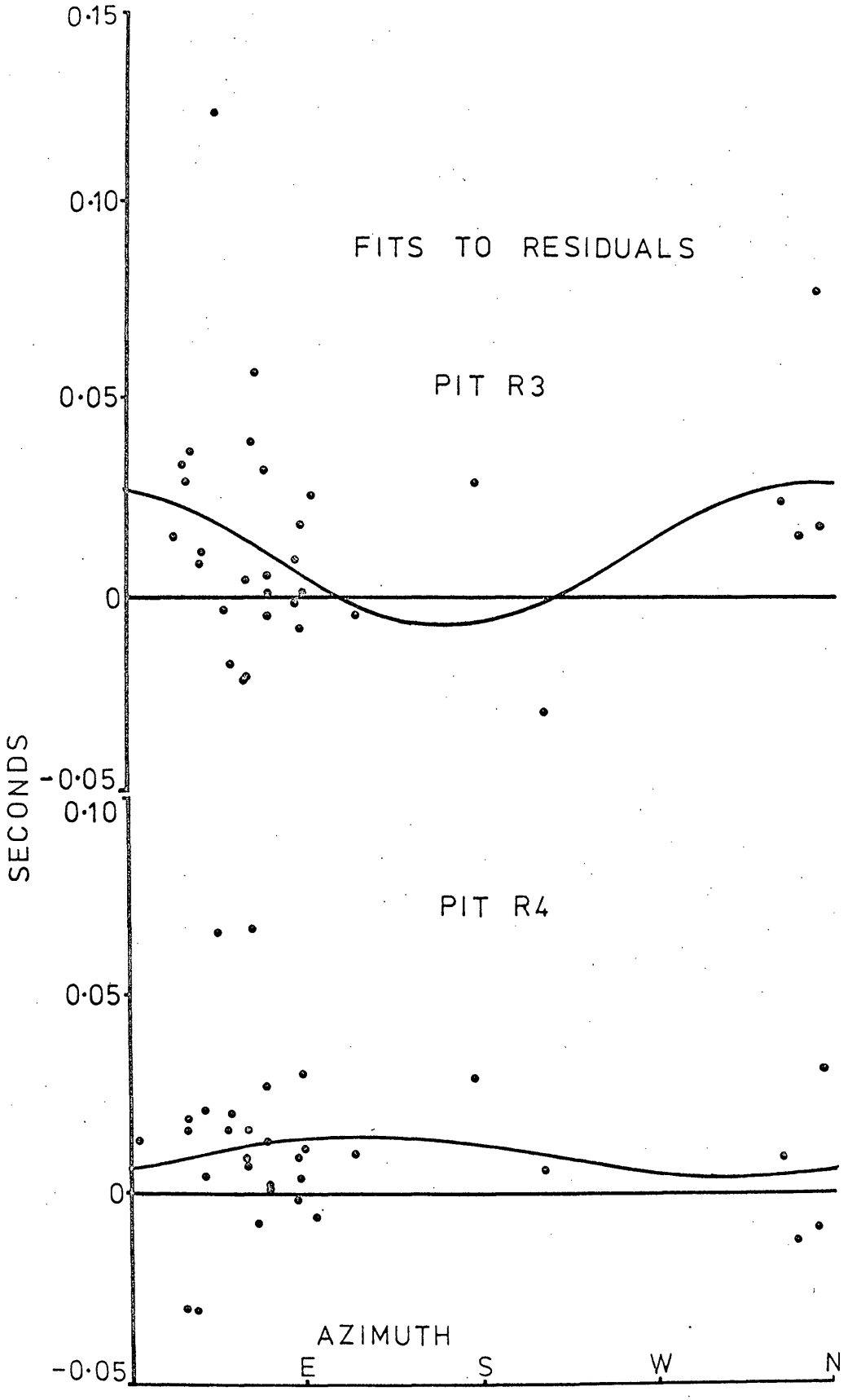

Fig.15. Onset time residuals for seismometers R3 and R4 with fitted sinusoids.

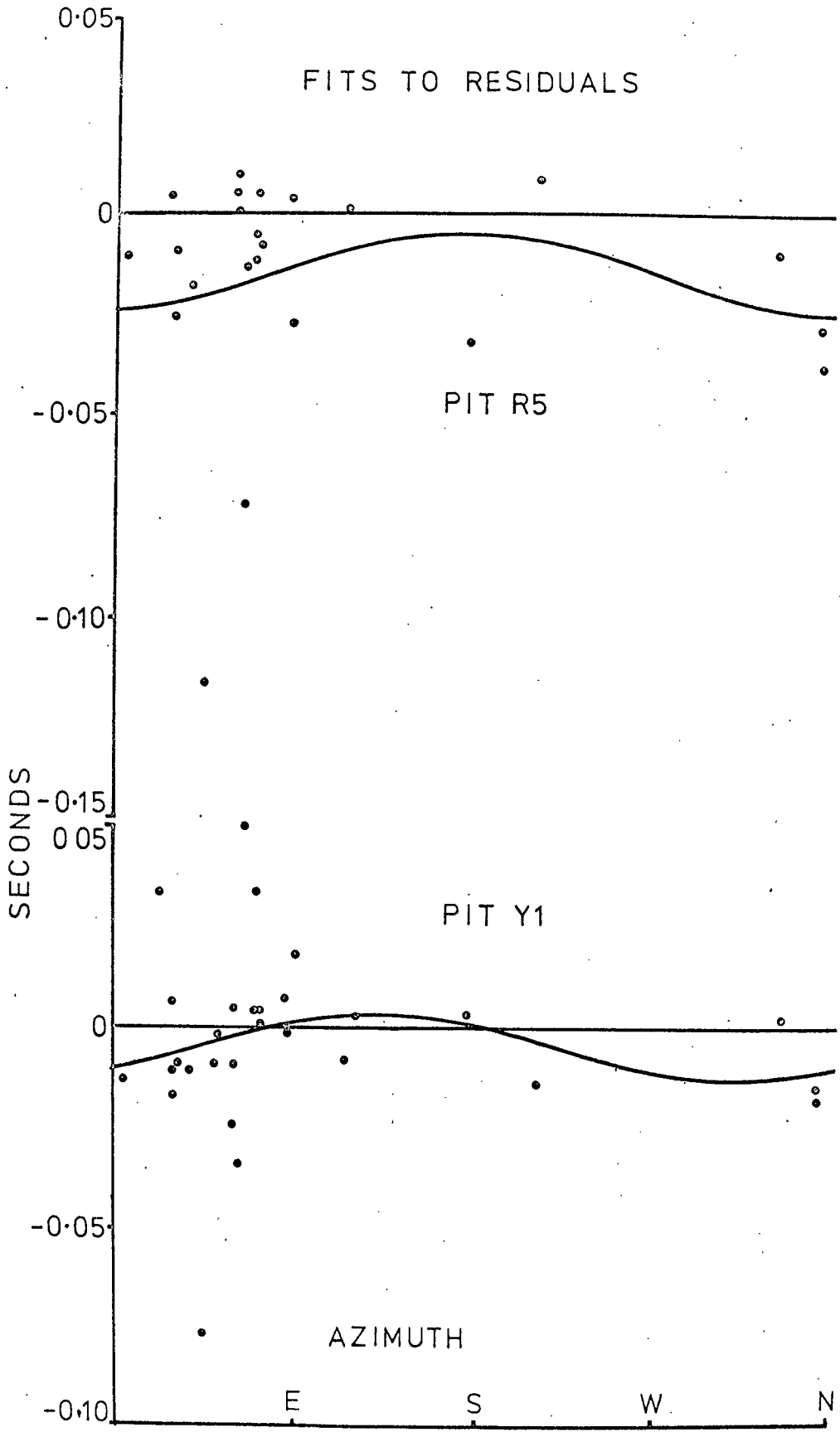

Fig.16. Onset time residuals for seismometers R5 and Y1 with fitted sinusoids.

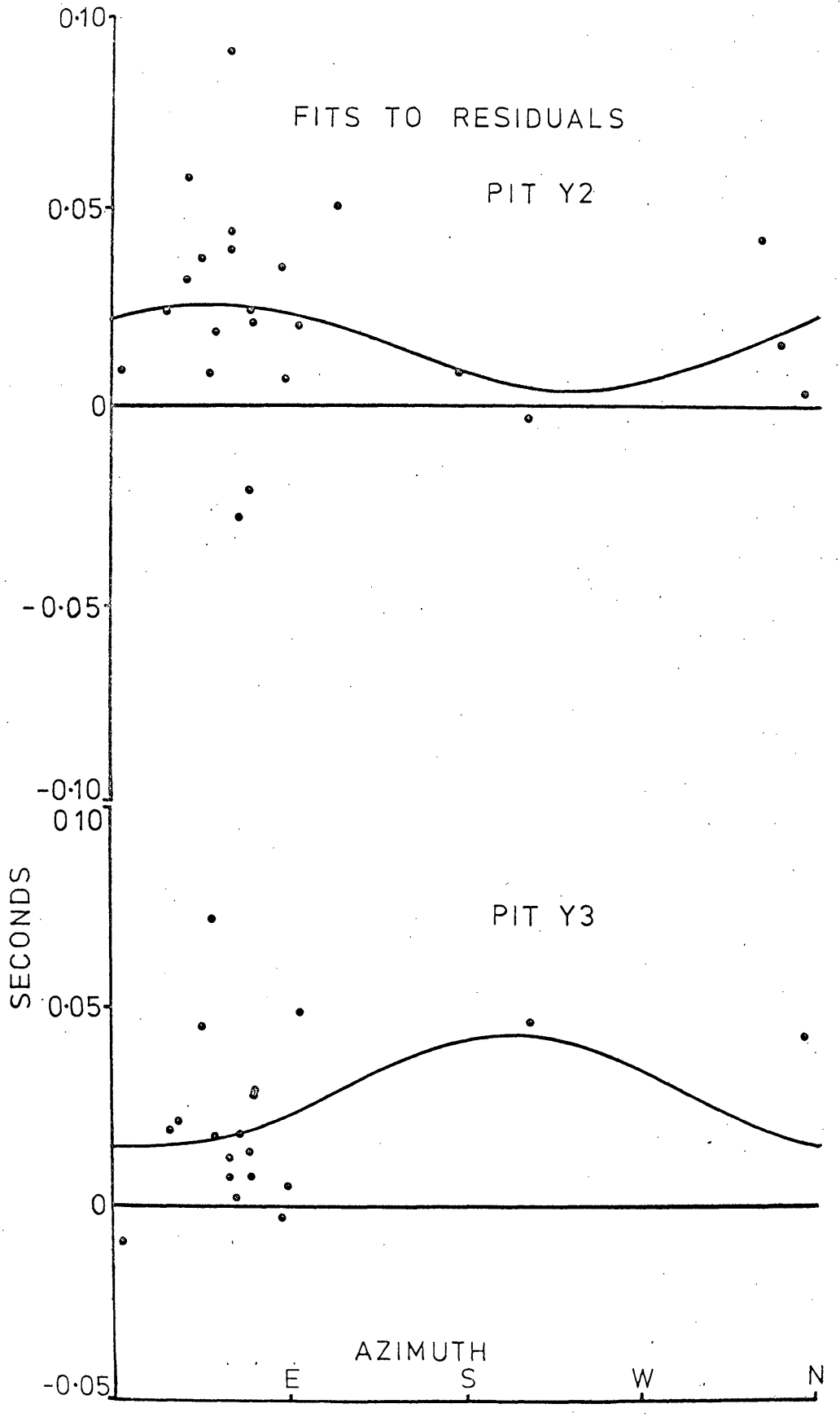

Fig.17. Onset time residuals for seismometers Y1 and Y3 with fitted sinusoids.

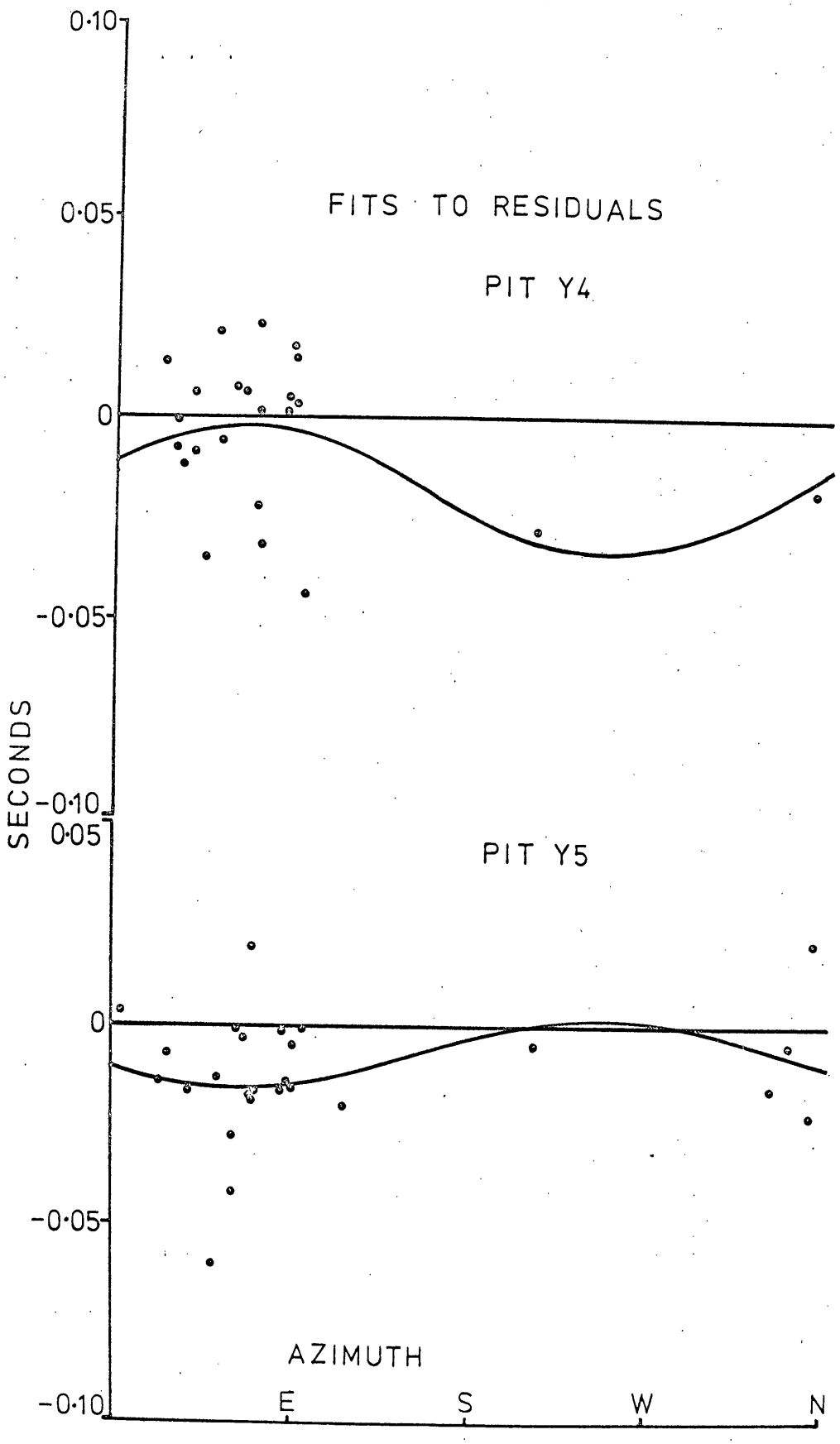

Fig.18. Onset time residuals for seismometers Y4 and Y5 with fitted sinusoids.

any lateral variations in deep structure, for instance in the upper mantle, will manifest themselves as values of slowness lower or higher than expected, but as these values are then used to compute the residuals, there will be little effect on the time corrections at individual seismometers. Thus the chief cause of the site corrections should be near the surface.

The values of A_i, B_i and E_i (Table 6) are calculated using all events as there is no marked effect on the onset time residuals due to the different epicentral distances involved. In general, A_i and B_i are fairly small and of the same order as those estimated for other arrays of comparable size (Corbishley, 1970). The constant terms Ai do not exceed $\pm$ 0.02 seconds, except for that associated with pit Y3. Hence, there do not seem to be any large lateral variations in near surface structure across the array. This conclusion is in accord with geological evidence as all seismometers are set on a substantial depth of phonolite which probably does not show large variations in composition immediately beneath the array (Jennings, 1964). In addition, these D.C. terms do not exhibit any simple trend across either arm of the array (Fig.19), and do not correlate well with the elevations of individual seismometers (Fig.20.). Thus, the corrections applied to the onset times (Section 3.1.7) before least squares analysis probably allow adequately for differing site heights.

The B_i terms are all below $\pm$ 0.02 seconds and, therefore, do not indicate any systematic anisotropy in wave propagation, which would tend to cause the azimuthally varying term to be large. The absence of regular azimuthal variation is confirmed by the scatter in the values for the phase angle E_i.

TABLE 6

ARRAY SITE CORRECTIONS

PIT	A_i (secs)	B_i (secs)	E_i (degrees)
Y1	-0.005 ± 0.015	0.008 ± 0.017	319.8
Y2	0.016 ± 0.019	0.011 ± 0.022	39.9
Y3	0.029 ± 0.021	0.014 ± 0.024	250.7
Y4	-0.017 ± 0.019	0.016 ± 0.020	24.3
Y5	-0.007 ± 0.011	0.008 ± 0.012	205.0
R1	-0.020 ± 0.012	0.008 ± 0.014	174.7
R2	0.00 ± 0.010	0.012 ± 0.012	180.4
R3	0.011 ± 0.021	0.018 ± 0.022	105.8
R4	0.010 ± 0.015	0.005 ± 0.016	323.5
R5	-0.014 ± 0.022	0.009 ± 0.024	276.2

Errors are 95% confidence limits.

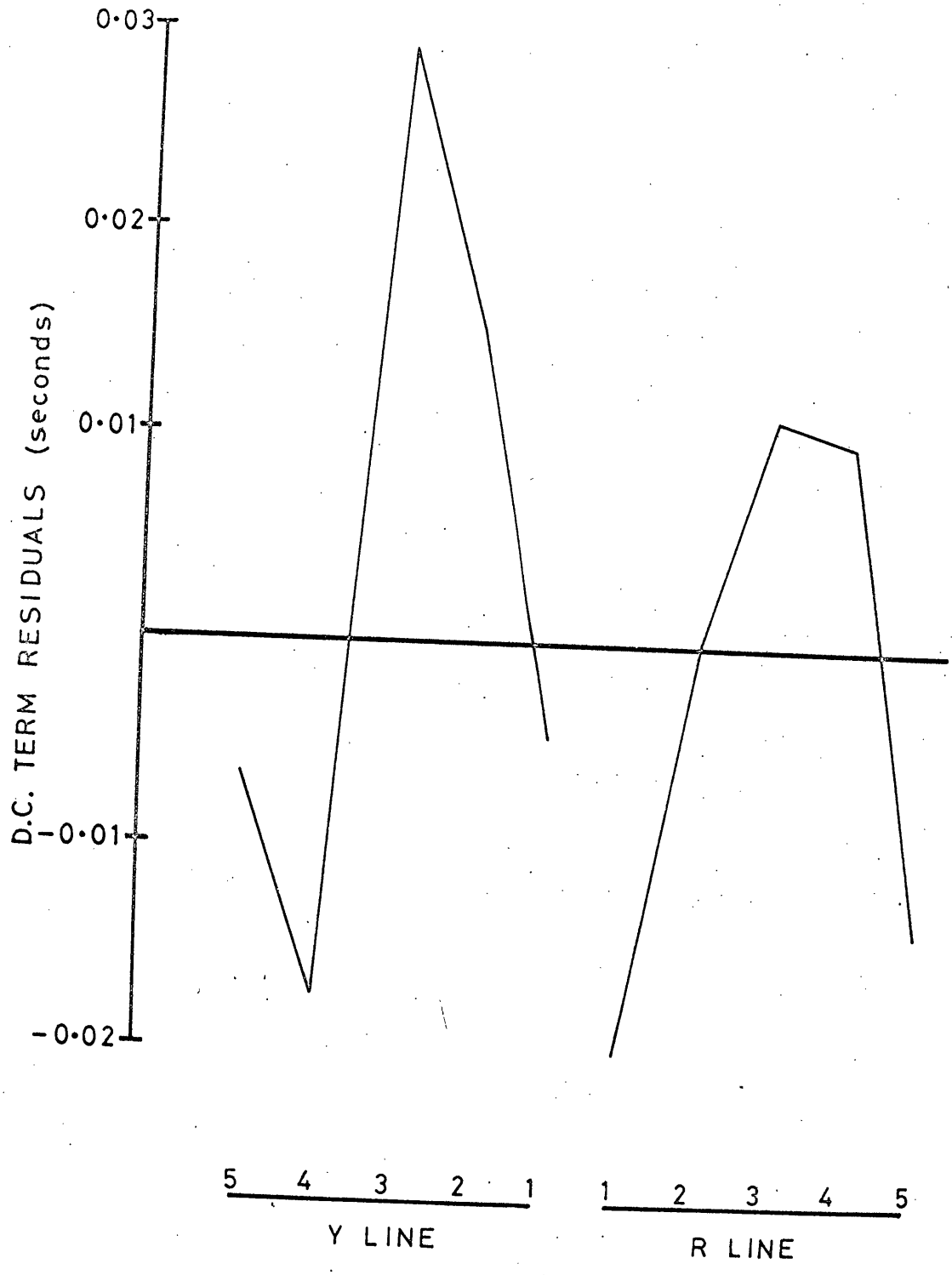

Fig.19. Constant term A of onset time residuals for each seismometer.

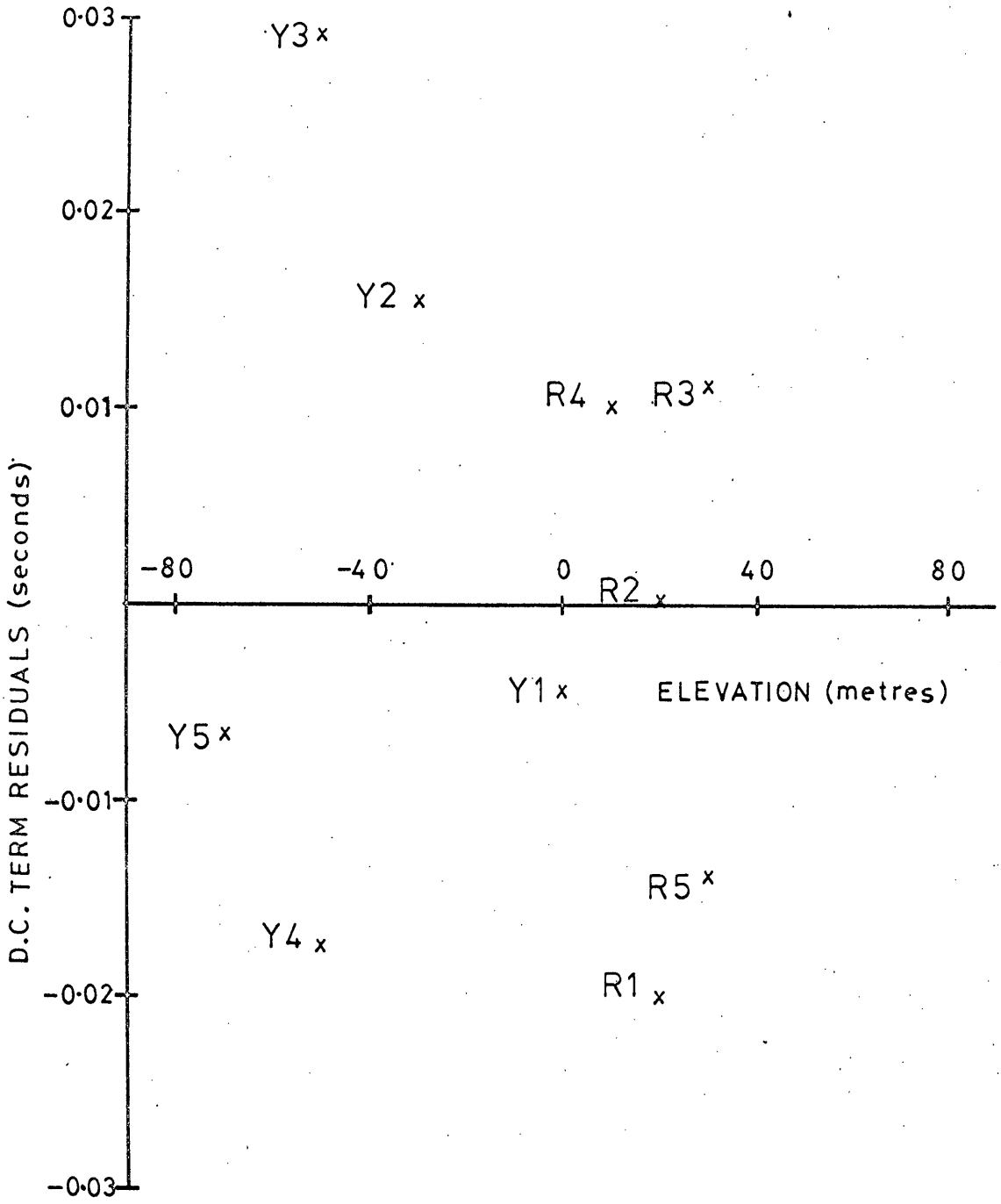

Fig.20. Constant term A of onset time residuals as a function of seismometer elevation relative to Y1.

CHAPTER 4

MEASUREMENT OF P-WAVE DELAY TIMES

4.1. Introduction

Considerable variation has been observed in the travel times of earthquake signals crossing different parts of Africa, indicating lateral variations in structure. Lilwall and Douglas (1970) computed the travel-time corrections for several African stations using the Joint Epicentre Method. A study of the DC component of these corrections shows that, in general, the stations within the rift system have positive corrections whereas outside the system, such corrections are smaller, particularly in southern Africa where negative values are common. This indicates a "slowing-down" of waves crossing the rift valleys relative to the rest of Africa. These results are similar to those from less extensive studies by Herrin and Taggart (1968) and Cleary and Hales (1966).

Fairhead (1968), again using the Joint Epicentre Method, found that for epicentral distances of 0° - 30°, African travel times differed significantly from the Jeffries-Bullen times, but such departures were reduced though not eliminated by using Herrin's tables as an alternative standard. Also, work on station corrections for events within this smaller distance range confirm the conclusions drawn from the results above. The shield regions of Africa have negative corrections, but those within the rift system have positive ones, indicative of anomalously low velocities beneath. This does not seem to be the case between the Eastern and Western Rifts (Fairhead and Girdler, 1971).

Sundaralingam (1971) measured the P-wave travel-time delays for East African stations relative to Bulawayo (BUL) using Herrin et al's tables and events only in the distance range 25^{o} - 90^{o}. He discovered large positive delays at Addis Abbaba (AAE) and Nairobi (NAI), but a smaller positive value at Lwiro (LWI) in the Western Rift (Table 3). This method uses the difference between residuals from standard travel-time tables for given events at a pair of stations, in this case Bulawayo being a standard in each of the three above cases. This procedure will be used here and is examined in detail in the next section.

Delay Time Analysis

Long and Mitchell (1970) have shown that the difference between the observed and expected travel times is given by the residual R, where:

$$R = T_o + T_E + T_t + T_s + E \qquad 4(i)$$

T_o arises from errors in the earthquake focal data.

T_E is due to anomalies at source.

T_t is the error in the calculated travel time due to inaccurate tabulated values.

T_s is the delay caused by anomalies beneath the station.

E is the error from poor timing and misreading of seismograms.

The two-station method, by taking the difference between residuals for given events at a station pair, attempts to isolate the T_s terms by cancellation or reduction of the other factors in order that the resulting relative delay provides a direct measure of the crust and upper mantle differences beneath the two stations.

Each term in the above expression will be considered in turn.

(1) Errors in focal data T_o can arise from an inadequate or non-symmetrical distribution of locating stations, or from station or source anomalies. This term will vary for different regions hence for different epicentral distances and azimuths, and also for events of differing magnitudes from the same region. When considering the relative delay between two stations, any errors in origin time will cancel, but the varying curvature of the travel-time curve implies that incorrect distance can give artificial delays. All the epicentres and focal depths here were determined by the NOAA and all but two have magnitudes of 4.8 or greater. From section 3.1.7., we have assumed that epicentral co-ordinates are not in error by more than 25 km and focal depths less than 75 km. The error in epicentral distance is a function of distance and also of the position of an epicentre with respect to the two stations. For the events in the range 25° - 99°, calculations show that the relative delays could be error by as much as 0.8 seconds from assuming incorrect distance alone. This is a maximum for events along a great circle bisecting and perpendicular to a line joining the stations and for a mislocation perpendicular to this great circle. The contribution towards T_o from miscalculating the focal depth is most pronounced for deep and close events along a great circle joining the pair of stations. For a location error of 75 km for a surface focus event, a maximum error of about 0.7 seconds would result for this study.

However, the actual error in each measurement of relative delay depends on the direction of the error in focal position. Because of the lack of detailed information for all the seismic

regions concerned, only the above maximum figures are presented.

(2) T_E is caused by anomalies in the crust and upper mantle at the source of an earthquake. The use of relative delay for a station pair should result in considerable reduction of this term, as the effect at source is likely to be in the same sense for both station paths and of similar magnitude unless the stations are far apart. However, this does not hold if there is a large degree of inhomogenieity near the source. For instance, the proposal that the descent of cold plates of oceanic material into hot mantle material beneath island arcs could lead to "fast" planes, would suggest negative travel-time residuals for rays travelling along this direction (Davies and McKenzie, 1969). These would tend to cancel out for relative delay at two stations very close together but as rapid lateral variations in structure and seismic velocity are implied, this might not hold for well separated stations. Such characteristics might be expected for the earthquakes in this study from the Philippines and the Celebes-Borneo area and this will be discussed in a later section (4.5.).

(3) T_t is the error in the expected travel time calculated from standard tables. Unless epicentral distances are the same for both stations, which is not usually the case, then inaccuracies in the tables should not cancel. Herrin et al's (1968) tables show much less scatter over many distances than the Jeffries-Bullen tables (Long and Mitchell, 1970; Fairhead, 1968) and have a similar shape to other tables (Lilwall and Douglas, 1970; Cleary and Hales, 1966). Thus the main difference is a small DC component which

will cancel with the station pair method. By using Herrin's tables, we can probably neglect the T_t term.

(4) T_s is the delay caused by crust and upper mantle anomalies beneath the stations, and is the quantity we normally wish to isolate. The relative delay between the two stations due to this term $(T_s - T_{s1})$ can act as a comparison between the structures beneath the two stations.

(5) E is due to misreading of the seismograms. This can be due to four types of errors (Freedman, 1968):

(a) Miscounting: due to incorrectly observing the seconds, minutes or even hours on the output time codes. Obviously large errors will be easy to detect and a second reading of the arrival time will largely eliminate any differences greater than a few tenths of a second.

(b) Misidentification: this arises largely through the signal onset being obscured by background noise. In practice, many records were discarded as onsets were indistinguishable to a precision better than about half a second or more. In marginal cases the onsets for adjacent seismometers were measured and if, after allowance for the propagation lags, the estimates differed by more than 0.5 seconds, then the record was rejected.

It has been suggested that some delays are "caused" by consistent late reading of records (Stefansson, 1964) with onsets lost in noise. Also, onsets picked from processed records tend to be earlier than those from unprocessed signals. The chosen signals were played out both unprocessed and processed by an

electronic band-pass filter. The filtered signal was used as a check, but the arrival time was taken off the unfiltered channel, as the first break was usually clearer.

(c) Instrumental Errors: these are caused by variations in instrumental response, recording or playout speed, and clock errors.

Instrumental error is probably negligible. The playouts were on paper with one second equivalent to 1 centimetre, ensuring that most onsets remained reasonably sharp and any variations in paper speed were negligible.

The treatment of clock errors is more difficult. Log sheets are prepared on site with details of three time checks every day, giving the clock error with respect to GMT. Also, Greenwich Mean Time was recorded on the radio channel. However, due to clock jumps, some arrivals could not be timed and were rejected. Where time or radio checks were missing and also when the clock had more than a very slow drift, the relevant records were not considered.

(d) Reading errors: even if the preceding sources of error are eliminated, there would still be a random error term incurred in reading the onset times. With the playout speed used, an accuracy of a few tenths of a millimetre is possible, corresponding to a time error less than 0.05 seconds.

After computation, some extreme values for relative delay were left which could not be removed by checking measurements and calculations. Therefore, assuming a normal distribution, all values outside three standard deviations from the mean were

rejected. This was thought to be reasonable as the probability of observing data outside this range in the normal case is only 0.003 and these values are probably contaminated with large values of E.

4.3. Corrections

Although the use of relative delay for a station pair reduces error terms, corrections have to be considered for the effects of the Earth's ellipticity, the station elevations, and the angle of emergence of rays at the surface. These were applied as described below, for each event at both stations.

1. Ellipicity Correction

Travel times from standard tables apply to a sphere of volume equal to that of the Earth - the mean sphere - and allowance has to be made for the elliptical shape of the Earth. The deviation from the mean sphere is about - 14 km at the poles and + 7 km at the equator (Bullen, 1965).

The time correction dE is given approximately by:

$$dE = f(\Delta) \left[h_o + h_1 \right]$$

$f(\Delta)$ is a function of distance only, and is tabulated in Bullen (1956) and Young and Gibbs (1968).

h_o and h_1 are the heights of sea level below the station and epicentre respectively above the mean sphere. In general this is given by:

$$h = E.R. \left(\tfrac{1}{3} - \sin^2 \theta \right)$$

E is the ellipicity of the Earth and R the radius of the mean

sphere. θ is the geocentric latitude of the station or epicentre. dE is added to the calculated travel time.

2. Elevation Correction

A correction to delay time for a station at elevation Z can be made by adding to the expected travel time for each event a term dL, where:

$$dL = Z\left[\frac{1}{V_c \cdot \cos i_c} - \frac{\tan i_c}{V_R}\right]$$

i_c is the angle the ray makes with the normal at the surface in a layer of velocity V_c.

V_R is the apparent surface velocity of the ray, chosen for the appropriate station-source distance.

Kaptagat and Bulawayo are, respectively, 2.39 km and 1.34 km above sea level. For Bulawayo, V_c was taken as 5.4 km/sec which has been suggested for the top 1.3 km of the crust in the Transvaal (Gane et al, 1956; Clark, 1966). At Kaptagat, several hundred feet of phonolite overlie the Precambrian basement gneisses (Jennings, 1964) and from density considerations, a velocity of 5.5 km/sec was used in the elevation correction.

3. Correction for Angle of Emergence

Usually delay times are interpreted in terms of plane parallel layers, so it is useful to correct the measured delay time to give a vertical travel time anomaly T_V.

$$T_V = T_S \cos\theta - T_{S1} \cos\theta^1$$

θ is the angle the ray makes with the vertical beneath Station S.

θ^1 is the angle the ray makes with the vertical beneath Station S1.

θ , θ^1 and also i_c in Section (2) can be calculated using the ray theory relationship $P = \frac{R \sin i}{V}$

Here i relates to i_c, θ or θ^1 and the other symbols are given in section 3.1.7.(3).

4.4. The Data

The arrival times at Kaptagat were read from paper playouts of the events stored on magnetic tape. All channels were played out, but, in general, the arrival time was measured from channel Y1. This was found to be the most reliable instrument and was also played out filtered. In a few cases Y1 was not recording clearly for otherwise suitable events and an adjacent trace was read, a small correction being made for the propagation delay between the two instruments. The data for Bulawayo was taken from picking lists prepared at the Goetz Observatory, Bulawayo, and obtained from the ISC, Edinburgh.

A computer program was written to facilitate the calculation of relative delays. The origin times, epicentral latitudes and longitudes, and focal depths of all the selected events were assumed from the NOAA data and inputted along with the observed arrival times at Kaptagat and Bulawayo. The distances and travel times are computed for each event and station and delays calculated after applying the above corrections. The delay at Kaptagat relative to Bulawayo can then be given as output.

4.5. Discussion of Results

Seventy-eight measurements of delay time were made for Kaptagat relative to Bulawayo and these are given, with source parameters, in Table 7. As with the $dT/d\Delta$ data, the distribution of delay time values shows a heavy concentration within the north-east quadrant and an especially high density of results associated with the active regions of Indonesia and the Philippines. Of the total of delays computed, those falling outside three standard deviations from the mean were rejected and the variance for the truncated set of seventy-eight was estimated using the method of Freedman (1968). The delays then have a mean of * 2.20 seconds and 95% confidence limits of 2.00 seconds.

Table 8 shows all the delays as a function of epicentral distance from Kaptagat. Although the group means are not by themselves very significant, because of the small numbers of measurements and substantial scatter, there does not seem to be any variation with distance above 40° with the values for smaller distances having differences that are not significant at the 67% level.

A detailed analysis of delay time variation as a function of azimuth will be given in Chapter 6, but a review of values from different regions does not reveal any large amplitude trends. For instance, group means are 2.0 for the Hindu Kush region (five events), 2.5 for the Nicobar Islands (eight events), and 2.6 for Sumatra (eight events). However, the lack of full circle coverage limits the reliability of such an analysis. The mean for the Sumatra group and also the means for the results from the Philippines (2.6 for five events) and the Celebes region (2.7 for eight events) are of interest

TABLE 7

	EPICENTRAL DATA			KAPTAGAT				BULAWAYO				RELATIVE
	LAT	LONG	DEPTH (KM)	DIST (DEG)	AZIM (DEG)	T-TIME (SECS)	DELAY (SECS)	DIST (DEG)	AZIM (SECS)	T-TIME (SECS)	DELAY (SECS)	DELAY
1	37.55	48.98	65	39.0	17.2	439.9	3.4	60.5	18.5	603.0	1.4	2.0
2	10.83	125.39	35	89.8	79.2	776.1	3.0	100.0	82.1	822.2	0.7	2.3
3	-43.14	41.66	33	43.8	173.4	482.4	5.8	25.4	157.4	324.1	3.2	2.6
4	36.47	70.47	210	48.3	38.3	500.6	2.8	68.8	35.2	641.7	1.1	1.7
5	49.96	77.76	0	61.1	29.8	615.2	3.2	82.2	29.5	742.6	1.3	1.9
6	25.71	88.50	33	56.9	59.3	582.2	3.3	73.9	54.3	692.0	1.6	1.7
7	-8.83	118.81	91	83.5	98.9	738.6	2.8	87.2	98.3	756.4	1.8	1.0
8	-56.01	-27.51	140	75.6	211.1	689.5	5.6	54.7	214.8	554.3	1.8	3.8
9	39.88	77.80	13	55.0	39.3	570.8	2.5	75.3	37.0	702.7	-0.1	2.6
10	26.02	95.40	59	63.0	60.9	620.8	3.1	79.4	57.3	720.1	0.6	2.5
11	37.82	55.88	19	41.7	24.6	467.4	2.5	63.1	24.0	626.0	1.4	1.0
12	14.26	51.84	33	21.2	49.0	283.4	1.7	41.1	35.6	461.0	0.2	1.5
13	2.60	97.98	38	62.5	87.3	620.3	3.1	71.6	80.1	678.0	0.5	2.6
14	11.86	-43.74	33	79.3	281.9	723.4	3.8	77.9	287.5	715.4	1.2	2.7
15	1.15	126.11	24	90.6	88.9	781.4	4.2	97.4	91.5	812.3	1.8	2.4
16	41.10	19.77	33	42.9	342.5	475.4	2.7	61.5	352.4	613.1	0.7	1.9
17	9.32	122.20	33	86.7	80.8	761.4	4.5	96.5	82.5	806.7	1.8	2.6
18	18.10	120.47	53	85.1	72.0	751.0	2.7	97.7	73.6	809.8	-0.4	3.2
19	-8.02	107.39	63	72.2	98.5	678.9	5.0	76.8	93.8	705.4	1.5	3.5
20	1.80	94.56	33	59.1	88.2	597.6	5.7	68.2	79.5	657.3	2.3	3.4
21	36.58	70.11	290	48.2	37.9	491.9	4.0	68.7	34.9	632.7	1.0	2.9
22	14.83	53.76	33	23.1	50.9	302.2	-0.5	42.7	37.3	473.6	0.3	-0.8
23	37.04	71.38	112	49.3	38.3	517.3	3.1	69.7	35.4	657.8	2.6	0.6
24	49.77	78.08	0	61.1	30.1	615.5	2.3	82.2	29.8	742.7	1.9	0.4
25	0.94	100.19	197	64.7	89.2	617.7	3.4	73.1	82.6	669.2	1.8	1.6
26	-0.57	121.83	33	86.4	90.6	759.8	2.1	92.8	91.6	789.9	-0.0	2.2
27	36.42	70.07	219	48.1	38.0	497.6	4.0	68.6	35.0	639.1	1.2	2.8
28	-23.49	37.29	33	23.9	175.8	310.1	4.6	8.7	114.0	123.8	2.4	2.2

TABLE 7 (continued)

	EPICENTRAL DATA			KAPTAGAT				BULAWAYO				RELATIVE
	LAT	LONG	DEPTH (KM)	DIST (DEG)	AZIM (DEG)	T-TIME (SECS)	DELAY (SECS)	DIST (DEG)	AZIM (SECS)	T-TIME (SECS)	DELAY (SECS)	DELAY
29	-23.47	37.18	33	23.8	176.1	309.8	3.6	8.6	114.1	122.5	3.3	0.3
30	51.12	-29.55	33	74.2	323.6	693.6	2.6	87.3	327.6	763.2	0.7	1.9
31	-43.23	41.48	33	43.8	173.6	483.0	4.8	25.4	157.7	324.3	0.7	4.1
32	-56.29	-27.29	107	75.6	210.8	693.1	4.9	54.7	214.5	557.5	1.2	3.7
33	34.96	13.67	33	39.9	331.6	451.1	4.2	56.6	345.3	579.5	2.1	2.1
34	-3.59	86.16	33	50.8	95.0	537.9	3.1	58.4	81.6	592.2	0.0	3.0
35	73.32	55.15	0	73.8	5.8	695.5	3.3	94.9	7.4	803.0	0.8	2.5
36	74.62	8.41	33	75.8	352.8	702.4	2.3	95.4	354.7	800.6	2.3	0.0
37	7.66	-37.60	33	73.1	277.8	688.2	3.2	70.7	286.1	673.2	2.2	1.1
38	9.06	94.02	33	58.9	79.8	596.2	4.8	70.6	72.2	672.3	2.0	2.8
39	9.02	94.02	33	58.9	79.8	596.2	4.6	70.6	72.3	672.2	2.4	2.1
40	9.11	94.04	33	58.9	79.7	596.4	3.9	70.6	72.2	672.6	2.1	1.8
41	36.77	45.13	19	37.2	12.9	430.4	3.1	58.7	15.5	596.1	2.5	0.6
42	-13.69	66.26	24	33.6	115.9	398.7	3.0	36.5	85.9	423.7	1.0	2.0
43	9.02	93.87	33	58.8	79.8	595.2	3.3	70.4	72.2	671.4	2.1	1.2
44	8.97	94.00	33	58.9	79.9	596.0	5.5	70.5	72.3	672.0	1.7	3.8
45	8.98	94.08	33	59.0	79.8	596.6	5.1	70.6	72.3	672.5	2.2	2.8
46	9.15	94.08	33	59.0	79.7	596.7	4.2	70.7	72.2	672.9	1.0	3.1
47	-40.89	80.55	33	58.0	140.7	589.4	1.4	48.5	127.2	519.6	0.7	0.7
48	18.51	120.88	55	85.5	71.6	752.7	3.1	98.2	73.3	811.9	-0.8	3.9
49	29.52	56.85	106	35.4	33.3	405.6	3.7	56.4	29.7	570.0	0.7	3.0
50	36.91	71.62	124	49.3	38.6	516.6	3.9	69.8	35.6	656.7	1.5	2.3
51	22.71	121.34	28	86.0	67.4	758.6	3.5	99.9	69.5	823.0	1.1	2.3
52	14.95	120.10	47	84.7	75.1	749.7	3.3	96.4	76.5	804.4	2.4	1.0
53	6.49	94.70	85	59.4	82.8	593.9	4.2	70.1	75.0	663.7	1.4	2.8
54	36.94	9.73	24	43.4	329.6	480.9	3.3	59.5	342.5	600.9	-0.1	3.4
55	0.70	124.93	56	89.5	89.3	771.8	3.7	96.2	91.5	802.4	1.3	2.5
56	35.90	105.49	28	73.6	52.7	691.3	2.4	91.5	52.3	784.1	1.2	1.2

TABLE 7 (continued)

	EPICENTRAL DATA			KAPTAGAT				BULAWAYO				RELATIVE
	LAT	LONG	DEPTH (KM)	DIST (DEG)	AZIM (DEG)	T-TIME (SECS)	DELAY (SECS)	DIST (DEG)	AZIM (SECS)	T-TIME (SECS)	DELAY (SECS)	DELAY
57	43.78	39.13	33	43.3	3.9	478.4	3.3	64.3	8.4	632.1	1.7	1.6
58	0.04	124.49	33	89.0	90.0	772.5	3.9	95.5	92.0	802.4	1.0	2.9
59	-6.27	130.14	118	94.7	96.2	788.8	2.7	98.6	99.9	806.2	0.9	1.8
60	2.39	94.88	21	59.4	87.5	601.5	3.8	68.7	79.1	662.2	0.5	3.3
61	43.85	54.77	0	46.5	19.3	508.9	3.9	68.0	20.1	660.8	1.8	2.1
62	-4.25	103.37	119	68.0	94.7	647.2	2.4	74.2	88.8	684.6	1.1	1.3
63	2.02	126.46	33	91.0	88.0	781.7	3.8	98.1	90.8	813.9	1.4	2.4
64	34.40	24.01	33	35.4	343.6	413.3	2.9	54.4	355.3	563.8	1.4	1.5
65	35.06	46.92	57	36.1	16.1	416.1	4.3	57.6	17.8	583.6	2.2	2.1
66	5.72	61.24	33	26.3	78.0	332.5	4.9	41.1	54.7	461.0	2.3	2.7
67	-7.80	122.67	196	87.3	97.8	745.4	2.4	91.1	98.7	763.1	0.6	1.9
68	1.66	126.38	33	90.9	88.3	781.3	2.7	97.9	91.1	813.0	-0.2	2.9
69	-26.02	27.94	13	27.3	194.9	344.2	2.7	5.9	185.9	86.8	0.9	1.9
70	1.88	99.16	116	63.7	88.1	619.6	3.2	72.4	81.3	674.3	0.9	2.4
71	23.76	91.76	48	59.2	62.5	596.6	2.3	75.4	57.6	699.1	0.9	1.4
72	0.65	98.84	33	63.4	89.5	626.6	2.1	71.7	82.3	679.2	-1.7	3.8
73	2.19	126.89	33	91.4	87.8	783.7	3.4	98.5	90.8	816.0	3.3	0.1
74	-63.45	-61.22	33	93.4	206.6	791.8	4.9	72.1	208.2	680.7	2.5	2.5
75	1.48	121.28	64	85.8	88.6	753.3	2.8	93.0	89.5	787.0	0.0	2.8
76	36.56	55.63	39	40.5	25.3	455.2	3.9	61.9	24.5	615.3	0.6	3.3
77	-59.78	-26.43	33	76.6	207.3	707.3	5.9	55.4	210.2	570.5	2.5	3.4
78	3.24	95.93	33	60.5	86.6	607.2	3.4	70.0	78.7	668.7	0.7	2.7

TABLE 8

KAPTAGAT P-WAVE DELAYS RELATIVE TO BULAWAYO

Distance (degrees)	Mean Delay (seconds)	Standard Deviation	Number of Observations
20 - 30	1.3	1.2	6
30 - 40	1.9	0.7	7
40 - 50	2.3	1.0	13
50 - 60	2.4	0.9	15
60 - 70	2.1	0.9	9
70 - 80	2.4	1.2	10
80 - 90	2.4	0.8	12
90 - 99	2.0	0.9	6

TABLE 9

TWO STATION DELAYS FOR EAST AFRICA

KAP - BUL	2.20 ± 2.00 secs	Present Study
NAI - BUL	2.3 ± 0.3 secs	Sundaralingam (1971)
AAE - BUL	2.7 ± 0.3 secs	
NAI - BUL	2.52 ± 0.70 secs	Lilwall and Douglas (1970)
AAE - BUL	2.73 ± 0.67 secs	
AAE - BUL	1.5 ± 0.3 secs	Cleary and Hales (1966)

as they are from trench areas where it is presumed that there is downthrusting of the oceanic plate into the upper mantle. This could result in an anomalous zone of the order of 100 km wide in which seismic velocities may be higher than normal (Cleary, 1967; Davies and McKenzie, 1969). As the relevant earthquake foci in the present study lie above this zone we would expect delays from these regions to be less than those from other areas, producing variations with azimuth and distance. However, the apparent absence of such effects may mean that either the speeding-up of seismic waves is not appreciable for the particular station-source paths used, or that the two-station method cancels such terms. Again, however, the scatter of the data ensures that such conclusions can only be very tentative.

Although all the delay time results except one are positive, the 95% confidence limits of $\pm$ 2.00 seconds show that there is considerable scatter. This, as we have discussed, is not caused by acute azimuthal or distance variations, although (see Chapter 6) the former may contribute towards this to some extent. Another small contribution may be from the mislocation of epicentres although there is no apparent correlation between the deviation of delay time values from the mean and the number of locating stations used. Systematic mislocation such as has been suggested can occur for earthquakes in trench regions of underthrusting would produce delay variations of the same sign which do not appear to be significant and are probably largely reduced by application of the two station analysis method.

A simple study of the relation between the approximate signal/noise ratio of the earthquake signal onsets and the dev-

iation of delays from the mean value again reveals no dependence. It seems likely that misreading of the seismograms would cause greater scatter in delay time for emergent signals than for sharp, large amplitude arrivals. This, however, does not appear to be the main cause of the diversity of results.

The picking lists from Bulawayo gave arrival times only to the nearest second, and so an uncertainty of up to ± 0.5 seconds could be introduced into the computations and this, coupled with the effects of timing errors for the Kaptagat records, probably contributes towards the scatter. The rejection of Kaptagat records because of suspected poor timing was somewhat subjective. Clock jumps were usually of large magnitude and hence easily detected. However, if the binary time code could not be directly and frequently checked against the GMT time checks and the radio time signal, and there was a slow drift of just a few tenths of seconds between such adjacent checks, then this drift was assumed to be linear and appropriate corrections applied. This may have led to errors but probably only of a few tenths of a second.

4.6. Comparison with other studies:

The mean value for delay time at Kaptagat of 2.2 seconds is very similar to that found by Sundaralingam (1971) for Nairobi, both being measured relative to Bulawayo. The individual values for Nairobi, which is south of Kaptagat but only 25 km east of the rift escarpment, showed no significant dependence on distance or azimuth. These two means are also of the same order as the delay for Addis Abbaba of 2.7 seconds (Sundaralingam, 1971), as shown in Table 9. Also listed in Table 9 are values of relative station

corrections attributed to Cleary and Hales (1966), and Lilwall and Douglas (1970). These represent the differences in the D.C. components of the travel-time corrections at the individual stations that form the pairs listed.

CHAPTER 5

INTERPRETATION OF THE ARRAY DATA

5.1. Cause of Anomalies

Large and systematic variations in the calculated values of $dT/d\Delta$ and azimuth of approach for teleseismic events have been found for the Kaptagat array. In section 3.1.7., corrections were outlined for the effects of varying focal depths and different seismometer pit elevations. Errors in the focal data used and the approximation to plane wave-fronts were found to be able to account for only small deviations in slowness and azimuth. Random reading errors vary with the azimuth of approach of signals but will be random for any direction and are not large enough to cause the observed variations. Several other possible causes will now be discussed.

(1) Errors in the Array Geometry

The maximum error in measuring the co-ordinates of the seismometer pits was estimated at ± 30 metres during the surveying, except for Y5, where the possible error may be as high as ± 60 metres. Consider an extreme case of an arm of the array being extended by a total of 90 metres. Then the observed slowness should not be in error by more than 0.25 sec/deg for any of the events used. A more detailed treatment of this problem has been made by Mr. P. K. H. Maguire (personal communication). Assuming that the position of each pit is known to ± 30 metres, their positions can be varied systematically and envelopes of maximum slowness and azimuth errors computed for all directions of approach. This

analysis confirms that although such errors in location could contribute towards the observed anomalies, they could not be a major cause.

The larger error on Y5 is due to difficulties encountered when surveying this area. However, the residuals for this pit do not suggest that it is significantly misplaced (Table 6).

(2) Inhomogeneity of Local Structure

We can estimate the effects of inhomogeneity in the near-surface structure by considering the onset time residuals in section 3.2.1. From the previous discussion, the apparent lack of significant trends in either the A or B terms and their small magnitude are not compatible with the major cause of the anomalies lying immediately beneath the array. It is useful, though, to be able to estimate the inhomogeneities that do exist. We can then reduce their effect on the measured slowness and azimuth by subtracting from the observed onset times t_{ik}, for the i th seismometer recording the k th event, the expression $A_i + B_i \sin (Z_k + E_i)$ where the symbols are as defined in 3.2.1.

These pit corrections have been applied and the event parameters are given in Table 10. In comparison with Table 5, for the uncorrected values, it can be seen that the mean errors in slowness and azimuth are reduced by 0.2 sec/deg and 1.6 degrees respectively. However, the pronounced anomalies remain.

It is difficult to establish how accurately these corrections compensate for the actual deviation in structure beneath the array. If events from a wide range of azimuths are recorded

TABLE 10

	EPICENTRAL DATA				MEASURED			MEASURED		
	LAT	LONG	DIST DEG	AZIM DEG	SLOWNESS	ERROR SEC/DEG	ANOMAL	AZIMUT	ERROR DEGREES	ANOMALY
1	75.32	55.15	73.8	5.8	7.89	0.45	2.00	352.3	3.8	-13.5
2	37.82	55.88	41.8	24.5	8.49	1.30	0.31	8.6	5.2	-15.9
3	35.51	58.22	40.9	28.9	10.30	0.57	2.06	17.8	4.0	-11.1
4	49.96	77.76	61.1	29.8	7.67	0.58	0.89	6.2	6.9	-23.6
5	49.82	78.09	61.2	30.0	7.72	0.27	0.94	2.2	2.9	-27.8
6	23.31	55.60	34.0	33.1	12.35	0.69	3.67	27.0	3.1	-6.1
7	36.42	40.07	49.4	38.0	7.83	0.22	0.21	11.5	1.7	-26.5
8	39.94	77.02	54.7	38.8	8.76	0.48	1.49	20.0	2.9	-18.8
9	12.86	48.53	18.2	45.8	10.90	1.71	-1.18	42.6	9.4	-3.2
10	14.83	53.75	23.3	50.8	11.46	1.06	1.62	41.9	5.0	-8.9
11	36.99	136.75	99.7	52.6	4.18	0.46	-0.38	9.2	5.3	-43.4
12	25.71	88.50	57.0	59.3	5.42	0.90	-1.66	32.9	10.0	-26.4
13	26.25	95.13	63.0	60.6	5.62	0.71	-1.04	34.3	7.4	-26.3
14	26.02	95.40	63.2	60.9	5.59	0.31	-1.07	35.3	3.4	-25.6
15	23.76	91.76	59.5	62.5	4.56	0.99	-2.35	46.9	12.1	-15.6
16	22.93	101.03	67.4	65.4	5.45	0.91	-0.90	37.6	10.3	-27.8
17	8.44	57.76	23.8	69.7	9.93	0.44	0.26	60.3	2.4	-9.4
18	19.75	121.33	86.2	70.4	2.74	0.55	-2.14	29.3	12.3	-41.1
19	8.21	58.27	24.2	70.6	9.27	0.39	-0.24	65.0	1.9	-5.6
20	18.63	120.99	85.7	71.5	3.65	0.16	-1.27	35.9	2.3	-35.6
21	18.43	120.88	85.8	71.7	3.62	0.48	-1.30	37.6	8.7	-34.1
22	4.67	97.71	62.4	85.0	3.50	0.24	-3.20	93.2	4.8	8.2
23	4.54	123.02	89.5	85.5	2.53	0.31	-2.18	69.4	7.9	-16.1
24	2.60	97.98	62.6	87.3	4.28	0.43	-2.42	93.8	5.1	6.5
25	1.88	99.16	64.2	88.1	4.09	0.51	-2.53	121.3	6.4	33.2
26	0.94	100.19	65.6	89.2	3.80	0.44	-2.71	91.2	8.1	2.0
27	-4.33	102.40	67.3	94.9	4.83	0.74	-1.52	88.3	10.6	-6.6
28	-13.69	66.26	33.7	115.9	6.01	0.52	-2.68	113.2	4.0	-2.7
29	-23.49	37.29	24.0	175.8	7.94	0.45	-1.64	173.3	4.1	-2.5
30	-56.01	-27.51	76.2	211.1	7.17	0.42	1.44	238.6	3.0	27.5
31	34.96	13.67	40.1	331.6	9.67	0.42	1.37	325.7	2.9	-5.9
32	43.96	15.96	46.7	340.7	10.39	0.39	2.56	341.1	1.9	0.4
33	74.62	8.41	75.9	352.8	7.56	0.41	1.83	351.3	3.9	-1.5
34	39.03	29.74	38.9	352.9	10.30	0.67	1.94	354.2	4.3	1.3

on all seismometers then a good estimate of pit corrections can be obtained. In the present study, the lack of full angular coverage will, no doubt, have introduced at least some bias. Also, if all ten instruments are not recording a useful signal and if the ones functioning on a line are bunched together at one end, then additional inaccuracies would be present in the residuals. Thus, when selecting events to be analysed, records that fell into this category were rejected.

A check on the effects of errors (1) and (2) can be obtained independently of the teleseismic data. Measurements of the velocities of regional earthquake arrivals at Kaptagat have been made (Long et al, 1972) and a summary of these from west of the rift is given in Fig.6. There are two main groups of events associated with crustal (6.5 - 6.7 km/sec) and sub-moho velocities (7.8 - 8.4 km/sec). Each group of mean values for different regions shows consistency and there is no systematic azimuthal variation in velocity as exhibited by the teleseismic signals. This suggests that the latter trend is not caused by errors in the array geometry or by local perturbations in the near-surface geology. Thus although they may contribute towards the anomalies, they cannot be a major cause.

In the subsequent sections, the slowness and azimuth values used in the interpretation are those computed from onset times adjusted by pit corrections (Table 10).

5.2. Effect of Dipping Interfaces

The azimuthal dependence shown by the teleseismic data in Fig.12 and Fig.13 might be expected for a dipping boundary beneath the array. This has been suggested to explain similar

variations observed at other arrays (Corbishley, 1970; Niazi, 1966; Otsuka 1966a, 1966b; Greenfield and Sheppard, 1969), although the magnitudes of the anomalies seen at Kaptagat are unusually high. Non-uniform layering could be inferred from the structural complexity suggested for the Eastern Rift (Griffiths et al, 1971; Khan and Mansfield, 1971; Sundaralingam, 1971). This concept will be developed in the following section.

The problem of the refraction of a seismic ray at a dipping interface with a velocity contrast has been treated by Otsuka (1966b). The theory is given in Appendix A along with details of the computational procedure. A summary of the results can be given with reference to Fig. A1.

For a seismic ray incident on a sloping boundary with an apparent slowness vector $\underline{P}_i$ and an apparent slowness vector after refraction $\underline{P}_r$ we can derive:

$$\underline{P}r = \underline{P}_i + \underline{R} \qquad 5(i)$$

where $$\underline{R} = \left(\sqrt{|\underline{S}_r|^2 - |\underline{S}_i|^2 \sin^2 i} - |\underline{S}_i| \cos i\right)\left[\underline{k} \wedge \underline{n}\right] \wedge \underline{k} \qquad 5(ii)$$

$|\underline{S}_i|$, $|\underline{S}_r|$ are the slownesses below and above the interface. $\underline{n}$ is the normal to the dipping interface and $\underline{k}$ defines the vertical. i is the angle of incidence of the ray at the dipping interface, and can be determined if $\underline{n}$ is known (Appendix A).

From the definitions of $\underline{P}r$ and $\underline{P}_i$,

Slowness Anomaly $\quad dS = |\underline{P}_r| - |\underline{P}_i|$

Azimuth Anomaly $\quad dA = \text{ang}(\underline{P}_i . \underline{P}_r)$

We can extend 5(i) to cover refraction at several layers, each with different dips, simply by summing the anomaly vectors

$\underline{R}_j$ for each layer.(Appendix A).

$\underline{R}$, the anomaly vector, will be perpendicular to the strike of the dipping interface. The azimuth of the incident slowness is taken from the NOAA data and its magnitude from Herrin et al's (1968) tables, for the appropriate distance. In the interpretation, we use the principle of least squares. The velocities on either side of the interface (hence $|\underline{S}_i|$ and $|\underline{S}_r|$) are assumed and the direction of dip and the angle of dip varied through a range of values, for each of which theoretical anomalies are calculated for all of the data points. The root mean square deviation of the observed points from the calculated anomalies can then be mapped over the range of the variables and a minimum deduced. For a two-layer case, the angles of dip for both boundaries and their direction are varied. Finally different velocity contrasts can be assumed and the dependence of the fit on these parameters investigated.

5.3. Location of Structural Features

(1) Dipping Moho

A sloping Moho could be inferred from seismic and gravity results. To the west of the Gregory Rift the structure of the crust and topmost upper mantle seems to be similar to that in shield areas. The velocities of regional earthquake arrivals measured at Kaptagat (Fig.6.) show values of 6.5 - 6.7 km/sec for epicentres less than 200 km away and values of 7.8 - 8.4 km/sec for more distant events. The latter are similar to those found by refraction studies in the Transvaal (Gane et al, 1956; Hales and Sachs, 1959; Willmore et al, 1952) which were between 7.96 km/sec

and 8.27 km/sec for the P_n phase. The Kaptagat data for close events are for earthquakes with focal depths of about 20 km, probably from within an intermediate crustal layer. These conclusions suggest a model with crust and sub-Moho P-wave velocities similar to those in the AFRIC model of Gumper and Pomeroy (1970) which is taken to represent the stable regions of Africa.

They are also in accord with the body wave results of Gumper and Pomeroy and the satisfactory propagation of the S_n phase between the Eastern and Western Rifts (Molnar and Oliver, 1969).

However, from the refraction study of Griffiths et al (1971) along the axis of the Gregory Rift, a body of material with P-wave velocity 7.5 km/sec is found to be within 20 km of the rift floor. This is presumed to be anomalous upper mantle. Khan and Mansfield (1971) have interpreted the positive Bouguer anomaly along the rift axis in terms of this body and postulated a wedge thinning away from the rift (Fig.5.). This could then indicate a Moho dipping towards the flanks of the rift overlying the high density and, presumably, high velocity material. However, this would give a high velocity wedge thinning away from the rift which would give rise to teleseismic anomalies at Kaptagat of the opposite sign to those observed. From Fig.A2., it can be seen that for seismic rays travelling up-dip before hitting a sloping Moho, the slowness anomaly is negative. The teleseismic anomalies are not, therefore, caused by a slope on the Moho.

(2) Thinning Low Velocity Zone within the Upper Mantle

The 7.5 km/sec velocity from Griffiths et al (1971) probably represents the upper surface of the low velocity zone

suggested to explain the long wavelength negative Bouguer anomaly over the Gregory Rift. Searle (1970) and Sowerbutts (1969) showed that this body appears to extend for some distance away from the rift. This is only compatible with the regional earthquake data from Kaptagat if the zone deepens westward to give way to 'normal' Sub-Moho material of velocity 7.8 - 8.4 km/sec. This could then result in a sloping boundary over the low velocity zone which would give teleseismic anomalies of the correct sign to explain the slowness and azimuth data in this study.

An interpretation of the array data was attempted in terms of a single sloping upper boundary to the low velocity zone. The velocity above the interface, V2, which gives $|\underline{S}_r|$, was fixed at 8.1 km/sec, the mean for the P_n phase at Kaptagat. The velocity V1 for the underlying low velocity zone, the dip on the interface D1 and the direction of dip Ψ were all varied through a wide range of values but no minimum could be found for fits to either the slowness or azimuth anomalies. This was because, in order to explain the large observed anomalies, extremely steep dips and large velocity contrasts would be required and under these conditions it was found that some rays travelling up dip would hit the interface at angles greater than the critical value defined by V1 and V2, and would be internally reflected. This is more pronounced for events at short distances, with relatively large angles of incidence i to the interface. Thus a single sloping boundary over a low velocity zone, with sharp velocity contrasts, is inadequate to explain the anomalies.

A subsequent interpretation was attempted in terms of two

layers with slopes of the same sign but with velocity contrasts across both, which were selected to represent a gradation in velocity from a low value V1 for the anomalous upper mantle to the 8.1 km/sec for V3, the velocity above the zone (Fig.21.) This did not overcome the problem of internal reflection and again no true minimum could be found.

(3) Low Velocity Wedge

An interpretation of the observed anomalies in terms of a single upper boundary to the low velocity zone does not seem possible. A more useful model is obtained when the slope of the lower boundary of this zone is also considered. A lower interface dipping towards the rift is presumed to overlie material having a higher seismic velocity, thus reinforcing the anomalies arising from refraction at the upper boundary. A somewhat similar model has been used to fit gravity measurements (Khan and Mansfield, 1971). For a model of this type (Fig.21), V3 was assumed at 8.1 km/sec from the array data and V1 taken as 8.3 km/sec from the AFRIC model, these being fixed during the computations. The depth to the lower interface was taken at 150 km, to calculate the radius R to this level (this scalar quantity is distinct from the anomaly vector $\underline{R}$). However, the theoretical anomalies are not very sensitive to changes in R of the order of 100 km.

The two interfaces are treated as lying in the same vertical plane so that the two slowness contributions peak in the same direction. The direction of the negative peak, that is, the direction of the maximum thickening of the wedge, Ψ, is varied, with the two angles of dip, D1 and D2, to find a minimum. Initially, V2 is fixed at 7.5 km/sec (Griffiths et al, 1971).

KAPTAGAT

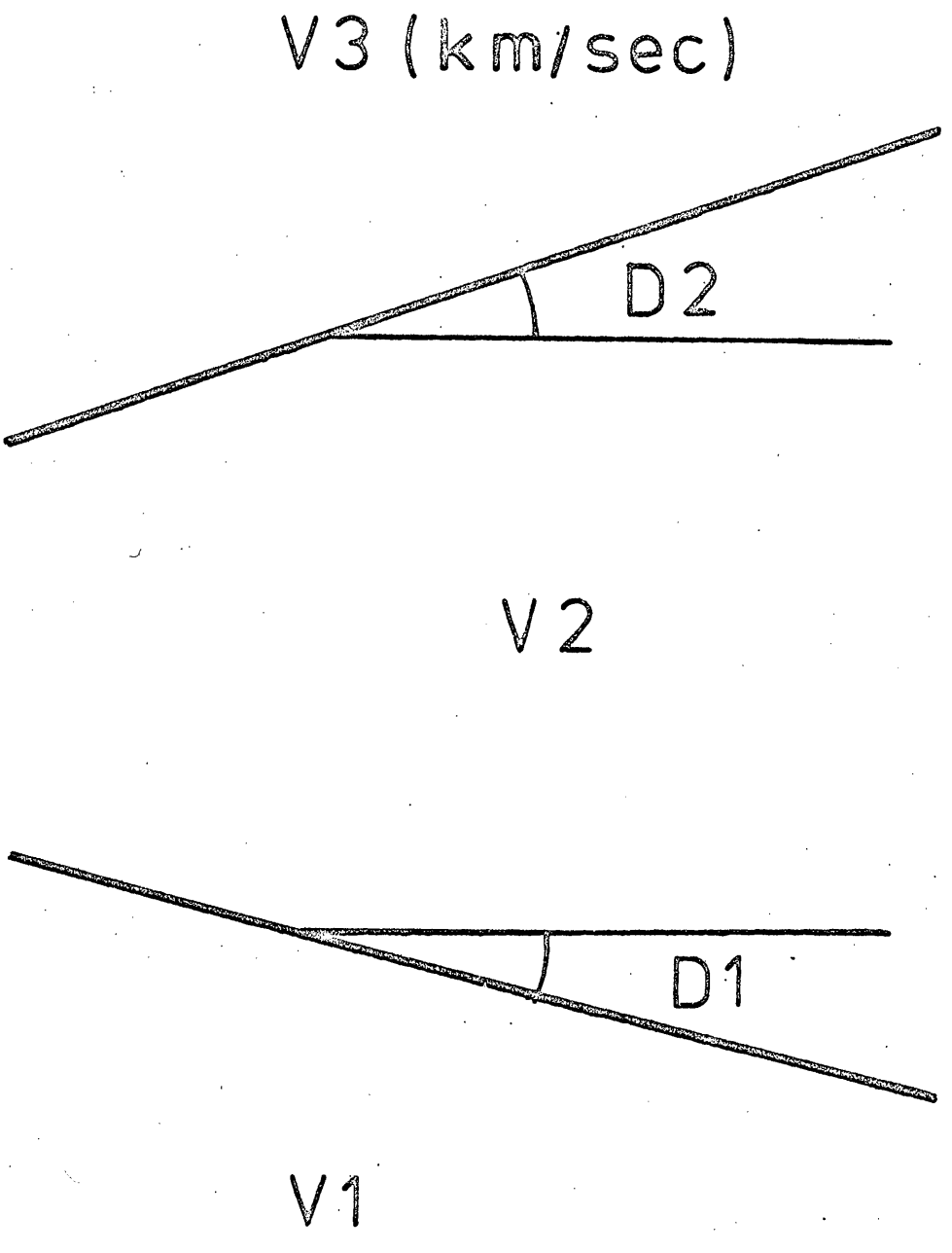

Fig.21. Schematic diagram of model, with two dipping interfaces, used in array data interpretation (Chapter 5).

Two sets of models are derived, the first with both slowness and azimuth data fitted, and the second using slowness data only.

5.4. The Models

(1) Model 1

The slowness and azimuth anomalies were both used in fitting Model 1, and the RMSD's for the two sets of observed points from their computed values combined. In fitting both simultaneously, the RMSD's for each were weighted inversely in the ratio of their mean magnitudes and errors of observation.

Constraining the wedge velocity V2 to 7.5 km/sec, the fits obtained for both slowness and azimuth are shown in Fig.22 and Fig.23 respectively. The vertical bars indicate 95% confidence limits on the observed points and the solid circles are the theoretical anomalies. It is important to realise that because we are considering rays from different distances, they will be incident on the dipping boundaries at different angles so that the computed anomalies are dependent on distance as well as azimuth and consequently the computed anomalies do not lie on a smooth curve. It can be more informative to plot the residuals of the observed points from the values calculated for the model. These are shown for slowness and azimuth, respectively, in Fig.24 and Fig.25.

The model for a wedge of velocity 7.5 km/sec is that with a lower slope of 36° and an upper slope of -26°. The direction of maximum thickening of the wedge is 125° east of north. From the graphs of the fitted anomalies it appears that the values for slowness would show a better match if the wedge angles were larger. From Fig.24 those events from azimuths 0° - 35° show predominantly

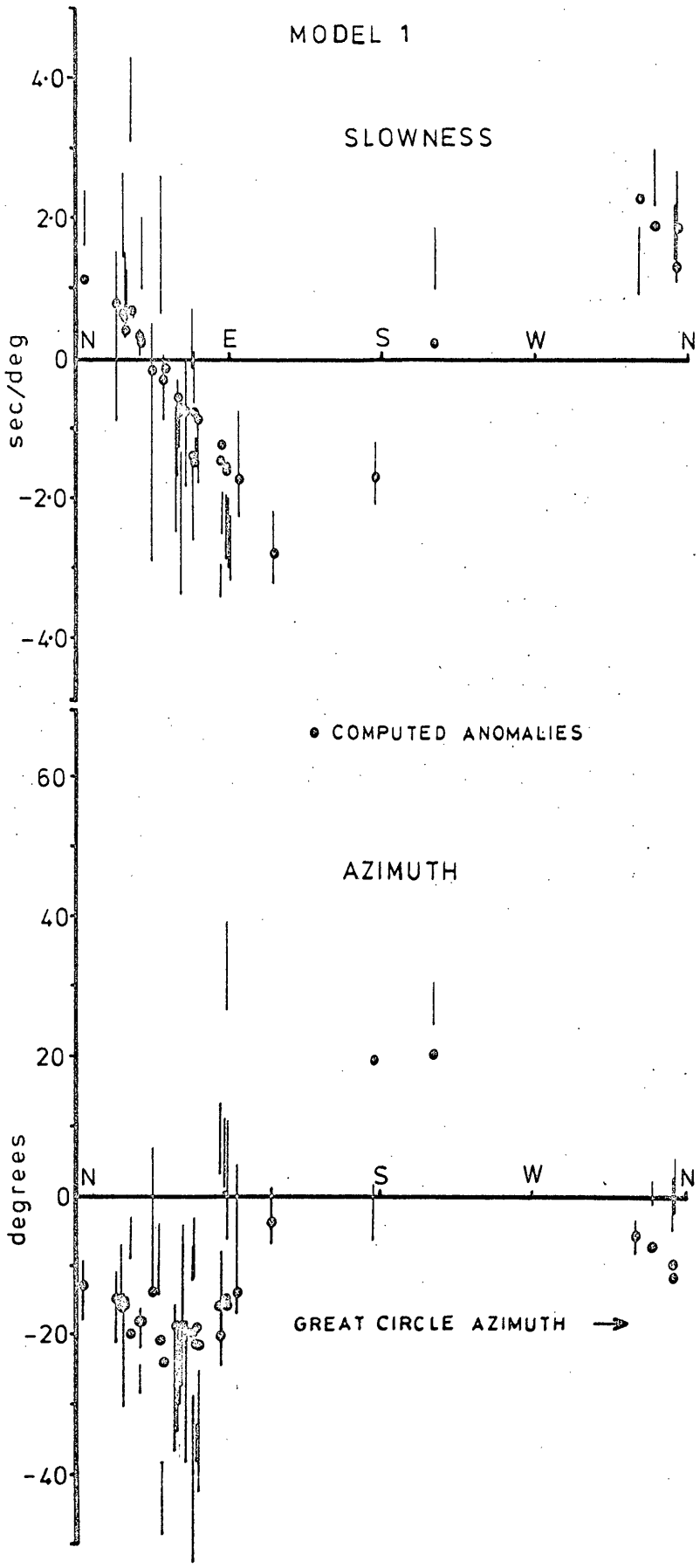

Figs. 22 & 23. Computed slowness and azimuth anomalies (dots) for wedge model 1 and observed anomalies (bars).

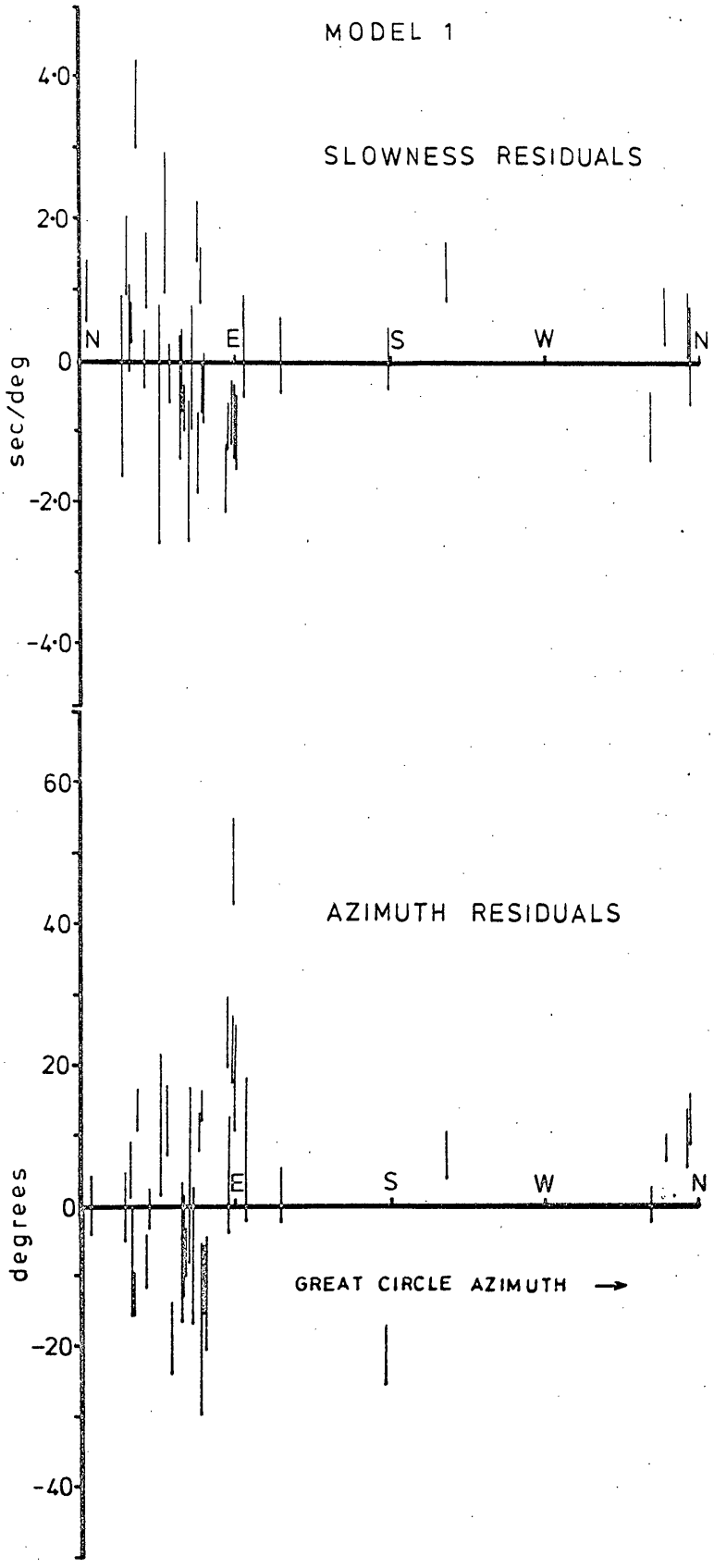

Figs. 24 & 25. Residuals from computed slowness and azimuth anomalies for wedge model 1. Bars indicate 95% confidence limits.

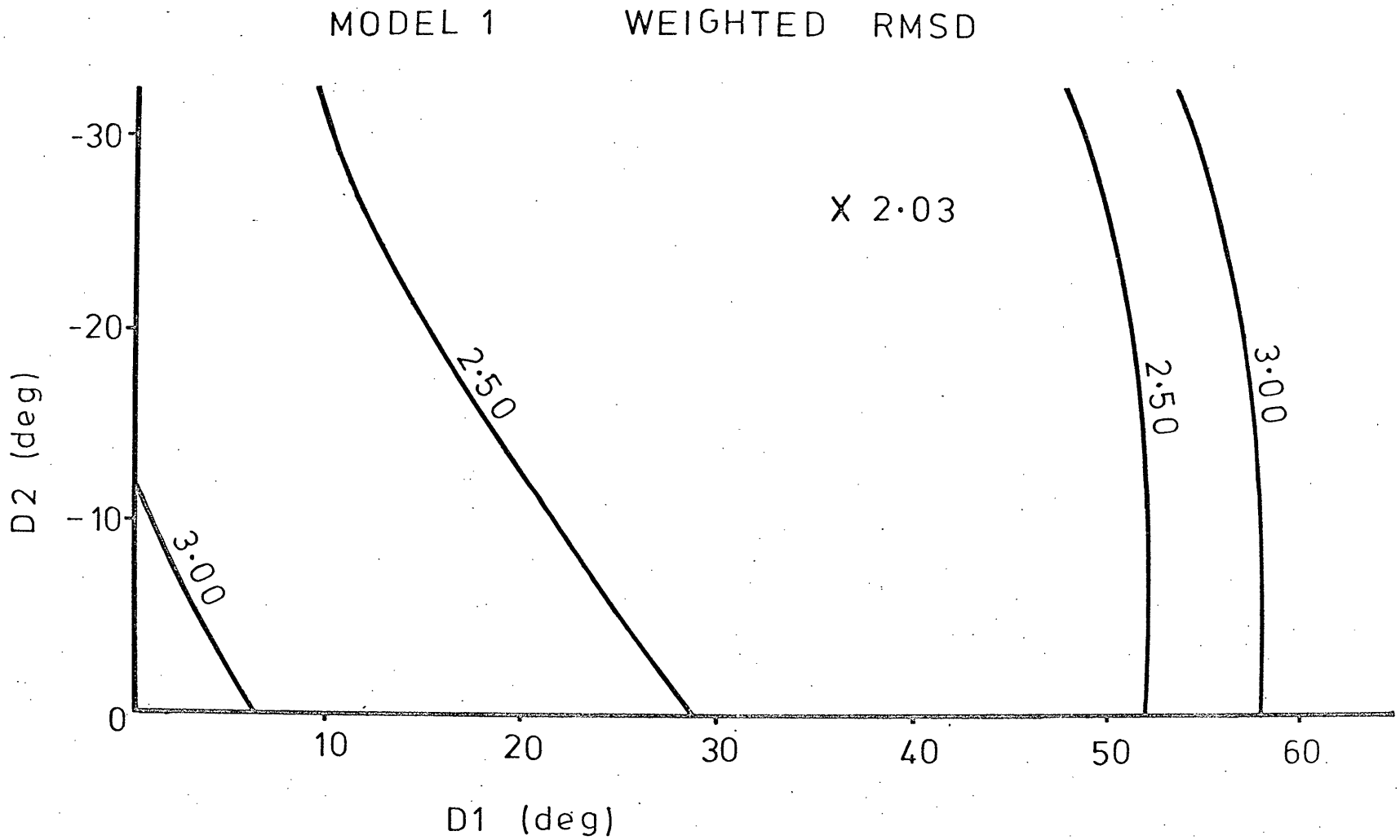

Fig.26. Contoured, weighted RMSD for model 1. RMSD at minimum is 2.03.

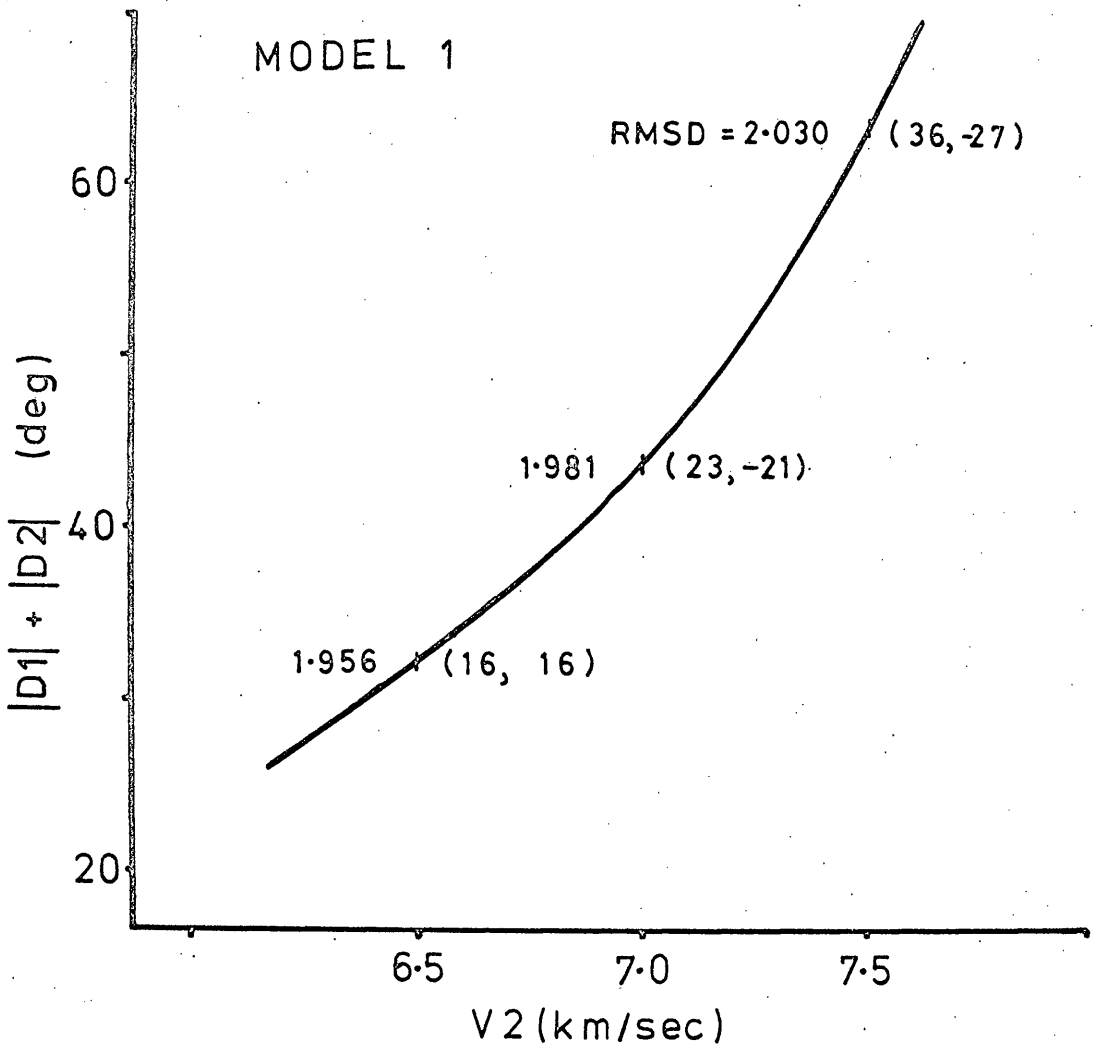

Fig.27. Variation in parameters for model 1 for differing values of wedge velocity V2. Explanation on pages 61 - 2.

positive residuals whereas those between 50° - 90° east of north are mainly negative. A change of sign of the theoretical anomalies between these two groups suggests that one or both of the boundaries should be dipping more steeply. For the azimuth anomalies, which should have a negative peak within the north-east quadrant and change sign at 125° east of north, less steep dips would probably give a better fit. Although the residuals (Fig.25.) do not show the marked trend evident for slowness, the slight predominance of positive residuals between great circle azimuths 80° - 120° and 330° - 360° favours smaller values of D1 and/or D2. A disturbing feature of the fit to both sets of data is the number of points deviating from the computed anomalies by more than their confidence limits. This is in part due to the apparent compromise in the best fit for the two anomalies if considered separately but seems mainly to reflect the scatter of the data. This is also evident if we plot the weighted RMSD as a function of the two angles of dip. Fig.26 shows this mapped over the parameter space defined by D1 and D2. It shows that adjustments can be made to the dips with relatively small effect on the RMSD. In particular, the contours are open-ended, which implies that D2 is very poorly determined.

We have initially considered the wedge velocity V2 to be 7.5 km/sec as from refraction results. However, as this may only represent the top surface of the anomalous mantle material we have fitted similar models with other values for V2. A summary of these is provided by Fig.27. This gives a plot of total wedge angle ($|D1| + |D2|$) against the velocity within, for a best fit to the data. At each of the values corresponding to velocities of 6.5, 7.0 and 7.5 km/sec, the individual values of D1 and D2 are shown in

brackets, with, to the left of the graph, the weighted RMSD of the observed points from those computed for the model. Although the RMSD decreases as V2 decreases for these fits, the wedge velocity is also indeterminate as, presumably, from consideration merely of the statistical fit, the preferred model would be a very thin wedge of unrealistically low P-wave velocity. Thus it appears that any lowering of the velocity between the two interfaces can be compensated by decreasing the angle between them and we cannot from the slowness and azimuth data alone distinguish between the different models represented in Fig.27.

In all the models in this group the direction of maximum thickening, Ψ, was about 125° east of north as derived for the model with V2 = 7.5 km/sec.

(2) Model 2

This interpretation used the slowness data only. From Fig.28, the correspondence between the computed and observed slowness anomalies for a wedge of velocity 7.5 km/sec is much better than for Model 1. As might be expected, the azimuth anomalies appropriate to this model show a worse fit (Fig.29.). This wedge requires slopes of 46° and -26° on the lower and upper boundaries respectively with a direction Ψ of 123° east of north. This means a steeper dip on the lower interface than for the model from the combined data. We can see (Fig.30) that the trend in the slowness residuals for Model 1 from predominantly positive to negative from 0° to 90° has disappeared. However, again, several of the computed slowness values fall outside the confidence limits on the observed points. The azimuth residuals (Fig.31.) for this model have a more positive trend which for the expected negative peak in the north-

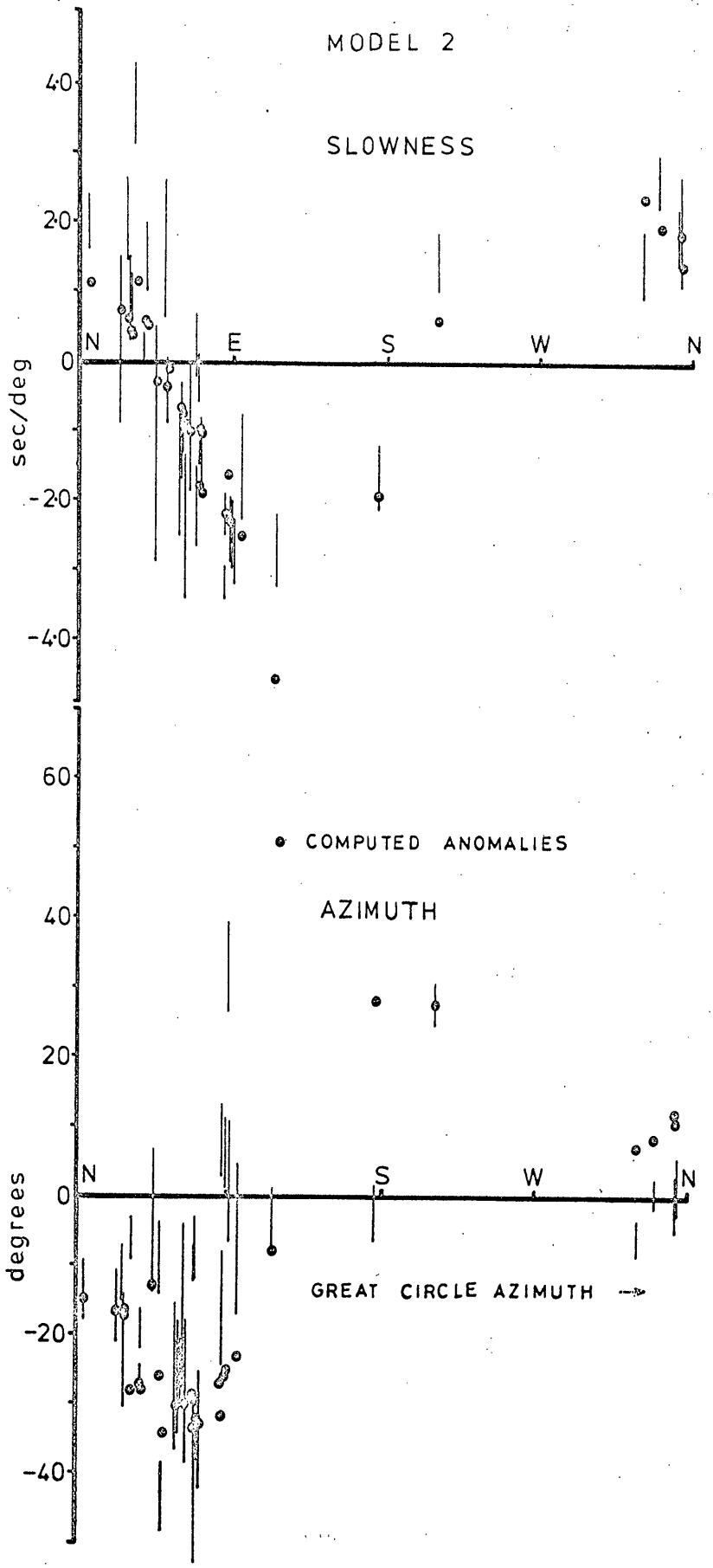

Figs. 28 & 29. Computed slowness and azimuth anomalies (dots) for wedge model 2, and observed anomalies (bars).

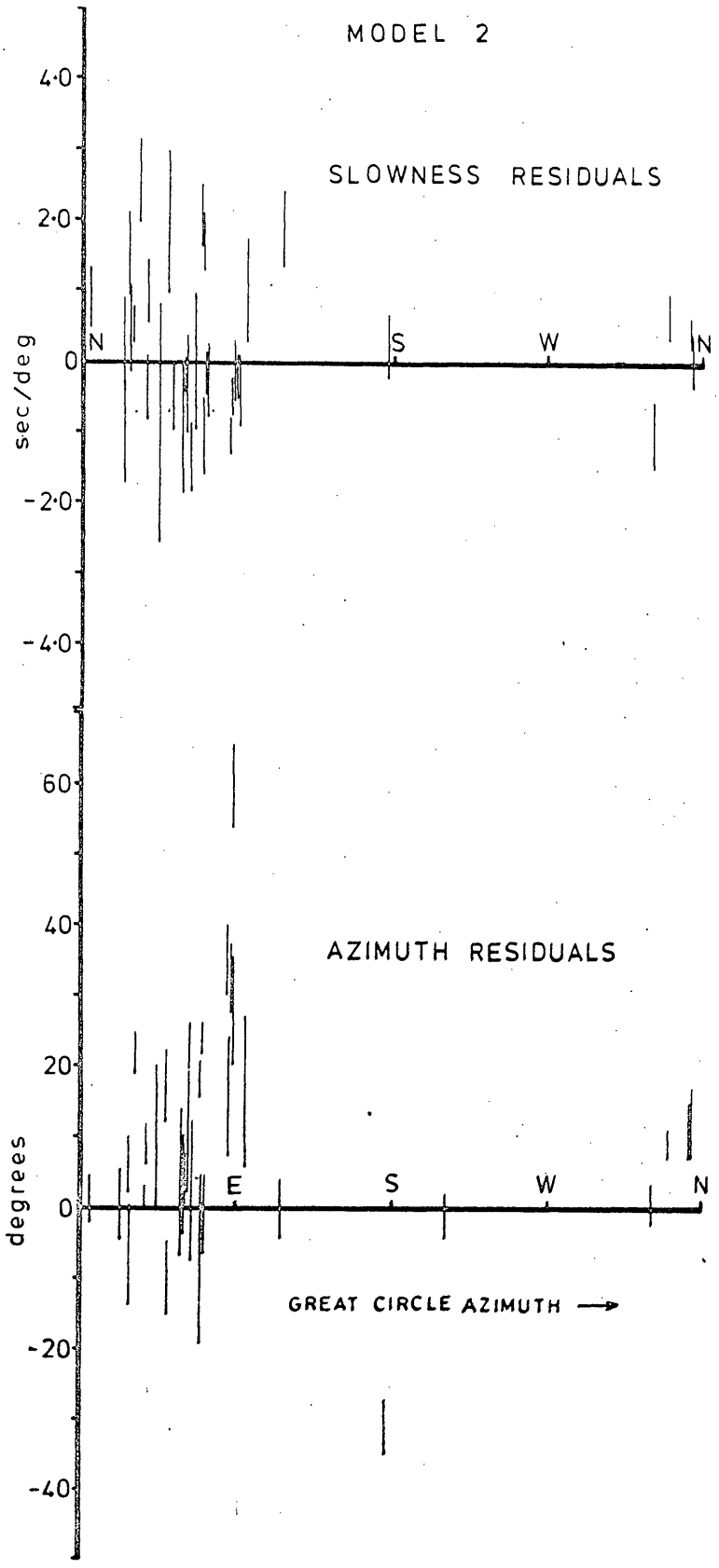

Figs.30 & 31. Residuals from computed slowness and azimuth anomalies for wedge model 2. Bars indicate 95% confidence limits.

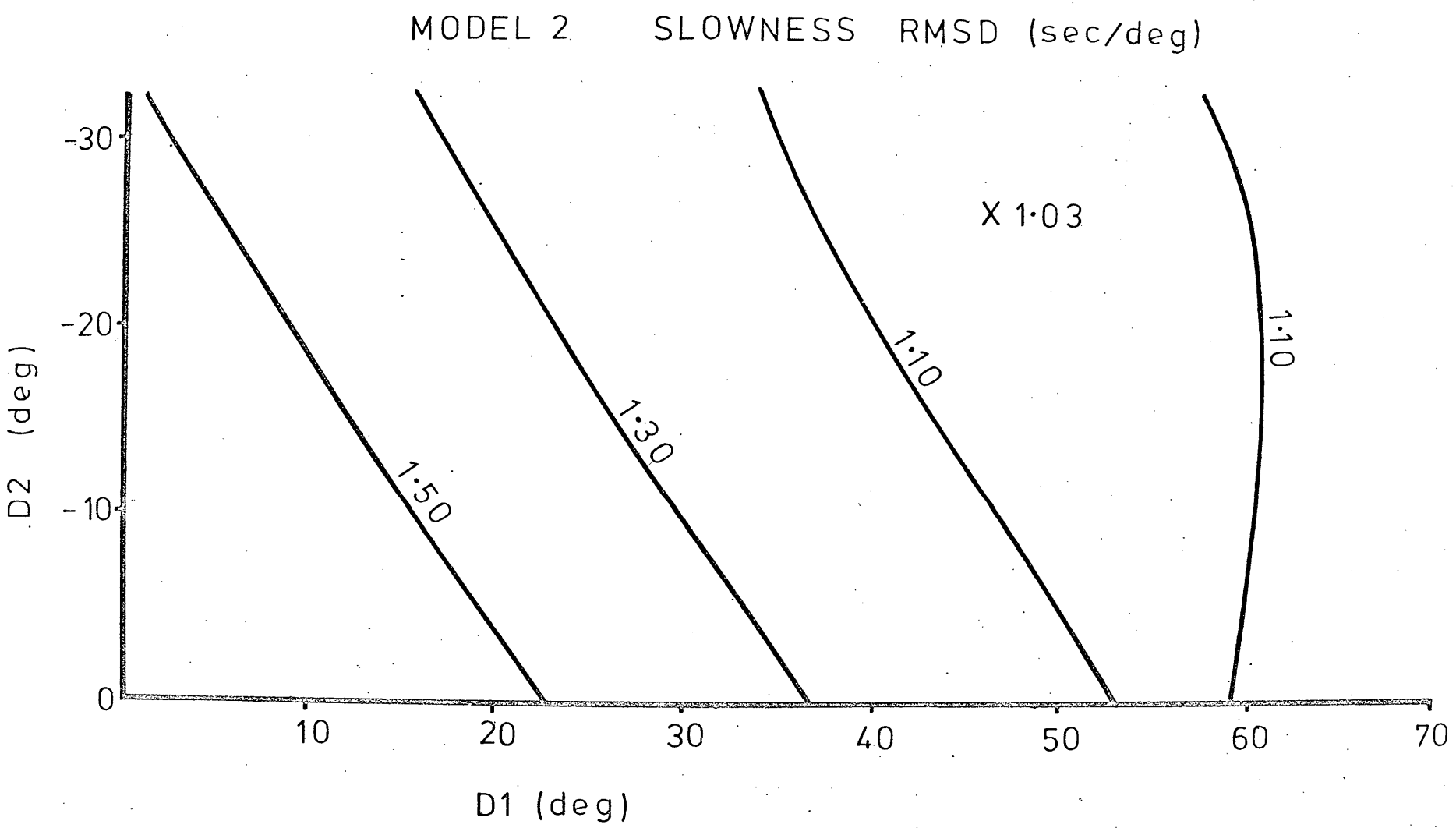

Fig.32. Contoured slowness RMSD for model 2. RMSD at minimum is 1.03 sec/deg.

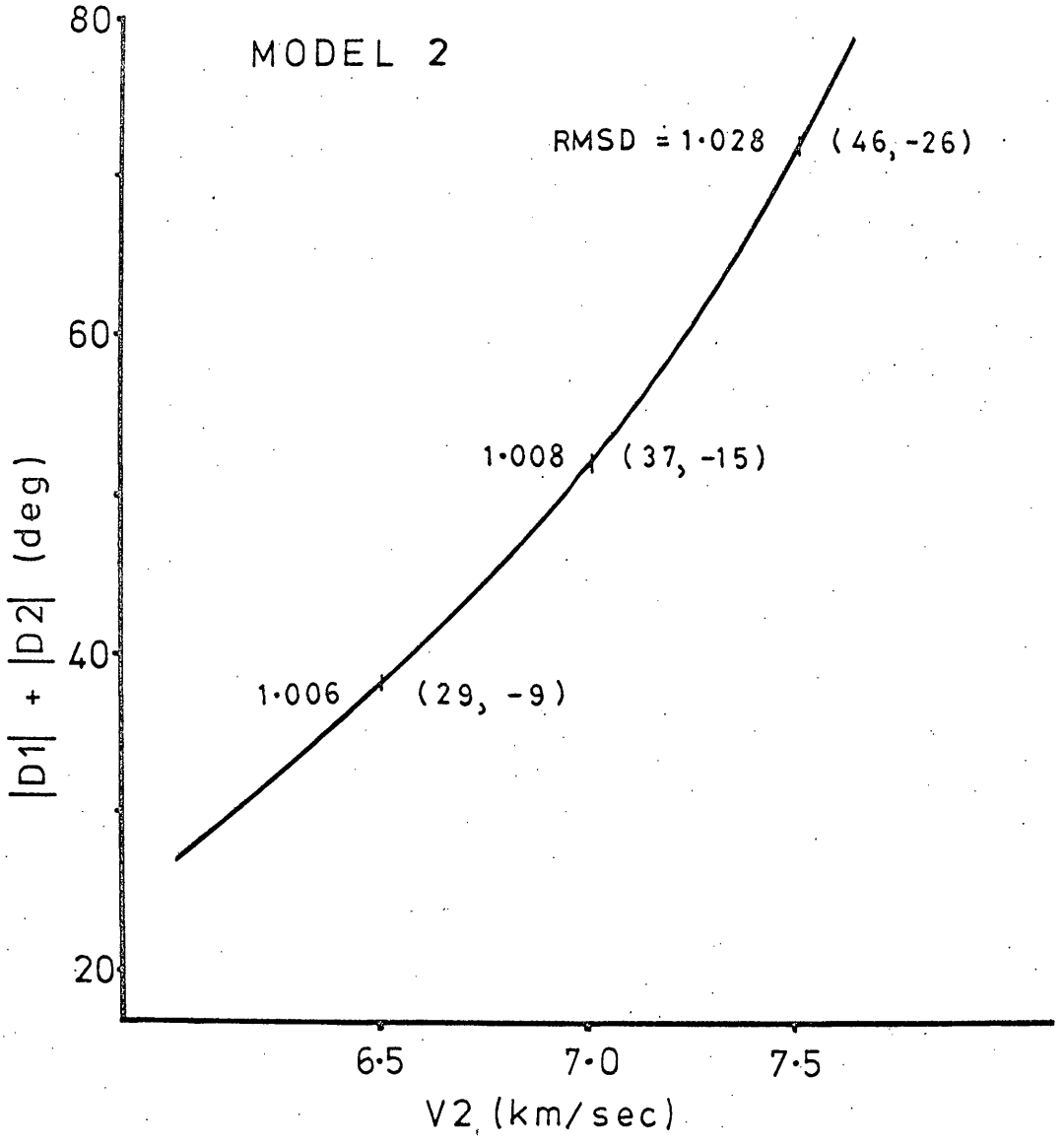

Fig.33. Variation in parameters for model 2 for differing values of wedge velocity V2. Explanation on pages 61 - 2.

east sector implies less steep dips are required to fit these data alone.

The direction of the wedge shows that it is thickening most rapidly for an angle of 123° east of north, which is not significantly different from that for Model 1. The plot of the RMSD for various values of D1 and D2 (Fig.32) shows that, again, individual dips are relatively indeterminate. A similar plot to Fig.27 shows the variation in parameters for different wedge velocities for the Model 2 group (Fig.32), with the same characteristics evident - general lowering of the RMSD as decreasing values of V2 are accompanied by less severe dips. The notation is as for Fig.27, with individual dip angles in brackets and the RMSD values for the slowness data to the left of the curve.

5.5. Discussion

From a comparison of Models 1 and 2 it would appear that the slowness anomalies require more extreme values for the dips and/or the wedge velocity than do the azimuth anomalies. Obviously, in the ideal case both sets of data, taken individually, should yield an identical range of possible models. It has been found elsewhere (Niazi, 1966) that azimuth anomaly can be unreliable as the errors can be of a magnitude comparable with the values themselves. This is not the case here, however, as the anomalies are large in comparison with the 95% confidence limits, but there is inconsistency in values even for events from similar directions - a range of almost 40° between great circle azimuths 80° and 100° east of north. Thus slowness anomaly is probably more useful in interpretation in this study. The scatter of values for both sets of data is probably due to rapid variations in structure and seismic velocity, deviating

locally from the simple model that has been suggested. Pairs of events (Table 10) from almost the same regions - 13 and 14, 17 and 19, 20 and 21 - have similar azimuth and slowness anomalies within the confidence limits but can differ considerably from values for slightly less adjacent earthquakes.

No formal errors have been determined for the final values of the variables, D1, D2 and V2. The plots of RMSD for the two angles of dip (Fig.26 and Fig.32) provide a simple two-dimensional representation of the difficulties involved. If we consider just these two variables, and estimate the range of values for each, corresponding to one standard deviation from the minimum, then some of the models thus described would not resemble a wedge. This does not mean that a wedge is not a suitable fit but it does mean that it is highly non-unique.

As a consequence of this non-uniqueness, before we can reduce the number of possible models, additional data are needed as constraints. Thus a range of models only is given, represented by Figs. 26, 32, 27 and 33.

Although all the models have sharp velocity contrasts across their boundaries, this does not rule out the possibility of more complex structures giving comparable fits to the data. Similar anomalies could arise if the sides of the wedge were gradations in velocity to a value at least as low as V2 somewhere within the wedge. As we cannot exclude the possibility of complexity within the wedge, the velocity measured at the top of the zone (e.g. by seismic refraction studies) might not give an appropriate value of V2.

From a plot of RMSD for the minima at various values of the angle Ψ, the standard error in determining the direction of the wedge is about $\pm 30^{\circ}$ for both Models 1 and 2. The angle Ψ, as defined previously, gives the direction of the maximum thickening of the wedge. The value obtained from Model 1 is 125° east of north and this can be related to the tectonics of the rift in Kenya. North of Kaptagat, from 2.0°N to 0.5°N, the rift valley trends 20° east of north whereas from 0.5°N to 1.0°S its direction is 20° west of north. South of 1.0°S it is again aligned 20° east of north. This has been taken as showing confirmation of McKenzie et al's (1970) pole of rotation for the opening of the East African Rift Valleys. Searle (1970b) calculates that this would involve relative motion of the two plates in Kenya in a direction 124° east of north. The angle Ψ can be correlated with other features, although only approximately. The wedge appears to thicken towards the area of particularly impressive uplift marked by the Aberdare and Nyambi Ranges. This is also a region of recent volcanism with Quaternary basalt eruptions and Upper Pliocene and Lower Pleistocene basalt-phonolite-trachyte volcanoes (Baker and Wohlenberg, 1971; Wright, 1970).

For the wedge models we do not know the thickness of the crust or the depth at which normal mantle gives way to anomalous material. Bonjer, Fuchs and Wohlenberg (1970), have studied the crustal structure over East Africa and found thicknesses of 39 km at Addis Abbaba, 43 km at Nairobi, and 35 km at Lwiro. The AFRIC model of Gumper and Pomeroy (1970), derived for Africa as a whole, has a 36.2 km crust. In the absence of any firm evidence as to this value beneath Kaptagat we will assume that for AFRIC. If the boundary between the crust and the 8.1 km/sec layer is horizontal,

we can estimate the minimum slope on the top of the anomaly in order that at some horizontal distance up-dip from Kaptagat this zone is still overlain by normal mantle material. Assuming the axial structure of Griffiths et al (1971), the top of this 7.5 km/sec zone must dip at more than 35° to give way to the 8.1 km/sec layer at a horizontal distance of 17 km from Kaptagat. This distance would be associated with a seismic signal recorded at Kaptagat coming from a direction Ψ and hitting the Moho at an angle of incidence of 30°. This would give about 12 km of the 8.1 km/sec material below Kaptagat. A thinner crust with, therefore, upper mantle material nearer the surface, would mean that such a slope would not need to be as great as 35°.

This is a limiting case in the sense that if the top of the anomalous zone cut into the crust instead of the mantle, the velocity contrast would be reversed and a contribution made to the slowness and azimuth anomalies that would contradict the observed variations. This need not be critical, as it could be compensated by velocity gradations below the top of the anomaly, or a steeper slope on the lower boundary, but it would suggest that rays from short distances (large angles of incidence) would feel less of the cause of the anomalies. A similar problem could occur at the lower interface, but is more difficult to treat quantitatively. The gravity interpretation of Khan and Mansfield (1971) suggests that the anomalous zone is roughly symmetrical about the rift axis which means that it is deepest below the centre of the rift. Even if this is only an approximation, for small velocity contrasts and hence steep dips on the wedge sides, a ray moving westward under the anomaly could hit the lower boundary of the zone to the east of its deepest point, resulting in such rays missing the refracting edge presumed to cause the slowness and azimuth variations. This problem would lessen with

larger velocity contrasts and less steep dips (these considerations assume that the total thickness of the zone can be partly controlled by some parameter such as delay time).

Whether or not these effects are appreciable is difficult to establish, but to give an indication, those events with epicentral distances greater than 60° from Kaptagat have been fitted separately to a wedge Model 3. These correspond to rays with fairly small angles of incidence, although the division of events was somewhat arbitrarily fixed at this particular distance value. Only slowness anomalies were fitted so that the Model 3 is to be compared with Model 2. The 18 events that were used give a very good fit, with values of 44° and - 38° for D1 and D2 respectively for V2 = 7.5 km/sec (Fig.34). The RMSD is 0.454 which confirms that the residuals are low (Fig.36), although azimuth again does not fit well (Figs.35 and 37). The preferred direction of the wedge is slightly changed, with the maximum thickening occurring at 118° east of north.

Two points are of particular interest. One is that an improved fit is obtained, (Fig.38), mainly it seems because the scatter on the observed points is less. Secondly this model, for the same value of V2, has total dips of 82° compared with 72° for Model 2. This supports the idea of a wedge having gradations in velocity from the outer boundaries to some very low value within. Although close events appear to suit a model less extreme than that for those more distant, the former still show large systematic variations in slowness and azimuth, which must indicate that they undergo appreciable deflection at dipping interfaces. A model consisting of gradations in velocity can be considered as several wedges inside each other. Thus close events might miss some of the wedges at the vertical extremities of the anomalous zone. However,

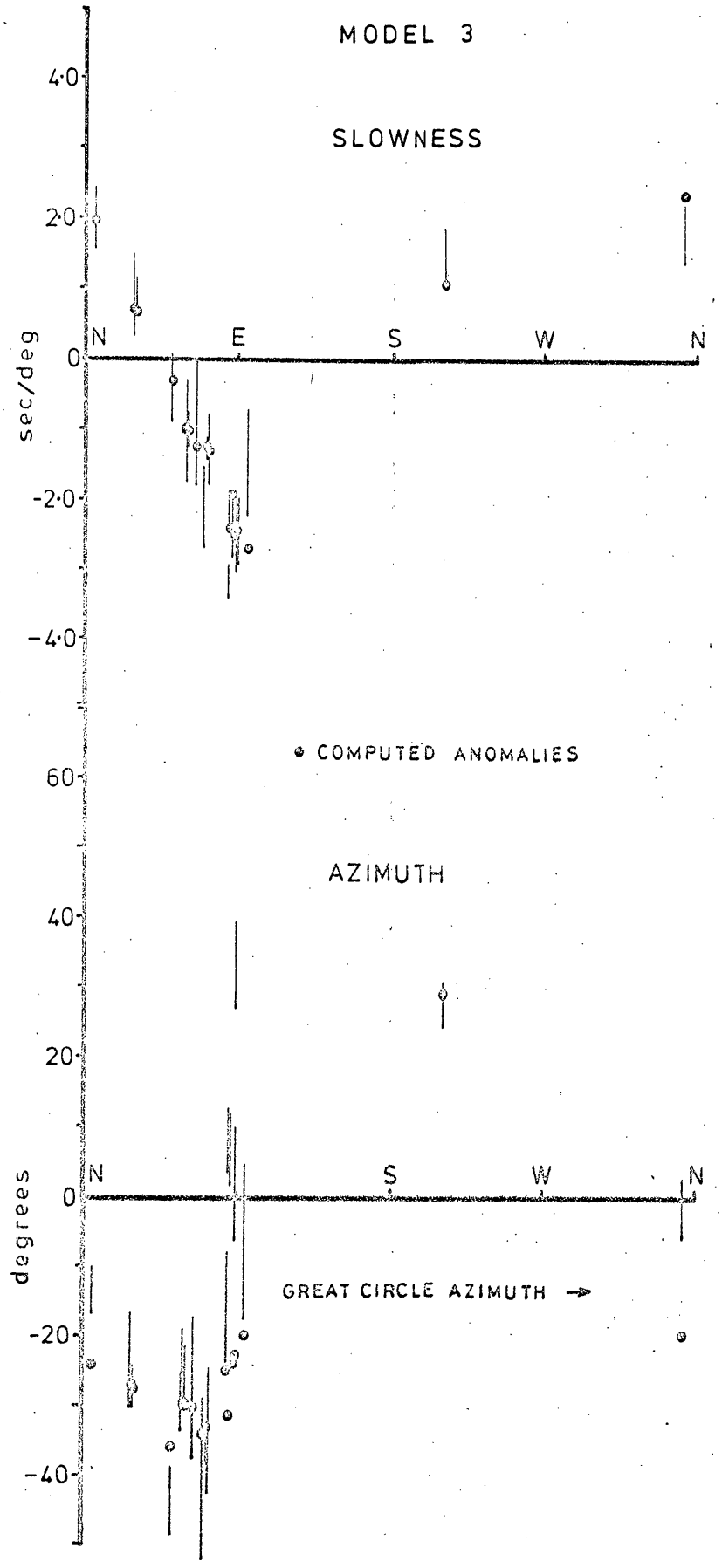

Figs. 34 & 35. Computed slowness and azimuth anomalies (dots) for wedge model 3 and observed anomalies (bars).

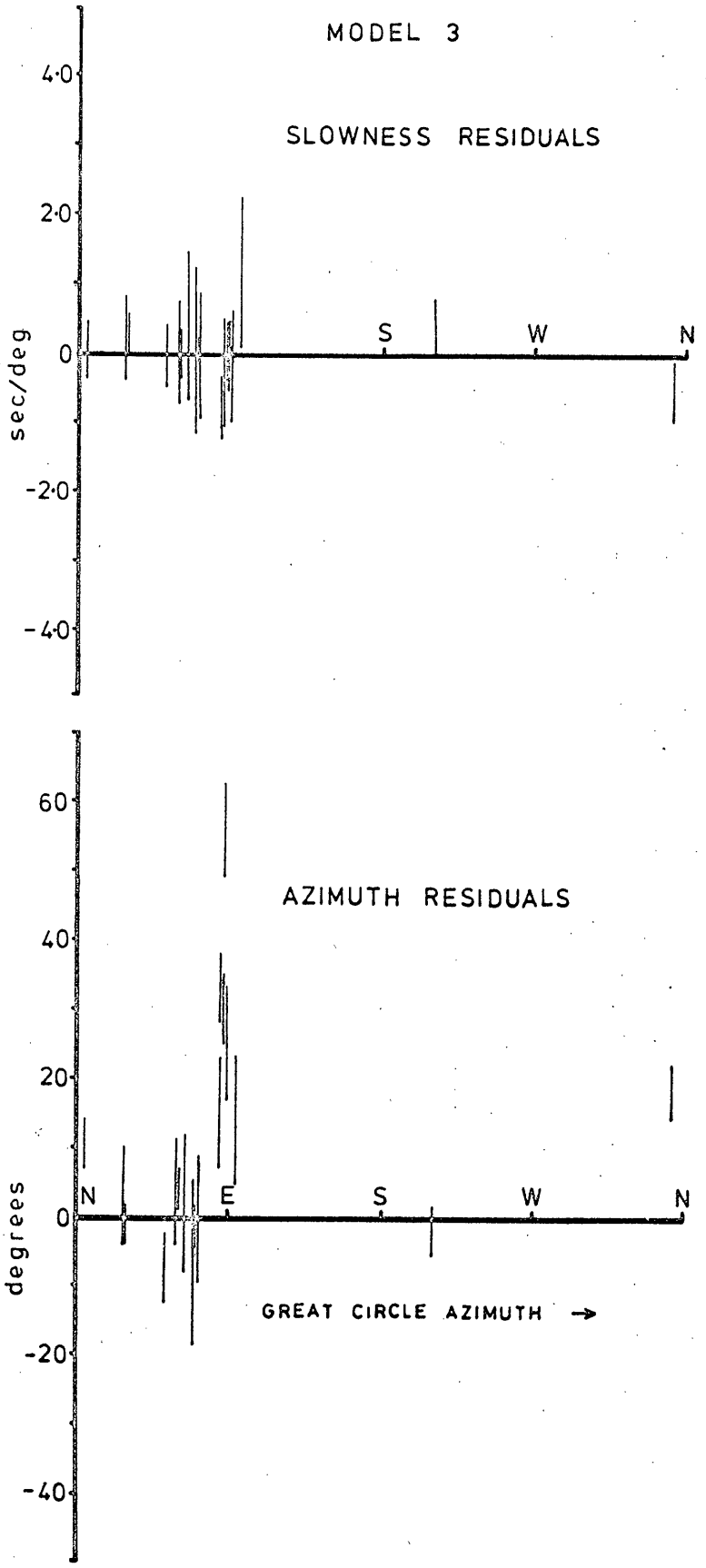

Figs. 36 & 37. Residuals from computed slowness and azimuth anomalies for wedge model 3. Bars indicate 95% confidence limits.

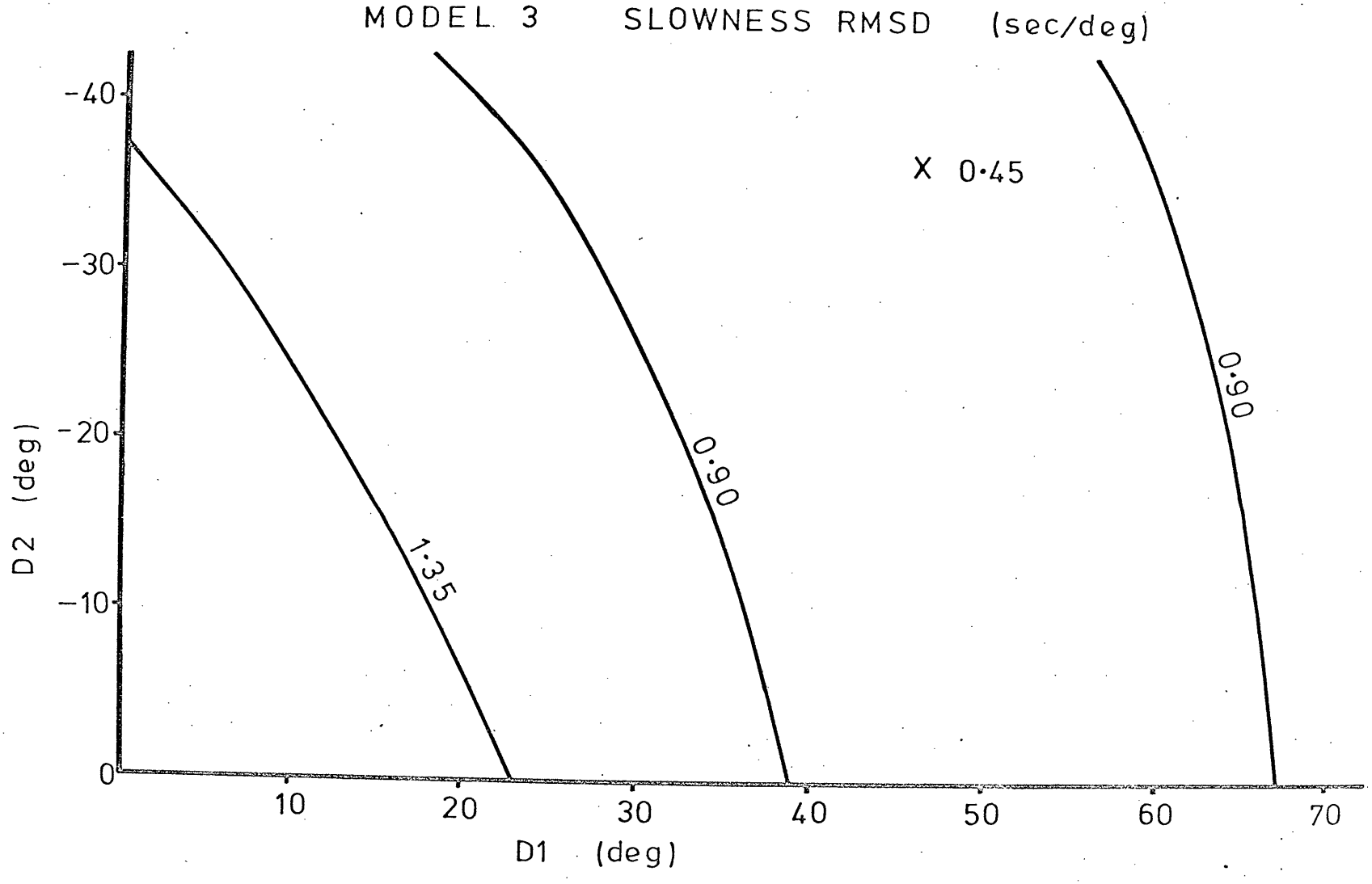

Fig.38. Contoured slowness RMSD for model 3. RMSD at minimum is 0.45 sec/deg.

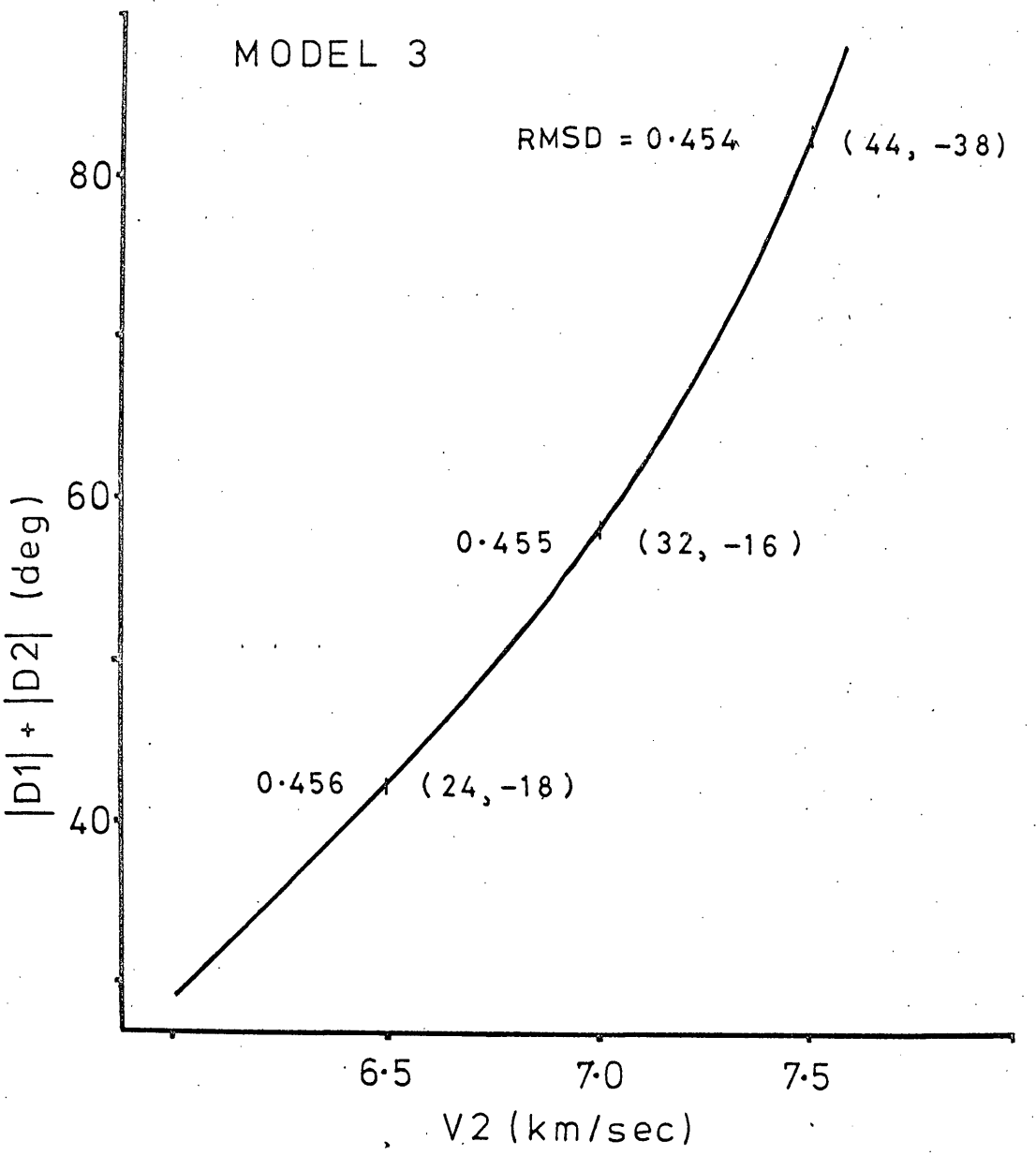

Fig.39. Variation in parameters for model 3 for differing values of wedge velocity V2. Explanation on pages 64 - 2.

the fact that events even for these small epicentral distances experience the effects of a large anomaly would tend to favour a very low velocity thin wedge rather than one much thicker with small velocity contrasts.

The severity of the models suggested here, with very steep slopes and low velocities, is unusual. Similar, but generally less extreme structures have been suggested for an anomalous upper mantle zone beneath the western United States. Slopes of the order of 30° for a P-wave velocity of 7.2 km/sec have been proposed by Nuttli and Bolt (1969) and Otsuka (1966b), with greater dips for higher channel velocities. An alternative interpretation would be that the anomalous material has almost zero rigidity (Hales and Bloch, 1969), with a P-wave velocity of about 6.0 km/sec and much reduced thickness and angles of dip (Nuttli and Bolt, 1969).

CHAPTER 6

INTERPRETATION OF P-WAVE DELAY TIMES

6.1. Introduction

P-wave delay times relative to Bulawayo (BUL) were measured for Kaptagat (Chapter 4), with a mean of 2.20 ± 2.00 seconds, where the errors are 95% confidence limits. The individual delays have been corrected for angle of emergence to facilitate interpretation in terms of plane, parallel layers. The cause of the delays will be discussed in relation to such a structure and then with regard to the type of model suggested to explain the anomalies in slowness and azimuth of approach.

6.2. Cause of Delays

The substantial positive delay at Kaptagat with respect to Bulawayo indicates the existence of anomalously low velocity material beneath the array station. From the array analysis of regional earthquake arrivals and surface wave dispersion results for the AAE-NAI path (Sundaralingam, 1971), it appears that the crustal structure away from the rift axis is similar to that for the stable parts of Africa, as represented by the AFRIC model. If then, AFRIC is typical of the crust and upper mantle beneath Bulawayo, it is likely that Kaptagat and Bulawayo are upon similar crustal structures. Therefore, the cause of the delays does not lie within the crust and it will be taken that the entire 2.20 seconds is a result of differences within the upper mantle underneath the two stations. It may be that the crustal structure for Bulawayo would be more accurately represented by, for instance, the SASD 2 model

of Bloch, Hales and Landisman (1969), shown in Table 2, or that the crust at Kaptagat is similar to that suggested for the Nairobi area by Bonjer, Fuchs and Wohlenberg (1970), in Fig.2. Calculations show, however, that the use of these alternative models does not greatly affect the value of the mean delay time attributable to the upper mantle.

From the array analysis of regional events, it has been concluded that an unknown depth of 'normal' mantle material of P-wave velocity 8.1 km/sec exists beneath Kaptagat. Assuming that this lid to the anomaly is thin and does not significantly affect delays relative to an AFRIC-type structure, a mean velocity within the anomalous mantle zone of 7.5 km/sec (Griffiths et al, 1971) would imply that a thickness of 207 ± 188 km is required to explain the mean delay time for Kaptagat. In the presence of such large 95% confidence limits, any conclusions to be drawn from this result must necessarily be tentative but the thickness is of the same order as those suggested for low-velocity zones beneath Addis Abbaba and Nairobi (Sundaralingam, 1971), Iceland, and the Mid-Atlantic Ridge (Tryggvason, 1964; Francis, 1969), and the Western United States (Nuttli and Bolt, 1969) when similar velocities are assumed. If, alternatively, a lower mean velocity is used to explain the Kaptagat measurements, the zone would be thinner - 114 ± 103 km for 7.0 km/sec and only 74 ± 67 km for 6.5 km/sec. We cannot, at the moment, determine the mean velocity for the anomalous zone.

The effect of a finite thickness of high velocity mantle material (P-wave velocity 8.1 km/sec) overlying the channel can be estimated. For instance, for a 20 km lid, the thickness of the anomaly for a mean velocity of 7.5 km/sec is only decreased by 7 km, with even

smaller alterations if a lower velocity is used.

6.3. Azimuthal Dependence of Delay Times

In the previous section, parallel layers have been assumed. However, the preferred model for the low velocity zone as derived from slowness and azimuth anomalies has steeply dipping boundaries. For this type of structure, it would be expected that relative delay times would vary with azimuth (Otsuka, 1966b; Nuttli and Bolt, 1969) assuming that the layering beneath the standard station (BUL) is roughly parallel. Anomalies here in layering or velocity beneath Bulawayo could complicate the pattern of relative delays at Kaptagat.

In Chapter 4, a crude analysis revealed no significant azimuthal variations, and this will be investigated now in more detail. We can represent delay time as being composed of constant and azimuthally varying terms (Herrin and Taggart, 1968; Bolt and Nuttli, 1967; Lilwall and Douglas, 1970) by fitting a sine curve to the delays:

$$T_{jk} = A_j + B_j \sin (Z_{jk} + U_j) \qquad 6(i)$$

where T_{jk} is the delay time relative to Bulawayo for the k th event in the j th distance range, Z_{jk} is the great circle azimuth of the k th event, and A_j, B_j and U_j are constants defining the delay time for the j th distance range. This equation can be solved by least squares in the presence of errors on T_{jk} in essentially the same way as for equation 3(vi) and a similar computer program to RESFIT is used.

In order to interpret the delays in terms of a structure

with dipping layers (section 6.4.), the individual values are not corrected for angle of emergence at the surface.

If all the data are fitted simultaneously, that is, only one distance range is considered, then the appropriate form of 6(i) is:

$$2.36 \quad + \quad 0.34 \sin (Z_{jk} + 284) \qquad 6(ii)$$

This implies a function of amplitude 0.34 ± 0.41 seconds and the phase angle U_j gives the direction of the maximum positive delay as $166^\circ \pm 72^\circ$ east of north. Hence the azimuthal term is not significant at the 95% level.

If the delays are divided into two groups about an epicentral distance from Kaptagat of 60°; there is sufficient azimuthal coverage in each to allow separate interpretations. The relative delays for events from distances less than and greater than 60° are shown in Fig.40 and Fig.41 respectively, with the solid lines giving the computed fits to the data. The A terms are not significantly different for the two groups, which suggests a lack of distance dependance for the constant part of the delay time function. However, whereas for the shorter distances there is no marked azimuthal variation -B is 0.32 ± 0.80 seconds - Fig.41 shows that delays for events from distances greater than 60° change systematically with the direction of approach. The amplitudes of the sine curve is 0.96 ± 0.68 seconds and the direction of the maximum positive delay is $177^\circ \pm 29^\circ$ east of north.

6.4. Delays for Dipping Interfaces

A structure such as that shown in Fig.42, with sloping

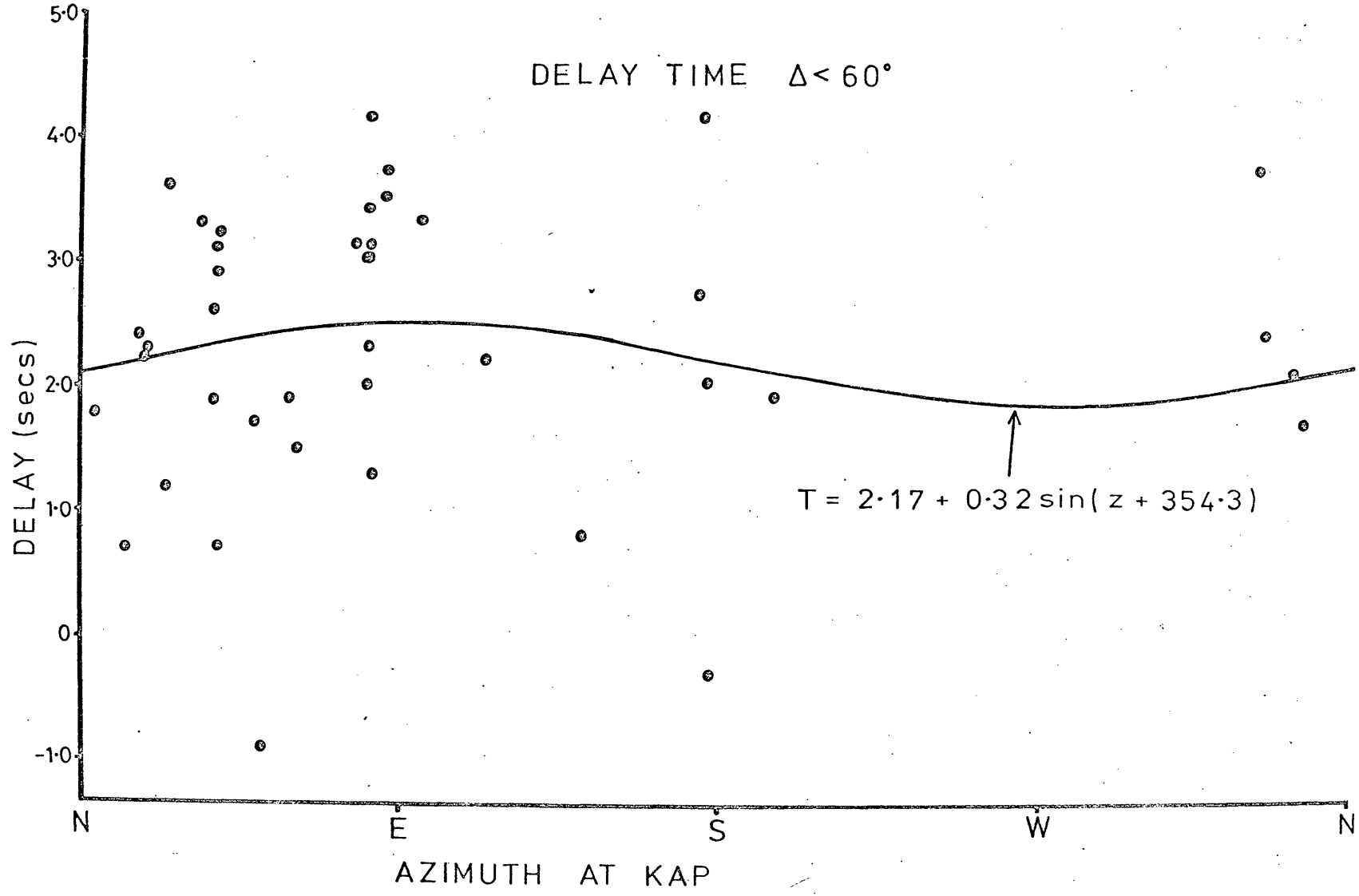

Fig.40. Observed delay time relative to Bulawayo as a function of azimuth at Kaptagat for events from distances less than 60°. Curve shows fitted sinusoid.

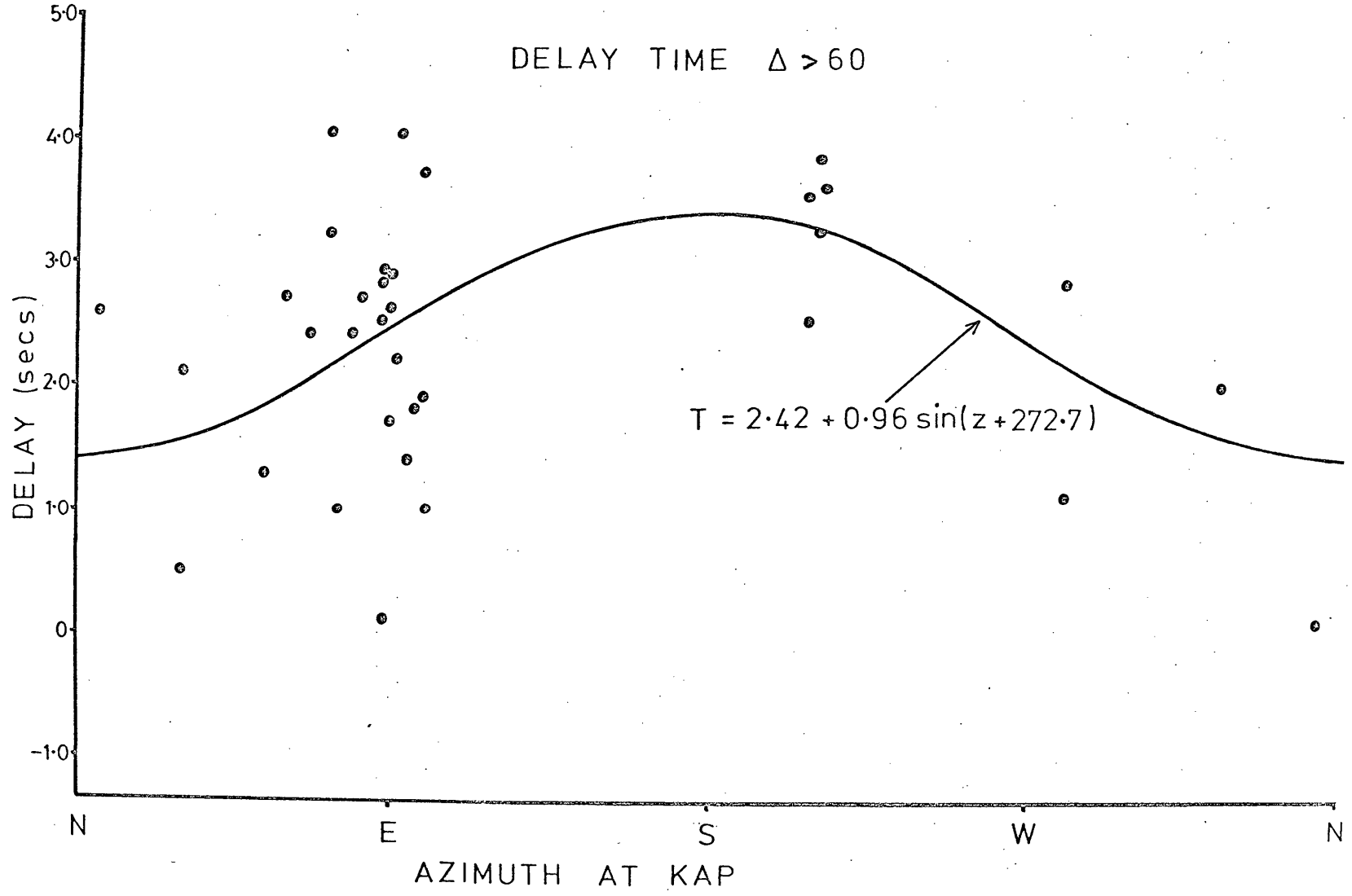

Fig.41. Observed delay time relative to Bulawayo as a function of azimuth at Kaptagat for events from distances greater than 60°. Curve shows fitted sinusoid.

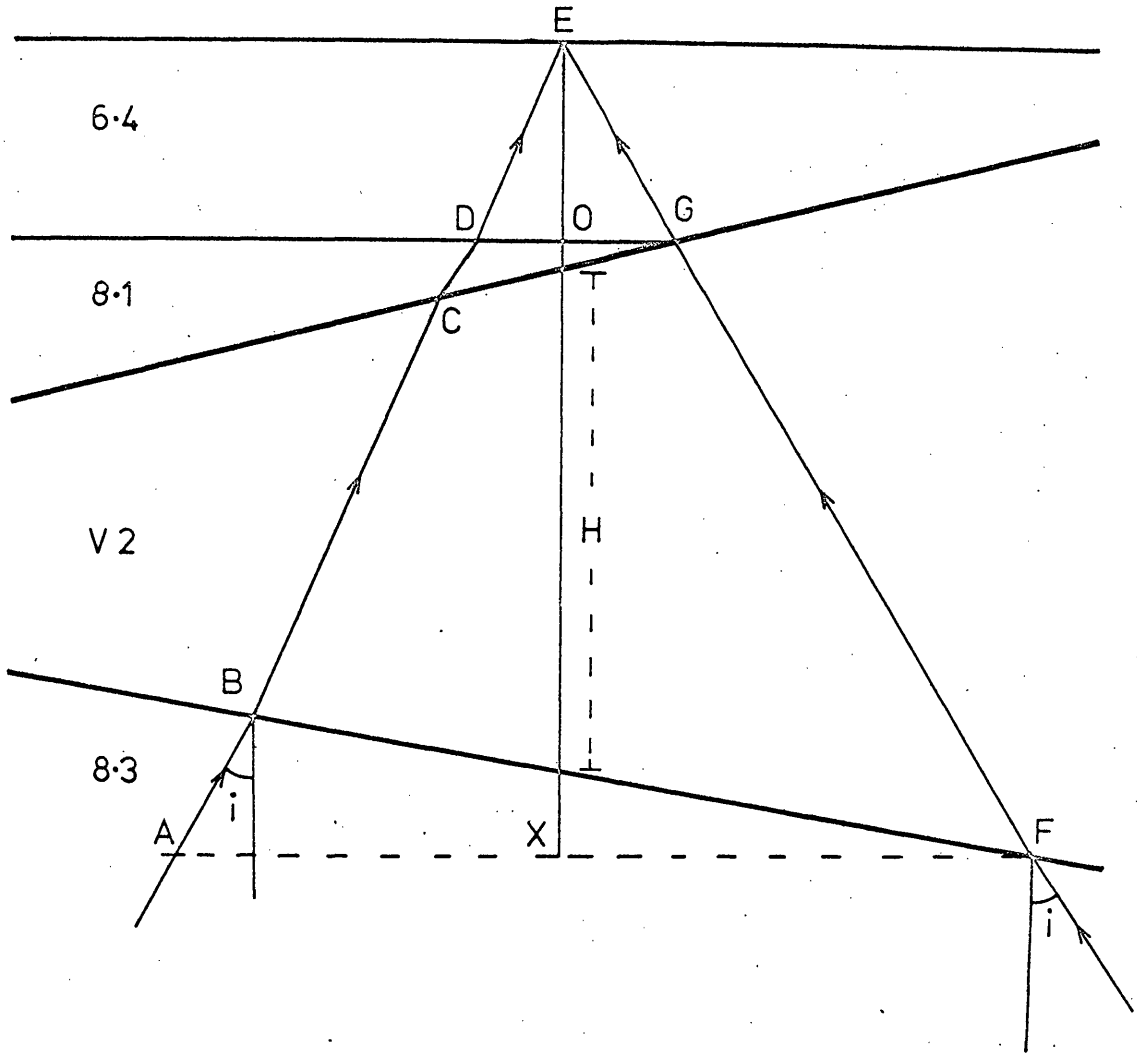

Fig.42. Crust and upper mantle model used to compute the azimuthal variation in delay time due to a low velocity (V2) wedge beneath the station at E.

boundaries to a low velocity zone, will produce relative delay times that are a cyclic function of azimuth which is not, in general, sinusoidal (Nuttli and Bolt, 1969). However, if it is assumed that the strike directions for both the upper and lower interfaces to the anomalous zone are the same, the difference in delay times relative to BUL for left-going and right-going rays perpendicular to the strike at Kaptagat (Fig.42) for events from the same distance can be determined. This will be approximately twice the amplitude of the cyclic delay time function.

Further simplifying assumptions are made with reference to Fig.42. It is assumed that the structure beneath BUL consists of parallel layers so that any azimuthal variation in delay time would be due to effects in the region of Kaptagat. The crust for Kaptagat is taken as having the same thickness as that for the AFRIC model, but with a mean velocity of 6.4 km/sec. The thickness of the high velocity lid to the anomaly is not known so it is taken as being almost negligibly thin for a left-going ray at G (Fig.42) and thickening westward. Thus a ray at G experiences refraction due to this layer but the travel time within it is disregarded. The thickness of the anomaly directly beneath Kaptagat, H, is calculated from the mean delay time from section 6.2., for a given velocity within the wedge.

The difference δT in delay time for a left-going and a right-going ray, both perpendicular to the strike direction for the wedge model, then follows from Fig.42.

$$\delta T = \frac{\overline{FG}}{V2} + \frac{\overline{EG}}{6.4} - \frac{\overline{AB}}{8.3} - \frac{\overline{BC}}{V2} - \frac{\overline{CD}}{8.1} - \frac{\overline{DE}}{6.4} + (\overline{AX} - \overline{XF}) \cdot \frac{dT}{d\Delta}$$

The two rays are taken as having the same angle of incidence i to the vertical in the 8.3 km/sec layer, and $dT/d\Delta$ is the slope of the travel time curve for the appropriate distance.

To estimate δT for the wedge models fitted to the slowness and azimuth anomalies, the values of V2, D1 and D2 are taken for Model 1 (Chapter 5). An approximate mean epicentral distance of 60° is assumed. From Fig.43 the quantity b is half δT, that is, roughly the amplitude of the delay time variation. Also plotted is the value of B from section 6.2. for all the data, with the hatched area giving the 95% confidence limits. The dashed horizontal line indicates the value of the azimuthal term for the direction 125° East of north, which corresponds to the direction of the maximum thickening of the wedge anomaly for Model 1.

If only the events for distance greater than 60° are considered, and the parameters adopted from Model 3 for slowness anomalies only, the computed values of b are as shown in Fig.44. The angle of incidence i required to compute b is taken for an epicentral distance of 80°. Here the dashed line is appropriate to a direction of 188° East of North from the optimum fit for the wedge direction Ψ .

For both interpretations, a larger assumed distance and hence a smaller angle of incidence to the vertical give smaller delay time variations, and vice versa.

6.5. Discussion

Equation 6(ii) gives the fit of the relative delay times

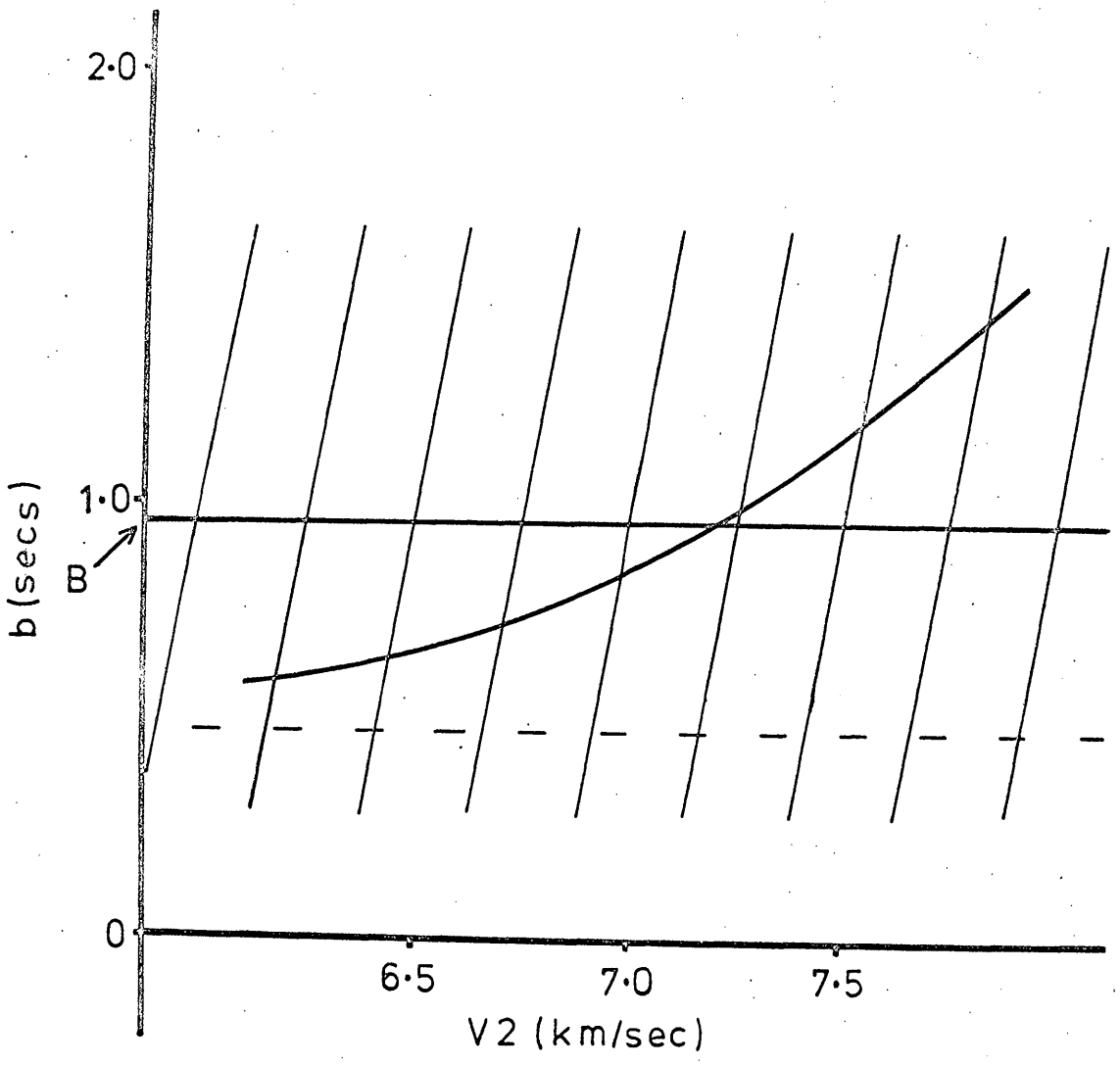

Fig.44. Variation in amplitude of azimuthal delay time term due to low velocity wedge model 3 with differing values of wedge velocity V2 (curved line). Hatched area gives 95% confidence limits on observed amplitude of azimuthal term (solid horizontal line) for events at distances greater than 60° from Kaptagat. Dotted line gives observed amplitude at angle Ψ for model 3.

for all events, in terms of constant and azimuthally varying terms. The value of the former, given by A = 2.36 seconds, implies that a substantial mantle anomaly is experienced by events from all azimuths. The value of A is derived for delays uncorrected for angle of emergence and is a little higher than if such a correction had been made. The factor $B_j \sin(Z_{jk} + U_j)$ is very small and for the data taken as a whole, the variation with azimuth is not significant.

However, for a wedge such as Model 1, for instance with a velocity of 7.5 km/sec for the anomalous mantle material, the difference in delays for rays travelling in opposite directions can be as great as 3.0 seconds for events a distance of 60° from Kaptagat. This occurs for rays perpendicular to the strike of the wedge and decreases for smaller values of V2. Assuming we can approximate a sinusoid to the delay time variation then the amplitude of the azimuthal term b computed for Model 1 is greater than the observed amplitude B even for a velocity V2 as low as 6.5 km/sec (Fig.43). The absence of a large B value implies that a wedge of very low velocity and moderately steep dips is required for the observed delay times to be compatible with the type of structure represented by Model 1.

In considering a low velocity zone with sloping boundaries, the effects of rays being deflected in a horizontal plane have been ignored. Because rays are deviated in this plane, they will tend to travel further than the distance between an epicentre and the station measured along a great circle. This will cause an additional delay relative to the standard station. If we assume

that the wedge exists for a distance of the order of 100 km in every direction from Kaptagat, and that the maximum azimuthal deflection suffered by rays from a distance of 60° is 25°, then the delay introduced can be as great as 0.6 seconds relative to Bulawayo. This factor will be zero perpendicular to the strike direction of the wedge, but elsewhere will always be positive.

This will give an additional cyclic variation of a different shape to that due to deflection of rays in the vertical plane. For wedge Model 1, however, the difference in relative delay times for rays travelling in opposite directions perpendicular to the strike direction should still be as great as shown in Fig.43 for any given value of V2.

From a comparison of Fig.40 and Fig.41 the constant terms are very similar but there is a significant azimuthal term only for the greater distances. Although the phase angle U for this group of events gives the direction of the maximum delay as 177° East of North (Fig.41+), whereas that derived from the slowness anomalies is 118° East of North, this difference is not critical in view of the large errors involved. It is again the case that the magnitude of the azimuthal variation in observed delay time requires very low velocities within the anomalous zone in order to be compatible with the wedge model for the slowness anomalies.

For the simple wedge model in Fig.42, rays from large distances will exhibit smaller azimuthal variations in delay time than those for rays from short distances, assuming that the same model applies to all events. This is the opposite of the observed trends, which would imply that the nearer rays arriving with large angles to the vertical miss some of the

anomaly and suffer less extreme deflections. This is broadly in agreement with the idea of velocity gradations rather than sharp contrasts arising from the interpretation of slowness anomalies, where more extreme wedge models were required to fit data for events from large epicentral distances. However, this is difficult to reconcile with the similarity of the constant delay time A terms for different distance ranges.

CHAPTER 7

INTERPRETATION OF SURFACE WAVE DISPERSION

7.1. Introduction

The preferred model from the analysis of teleseismic arrivals is that of shield-type topmost mantle thinning towards the rift axis to give way to material of anomalously low velocity. Sundaralingam (1971) has studied surface wave dispersion beneath East Africa and from Rayleigh wave phase and group velocity data he derived a model of the crust and upper mantle for the inter-station path Nairobi (NAI) to Addis Abbaba (AAE) (Table 11). The NAI-AAE path falls off the rift axis for much of its length. If the mantle low velocity zone attenuates to the east as has been suggested it does to the west, then it would be expected that surface wave sampling along this path might show evidence of this in the form of a high velocity lid over the anomalous mantle zone. To test whether this structural framework is compatible with the dispersion data of Sundaralingam, a new interpretation will be suggested.

7.2. The Data

Sundaralingam determined Rayleigh wave phase and group velocities for the NAI-AAE path from the earthquakes listed in Table 12. These were selected as having epicentres close to the great circle between the stations, and all are shallow focus events with clear, well dispersed wave trains. The Rayleigh wave phase velocities were determined by the Fourier Analysis Method used by Sato (1958) and Toksoz and Ben-Menahem (1963). The Multiple Filter Technique (Dziewonski et al, 1969) is used to calculate the group velocities.

TABLE 11

MODEL EA1 (Sundaralingam, 1971)

H(km)	α (km/sec)	β (km/sec)	ρ (gm/cc)
0.86	3.50	2.00	2.77
7.0	5.90	3.40	2.67
10.5	6.15	3.55	2.77
19.3	6.90	3.96	2.98
81.0	7.35	4.22	3.24
99.0	7.89	4.53	3.30
100.0	8.30	4.65	3.53
	8.70	4.85	3.70

Parameters underlined were taken as active.

TABLE 12

EARTHQUAKES USED FOR SURFACE WAVE INTERPRETATION

Location	Date	Origin Time Hr.Min.Secs.	Co-ordinates (degrees)
South Africa	5.1.1964	23 46 10.7	52.26S 28.3E
Prince Edward Isle	25.2.1964	00 34 32.0	44.60S 37.34E
South Africa	19.3.1966	14 51 49.4	52.70S 19.8 E
South Africa	19.3.1966	17 16 40.9	52.70S 19.9 E
S. Iran	20.4.1966	16 42 3.7	41.7 N 48.2 E

TABLE 13

TRIAL MODEL FOR PARTIAL DERIVATIVES

H(km)	α (km/sec)	β (km/sec)	ρ (gm/cc)
7.0	5.90	3.35	2.67
10.5	6.15	3.55	2.77
18.7	6.60	3.72	2.98
30.0	7.4	4.3	3.24
50.0	7.4	4.3	3.24
100.0	7.4	4.3	3.30
100.0	8.30	4.65	3.53
	8.70	4.85	3.70

The phase velocity measurements cover the period range 14 - 59 seconds and the group velocity values a slightly smaller range of 16 - 48 seconds (Fig.45). The effective depth of penetration of Rayleigh waves is about 0.45 of the wavelength, so the data provides information on the crust and upper mantle from 20 to 105 km. There are two important general features of the curves. At shorter periods the curves tend to merge with those for the AFRIC model (Gumper and Pomeroy, 1970) indicating some uniformity in the crust throughout Africa. However, at longer periods, those for the NAI-AAE dispersion show much lower velocities, presumably due to material of low shear velocity at depth.

The phase velocity curve is fairly smooth at short periods but for larger values the scatter is as much as 0.04 km/sec. The group velocity curve shows considerably worse scatter, up to 0.25 km/sec. It is, however, difficult to make a meaningful estimate of the accuracy of the data. After considering errors due to refraction, epicentral mislocation, misreading seismograms and uncertainty in instrumental response, Sunderalingam deduced that the overall error in the Rayleigh wave phase velocity measurements is of the order of 0.03 km/sec, although the error in group velocity would seem, from the observed dispersion curve (Fig.45), to be several times larger than this and may be as much as 0.1 - 0.15 km/sec.

The effects of lateral refraction can be important and they can introduce systematic errors and an increase in velocities. In this case, the interstation path is sampled from both directions and data points from different events show close agreement so it is unlikely that the curves are strongly affected by refraction or other effects outside this path.

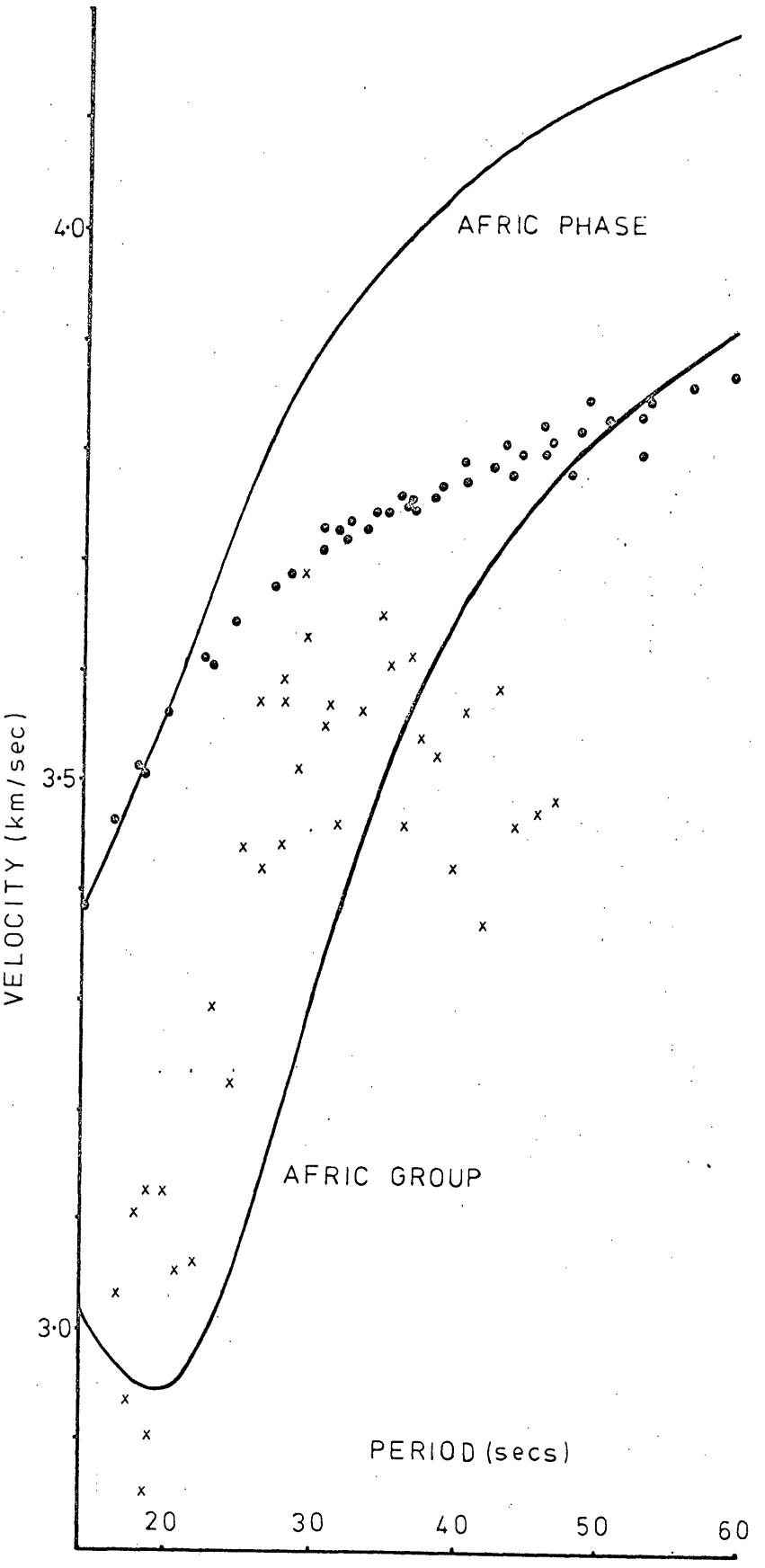

Fig.45. Observed Rayleigh wave phase (dots) and group velocities (crosses) for the AAE - NAI path (Sundaralingam, 1971) with computed dispersion curves for AFRIC model of Gumper and Pomeroy (1970).

7.3. Interpretation Techniques

The methods used to re-interpret the Surface wave data use as a criterion for fitting a theoretical model the root mean square deviation (RMSD) of the observed curves from those calculated for the model. A horizontally layered structure is derived using as parameters shear and compressional wave velocities, depth, and density. Certain selected parameters are varied so as to obtain a minimum value of the RMSD within the space defined by these variables. A non-linear optimisation technique is used in conjunction with the mapping of the RMSD within the parameter space.

(1) The Powell Conjugate Direction Method

A full mathematical treatment is given by Powell (1964, 1965) and Sundaralingam (1971). A description of the general principles only will be given here.

Assume we want to minimise some function $F(x)$. We can calculate it to be f_1 at some base point x_1, which corresponds to our initial model, and then to be f_2 at some point x_2 where $x_2 = x_1 + S$. S is the step-size which is specified to control the accuracy and swiftness of the search. $F(x)$ can then be evaluated at a third point x_3, such that:

$$x_3 = x_1 + 2S \quad \text{if} \quad f_1 \geqslant f_2$$

$$x_3 = x_1 - S \quad \text{if} \quad f_1 < f_2$$

It can be shown that the optimum x_m of a quadratic passing through the three points is given by:

$$x_m = \frac{1}{2} \cdot \frac{(x_2^2 - x_3^2)\, f_1 + (x_2^2 - x_1^2)\, f_2 + (x_1^2 - x_2^2)\, f3}{(x_2 - x_3)\, f_1 + (x_3 - x_1)\, f_2 + (x_1 - x_2)\, f_3}$$

If x_m and which ever of x_1, x_2 or x_3 gives the smallest value of F(x) differ by less than the required accuracy, which is also specified, then the minimum is found. If this is not the case, then one of x_1, x_2, x_3 is discarded, this being the one corresponding to the largest value of F(x). Then the quadratic interpolation continues using the remaining two function values and that for x_m.

The function to be minimused F(x) is given by:

$$F(x) = n_o (RMSD)^2$$

where n is the number of active parameters, that is, those that are varied in order to find the minimum. These parameters can be constrained within specified limits, and the current value of the parameter is X, where

$$X = X_1 + (X_u - X_1) \sin^2 Y.$$

X_1 and X_u are the lower and upper bounds of the variable respectively, and Y is the initial value.

This non linear method of optimisation has several advantages. Convergence is rapid especially near the optimum, where the function is well approximated by a quadratic. All parameters used in the model can be designated active or passive, and the former, as variables, can be constrained within reasonable limits, such as those defined by geological plausability. This is useful as it can be used to avoid unreasonable variations in the active parameters.

(2) Mapping

The fit of models to the dispersion data is also inves-

tigated by calculating the RMSD for different values of the active parameters and then taking a succession of two-dimensional sections of this parameter space. This can be used to give an approximate position for the required minimum which will serve as a starting point for the Powell optimisation. This shortens the computing time needed. After the optimised values of the variables have been determined, the variation of the RMSD within the vicinity of the minimum can be mapped. This shows the shape of the minimum, which can be highly variable, and the uncertainty with which we can define the final parameter values.

The PV7 computer program of J. Dorman is used to calculate the group and phase velocities for a given model. This is coupled with statistical and optimising routines for both the Powell and mapping processes, given by Sundaralingam (1971). The PV7 program also corrects for the effects of Earth curvature. The approximation of Bolt and Dorman (1961) is used for Rayleigh wave phase velocities and that of Knopoff and Schwab (1968) for group velocities.

7.4. Limits on Interpretation

Backus and Gilbert (1968) have shown that there is a fundamental limit to the detail of earth structure that can be derived from gross earth data, and this reasoning has been applied to surface wave inversion. Der, Masse and Landisman (1970) have shown that the resolution of the data can be expressed as a minimum thickness of a zone over which velocity may be determined to a given accuracy. Thus thicknesses within a model can be chosen so as to determine shear velocities within satisfactory limits. If we choose layer thicknesses to be too small, then we lose accuracy in the determination of the shear velocity over that thickness.

Also, resolution decreases with increasing depth. The interfaces between layers are not structural boundaries but define limits over which a mean velocity value is derived.

Knopoff (1969) has obtained the following expressions for the interstation phase and group velocities as a function of distance:

$$\frac{1}{c} = \frac{\int_{x_1}^{x_2} \frac{dx}{c(x)}}{\int_{x_1}^{x_2} dx} \qquad \frac{1}{u} = \frac{\int_{x_1}^{x_2} \frac{dx}{u(x)}}{\int_{x_1}^{x_2} dx}$$

c and u are the interstation phase and group velocities, respectively, which constitute the dispersion data.
c(x) and u(x) are the phase and group velocities at distance x along the interstation path, the limits of which are x_1 and x_2. It follows that the reciprocals of the measured velocities, the phase and group slownesses, are the distance averages of these quantities between the stations. Therefore any model we derive from the data represents a mean structure beneath the interstation path.

In their study of surface wave propagation beneath the Canadian shield, Brune and Dorman (1963) drew some general conclusions concerning inversion of the dispersion data. They found that it is critical to select the proper framework for a model in terms of the number and thicknesses of layers and to designate parameters active or passive. This should be done by considering the amount of information contained in the data, by examining partial derivatives and by deriving trial models under constraints. Allowing

too much or too little freedom results in either unreasonable final values for parameters or a non-converging system.

In particular they found that if density and shear velocity were varied within the same depth range then large and unreasonable variations in these quantities could occur without significant improvement in the fit. If the number of layers in any depth range was too great, shear velocity and depth could vary erratically with adjacent layers also developing wildly high or low velocities. Also, where the shear velocity contrast across an interface is small, the depth to that boundary cannot be accurately determined.

If we only vary shear velocity then we can recover a final value to some particular accuracy. If we also vary depths, then we may not be able to obtain such a high degree of precision in velocity. From Der et al (1970) this loss corresponds to a proportional change in layer thicknesses. It is often useful, therefore, to fix the total depth range of a model and vary the individual thicknesses within this framework.

7.5. Previous Work

Sundaralingam (1971) derived a trial model to use in the calculation of partial derivatives (Table 13). The framework of the model is very similar to that of the AFRIC model for the African continent (Gumper and Pomeroy, 1970), but with lower velocities in what correspond to the top two upper mantle layers for AFRIC.

The partial derivatives for phase (c) and group velocity (u) with respect to shear velocity are shown in Fig.46 and Fig.47 respectively. From these curves a check on the layering can be made.

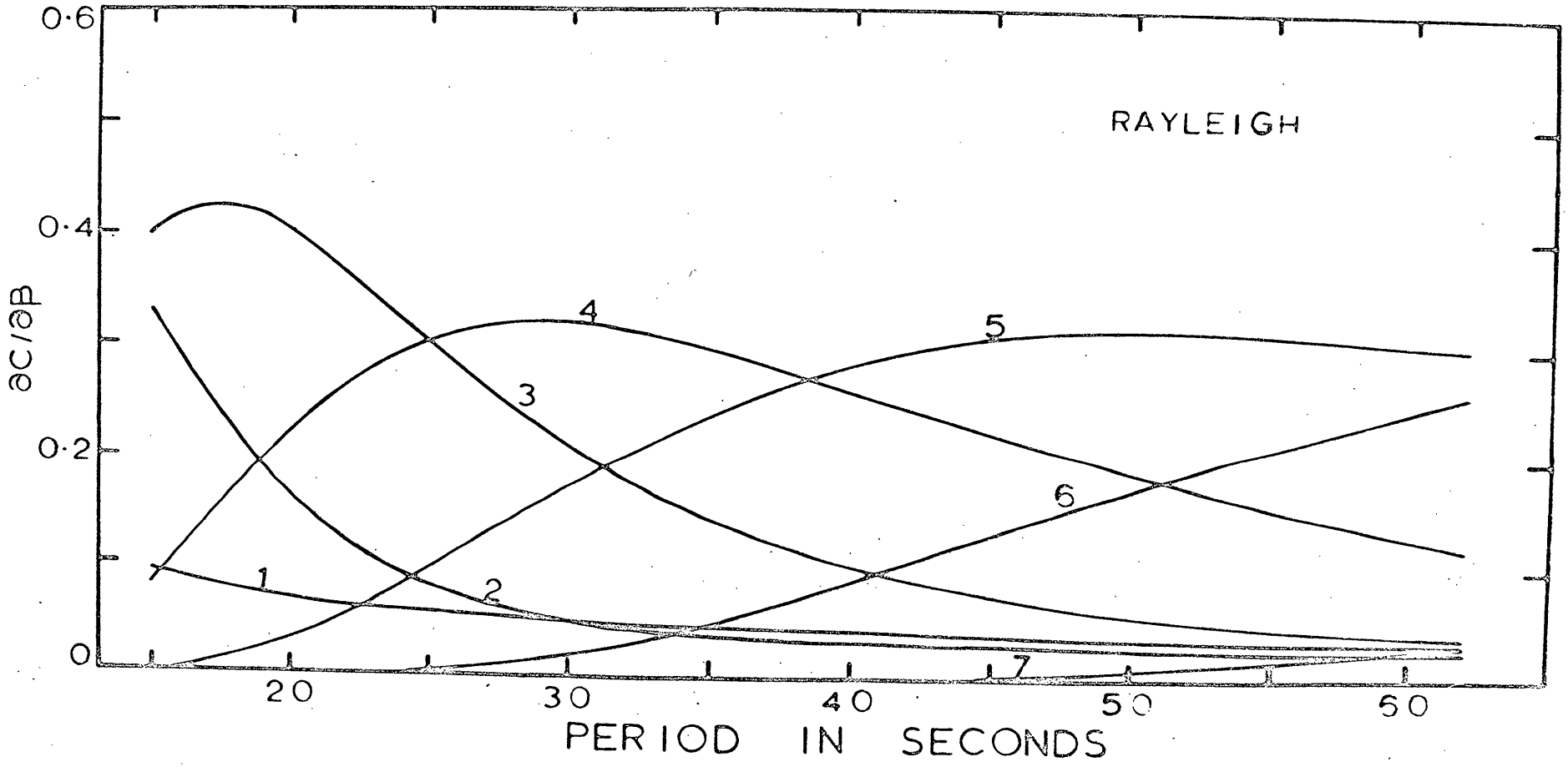

Fig.46. Partial derivatives of phase velocity with respect to shear velocity for different layers of a trial model (Table 13).

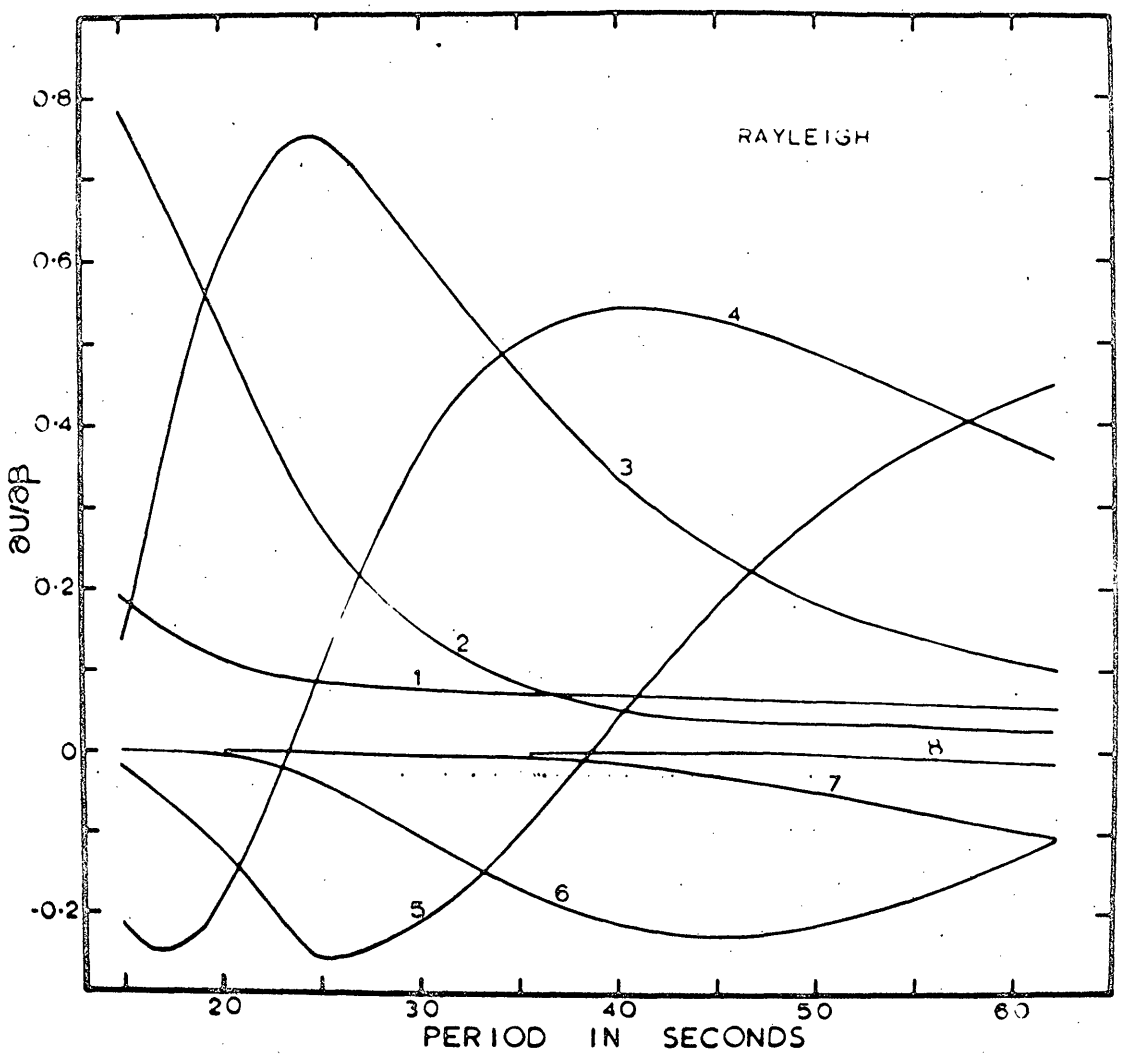

Fig.47. Partial derivatives of group velocity with respect to shear velocity for different layers of a trial model (Table 13).

If the number of layers is too great, then it should be possible to combine two of the curves to approximate a third (Brune and Dorman, 1963). However, this does not seem to be the case for the trial model used here and the layering is roughly correct. From the partial derivative curves, we can also deduce that the shear velocities most affecting the dispersion curves are those for layers 3 - 5. These can be combined to give a single upper mantle layer (Table 11), under the lower crustal layer.

Partial derivatives with respect to the other parameters, although not shown here, reveal that the phase and group velocity data are not sensitive either to density, ρ, or to compressional wave velocity, α, and in deriving the EA1 model only shear velocities and depths were varied. A shallow sedimentary layer was introduced and the shear velocities of the bottom two crustal layers and the top two mantle layers allowed to change. Depths were generally not well determined by these data but the thickness of the lower crustal layer was also taken as an active parameter.

From Tables 11 and 1 we can compare the EA1 and AFRIC models as their frameworks are very similar. If AFRIC is taken to represent the crust and upper mantle for the African continent outside the rift zones, then the path Addis Abbaba (AAE) - Nairobi (NAI) is characterised by anomalously low velocity material in the upper mantle. The crustal structures are similar with the exception of the lower crustal layer which, although being of roughly the same thickness as that for AFRIC, has a higher shear velocity.

7.6. The Lid Model

If we take the structure suggested by Griffiths et al (1971) as typical of that below the rift axis, with a crust only 20 km

thick, then this is much different from that thought to lie beneath Nairobi to the east of the rift. Bonjer, Fuchs and Wohlenberg (1970) deduced that a two-layer crustal model required a thickness of 43 km below Nairobi. This suggests that the surface of the upper mantle anomaly does sink eastwward away from the rift although not necessarily at the same rate as to the west. The interstation path AAE - NAI in general lies off the axis of the rift so it is possible that the path as a whole is compatible with a lid of normal AFRIC-type upper mantle overlying the anomalous zone.

For the path NAI - AAE, a framework similar to that for the AFRIC model will be assumed. Three types of lid model will be used. Models UM1 and LC1 have a lid of normal mantle immediately below and above the AFRIC Moho level respectively, while model CM1 incorporates both these features.

The Powell Conjugate Direction Method requires the separation of the model parameters into the categories active or passive, the former being used as variables in the optimisation. The depth of penetration of Rayleigh waves is about 0.45λ where λ is the wavelength, which gives a depth range of 20 - 105 km. This implies that the dispersion curves are sensitive to parameters for the lower crustal layer and the topmost upper mantle layer. This can also be seen from the partial derivatives where these two layers correspond to layers 3, 4 and 5 for the trial models (Table 13). In practice, three parameters were varied for the lid models; the thickness of the lid and the shear velocities for one layer on either side, these being approximately comparable to layers 4 and 5 for the EA1 model. Because these data do not determine depths well, the total depth of each model was fixed and only the individual thicknesses within this framework were varied. The compressional wave

velocity for the lid was fixed at 8.1 km/sec from the Kaptagat array measurements.

The parameters for layers outside the range of the data were generally fixed at the AFRIC values. Thus the second upper mantle layer - layer 6 in the EA1 model - was assigned a shear velocity fixed at 4.78 km/sec. The data are insensitive to changes in densities and compressional wave velocities. Therefore densities were taken at the AFRIC values except where these appeared to be inappropriate to East Africa, when they were deduced from the gravity interpretation of Searle (1970). For the two layers in which shear velocity β was varied, the P-wave velocity, α, was calculated using the relation $\alpha = 1.74\beta$ (Anderson, 1965). This was also applied to the lid, giving a shear velocity of 4.66 km/sec for a P-wave velocity of 8.1 km/sec.

Because the errors on the group velocity measurements are greater than those for phase velocity, a weighting procedure was used. The RMSD's were calculated for the two curves and then combined with a weighting inversely proportional to their approximate RMSD's for the EA1 model. This meant that phase velocity had unit weighting but was favoured more than if the RMSD's had merely been summed.

7.7, Models from Powell Conjugate Direction Method

The final model for UM1 is shown in full in Table 14, with layers 4 - 7 for LC1 and CM1 also shown. The parameters underlined were varied. UM1 has a lid below the Moho with thickness H(5) and the thickness of the topmost mantle layer is H(6) = 80.0 - H(5). Similarly, for LC1, H(4) was constrained to be 18.7 - H(5). These two lid features were combined for CM1

TABLE 14

MODEL UM1

Layer	H(km)	α (km/sec)	β (km/sec)	ρ (gm/cc)
1	0.86	3.5	2.0	2.77
2	7.0	5.9	3.35	2.67
3	10.5	6.15	3.55	2.77
4	18.7	6.81	3.91	2.85
5	16.0	8.1	4.66	3.3
6	64.0	6.96	4.00	3.22
7	100.0	8.2	4.78	3.44
8	100.0	8.3	4.65	3.53

Weighted RMSD = 0.028 km/sec (RMSD phase = 0.015 km/sec)

MODEL LC1

4	8.5	6.27	3.60	2.85
5	10.2	8.1	4.66	3.3
6	80.0	6.15	4.11	3.22
7	100.0	8.2	4.78	3.44

Weighted RMSD = 0.033 km/sec (RMSD phase = 0.019 km/sec)

MODEL CM1

4	12.4	6.47	3.72	2.85
5	15.5	8.1	4.66	3.3
6	70.8	7.06	4.06	3.22
7	100.0	8.2	4.78	3.44

Weighted RMSD = 0.030 km/sec (RMSD phase only = 0.017 km/sec)

Parameters underlined were taken as active.

so that:

$H(4) = 18.7 - H_1(5)$ and $H(6) = 80.0 - H_2(5)$, where $H(5) = H_1(5) + H_2(5)$. The individual thicknesses here were both varied and had final values of 6.3 km and 9.2 km.

In all three of the models, the lid is thin, about 16 km for UM1 and CM1 and only 8.6 km for LC1. The effect of introducing the lid is to depress the shear velocities in the layer beneath, where the shear and compressional wave values are in the ranges 4.00 - 4.11 km/sec and 6.96 - 7.15 km/sec respectively. These compare with the EA1 velocities for the topmost mantle layer of 4.22 km/sec and 7.35 km/sec. One would anticipate too that if the lid is omitted, it would have the effect of raising the shear velocity of the lower crustal layer also. In models LC1 and CM1, in fact, the values are lower than for EA1 and correspond more closely to the shear velocity of 3.72 km/sec for this layer in the AFRIC model. However, these shear velocities, and the compressional wave velocities calculated from $\alpha = 1.74\beta$, are lower than those suggested for an intermediate layer in the crust from seismic refraction work in the Transvaal (Willmore et al, 1952; Hales and Sachs, 1959). Model UM1 shows P- and S-wave velocities of 6.81 km/sec and 3.91 km/sec for this layer, more in agreement with the refraction work but higher than those for AFRIC.

For EA1 the combined RMSD for phase and group velocity data was 0.039 km/sec (RMSD for phase only was 0.020 km/sec), using the same weighting for the individual RMSD's (7 : 1) as for the lid models. For the latter both individual RMSD's for the phase and group velocity are lower (Table 14) and this can be seen qualitatively from Fig.48, showing the computed dispersion curves for the three lid models and for EA1.

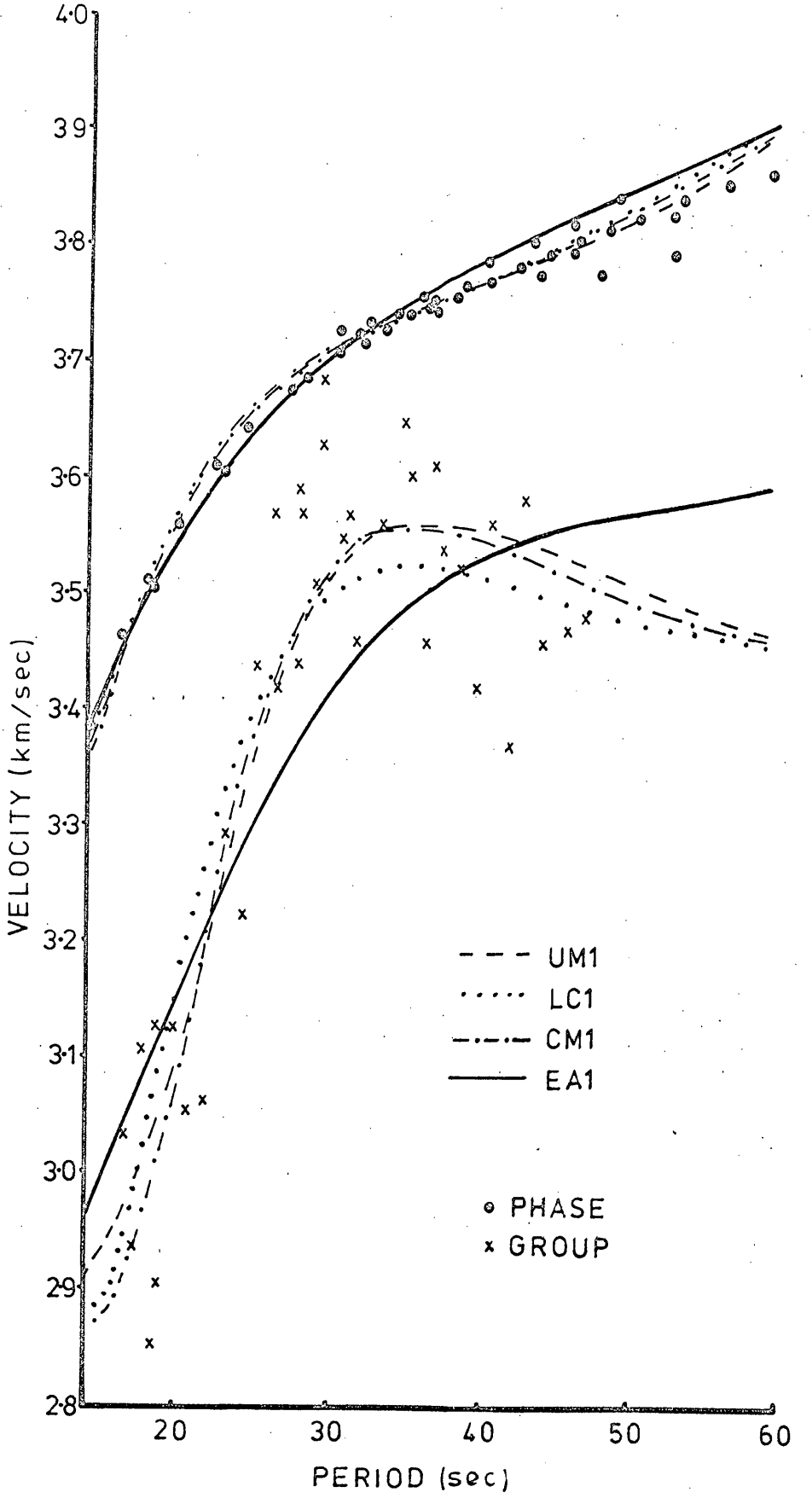

Fig.48. Observed phase (dots) and group velocities (crosses) for the AAE - NAI path with the computed dispersion curves for the EA1 model (Sundaralingam, 1971) and the three lid models.

For phase velocity, the lid models suggest a steeper gradient at short periods, which is marginally a poorer fit than that for EA1 but at longer periods the effect of the lower shear wave velocities in the upper mantle layer for the lid models gives a shape closer to that of the observed points. For periods greater than about 50 seconds, the computed curves tend to reach higher values than those for the observed points.

However, the chief differences in the dispersion produced by a lid model and that for EA1 can be seen in the group velocity curve. The velocities for short periods rise much more steeply than for EA1 and fit the observed data more closely. The main feature of the curve is the negative slope at long periods for a lid. This would seem to be characteristic of a high velocity channel, and has also been observed for phase velocity curves under these conditions (Knopoff, Schlue, and Schwab, 1970; Berry and Knopoff, 1967). There is some confirmation of this sign change in the observed curve, although the points are relatively few and quite well scattered. In general, the shape of the observed group velocity curves is more compatible with those computed for the lid models than for EA1.

7.8. Mapping and the Problem of Non-Uniqueness

To estimate the reliability of the inversion results for the lid models we can map the RMSD over ranges of the active parameters. These maps are presented for the model UM1, although the two other models show essentially similar features. They are given as a series of two-dimensional plots for the three variables, and the contours shown correspond to one and two RMSD's from the minimum value for the model, all using the combined, weighted RMSD for phase and group velocity.

A characteristic of all three RMSD maps, Figs. 49, 50 and 51, is that the contours are inclined to the axes and elongated. More specifically, from Fig.49, the change in RMSD for unit change in the shear velocity for layer 4 is only two-thirds of the RMSD change for a similar change in the shear velocity for layer 6. If the changes in RMSD were equal, then the contours would be circular.

The inclination and elongation of the contours seem to characterise important contributions towards non-uniqueness. If the contours were small circles, then each of the two quantities can be specified within fairly narrow limits and one quantity cannot, for instance, be increased away from the minimum and the rise in RMSD diminished, even in part, by a change in the other quantity. If the contours are elliptical and roughly parallel to one of the axes then the quantity along the major axis is badly determined by the data but a change in this cannot be significantly compensated by a change in the variable along the minor axis of the ellipse. However, in the present study, the contours are inclined and elongated. Thus, from Fig.49, an increase in $\beta(4)$ away from the minimum produces a rise in RMSD that can be partly reduced by decreasing the value of $\beta(6)$. The inclination, then, is a representation of the auto-correlation function of the two layers 4 and 6. The considerable elongation of contours in Figs. 50 and 51 also suggests that depths are not well determined by the data.

From the maps we can see that UM1 - this also applies to LC1 and CM1 - is highly non-unique. There appears to be interference between layers 4, 5 and 6 and in this situation the assigning of confidence limits to the variables becomes difficult. If we neglect the problem of interference we can calculate errors by, for instance,

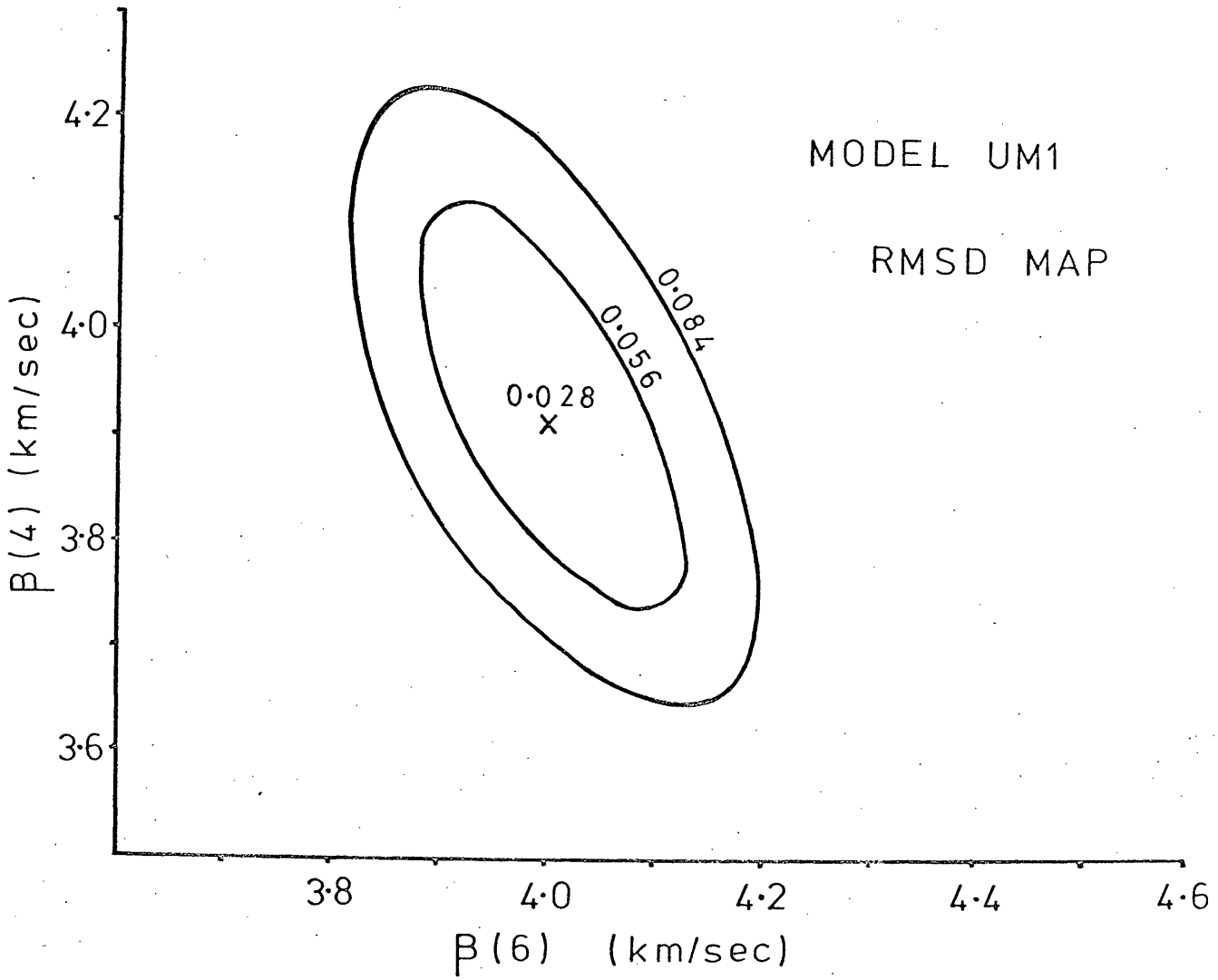

Fig.49. Contoured weighted RMSD (in km/sec) for model UM1 for varying shear velocities in layers 4 and 6.

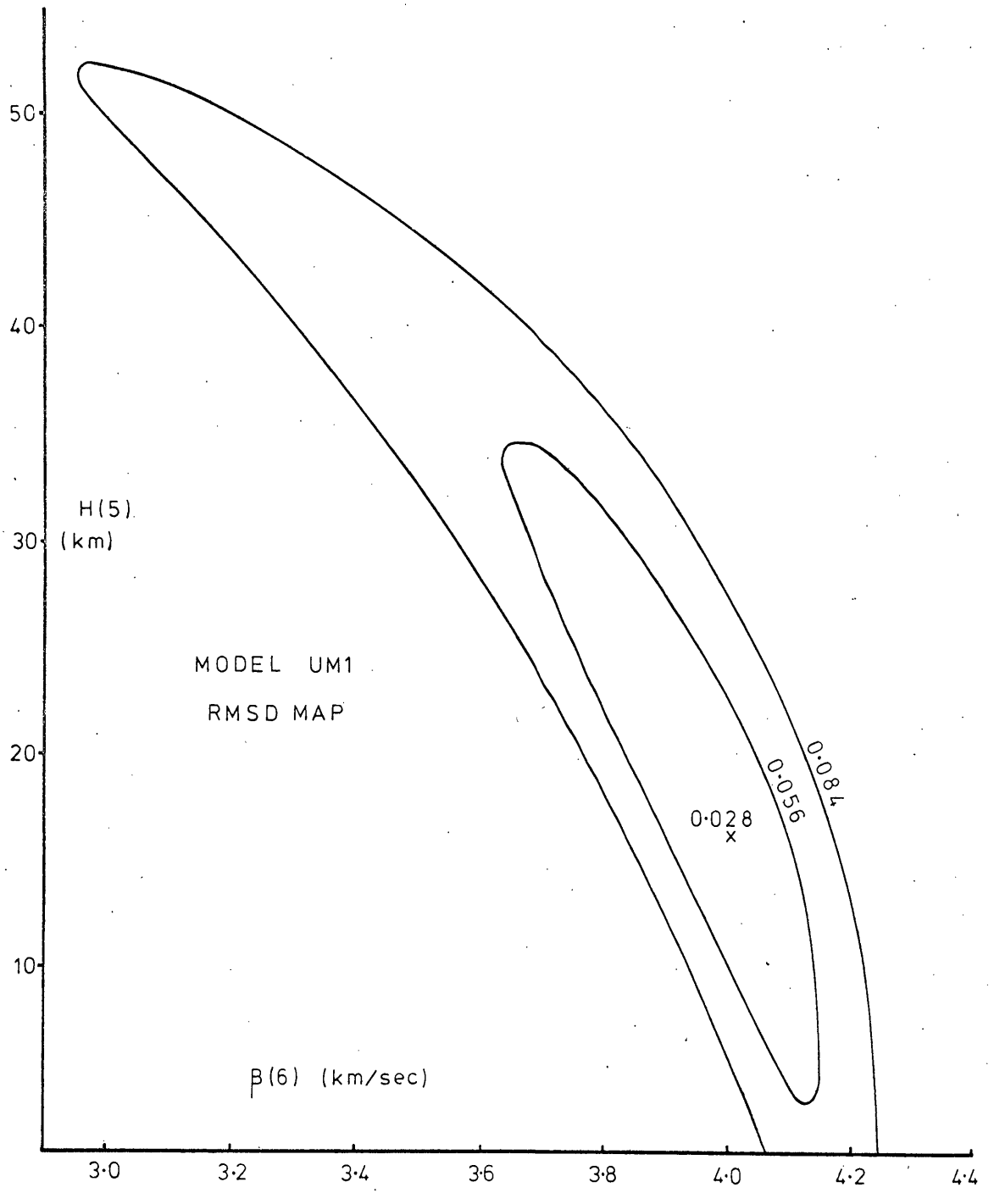

Fig.51. Contoured weighted RMSD (in km/sec) for model UM1 for varying thickness of layer 5 and shear velocity in layer 6.

finding what significance a shift dv of the dispersion curves has on each parameter separately, where dv defines some acceptable range (Berry and Knopoff, 1967). Similarly, if the contours were perfect circles, we could consider each active parameter in turn and find its extreme values for, say, one RMSD from the minimum for the model. This is not a satisfactory procedure in the present case, with interference between the layers, and we cannot treat one active parameter in isolation from the others.

In this situation, it may be more constructive to give ranges of possible models. To this end, the RMSD mapping technique is used to compile Fig.52, which represents extreme values of the variables, but with all solutions falling within one RMSD of the minimum. We could have taken as a criterion of acceptance two RMSD's from the minimum, in which case more extreme models would be possible. In particular, these would have included the possibility of having no high velocity lid with a shear velocity for the anomalous mantle layer of 4.1 - 4.3 km/sec. Also, for model LC1, this possibility exists even for an RMSD of less than 0.056 km/sec for large values of $\beta(4)$. This is in some ways a less flexible framework than that for UM1, as the lid thickness is effectively constrained to 18.7 km.

From Fig.52, $\beta(4)$ can be as low as 3.75 km/sec which is very similar to the value for the AFRIC model and is also seen for LC1 and CM1. Also there is the possibility of having ultra-low-velocities in the anomalous mantle zone, if the lid is thick. Such a small shear velocity with a similar thickness has been proposed to explain surface wave dispersion results from the East Pacific Rise (Knopoff, Schlue and Schwab, 1970), although with a thicker lid.

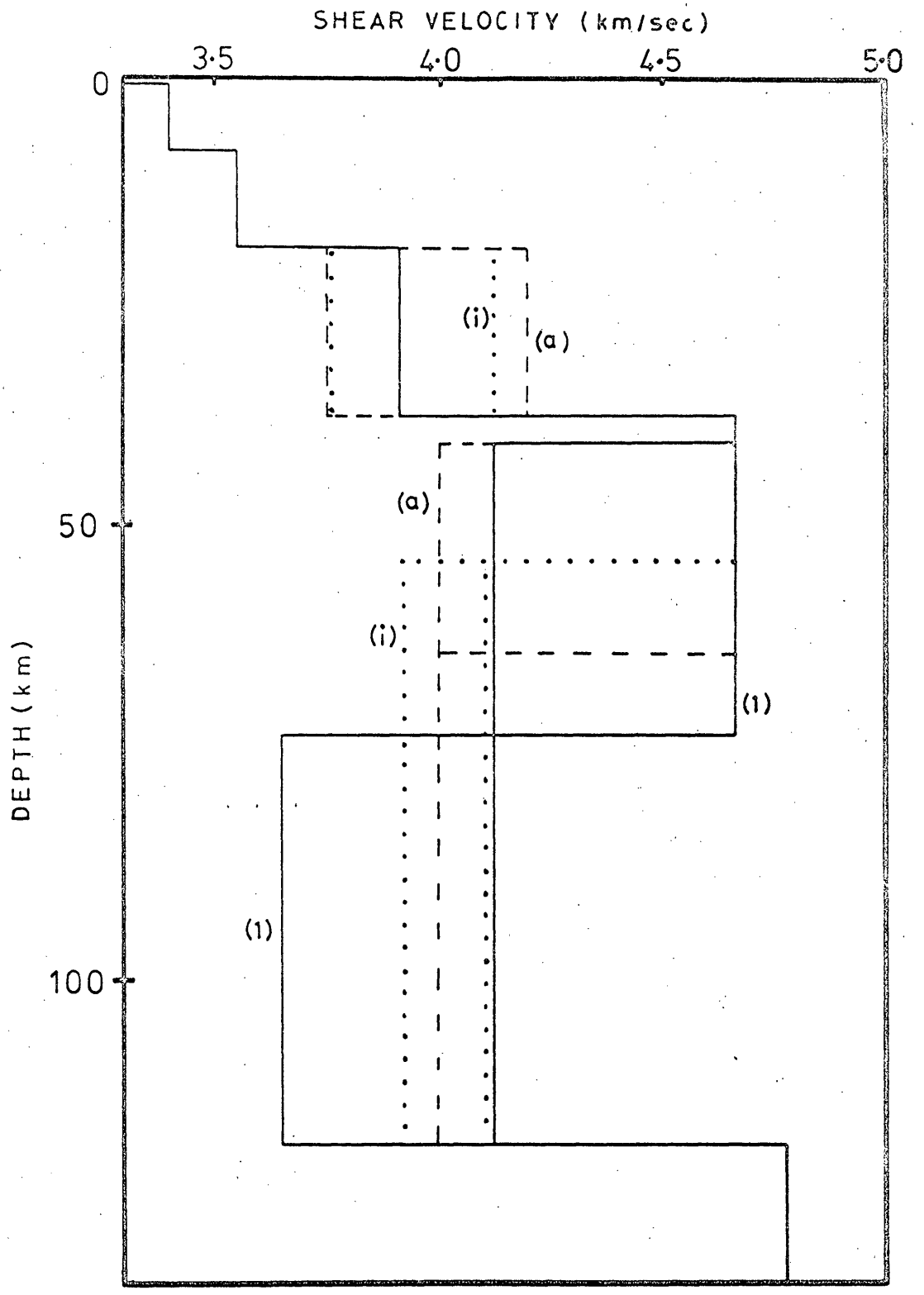

Fig.52. Extreme models for UM1 all within one RMSD of the minimum, compiled from Figs. 49 - 51. Lines of same type indicate the extremities allowed by varying any two $\beta(4)$, $\beta(6)$ or H(5). Numbering indicates the continuity of one extreme model of each of such pairs.

All the solutions from Fig.52 involve a zone in the mantle with a shear velocity much lower than that for the equivalent depth range for the AFRIC model.

We can use the RMSD mapping technique to check the effect of introducing a second anomalous upper mantle layer, that is, varying the shear velocity for the layer 7 in the lid models. If we take the UM1 model and introduce $\beta(7)$ as a fourth variable, the best fit is for a model UM2 with a lid 12 km thick under a crust of shear velocity 3.91 km/sec (P-wave velocity 6.83 km/sec) and overlying the two anomalous mantle layers 6 and 7 with shear velocities 4.08 km/sec and 4.59 km/sec (P-wave velocities 7.10 km/sec and 7.99 km/sec) respectively. The only marked change in the active parameters is that for $\beta(7)$ which is lower than the constrained value of 4.78 km/sec in UM1. The dispersion curves (Fig.53) show slight deviation from those for the three-parameter lid models, with a small depression in phase velocity at long periods but an increase in group velocity for the same region.

We can check the relevance of treating $\beta(7)$ as a variable by examining the RMSD contours for $\beta(6)$ against $\beta(7)$. From Fig.54, the RMSD for a value of 4.59 km/sec is not significantly different from that for $\beta(7)$ = 4.78 km/sec. The contours are open-ended even for one RMSD from the minimum indicating that $\beta(7)$ could take on a large range of acceptable values. Thus it cannot be accurately determined from the present data.

7.9. Delay Times

Sundaralingam (1971) has measured P-wave delay times for Addis Abbaba and Nairobi relative to Bulawayo using the method outlined in Chapter 4, and obtained mean values of 2.7 and 2.3

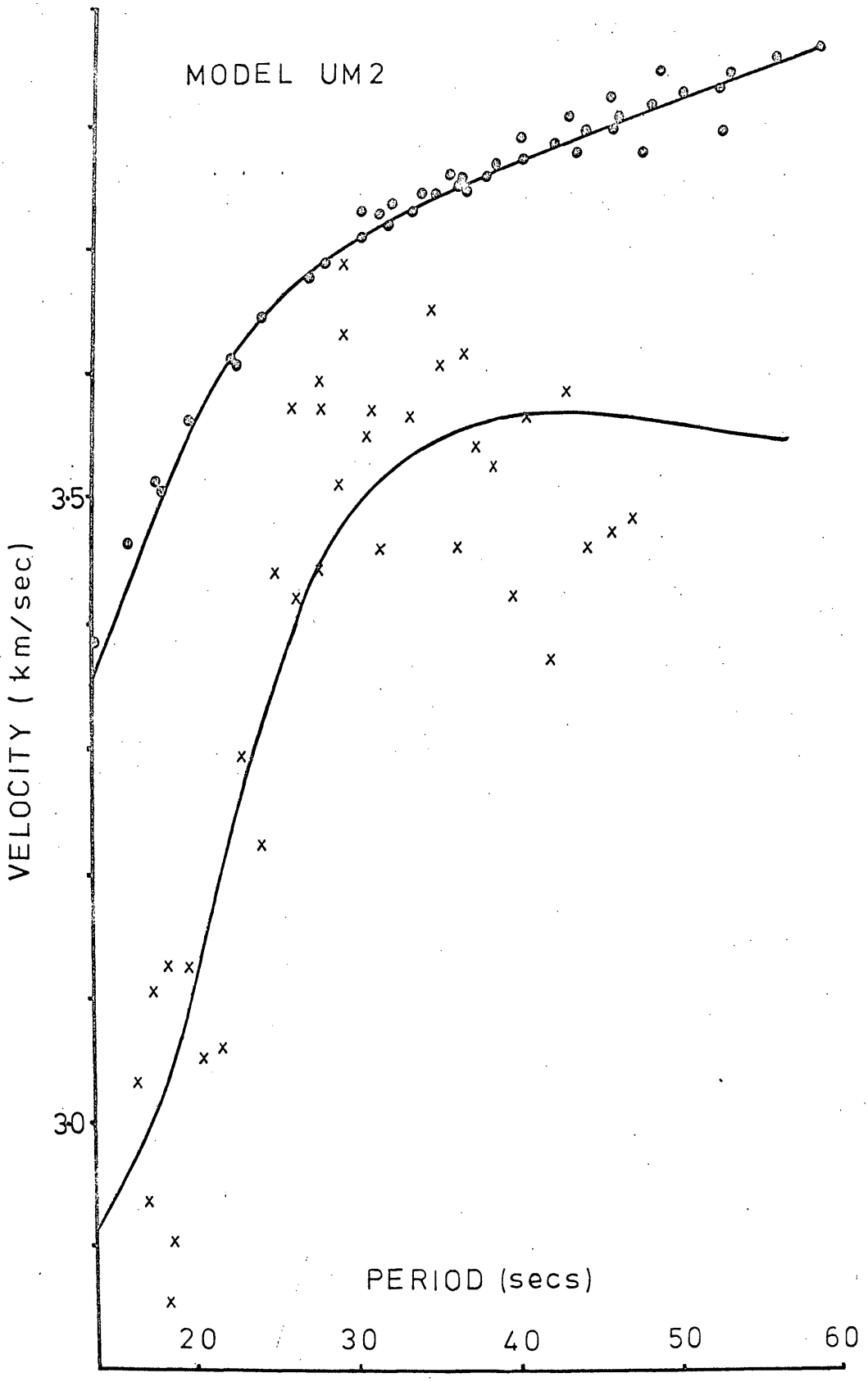

Fig.53. Observed Rayleigh wave phase (dots) and group velocities (crosses) for the AAE - NAI path. Solid curves are those computed for model UM2 with the shear velocity of layer 7 varied.

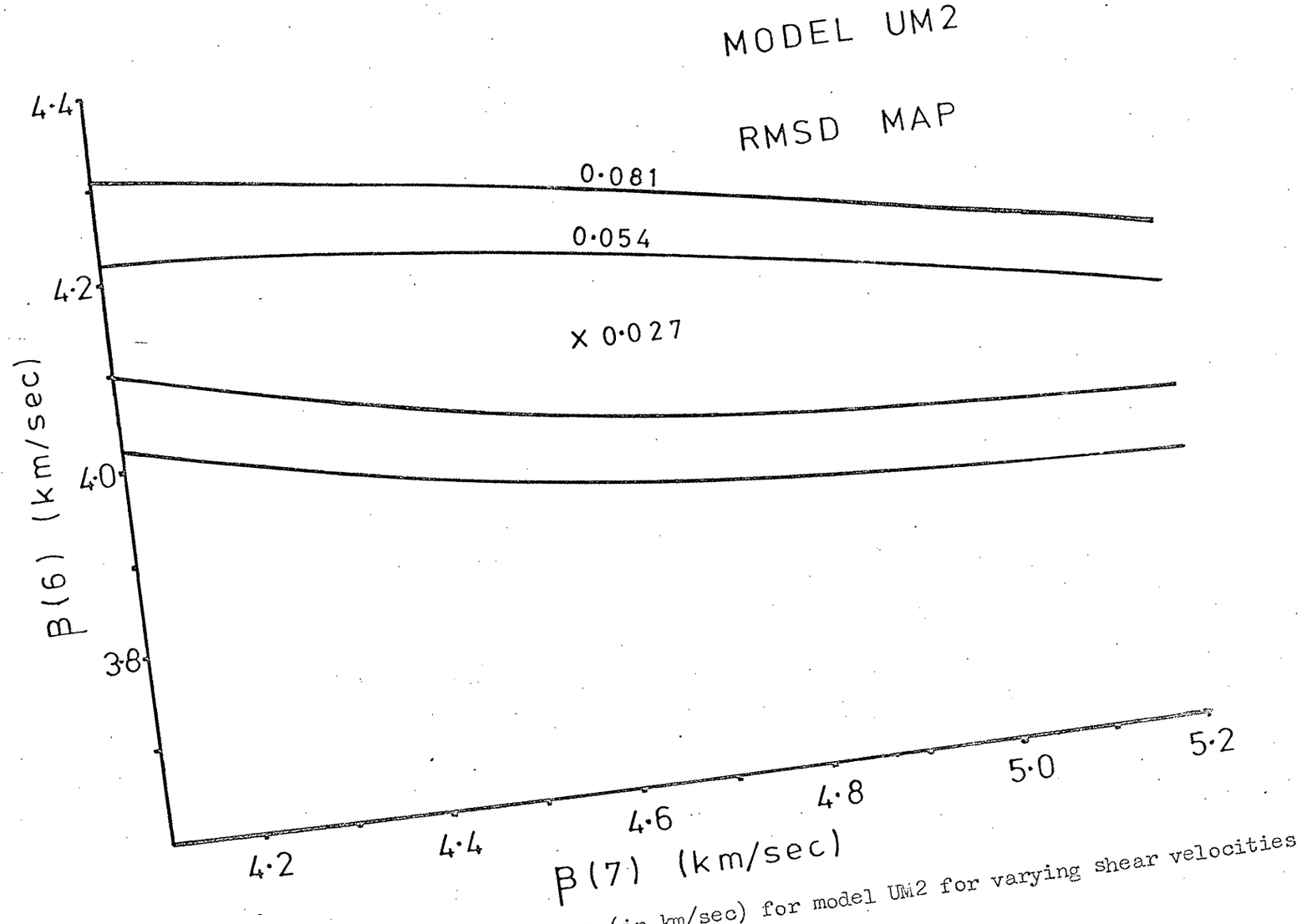

Fig.54. Contoured weighted RMSD (in km/sec) for model UM2 for varying shear velocities in layers 6 and 7.

seconds for the two stations (Table 9).

If we assume Bulawayo is on a structure similar to that given by the AFRIC model we can calculate the delay for the Rayleigh wave models for AAE-NAI relative to BUL. This gives positive delays for the models UM1, LC1 and CM1 of 1.39, 1.28 and 1.33 seconds respectively. These are lower than the 1.53 seconds associated with model EA1, with two low velocity layers in the upper mantle. However, they are also more than 1 second smaller than the mean of the observed delays at AAE and NAI. There are a number of possible explanations for this.

(1) Some of the anomaly may be outside the range of the data. As the lid models only incorporate one low velocity mantle layer with respect to the AFRIC model, this gives a maximum of 80 km for the anomaly thickness but it is quite possible that anomalous material extends well below this. If, for instance, the zone was 100km thicker this would involve layer 7 in the lid models having a P-wave velocity of about 7.4 km/sec and a shear wave velocity of 4.25 km/sec. This would be lower than as derived for the corresponding layer 6, for EA1, and also for the lid model UM2 with $\beta(7)$ variable, but as the phase and group velocities are not sensitive to shear velocity variations at such depths, we cannot accurately determine these values.

(2) The structure along the interstation path could be complex. Surface waves sample the whole of the path between NAI and AAE and so the velocities and depths derived refer to some mean structure along that line. On the other hand, relative P-wave delays, it is assumed, are relevant to the crust and upper mantle immediately beneath the stations. The interstation path lies well to the east

of the rift in northern Kenya. From gravity measurements the negative Bouguer anomalies are greater at NAI and AAE by about 60 - 80 mgals than near Lake Rudolf. Thus the central section of the interstation path may have less mantle anomaly than exists below the two stations, where there are similar large Bouguer anomalies. If, therefore, the structure beneath the NAI and AAE sections is more typical of AFRIC than that actually below the stations, the mean mantle anomaly experienced by surface waves will be less than that revealed by the relative delays for the two stations.

(3) The estimates of compressional wave velocities may be in error. The relationship $\alpha = 1.74\beta$ is used to evaluate P-wave velocities from the derived S-wave values. For the crust, a better figure might be 1.73 while, although this ratio generally increases with depth, values as small as 1.71 - 1.72 have been found for the upper mantle (Anderson, 1965). However, a more direct estimate of the relationship between α and β for the structure beneath the rifts might be made by applying the formula $\alpha^2 = \frac{4}{3}\beta^2 + \frac{k}{\rho}$ using to derive k/ρ the α and β measured by seismic refraction (Griffiths et al, 1971). Considering the anomalous upper mantle layer 6 in the lid models, for the optimum shear velocity values the corresponding compressional wave velocities then become 7.07 - 7.15 km/sec. These are slightly higher than those using $\alpha = 1.74\beta$ and would tend to give the models even smaller delay times.

7.10 Discussion

The type of model suggested in this study, that of a crust and topmost upper mantle very similar to that for AFRIC

but underlain by a low velocity layer, gives a good fit to the data. It is difficult to estimate reliably the errors on the observed velocities, although the RMSD for phase only of 0.015 - 0.019 km/sec compares favourably with Sundaralingam's figure of 0.03km/sec for the overall error of observation for the phase velocities. Group velocity is less accurate in this case with the unweighted RMSD for this alone being 0.094 - 0.101 km/sec.

From a consideration of the RMSD's for the models, those with a lid seem to give a marginally better fit to the data than EA1. This does not mean that one of the lid models represents the best fit to the observed curves, but that for the framework chosen, each model corresponds to an RMSD minimum within the parameter space defined by the ranges of the variables. Although the choice of a lid-type model appears to match more closely the shape of the observed curves, we can only say that these final models are compatible with the data and not that one of them represents uniquely the structure beneath the station path. Because to a certain extent the depths to the layer interfaces were pre-selected these are not structural models and the velocities are means over the layer thicknesses. An exception to the former was that one or both of the bouhdaries of the lid were varied to give some idea of its thickness. Although we cannot determine the depth either to the top or the bottom of the lid, the preferred solutions indicate a fairly thin layer with a lower crustal layer above it that may also have velocities similar to those in the stable shield regions of Africa. The anomalous mantle beneath the lid is, of course, still present, but showing lower velocities than the model without such a lid.

Although the shear velocities are mean values determined

over the layer thicknesses, this does not exclude the possibility of complexity within layers, and velocities could change by gradations involving at some point a value lower than the mean, and hence velocities for the final models could fall below the means of 6.96 - 7.15 km/sec somewhere within the channel. The suite of possible models within one RMSD of the minima (Fig.52) for UM1 includes a structure with an ultra-low velocity channel beneath a thick lid of normal upper mantle material. Such low shear velocities have been suggested from Rayleigh wave phase velocity dispersion for paths crossing the East Pacific Rise (Knopoff, Schlue and Schwab, 1970), although a channel of velocity as low as 3.5 km/sec lies beneath a much thicker lid, which is required to explain higher phase velocity values than for the AAE-NAI path in the period range 25 - 40 seconds (Table 15). An alternative model, for almost identical phase velocities from the Western Mediterranean Basin, is also shown in Table 15 (Berry and Knopoff, 1967). The computed phase velocity curves for these models, and that for the Mid-Atlantic Ridge (Francis, 1969) are shown in Fig.55, the mantle layers being overlain by assumed AFRIC crust. The higher phase velocities in the period range 20 -45 seconds for the Mediterranean Basin and the East Pacific Rise illustrate the effects of a thick lid, whereas the only model without this feature, that for the Mid-Atlantic Ridge, has phase velocities lower than for UM1.

The upper mantle beneath the central part of the inter-station path (section 7.6.) may be closer to the AFRIC type of structure than that underlying the two stations. As the surface waves give velocities relevant to the path as a whole, with the apparent phase and group slownesses being the distance averages

TABLE 15

UPPER MANTLE MODELS

EAST PACIFIC RISE - LAP (1) (Knopoff, Schwab and Schlue, 1970)

H(km)	α (km/sec)	β (km/sec)	ρ (gm/cc)
86	8.0	4.45	3.44
46	7.95	3.50	3.44
47	8.23	4.54	3.44
100	8.49	4.77	3.53
90	8.81	4.89	3.60
	9.32	5.19	3.76

WESTERN MED. BASIN (Berry and Knopoff, 1967)

H(km)	α (km/sec)	β (km/sec)	ρ (gm/cc)
18	7.70	4.45	3.44
20	8.17	4.80	3.44
139	8.17	4.10	3.44
100	8.49	4.77	3.53
90	8.81	4.89	3.60
	9.32	5.19	3.76

MID-ATLANTIC RIDGE (Francis, 1969)

H(km)	α (km/sec)	β (km/sec)	ρ (gm/cc)
240.0	7.4	4.20	3.24
100.0	8.2	4.50	3.53
	8.7	4.85	3.70

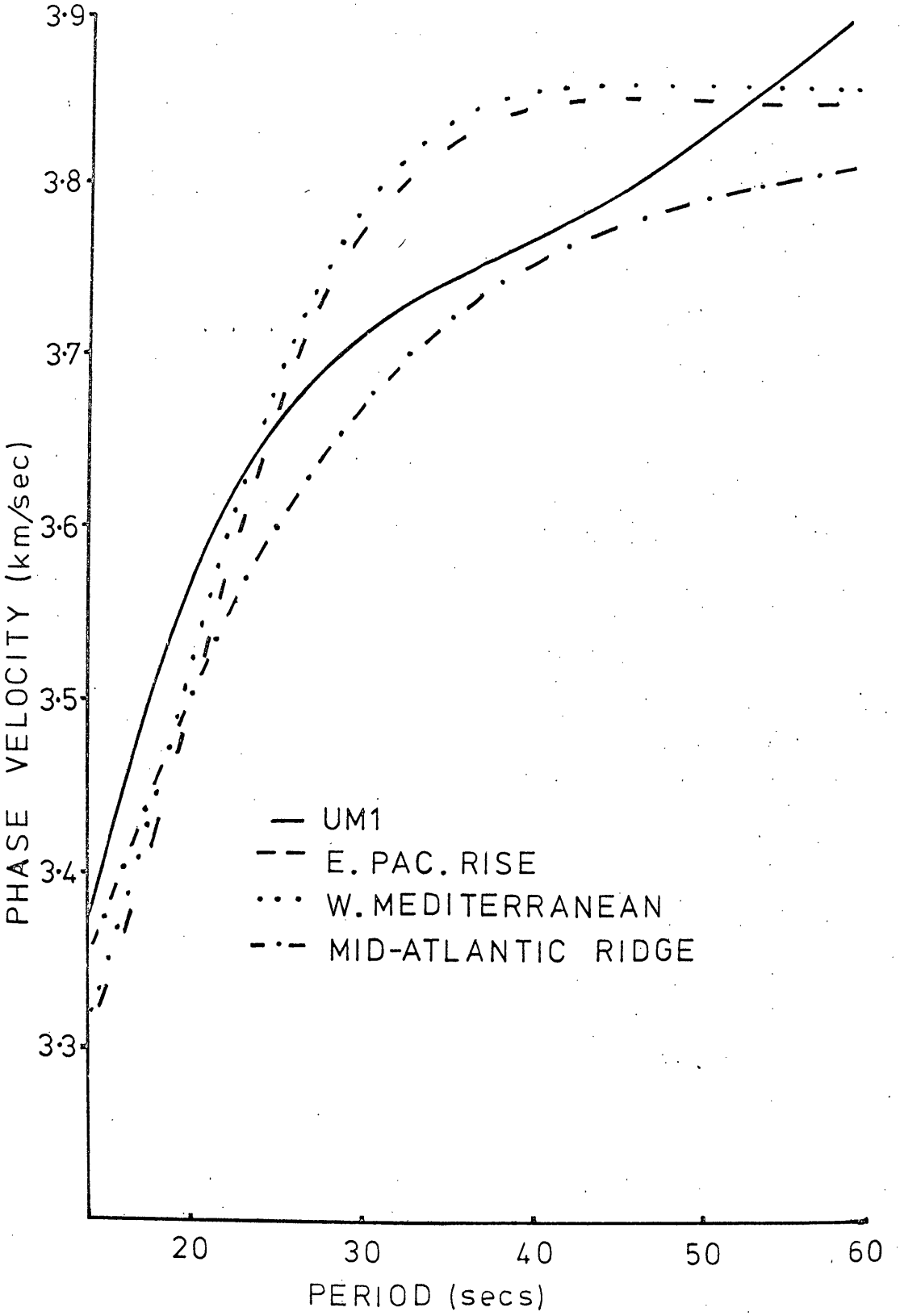

Fig.55. Computed Rayleigh wave phase velocities for lid model UM1 and structures shown in Table 15.

of the phase and group slownesses for the different regions (Knopoff, 1969), it might be more accurate to interpret this as a mixed path. This would presumably result in lower shear velocities within the low velocity channel for the sections of the path including Addis Abbaba and Nairobi than for the path as a whole.

The derived models do not contradict the structure of Griffiths et al (1971) which relates to the axial part of the Rift, but they do imply that there is rapid modification of the crust and upper mantle eastward. The velocities within the anomalous mantle zone for the surface wave models are lower than those for P and S waves of 7.5 km/sec and 4.53 km/sec observed within the Rift. This could be due to lateral variations in velocity or may indicate that the values from the refraction work are representative of the top surface of the anomaly but that there is a decrease in velocity for some depth beneath.

CHAPTER 8

DISCUSSION AND CONCLUSIONS

8.1. Discussion

An explanation has been given of the array data for teleseismic events in terms of sloping boundaries associated with a zone of anomalously low P-wave velocity within the upper mantle beneath Kaptagat. A simple model of two sloping interfaces with sharp velocity contrasts suggests a wedge shape for the zone (Fig.56), which cuts into the crust underneath the rift (Griffiths et al, 1971) but thins westward away from the axis. The anomalous material then gives way underneath the array station to topmost upper mantle similar to that in the stable areas of Africa. These data do not provide information on the structure to the east of the rift and any possible thinning of the mantle anomaly eastward. However, Rayleigh wave phase and group velocities for the interstation path AAE-NAI are compatible with a lid of 'normal' mantle material overlying a low-velocity channel. The absence of large azimuthal variations in delay time at Kaptagat implies that ultra-low velocities are present within the anomalous zone. Instead of sharp velocity contrasts at boundaries, a more realistic model probably involves a wedge with velocity gradations, the 7.5 km/sec determined by refraction work within the Gregory Rift representing a higher velocity upper surface to the anomaly. There appear to be strong similarities between the structure beneath the Gregory Rift, as derived from these and other geophysical data, and that underneath both oceanic ridges and some continental features. The Gregory Rift is characterised by considerable uplift

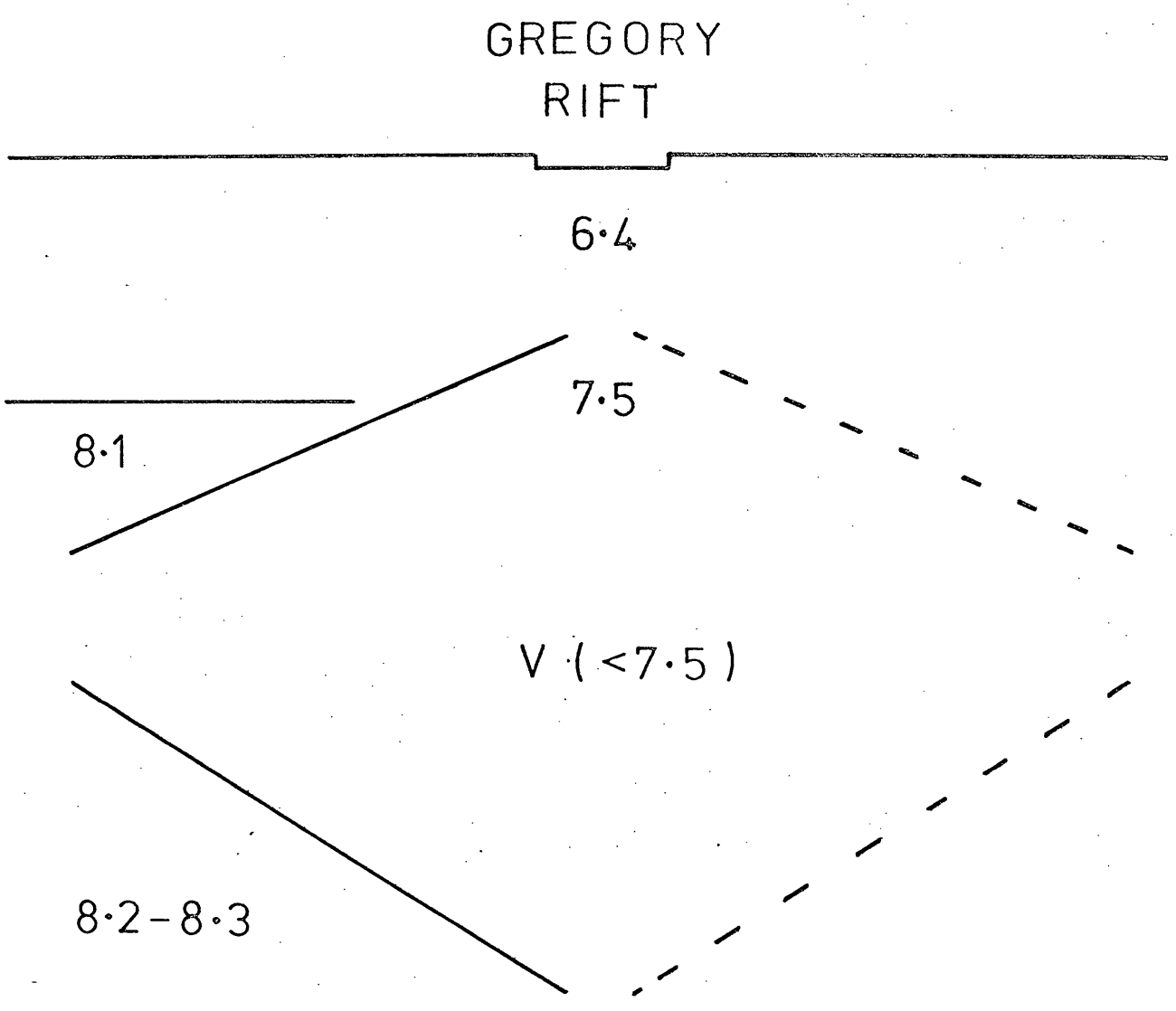

Fig.56. Crust and upper mantle model suggested from interpretation of the array data Dashed lines show structure not defined by these results but compatible with surface wave interpretation. Velocities are in km/sec.

over a wide area, as much as 1.7 km since Mid-Tertiary times (Baker and Wohlenberg, 1971), with axially a shallow crust of P-wave velocity 6.4 km/sec overlying anomalous mantle with a velocity from refraction studies of 7.5 km/sec (Griffiths et al, 1971). The oceanic ridges generally stand 2 - 4 km above the mean depth of the oceans and the western United States, forming an extension to the uplift of the East Pacific Rise, has been raised 2 km since the Eocene (Bott, 1965). Other continental features such as the Rhine Graben and the Baikal Rift also reach elevations of 2 km or more (Illies, 1969). From refraction studies, similar upper mantle velocities are found beneath these regions - 7.1 - 7.5 km/sec for the Baikal Rift (Artemjev and Artyushov, 1971), 7.2 - 7.7 km/sec below the Rhine Graben (Illies, 1969; Mueller et al, 1969), 7.3 - 7.4 km/sec for the Mid-Atlantic Ridge (Båth, 1960; Ewing and Ewing, 1959; Le Pichon et al, 1965) and 7.3 - 7.6 km/sec for the East Pacific Rise off South America (Le Pichon et al, 1965). Velocities of 7.2 - 7.6 km/sec have also been suggested for the upper mantle beneath the western United States (Nuttli and Bolt, 1969; Otsuka, 1966b).

There are some particularly compelling comparisons between the geophysical models of the Gregory Rift and those for oceanic ridges. The crustal structure of Griffiths et al (1971), is very much like that suggested by Båth (1960) for Iceland (Table 16). The wedge model proposed here for the mantle anomaly (Fig.56) is broadly similar in shape not only to that suggested from gravity studies over the Gregory Rift (Khan and Mansfield, 1971; Fig.5) but also that for the Mid-Atlantic Ridge (Talwani et al, 1965; Fig.57). The latter also has the top surface of the anomaly sinking below normal mantle away from the centre. However, if the velocity from refraction work is taken as being appropriate to the gravity model of Khan and Mansfield, this is inadequate to explain the large mean P-wave delay time measured for Kaptagat (Chapter 4) and also that for Nairobi (Sundaralingam, 1971). This

TABLE 16

CRUSTAL STRUCTURE OF ICELAND

FROM SEISMIC REFRACTION

Bath(1960)

H (km)	V_p (km/sec)
2.1	3.69
15.7	6.71
	7.38

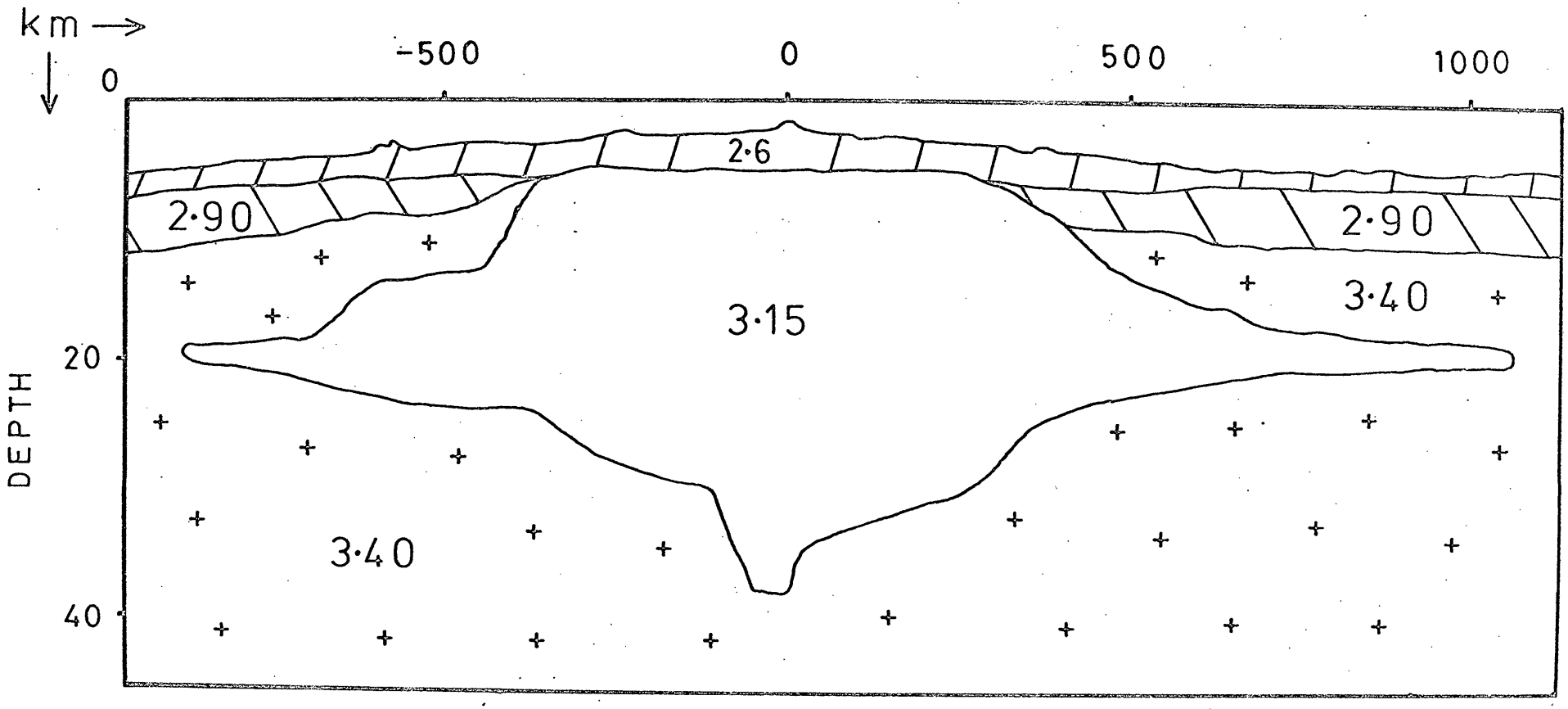

Fig.57. Crust and upper mantle model for the Mid Atlantic Ridge from gravity interpretation (Talwani et al, 1965). Densities are in gm/cc.

problem can be resolved in two ways, both of which are in agreement with the Kaptagat data as a whole. Firstly, if the boundaries on the anomalous material represent gradations in velocity, as suggested in sections 5.5. and 6.5., and the 7.5 km/sec is only appropriate to the upper surface of the zone, there could be a decrease in velocity for some depth below this, producing a greater delay time than for the case with a vertically constant velocity. Secondly, if there is partially molten material at depth, the density contrast with the surrounding mantle should be quite small (Bott, 1965), implying, from consideration of the gravity field, a deeper zone than for the solid case. As the rigidity modulus is zero on fusion, partial melting would cause a stronger reduction in P-wave velocity than in density, possibly producing ultra-low velocities. A combination of these two factors could then give a model to satisfy the gravity data which also agrees with the considerable D.C. term and absence of large azimuthal term in delay time, as observed at Kaptagat.

Partial melting could then be responsible for the production of large quantities of magma (Green, Green and Ringwood, 1967) and hence provide the voluminous volcanics in the area. A partially molten zone also implies very low shear velocities. Surface wave interpretation gives shear velocities generally about 4.0 km/sec for the low velocity channel beneath the interstation path AAE-NAI and models with deeper zones of lower velocity are also possible. In addition, it may be more realistic to consider the interstation path as made up of three sections, with the main anomalies being associated with the end portions. Thus the shear velocity in the upper mantle beneath Nairobi should be lower than 4.0 km/sec. This suggests an ultra-low velocity zone such as that below the East Pacific Rise off the Gulf of California (Knopoff, Schlue and Schwab, 1970; Table 15).

It seems unlikely that the structure proposed here is linear along the length of the East African rift system. The positive Bouguer anomaly along the axis of the Gregory Rift, which marks anomalous material cutting into the crust, is known to stretch at least from 1.^{o}N to 1.25^{o}S (Khan and Mansfield, 1971; Searle, 1970). However, the Ethiopia-Kenya-Tanzania-Malawi rift valleys are physically discontinuous (Le Bas, 1971) and Baker and Wohlenberg (1971) believe that dilatation is much less in the northern and southern extremities of the Kenya Rift than in its centre. The direction of maximum thickening of the wedge models - 125^{o} east of north for Model 1 - coincides with the direction of motion expected from plate tectonics if the East African rift system can be regarded as opening about a single pole of rotation (McKenzie, Davies and Molnar, 1970; Searle, 1970b). For the above reasons and others there are strong objections to this assumption. The direction of thickening points towards a region of considerable uplift defined by the Aberdare and Nyambi ranges and the shape of the anomalous mantle may well be more relevant to local phenomenon such as the uplift of the Kenya Dome.

Although the structure suggested in this study is probably not continuous throughout the East African rift system, it does suggest that the mantle beneath the Gregory Rift, and probably other regions of the rift system, is similar to that beneath oceanic ridges.

8.2. Conclusions

The array analysis of teleseismic events suggests that the Gregory Rift consists of a zone of anomalous low-velocity material between thinning lithosphere. The anomalous mantle cuts into the crust along a fairly narrow axial zone. Ultra-low velocities within the mantle such as are thought to exist below the East Pacific Rise

(Knopoff, Schlue and Schwab, 1970) seem to be required. With axially a crust and topmost mantle very much like that found in Iceland, a structure similar to that beneath oceanic ridges is indicated.

Because of the apparent rapid lateral variations in structure for the crust and topmost mantle, a more exhaustive study of regional earthquakes is recommended. Analysis of focal depths and velocities across the array could be used to give detailed structure to the west of the rift and more information on the axial zone of the anomaly could be obtained from hypocentres to the east of the rift. Fault plane mechanisms for local events would provide information on the principal stresses involved in the region of the Gregory Rift and also for such areas as the Kavirondo Gulf.

Useful extensions of the present work would be the calculation of relative delay time using Nairobi as a standard and re-interpretation of the AAE-NAI surface wave dispersion in terms of a mixed path.

APPENDIX A

A.1. SEISMIC REFRACTION AT A DIPPING INTERFACE

Consider a seismic ray of slowness $\underline{S}_i$ incident on a dipping interface defined by its normal $\underline{n}$, with a refracted ray of slowness $\underline{S}_r$ (Fig.A1).

$\underline{P}_i$ and $\underline{P}_r$ are apparent slowness vectors - projections on to the horizontal surface of $\underline{S}_i$ and $\underline{S}_r$.

The lengths of the vectors are proportional to their slownesses.

From Snell's Law:

$$|\underline{S}_i| \sin i = |\underline{S}_r| \sin r \qquad A(i)$$

where i is the angle between $\underline{n}$ and $\underline{S}_i$, and r is the angle between $\underline{n}$ and $\underline{S}_r$.

$\underline{S}_r$ is in the same plane as $\underline{n}$ and $\underline{S}_i$. We can resolve $\underline{S}_r$ into components along OA and OB.

$$\underline{S}_r = (\underline{S}_r \circ \underline{n})\,\underline{n} + (\underline{n} \wedge \underline{S}_i) \wedge \underline{n}$$

$$\underline{S}_r = (\underline{S}_r \cdot \underline{n})\,\underline{n} + \underline{S}_i - (\underline{S}_i \circ \underline{n})\,\underline{n} \qquad A(ii)$$

$$\therefore \quad \underline{S}_r = \underline{S}_i + (\underline{S}_r \cdot \underline{n} - \underline{S}_i \cdot \underline{n})\,\underline{n}$$

$$= \underline{S}_i + (|\underline{S}_r| \cos r - |\underline{S}_i| \cos i)\,\underline{n}$$

From Snell's Law,

$$|\underline{S}_r| \cos r - |\underline{S}_i| \cos i = \sqrt{|\underline{S}_r|^2 - |\underline{S}_i|^2 \sin^2 i} - |\underline{S}_i| \cos i = f(i)$$

Then $$\underline{S}_r = \underline{S}_i + f(i) \cdot \underline{n} \qquad A(iii)$$

Now if we take the projections of $\underline{S}_i$, $\underline{S}_r$ on to the horizontal plane to give $\underline{P}_i$ and $\underline{P}_r$, the apparent slowness vectors,

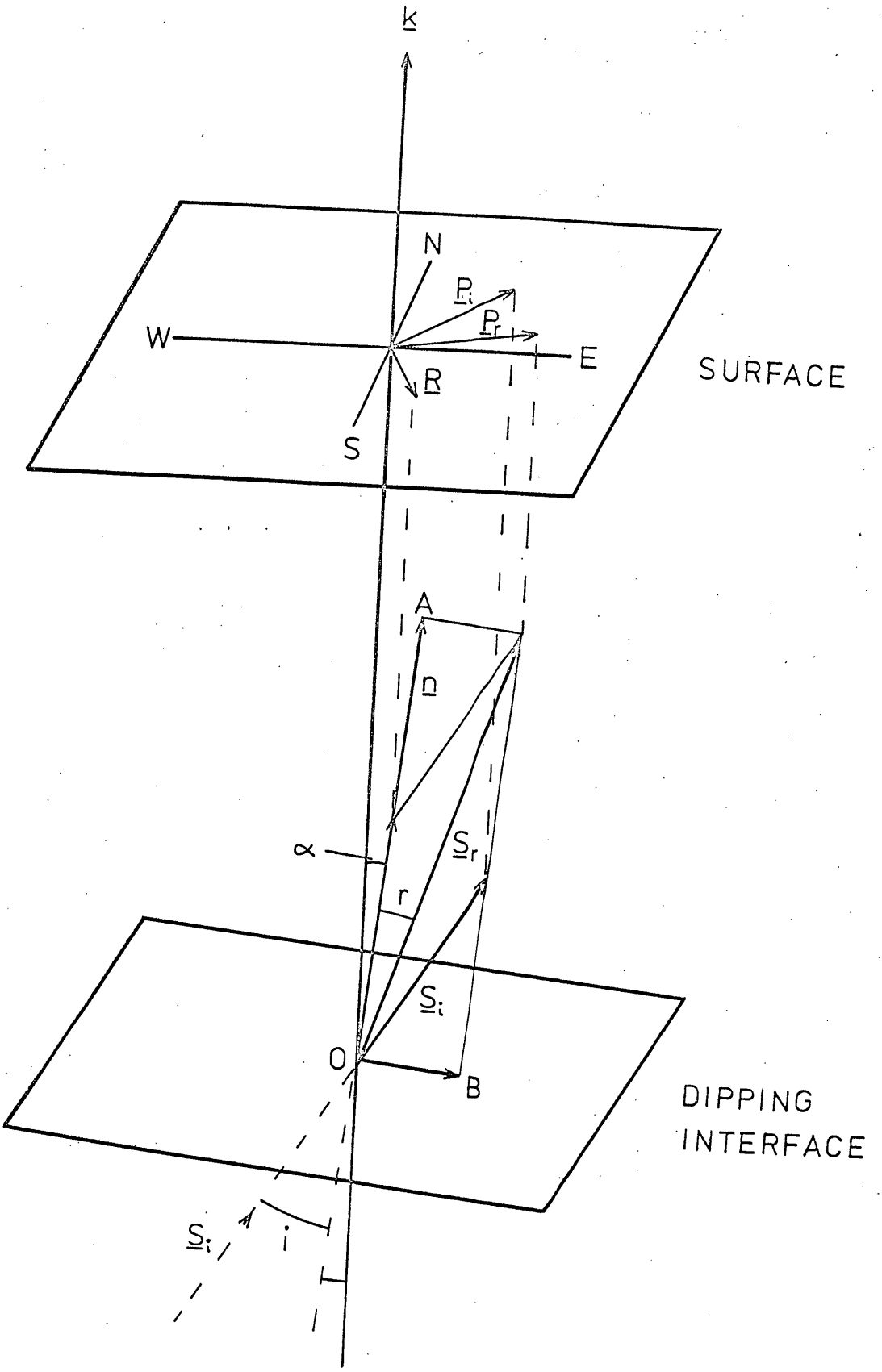

Fig.A.1. Effect of refraction of a seismic ray at a dipping interface.

$$\underline{P}_i = (\underline{k} \wedge \underline{S}_i) \wedge \underline{k} = \underline{S}_i - (\underline{S}_i \cdot \underline{k})\,\underline{k} \qquad A(iv)$$

$$\underline{P}_r = (\underline{k} \wedge \underline{S}_r) \wedge \underline{k} = \underline{S}_r - (\underline{S}_r \cdot \underline{k})\,\underline{k}$$

Here $\underline{k}$ defines the vertical.

We know $\underline{S}_r$ from A(iii)

$$\underline{P}_r = \underline{S}_i + f(i)\,\underline{n} - (\underline{S}_i \cdot \underline{k})\,\underline{k} - f(i)\,(\underline{n} \cdot \underline{k})\,\underline{k}$$

$$= \underline{S}_i - (\underline{S}_i \cdot \underline{k})\underline{k} + f(i)\left[\underline{n} - (\underline{n} \cdot \underline{k})\,\underline{k}\right]$$

From A(iv),

$$\underline{P}_r = \underline{P}_i + \left[(\underline{k} \wedge \underline{n}) \wedge \underline{k}\right] f(i) \qquad A(v)$$

We can define SLOWNESS ANOMALY $dS = (|\underline{P}_r| - |\underline{P}_i|)$

AZIMUTH ANOMALY $dA = \text{ang}\,(\underline{P}_i . \underline{P}_r)$

Also $$\underline{P}_r = \underline{P}_i + \underline{R} \qquad A(vi)$$

and $\underline{R} = f(i)\left[(\underline{k} \wedge \underline{n}) \wedge \underline{k}\right]$ = the anomaly vector.

A.2. ZERO DIP CONDITION

If the interface is horizontal and not dipping, $\underline{n}$ is vertical, and $\underline{k} \wedge \underline{n} = 0$. Therefore, $\underline{R} = 0$ which implies that a horizontal interface cannot cause an anomaly.

A.3. MULTIPLE INTERFACES

If we have m interfaces,

$$\underline{P}_{r,1} = \underline{P}_{i,1} + \underline{R}_1$$

$$\vdots$$

$$\underline{P}_{r,m} = \underline{P}_{i,m} + \underline{R}_m$$

For the j th interface, $\underline{R}_j = f(\mathbf{i}_j) \left[\underline{k} \wedge \underline{n}_j\right] \wedge \underline{k}$

But $\underline{P}_{i,j} = \underline{P}_{r,(j-1)}$

$\therefore$ $\underline{P}_{r,m} = \underline{P}_{i,1} + \sum_{j=1}^{m} \underline{R}_j$

Hence we can extend the problem to cover several layers so long as we know the angle of incidence of a ray to the lowest interface, and its incident slowness there. The anomaly vectors for each layer are then summed.

A.4. Parallel Dipping Layers.

The velocity of a layer with parallel boundaries does not affect the results.

From A(ii), for the j th interface,

$$\underline{S}_{r,j} = \underline{S}_{i,j} + (\underline{S}_{r,j} \cdot \underline{n}_j - \underline{S}_{i,j} \cdot \underline{n}_j)\ \underline{n}_j$$

if we take $j = 1, (1 + 1) \ldots . m$.

$$\underline{S}_{r,1} = \underline{S}_{i,1} + (\underline{S}_{r,1} \cdot \underline{n}_1 - \underline{S}_{i,1} \cdot \underline{n}_1)\ \underline{n}_1$$

$$\underline{S}_{r,m} = \underline{S}_{i,m} + (\underline{S}_{r,m} \cdot \underline{n}_m - \underline{S}_{i,m} \cdot \underline{n}_m)\ \underline{n}_m$$

If the interfaces are all parallel, $\underline{n}_1 = \underline{n}_{1+1} = \ldots\ldots \underline{n}_m$

But again, $\underline{S}_{r,1} = \underline{S}_{i,(1+1)}$

Therefore, if we add all equations for 1, 1+1, ... m and apply the above condition,

$$\underline{S}_{r,m} = \underline{S}_{i,1} + (\underline{S}_{r,m} \cdot \underline{n} - \underline{S}_{i,1} \cdot \underline{n})\ \underline{n}$$

This does not include the slowness for layers between j = 1 and j = m, so that, for instance, an interface need not be a sharp discontinuity

but can be a gradual change in slowness between parallel layers.

A.5. Computational Procedure

The apparent incident slowness $\underline{P}_i$ is assumed from the NOAA azimuth and Herrin et al's (1968) travel time tables. The anomaly vector $\underline{R}$ is in the direction of dip of the interface and can be seen to be a function of the angle of incidence i of the ray at the interface. This angle can be calculated from

$$i^1 = \frac{1}{R|\underline{S}_i|} \cdot \left(\frac{dT}{d\Delta}\right) \qquad A(vii)$$

Where i^1 is the angle of incidence of the ray to the vertical from which we can calculate i if the angle of dip, defined by $\underline{n}$, is known. $dT/d\Delta$ is the gradient of the travel-time curve for the relevant signal with slowness $\underline{S}_i$ at radius R to the interface, where R is a scalar distinct from the anomaly vector $\underline{R}$. This is dependent upon the depth to the interface which is taken at 50 km for a one layer case and 150 km for two layers. These values are order of magnitude figures as the theoretical anomalies are not very sensitive to small changes both in R, and correspondingly, in the depth to the lower boundary.

The anomalies produced are dependent upon the angle of incidence, i, and, therefore, the epicentral distance, Δ, of an earthquake. This is illustrated in Fig.A2., which shows the slowness and azimuth anomalies due to a dipping Moho of velocity contrast 6.7 to 8.1 km/sec and a dip of 10^o, with a direction of dip of 90^o east of north.

The principle of least squares is used to obtain a fit of the data to some theoretical model. Considering a wedge model as in Fig.21, with dip angles of D1 and D2 and velocity contrasts V2 - V1 and V3 - V2 at the two boundaries and with a direction of maximum negative slowness

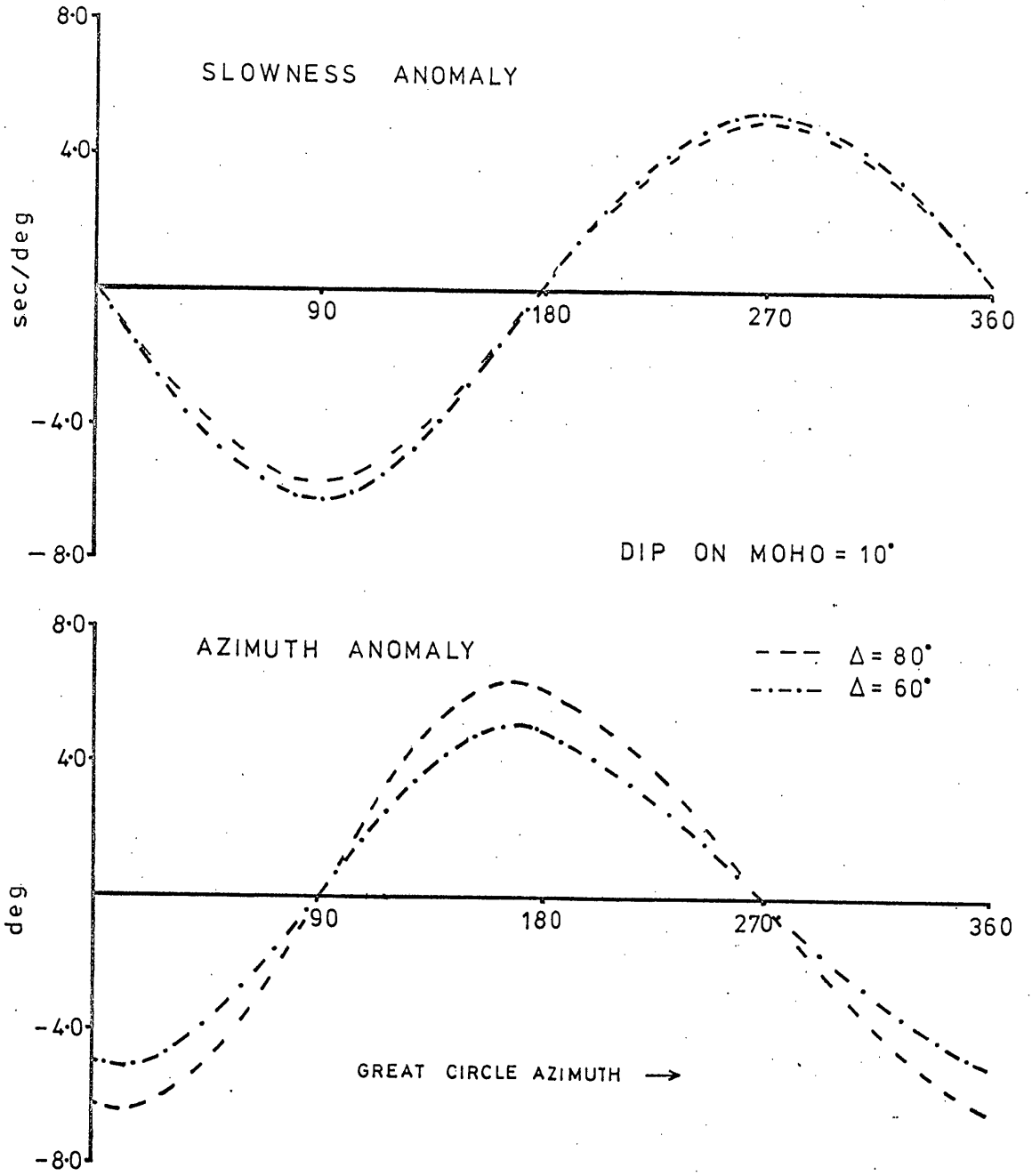

Fig.A.2. Computed slowness and azimuth anomalies caused by a sloping Moho with a velocity contrast of 6.7 : 8.1 km/sec.

anomaly at some azimuth Ψ ; the following procedure is used:

(a) Values for V1, V2 and V3 are assumed and D1, D2 and Ψ taken as variables.

(b) The theoretical anomalies for each event are computed for the appropriate epicentral distance, and angle i, for given ranges of the variables.

(c) For each value of the variables, the root mean square deviation of the observed points from the computed theoretical values is calculated.

(d) The RMSD values for the combinations of variables are mapped and the minimum taken as giving a best fit to the observed data.

(e) This can then be repeated for different values of the wedge velocity V2.

REFERENCES

Al-Chalabi, M. (1971) — Reliability of the rotation pole in continental fitting. Earth. Planet. Sci. Letters., 11, 257-262.

Anderson, D.L. (1965) — Recent evidence concerning the structure and composition of the Earth's mantle. Physics and Chemistry of the Earth., 6, 1 - 131.

Artemjev, M.E. and Artyushkov, E.V. (1971) — Structure and isostasy of the Baikal Rift and the mechanism of rifting. J. Geophys. Res., 76, 1197 - 1211.

Backus, G. and Gilbert, F. (1968) — The resolving power of gross Earth data. Geophys. J. Roy. Astr. Soc., 16, 169 - 205.

Bailey, D.K. (1964) — Crustal warping - a possible tectonic control of alkaline magmatism. J. Geophys. Res., 69, 1103 - 1111.

Baker, B.H. (1969) — Structural evolution of the rift zones in the Middle East - a comment. Nature., 224, 359 - 360.

Baker, B.H., and Wohlenberg, J. (1971) — Structure and evolution of the Kenya Rift Valley. Nature., 229, 538 - 542.

Banghar, A.R., and Sykes, L.R. (1969) — Focal mechanisms of earthquakes in the Indian Ocean and adjacent areas. J. Geophys. Res., 74, 632 - 649.

Båth, M. (1960) — Crustal structure of Iceland. J. Geophys. Res., 65, 1793 - 1807.

Berry, M.L. and Knopoff, L. (1967) — Structure of the upper mantle under the Western Mediterranean Basin. J. Geophys. Res., 72., 3613 - 3626.

Birtill, J.W. and Whiteway, F.E. (1965) — The application of phased arrays to the analysis of seismic body waves. Phil. Trans. Roy. Soc. Lon., Series A., 258, 421 - 443.

Bloch, S., Hales, A.L., and Landisman, M. (1969) — Velocities in the crust and upper mantle of southern Africa from multi-mode surface wave dispersion. Bull. Seism. Soc. Am., 59, 1599 - 1629.

Bolt, B. A., and Dorman, J. (1961) — Phase and group velocities of Rayleigh wave in a spherical, gravitating Earth. J. Geophys. Res., 66, 2965 - 2981.

Bolt, B.A., and Nuttli, O. (1966) — P-wave residuals as a function of azimuth, 1. Observations. J. Geophys. Res., 71, 5977 - 5985.

Bonjer, K.P., Fuchs, K., and Wohlenberg, J. (1970) — Crustal structure of the East African rift system from spectral response ratios of long-period body waves. Zeitschrift. Geophys., 36, 287 - 297.

Bott, M.H.P. (1965) — Formation of oceanic ridges. Nature, 207, 840 - 843.

Brune, J.N., and Dorman, J. (1963) — Seismic waves and Earth Structure in the Canadian Shield. Bull. Seism. Soc. Am., 53, 167 - 210.

Bullard, E.C. (1936) — Gravity measurements in East Africa. Phil. Trans. Roy. Soc. Series A., 235, 445 - 531.

Bullen, K.E. (1956) — Encylopaedia of Physics., Vol. XLVII. Springer-Verlac.

Bullen, K.E. (1965) — Introduction to the theory of seismology, Cambridge.

Carpenter, E.W. (1966) — Onset time analysis. AWRE Blacknest Note PA4/AG, 66.

Clark, S.P. (1966) — Handbook of physical constants. Geol. Soc. Am., Memoir, 97.

Cleary, J. (1967) — Azimuthal variation of the LONGSHOTT source term. Earth. Planet. Sci. Letters., 3, 29 - 37.

Cleary, J. and Hales, A.L. (1966) — An analysis of the travel times of P-waves to North American stations in the distance rance 32° to 100°. Bull. Seism. Soc. Am., 56, 467 - 489.

Cleary, J., Wright, C., and Muirhead, K.J. (1968)
The effects of local structure upon measurements of the travel time gradient at the Warramunga seismic array. Geophys. J. Roy. Astr. Soc., 16, 21 - 29.

Corbishley, D.J. (1969)
Measurements of the derivative of the P-wave travel time curve by means of an array network. Ph.D. thesis, University of Durham.

Corbishley, D.J. (1970)
Structure under seismic arrays. Geophys. J. Roy. Astr. Soc., 21, 415 - 425

Davies, D., and McKenzie, D.P. (1969)
Seismic travel-time residuals and plates. Geophys. J. Roy. Astr. Soc., 18, 51 - 63.

De Bremaecker, J. Cl. (1959)
Seismicity of the East African Rift Valley. J. Geophys. Res., 64, 1961 - 1966.

Der, Z., Masse, R., and Landisman, M. (1970)
Effects of observational errors on the resolution of surface waves at intermediate distances. J. Geophys. Res., 75, 3399 - 3409.

Dixey, F. (1956)
The East African rift system. Bull. Colon. Geol. Mineral Resources Suppl.

Dopp, S. (1964)
Preliminary note on the refraced P-phase in the Western Rift Valley of Africa. J. Geophys. Res., 69, 3027 - 3031.

Douglas, A. (1967)
A special purpose least squares program. AWRE Blacknest Report No. 0 - 54/66.

Douglas, A. (1967b)
Joint epicentre determination. Nature, 215, 47 - 8.

Douglas, A. and Lilwall, R.C. (1968)
Does epicentre source bias exist? Nature, 220, 469 - 470.

Drake, C.L., and Girdler, R.W. (1964)
A geophysical study of the Red Sea. Geophys. J. Roy. Astr. Soc., 8, 473 - 495.

Dziewonski, A., Bloch, S., Landisman, M. (1969)
A technique for the analysis of transient seismic signals. Bull. Seism. Soc., Am., 59, 427 - 444.

Elder, J.W. (1966) — Penetrative convection : its role in volcanism. Bull. Vulc., 29, 327 - 343.

Evernden, J.F. (1953) — Direction of approach of Rayleigh waves and related problems. Bull. Seism. Soc. Am., 43, 335- 374.

Ewing, J. and Ewing, M.(1959) — Seismic refraction measurements in the Atlantic Ocean basins, in the Mediterranean Sea, on the Mid-Atlantic Ridge, and in the Norwegian Sea. Bull. Geol. Soc. Am., 70, 291 - 318.

Fairhead, J.D. (1968) — The seismicity of the East African rift system 1955 to 1968. M.Sc. Dissertation, University of Newcastle-upon-Tyne.

Fairhead, J.D. and Girdler, R.W. (1969) — How far does the rift system extend through Africa? Nature, 221, 1018 - 1020.

Fairhead, J.D. and Girdler, R.W. (1970) — The seismicity of the Red Sea, Gulf of Aden and Afar triangle. Phil. Trans. Roy. Soc. Lon. Series A., 267, 49 - 74.

Fairhead, J.D. and Girdler, R.W. (1971) — The seismicity of Africa. Geophys. J. Roy. Astr. Soc., 24, 610 - 631.

Francis, T.J.G. (1969) — Upper mantle structure along the axis of the Mid-Atlantic Ridge near Iceland. Geophys. J. Roy. Astr. Soc., 17, 507 - 520.

Freedman, H.W. (1968) — Seismological measurements and measurement error. Bull. Seism. Soc. Am., 58, 1261 - 1271.

Freund, R. (1966) — Rift Valleys. In 'The World Rift System', Report 66 - 14. 330 - 344.

Freund, R. (1970) — Plate tectonics of the Red Sea and Africa. Nature, 228, 453.

Gane, P.G., Atkins, A.R., Sellschop, J.P.F., and Seligman, P. (1956) — Crustal structure in the Transvaal. Bull. Seism. Soc. Am., 46, 293 - 316.

Gass, I.G. (1970) — Tectonic and magmatic evolution of the Afro-Arabian dome. In 'African Magmatism and Tectonics', 285 - 297. Oliver and Boyd.

Gass, I.G. (1972) — Proposals concerning the variation of volcanic products and processes within the oceanic environment. Phil. Trans. Roy. Soc. Lon. Series A., 271, 131 - 140.

Gass, I.G. and Gibson, I.L. (1969) — Structural evolution of the rift zones of the Middle East. Nature, 221, 926 - 930.

Gill, R.R. (1972) — The seismicity of East Africa. M.Sc. Dissertation, University of Durham.

Girdler, R.W. (1958) — The relationship of the Red Sea to the East African rift system. Quart. J. Geol. Soc. Lon., 114. 79 - 105.

Girdler, R.W. (1964) — Geophysical studies of rift valleys. Physics and Chemistry of the Earth, 5, 121 - 156.

Girdler, R.W., Fairhead, J.D., Searle, R.C. and Sowerbutts, W.T.C., (1969) — Evolution of rifting in Africa. Nature, 224, 1178 - 1182.

Green, T.H., Green, D.H., and Ringwood, A.E. (1967) — The origin of high-alumina basalts and their relationships to quartz, tholeiites and alkali basalts. Earth. Planet. Sci. Letters., 2, 41 - 51.

Greenfield, R.J. and Sheppard, R.M. (1969) — The Moho depth variations under the LASA and their effect on $dT/d\Delta$ measurements. Bull. Seism. Soc. Am., 59, 409 - 420.

Gregory, J.W. (1921) — The rift valleys and geology of East Africa. Seeley and Service Co. Ltd.

Griffiths, D.H., King, R.F., Khan, M.A., and Blundell, D.J. (1971) — Seismic refraction line in the Gregory Rift. Nature, 229, 69 - 71.

Gumper, F. and Pomeroy, P.W. (1970) — Seismic wave velocities and Earth structure on the African continent. Bull. Seism. Soc. Am., 60, 651 - 668.

Hales, A.L. and Bloch, S. (1969) — Upper mantle structure : are the low velocity layers thin? Nature, 221, 930 - 933.

Hales, A.L. and Sachs, F.S. (1959) — Evidence for an intermediate layer from crustal structure in the Eastern Transvaal. Geophys. J. Roy. Astr. Soc., 2, 15 - 33.

Harris, P.G. (1969) — Basalt type and rift valley tectonism. Tectonophysics, 8, 427 - 436.

Harris, P.G. (1970) — Convection and magmatism with reference to the African continent. In 'African Magmatism and Tectonics', 419 - 435. Oliver and Boyd.

Heiskanen, W.A. and Vening Meinesz, F.A. (1958) — The Earth and its gravity field. Mc-Graw Hill.

Herrin, E., Arnold, E.P. Bolt, B.A., Clawson, G.E. Engdahl, E.R., Gordon, D.W., Hales, A.L., Lobdell, J.L., Nuttli, O., Romney, C., Taggart, J., and Tucker, W. (1968) — 1968 Seismological tables for P phases. Bull. Seism. Soc. Am., 58. 1193 - 1241.

Herrin, E., and Taggart, J. (1968) — Regional variations in P travel times. Bull. Seism. Soc. Am., 58, 1325 - 1337.

Herrin, E., Tucker, W., Taggart, J., Gordon, D.W., and Lobdell, J.L. (1968) — Estimation of surface focus P travel times. Bull. Seism. Soc. Am., 58, 1273 - 1291.

Holmes, A. (1965) — Principles of physical geology. Nelson.

Hutchinson, R., and Gass, I.G. (1971) — Mafic and ultramafic inclusions associated with undersaturated basalt on Kod Ali Island, southern Red Sea. Contr. Mineral. and Petrol., 31, 94 - 101.

Illies, J.H. (1969) — An intercontinental belt of the world rift system. Tectonophysics, 8, 5 - 29.

Jeffreys, H., and Bullen, K.E. (1940) — Seismological Tables. Brit. Assn. Gray-Milne Trust.

Jennings, D.J. (1964) — Geology of the Kapsabet-Plateau area. Geol. Surv. Kenya. Report No. 63.

Kelly, E.J. (1964) — Limited network processing of seismic signals. M.I.T. Lincoln Lab. Group Report 44.

Khan, M.A. and Mansfield, J. (1971) — Gravity measurements in the Gregory Rift. Nature, 229. 72 - 75.

King, B.C. (1970) — Vulcanicity and rift tectonics in East Africa. In 'African magmatism and tectonics', 263-28; Oliver and Boyd.

King, B.C. and Chapman, G.R. (1972) — Volcanism of the Kenya Rift Valley. Phil Trans. Roy. Soc. Lon. Series A., 271, 185 - 208.

Knopoff, L. (1969) — Phase and group slownesses in inhomogeneous media. J. Geophys. Res., 73, 755 - 760.

Knopoff, L., and Schwab, F.A. (1968) — Apparent initial phase of a source of Rayleigh waves. J. Geophys. Res., 73, 755 - 760.

Knopoff, L., Schlue, J.W., and Schwab, F.A. (1970) — Phase velocities of Rayleigh waves across the East Pacific Rise. Tectonophysics, 10, 321 - 334.

Le Bas, M.J. (1971) — Per-alkaline volcanism, crustal swelling, and rifting. Nature. Phys. Sci., 230, 85 - 87.

Le Pichon, X. (1968) — Sea-floor spreading and continental drift. J. Geophys. Res., 73, 3661 - 3697.

Le Pichon, X., Houtz, R.E., Drake, C.L., Nafe, J.E. (1965) — Crustal structure of the mid-ocean ridges (1) Seismic refraction measurements. J. Geophys. Res., 70, 319 - 340.

Lilwall, R.C., and Douglas, A. (1970)
Estimation of P-wave travel times using the Joint Epicentre Method.
Geophys. J. Roy. Astr. Soc., 19, 165 - 181

Lipman, P.W. (1969)
Alkalic and tholeiitic basaltic volcanism related to the Rio Grande Depression, southern Colorado, and northern New Mexico.
Bull. Geol. Soc. Amer., 80, 1343 - 1354.

Long, R.E. (1968)
Temporary seismic array stations.
Geophys. J. Roy. Astr. Soc., 16, 37 - 45.

Long, R.E., and Mitchell, M.G.
Teleseismic P-wave delay time in Iceland.
Geophys. J. Roy. Astr. Soc., 20, 41 - 48.

Long, R.E., Backhouse, R.W., Maguire, P.K.H., Sundaralingam, K. (1972)
The structure of East Africa using surface wave dispersion and Durham seismic array data.
Tectonophysics, 15 (1/2), 165-178.

Magnitsky, V.A. and Kalashnikova, I.V. (1970)
Problem of phase transitions in the upper mantle and its connection with the Earth's crustal structure.
J. Geophys. Res., 75, 877 - 885.

McBirney, A.R. and Gass, I.G. (1967)
Relations of oceanic volcanic rocks to mid-oceanic rises and heat flow.
Earth. Planet. Sci. Letters, 2, 265 - 276.

McConnell, R.B. (1970)
Evolution of rifting in Africa, Nature, 227, 699.

McKenzie, D.P., Davies, D., and Molnar, P. (1970)
Plate tectonics of the Red Sea and East Africa.
Nature, 226, 243-248.

Mitchell, M.G. (1969)
The crust and upper mantle beneath Iceland.
Ph.D. thesis, University of Durham.

Mohr, P.A. (1963)
The Ethiopian Cainozoic lavas - a preliminary study of some trends : spatial, temporal, and chemical.
Bull. Geophys. Addis Abbaba, 3, 103-144.

Mohr, P.A. (1970)
Plate tectonics of the Red Sea and East Africa.
Nature, 228, 547 - 8.

Mohr, P.A. (1971) — Ethiopian Rift and Plateau : some volcanic petrochemical differences. J. Geophys. Res., 76, 1967 - 1984.

Molnar, P. and Aggarwal, Y.P. (1971) — A microearthquake survey in Kenya. Bull. Seism. Soc. Am., 61, 195 - 201.

Molnar, P. and Oliver, J. (1969) — Lateral variations of attenuation in the upper mantle and discontinuities in the lithosphere. J. Geophys. Res., 74, 2648 - 2682.

Mueller, St., Peterschmitt, E., Fuchs, K., and Ansorge, J. (1969) — Crustal structure beneath the Rhine Graben from seismic refraction and reflection measurements. Tectonophysics, 8, 529 - 542.

Murray, C.G. (1970) — Magma genesis and heat flow: differences between mid-oceanic ridges and African rift valleys. Earth. Planet. Sci. Letters., 9, 34 - 38.

Niazi, M. (1966) — Corrections to apparent azimuths and travel-time gradients for a dipping Moho-rovicic discontinuity. Bull. Seism. Soc. Am., 56, 491 - 509.

Nuttli, O., and Bott, B.A. (1969) — P-wave residuals as a function of azimuth. (2) Undulations of the mantle low-velocity layer as an explanation. J. Geophys. Res., 74, 6594 - 6602.

Osmaston, M.F. (1971) — Genesis of ocean ridge median valleys and continental rift valleys. Tectonophysics, 11, 387 - 405.

Otsuka, M. (1966a) — Azimuth and slowness anomalies of seismic waves measured on the Central California Seismographic Array. Part 1: Observations. Bull. Seism. Soc. Am., 56, 223-239.

Otsuka, M. (1966b) — Azimuth and slowness anomalies of seismic waves measured on the Central California Seismographic Array. Part 2: Interpretation. Bull. Seism. Soc. Am., 56, 655- 675.

Philips, J.D. (1970) Magnetic anomalies in the Red Sea. Phil. Trans. Roy. Soc. Lon. Series A., 269, 205 - 217.

Powell, J.D. (1964) An efficient method for finding the minimum of a function of several variables without calculating derivatives. Computer Journal, 7, 155.

Powell, J.D. (1965) A method for minimising of sum of squares of non-linear functions without calculating derivatives. Computer Journal, 8, 303 - 307.

Roberts, D.G. (1969) Structural evolution of the rift zones in the Middle East. Nature, 223, 55 - 57.

Rothe, J.P. (1954) La zone seismique mediane Indo-Atlantique. Proc. Roy. Soc. Lon. Series, A., 222, 389- 397.

Sato, Y. (1958) Attenuation, dispersion, and the wave guide of the G wave. Bull. Seism. Soc. Am., 48, 231 - 251.

Searle, R.C. (1970) Evidence from gravity anomalies for thinning of the lithosphere beneath the rift valley of Kenya. Geophys. J. Roy. Astr. Soc., 21, 13 - 31.

Searle, R.C. (1970b) Lateral extension in the East African rift valleys. Nature, 227, 267-268.

Sowerbutts, W.T.C. (1969) Crustal structure of the East African Plateau and rift valleys from gravity measurements. Nature, 223, 143 - 146.

Stefansson, R. (1967) Some problems of studies on the Mid-Atlantic Ridge, Iceland, and the mid-ocean ridges. Soc. Sci. Islandica 'Rit', 38, 80 - 90.

Sundaralingam, K. (1971) Seismic investigation of the crust and upper mantle of East Africa. Ph.D. thesis, University of Durham.

Sutton, G.H., and Berg, E. (1958) — Seismological studies of the Western Rift valley of Africa. Trans. Am. Geophys. Union., 39, 474-481.

Sykes, L.R., and Landisman, M. (1964) — The seismicity of East Africa, the Gulf of Aden, and the Arabian and Red Seas. Bull. Seism. Soc. Am., 54, 1927-1940.

Talwani, M., Le Pichon, X., and Ewing, M. (1965) — Crustal structure of the mid-ocean ridges. (2) Computed model from gravity and seismic refraction data. J. Geophys. Res., 70, 341 - 352.

Talwani, M., Sutton, G.H., amd Worzel, J.L. (1959) — A crustal section across the Puerto Rico Trench. J. Geophys. Res., 64, 1545- 1555.

Tobin, D.G., Ward, P.L., and Drake, C.L. (1969) — Microearthquakes in the rift valley of Kenya. Bull. Geol. Soc. Am., 80, 2043 - 6.

Toksoz, M.N., Ben-Menahem, A. (1963) — Velocities of mantle Love and Rayleigh waves over multiple paths. Bull. Seism. Soc. Am., 53, 741 - 764.

Tramontini, C., and Davies, D. (1969) — A seismic refraction survey in the Red Sea. Geophys. J. Roy. Astr. Soc., 17, 225 - 241.

Tryggvason, E. (1964) — Arrival times of P waves and upper mantle structure. Bull. Seism. Soc. Am., 54, 727 - 736.

Underwood, R., and Lilwall, R.C. (1969) — The systematic error in seismic location. Geophys. J. Roy. Astr. Soc., 17, 521 - 526.

Vine, F.J. (1966) — Spreading of the ocean floor : new evidence. Science, 154, 1405 - 1415.

Von Herzen, R.P., and Vacquier, V., (1967) — Terestial heat flow in Lake Malawi, Africa. J. Geophys. Res., 72, 4221 - 4226.

Ward, P.L., Palmason, G., and Drake, C. (1969) — Microearthquake survey and the Mid-Atlantic Ridge in Iceland. J. Geophys. Res., 74, 665- 684.

Whiteway, F.E. (1965) — The recording and analysis of seismic body waves using linear cross arrays. Radio and Electronic Engineer, 29, 33 - 46.

Williams, L.A.J. (1970) — The volcanics of the Gregory Rift Valley, Kenya. Bull. Vulc., 34, 439 - 465.

Willis, B. (1936) — East African Plateau and Rift Valley. Carnegie.

Willmore, P.L., Hales, A.L., and Gane, P.G. (1952) — Seismic investigation of crustal structure in the Western Transvaal. Bull. Seism. Soc. Am., 42, 58 - 80.

Wilson, J.T., (1969) — Static or mobile belts : the current scientific revolution. Tectonophysics, 7, 600 - 601.

Wohlenberg, J. (1970) — On the seismicity of the East African Rift System. In 'Graben Problems'. I.U.M.P., Report No. 27, 289 - 295.

Woollard, G.P. (1959) — Crustal structure from gravity and seismic measurements. J. Geophys. Res., 64, 1521 - 1544.

Wright, J.B. (1970) — Distribution of volcanic rocks about mid-ocean ridges and the Kenya Rift Valley. Geol. Mag., 107, 125 - 131.

Young, J.B. and Gibbs, P.G. (1968) — GEDESS : A series of computer programs for deriving information at selected seismic recording sites, for signals from known hypocentres. AWRE Blacknest Report No. O 54/68.

COMPUTER PROGRAMS

PROGRAM 1. ARRAN

Given the onset times at a specified number of seismometers with known co-ordinates, ARRAN computes the apparent velocity and azimuth of approach of the signal and the onset time residuals at each pit. If the epicentral distance is known, Herrin et al's (1968) apparent velocity is also found for the appropriate distance and this can be corrected for focal depth (see section 3.1.7.) if the latter is given as input. Site corrections of the form A + B sin (Az + E) can be inputted (section 3.2.1.).

```
      BLOCK DATA
      DIMENSION DM(2),VM(3),VPHA(100),PIT(10)
      COMMON/CAL/DM,VM,VPHA
      COMMON/TI/PIT
      DATA PIT/'P1','P2','P3','P4','P5','Y1','Y2','Y3','Y4','Y5'/
      DATA DM/15.0,40.0/
      DATA VM/6.0,6.75,8.049/
      DATA VPHA/7.9,7.8,7.8,7.8,7.9,7.9,7.9,8.0,8.0,8.1,
     18.2,8.2,8.3,8.3,8.4,8.6,8.8,9.1,9.4,9.9,
     210.3,10.7,11.2,11.6,11.9,12.2,12.3,12.4,12.5,12.5,
     312.6,12.7,12.7,12.8,12.9,13.0,13.1,13.2,13.3,13.4,
     413.5,13.6,13.7,13.9,14.0,14.1,14.2,14.4,14.5,14.7,
     514.8,15.0,15.1,15.2,15.4,15.6,15.7,15.9,16.0,16.2,
     616.4,16.5,16.7,16.8,17.0,17.2,17.4,17.6,17.9,18.0,
     718.2,18.5,18.7,19.0,19.2,19.4,19.7,20.0,20.3,20.6,
     820.9,21.2,21.6,22.0,22.3,22.7,23.0,23.2,23.5,23.7,
     923.8,24.0,24.1,24.2,24.3,24.3,24.4,24.4,24.4,24.4/
      END
C     PROGRAM ARRAY
C
C     PROGRAM TO DETERMINE APPARENT VELOCITY (HENCE SLOWNESS) AND
C     AZIMUTH OF APPROACH FROM ONSET TIMES ACROSS AN ARRAY
C     ADAPTED FROM 'PICORA' - A.W.B.F. BLACKNEST
C
C     READ IN ON 4=FILENAME
C
C     CARD 1
C
C     HI(I) -  PIT HEIGHTS RELATIVE TO SOME REFERENCE POINT
C     A(I),B(I),EA(I) - CONSTANTS FOR PIT CORRECTIONS
C     FROM R=A(I)+B(I)*SIN(AZ+EA(I))
C
C     READ ON 5=FILENAME   CARD 1
C
C     NNN - =0 ANOTHER SET OF ONSET TIMES FOR SAME EVENT
C           =1 END OF DATA
C           =2 NEW EVENT  BUT FIRST EVENT,FIRST ONSET TIMES MUST HAVE
C                     NNN=0
C     STN - STATION NAME IF NEW SET OF DATA
C     NEVEN - EVENT IDENTIFIER
C
C     CARD 2
C
C     DEL - DISTANCE OF EVENT
C     DEP - FOCAL DEPTH OF EVENT
C     USAZ - NOAA AZIMUTH
C
C     CARD 3
C
C     NPIT - NO. OF PITS WORKING
```

```
C    TFACT - SCALING FACTOR FOR ONSET TIMES TO CONVERT TO SECONDS
C
C    CARE 4 TO CARD NPIT+3
C
C    NPIT - PIT IDENTIFIER
C    T - ONSET TIME AT PIT NPIT
C
C    IF END OF DATA PACK TO CARD 1   NNN=1
C    IF NEW EVENT PACK TO CARD 1   NNN=2
C    IF SAME EVENT BUT MORE ONSET TIMES BACK TO CARD 1   NNN=3, STN=BLANK
C
C    OUTPUTS - APPARENT VELOCITY,AZIMUTH,ERRORS ON BOTH,PIT RESIDUALS
C
      DIMENSION PIT(10),X(10),Y(10),AT(15),F(15),C(15),L(100),
     1SUMR(90),SUMC(90),VV(90),AAZ(90),FF(20,15),CR(20,15),
     2AINC(90),CCR(90),TIME(90),P(100,4),S(3),R(3,4),SI(3),H(3,4),
     3AVR(90),AVC(90),AVSE(90),AVSC(90),SUMSC(90),SUMSE(90),
     4SEC(20,20),SER(20,20),ASIGV(20),ASIGA(20),AERRV(20),ST(25),
     5ERR(3),D(3),UNIV(90),VPHA(100),EM(2),VM(3),A(10),PI(10),HI(10),
     6EA(10),ENTA(10),PVV(10),TP(10)
      COMMON/DAL/DM,VM,VPHA
      COMMON/DALTI/DEL,DEP,CDEL,CV
      COMMON/TI/PIT
      COMMON/P1/NNEVEN,AVV,USCOS,AVAZ,EAVV,EAVAZ
      COMMON/P2/NPIT,AVR,AVC,L
      REAL*8 BLANK/'    '/
      DATA ST/12.706,4.303,3.182,2.776,2.571,2.447,2.365,2.306,
     12.262,2.228,2.201,2.179,2.160,2.145,2.131,2.120,2.110,2.101,
     22.093,2.086,2.080,2.074,2.069,2.064,2.060/
      DATA X/-0.098,-0.114,-0.265,-0.663,-0.925,-0.446,-1.888,-2.645,-3.
     1720,-4.750/
      DATA Y/-0.766,-1.425,-3.077,-3.736,-5.200,.166,.003,.025,-0.013,-0
     1.25/
      PI=4.0*ATAN(1.0)
      RTOD=180.0/PI
      RADIUS=6371.024.
      DTOK=RADIUS/RTOD
      READ(4,8)EMIN,VTOP
    8 FORMAT(3X,F7.1,1X,F6.2)
      READ(4,9)(HI(I),A(I),PI(I),EA(I),I=1,10)
    9 FORMAT(1X,F7.1,1X,F8.5,1X,F8.5,F7.2)
      NPUNCH=1
C
C    READ IN PARAMETERS FOR ARRAY AND EVENT
C
  100 READ(5,1000)NNN,STN,NEVEN
 1000 FORMAT(2X,I2,2X,A4,2X,I6)
      ASTN=BLANK
      YINC=FLOAT(NNN)
      IF(YINC.GT.0.0)GO TO 1001
```

```
      N=3
      IF(ASIN.EQ.SIN)GO TO 150
      WRITE(6,508)
  508 FORMAT(1H1)
      NR=0
      NREVEN=NEVEN
      READ(5,3)DEL,DEP,USAZ,NMEAN
    3 FORMAT(5X,F8.3,2X,F8.3,F7.2,2X,I1)
      USCGS=USAZ
      USAZ=USAZ/RTOD
  150 CONTINUE
      NR=NR+1
  190 CONTINUE
      GO TO 170
  170 READ(5,14)NPIT,TFACT
   14 FORMAT(2X,I3,F8.0)
C
C    READ IN OBSET TIMES AND INTO MATRIX
C
      DO 10 K=1,NPIT
      READ(5,12) APIT,T
   12 FORMAT(7X,A2,6X,F10.5)
      DO 11 I=1,20
      IF(APIT-PIT(I))11,13,11
   11 CONTINUE
   13 AT(I)=T/TFACT
      L(K)=I
      GA=(USCGS+EA(I))/RTOD
      HITI=(HI(I)-HMIN)/1000.0
      F(K,1)=-Y(I)
      F(K,2)=-X(I)
      F(K,3)=1.0
      AT(I)=AT(I)-HITI/VTOP-(A(I)+BI(I)*SIN(GA))
      F(K,4)=AT(I)
   10 CONTINUE
   17 M=NPIT
      NC=N+1
C
C    SOLVE EQUATIONS OF CONDITION BY LEAST SQUARES
C
      CALL NORM(F,S,B,N,M,IMTRX)
      CALL SOLVE(F,S,B,N,M,IMTRX,D)
C
C    THEN DEDUCE VELOCITY AND AZIMUTH
C
      VBAR=1.0/SQRT(S(1)*S(1)+S(2)*S(2))
      VV(NP)=VBAR
      AZBAR=ATAN2(VBAR*S(2),VBAR*S(1))
      AZBAR=AZBAR*RTOD
      IF(AZBAR.GE.0.0)GO TO 50
```

```
      DAZ=360.0+AZBAR
      GO TO 51
   50 DAZ=AZBAR
   51 CONTINUE
      AAZ(NR)=DAZ
      WRITE(6,2001)NR,VBAR,DAZ
 2001 FORMAT('PLAYCUT ',I3,' VELOCITY= ',F6.2,
     1' AZIMUTH= ',F7.2)
C
C    RESIDUALS COMPUTED BY SUBSTITUTION OF REGRESSION COEFFICIENTS
C
      CCP=S(3)
      SUMES=0.0
      DO 261 I=1,NPIT
      C(I)=0.0
      E(I)=0.0
  261 CONTINUE
      DF=FLOAT(M-3)
      T=ST(M-3)
      SUMSQ=0.0
      ADD=0.0
      DO 226 K=1,M
      I=L(K)
      E(I)=AT(I)+S(1)*Y(I)+S(2)*X(I)-S(3)
      C(I)=-S(1)*Y(I)-S(2)*X(I)+S(3)
      ER(NR,I)=E(I)
      CR(NR,I)=C(I)
      EE=E(I)
      CC=C(I)
      PPIT=PIT(I)
      ADD=ADD+E(I)
      SUMSQ=SUMSQ+E(I)*E(I)
  226 CONTINUE
C
C    CONFIDENCE LIMITS COMPUTED ON
C    (1) COS(AZBAR)/V,SIN(AZBAR)/V AND C
C    (2) VELOCITY ,AZIMUTH AND C
C
      AVSQ=SUMSQ/DF
      SD=T*SQRT(AVSQ)/2.0
      ERR(1)=T*SQRT(AVSQ*D(1))
      ERR(2)=T*SQRT(AVSQ*D(2))
      ERR(3)=T*SQRT(AVSQ*D(3))
      SIGV=VBAR*VBAR*VBAR*SQRT((S(1)*ERR(1))**2+(S(2)*ERR(2))**2)
      SIGAL=RTOD*VBAR*VBAR*SQRT((S(1)*ERR(2))**2+(S(2)*ERR(1))**2)
      EC=ERR(3)
      SERC=EC
      ASIGA(NR)=SIGAL
      ASIGV(NR)=SIGV
      DO 112 LL=1,100
```

```
      TA=FLOAT(LL-1)
      TC=FLOAT(LL)
      IF(DEL.GE.TA.AND.DEL.LT.TC)GO TO 113
  112 CONTINUE
  113 VOS=VPHA(LL-1)+(DEL-TA)*(DEL-TA)*(VPHA(LL)-VPHA(LL-1))
      GO TO 100
 1001 CONTINUE
C
C    IF NMEAN=0,THEN THE RESULTS ARE AVERAGED FOR ALL THE PLAYOUTS
C    PRECEDING.
C
      IF(NMEAN.NE.0)GO TO 673
      NSR=NR
      DO 81 K=1,NPIT
      I=L(K)
      SUMV=0.0
      SUMA=0.0
      SUMEV=0.0
      SUMEA=0.0
      SUMC(I)=0.0
      SUMR(I)=0.0
      DO 80 NR=1,NSR
      SUMR(I)=SUMR(I)+ER(NR,I)
      SUMC(I)=SUMC(I)+CR(NR,I)
      SUMV=SUMV+VV(NR)
      SUMA=SUMA+AAZ(NR)
      SUMEV=SUMEV+(ASIGV(NR)**2)
      SUMEA=SUMEA+ASIGA(NR)**2
   80 CONTINUE
   81 CONTINUE
      AVV=SUMV/FLOAT(NSR)
      AVAZ=SUMA/FLOAT(NSR)
      VEV=SQRT(SUMEV)/FLOAT(NSR)
      VEZ=SQRT(SUMEA)/FLOAT(NSR)
      FNSR=FLOAT(NSR)
      EAVV=VEV
      EAVAZ=VEZ
      WRITE(6,40)
   40 FORMAT(////////)
      WRITE(6,88)NMEVEN,NSR
   88 FORMAT(2X,'EVENT',I6,3X,I4,' PLAYOUTS')
      WRITE(6,841)AVV,EAVV
  841 FORMAT(//'CALCULATED VELOCITY= ',F8.2,' +OR- ',F7.2)
      WRITE(6,842)AVAZ,EAVAZ
  842 FORMAT('CALCULATED AZIMUTH= ',F8.2,' +OR- ',F8.2)
      WRITE(6,844)LSOGS
  844 FORMAT('LSOGS AZIMUTH= ',F8.2)
      DO 83 K=1,NPIT
      I=L(K)
      AVR(I)=SUMR(I)/FLOAT(NSR)
```

```
      AVC(I)=SUMC(I)/FLOAT(NSR)
      CAVR=AVR(I)
      CAVC=AVC(I)
      PPPIT=PIT(I)
      WRITE(6,85)PPPIT,CAVR,CAVC
   85 FORMAT(1X,A4,2X,F7.4,2X,F7.4)
   83 CONTINUE
  673 CONTINUE
      WRITE(6,7065)DEP
 7065 FORMAT(//' CORRECTING DEL AND V FOR DEPTH=',F5.1)
      CALL DALT
  301 CONTINUE
      CALL PLN
      IF(YIND.EQ.2.0)GO TO 100
      STOP
      END
      SUBROUTINE NORM(Y,X,A,N,M,IMTRX)
      DIMENSION Y(100,4),X(3),A(3,4)
      NC=N+1
      DO 10 I=1,N
      DO 15 J=1,NC
      A(I,J)=0.0
      DO 20 K=1,M
      A(I,J)=A(I,J)+Y(K,I)*Y(K,J)
   20 CONTINUE
      IF(J.EQ.NC) GO TO 15
      A(J,I)=A(I,J)
   15 CONTINUE
   10 CONTINUE
      RETURN
      END
C
C    LEAST SQUARES SOLUTION BY MATRIX INVERSION
C
      SUBROUTINE SOLVE(Y,X,A,M,N,IMTRX,C)
      DIMENSION IND(231),C(231),Y(100,4),X(3),A(3,4)
      DIMENSION B(3),D(3)
  100 AMAX=0.0
      DO 2 I=1,M
      IND(I)=I
      IF(ABS(A(I,1))-AMAX)2,2,3
    3 AMAX=ABS(A(I,1))
      IF=I
    2 CONTINUE
      MM=M-1
      DO 111 J=1,MM
      IF(IF-J)6,6,4
    4 ISTO=IND(J)
      IND(J)=IND(IF)
      IND(IF)=ISTO
```

```
      DO 5 K=1,N
      STO=A(IF,K)
      A(IF,K)=A(J,K)
      A(J,K)=STO
    5 CONTINUE
    6 AMAX=0.0
      JC=J+1
      DO 11 I=JC,N
      A(I,J)=A(I,J)/A(J,J)
      DO 10 K=JC,N
      A(I,K)=A(I,K)-A(I,J)*A(J,K)
      IF(K-JC)14,14,10
   14 IF(ABS(A(I,K))-AMAX)10,10,17
   17 AMAX=ABS(A(I,K))
      IF=I
   10 CONTINUE
   11 CONTINUE
  111 CONTINUE
   65 DO 140 IC=1,NN
      I=N+1-IC
      IT=I-1
      DO 41 JC=1,IT
      J=IT+1-JC
      JT=J+1
      WO=-A(I,J)
      IF(IT-JT)141,43,43
   43 DO 42 K=JT,IT
      WC=WO-A(K,J)*C(K)
   42 CONTINUE
  141 C(J)=WC
   41 CONTINUE
      DO 40 K=1,IT
      A(I,K)=C(K)
   40 CONTINUE
  140 CONTINUE
      DO 150 IC=1,N
      I=N+1-IC
      IT=I+1
      W=A(I,I)
      DO 56 J=1,N
      IF(I-J)52,53,54
   52 WO=0.0
      GO TO 55
   53 WC=1.0
      GO TO 55
   54 WC=A(I,J)
   55 IF(IC-1)156,156,57
   57 DO 58 K=IT,N
      WC=WO-A(I,K)*A(K,J)
   58 CONTINUE
```

```
  156 C(J)=WC
   56 CONTINUE
      DO 50 J=1,M
      A(I,J)=C(J)/W
   50 CONTINUE
  150 CONTINUE
      DO 60 I=1,M
   63 IF(IND(I)-I)61,60,61
   61 J=IND(I)
      DO 62 K=1,M
      STO=A(K,I)
      A(K,I)=A(K,J)
      A(K,J)=STO
   62 CONTINUE
      ISTO=IND(J)
      IND(J)=J
      IND(I)=ISTO
      GO TO 63
   60 CONTINUE
      DO 90 I=1,M
      B(I)=A(I,M+1)
   90 CONTINUE
      DO 66 J=1,M
      STO=0.0
      DO 67 I=1,M
      STO=STO+A(I,J)*B(I)
   67 CONTINUE
      X(J)=STO
      C(J)=A(J,J)
   66 CONTINUE
      RETURN
      END
C    CORRECTS FOR FOCAL DEPTH USING STRUCTURE OF HERRIN(1968)
      SUBROUTINE CALT
      DIMENSION VM(3),DM(2),FR(3),FC(3),V(100),R(2)
      COMMON/CAL/DM,VM,V
      COMMON/CALTI/DEL,DEP,CDEL,CV
      RAD=6371.029
      PI=4.0*ATAN(1.0)
      RTOD=180.0/PI
      DTOK=RAD/RTOD
      DO 10 K=1,3
      FR(K)=0.0
      FC(K)=0.0
   10 CONTINUE
      DO 11 KK=1,2
      R(KK)=RAD-DM(KK)
   11 CONTINUE
      DO 12 L=1,100
      TA=FLOAT(L-1)
```

```
      TC=FLOAT(L)
      IF(DEL.GL.TA.AND.DEL.LT.TC)GO TO 13
   12 CONTINUE
   13 P=RAD/(V(L-1)+(DEL-TA)*(V(L)-V(L-1)))
      VLN=RAD/P
      RH=RAD-DEP
      IF(DEP.GT.DM(1))GO TO 3
      X=VM(1)*P/RH
      FB(1)=ATAN(X/SQRT(1.0-(X*X)))
      FD(1)=DEP*TAN(FB(1))/DTOK
      CDEL=DEL+FD(1)
      WRITE(6,64)FD(1)
   64 FORMAT(/' FD(1)=',F7.3)
      GO TO 2
    3 X=VM(1)*P/R(1)
      FB(1)=ATAN(X/SQRT(1.0-(X*X)))
      FD(1)=DM(1)*TAN(FB(1))/DTOK
      IF(DEP.GT.DM(2))GO TO 5
      X=VM(2)*P/RH
      FB(2)=ATAN(X/SQRT(1.0-(X*X)))
      FD(2)=(DEP-DM(1))*TAN(FB(2))/DTOK
      CDEL=DEL+FD(1)+FD(2)
      WRITE(6,65)FD(1),FD(2)
   65 FORMAT(/' FD(1)=',F7.3,'  FD(2)=',F7.3)
      GO TO 2
    5 X=VM(2)*P/R(2)
      FB(2)=ATAN(X/SQRT(1.0-(X*X)))
      FD(2)=(DM(2)-DM(1))*TAN(FB(2))/DTOK
      X=VM(3)*P/RH
      FB(3)=ATAN(X/SQRT(1.0-(X*X)))
      FD(3)=(DEP-DM(2))*TAN(FB(3))/DTOK
      CDEL=DEL+FD(1)+FD(2)+FD(3)
      WRITE(6,66)FD(1),FD(2),FD(3)
   66 FORMAT(/' FD(1)=',F7.3,'  FD(2)=',F7.3,'  FD(3)=',F7.3)
    2 CONTINUE
      DO 14 L=1,100
      TA=FLOAT(L-1)
      TC=FLOAT(L)
      IF(CDEL.GE.TA.AND.CDEL.LT.TC)GO TO 16
   14 CONTINUE
   16 CV=V(L-1)+(CDEL-TA)*(V(L)-V(L-1))
      WRITE(6,68)DEL,VLN
   68 FORMAT(/'UNCORRECTED    DEL=',F6.1,'  V=',F6.1)
      WRITE(6,69)CDEL,CV
   69 FORMAT('CORRECTED    CDEL=',F6.1,'  CV=',F6.1)
      RETURN
      END
C     PUNCHES CUT,IF REQUIRED,RESIDUALS AND EVENT PARAMETERS
      SUBROUTINE PUN
      DIMENSION FIT(20),AVR(90),AVC(90),L(100)
```

```
      COMMON/P1/NNEVEN,AVV,LSCGS,AVAZ,EAVV,EAVAZ
      COMMON/P2/NPIT,AVR,AVC,L
      COMMON/DALTI/DEL,DEP,CDEL,CV
      COMMON/TI/PIT
      CV=AVV-CV
      DAZ=AVAZ-LSCGS
      IF(DAZ.GT.-180.0.AND.DAZ.LT.180.0)GO TO 30
      IF(DAZ.GT.180.0)GO TO 31
      DAZ=360.0+DAZ
      GO TO 30
   31 DAZ=DAZ-360.0
   30 CONTINUE
      WRITE(3,1)NNEVEN,CV,DV,LSCGS,DAZ,CDEL,DEP,EAVV,EAVAZ
    1 FORMAT(I6,F6.1,F6.1,F6.1,F6.1,F6.1,F6.1,F7.2,F6.2)
      WRITE(2,2)NPIT,NNEVEN
    2 FORMAT(2X,I3,2X,I6)
      WRITE(2,3)AVV,AVAZ,CV,LSCGS,CDEL
    3 FORMAT(3X,F7.3,3X,F8.3,2X,F6.1,2X,F8.3,2X,F6.1)
      DO 11 K=1,NPIT
      I=L(K)
      PPIT=PIT(I)
      RES=AVR(I)
      REC=AVC(I)
      WRITE(2,4)PPIT,RES,REC
    4 FORMAT(6X,A3,3X,F10.5,3X,F10.5)
   11 CONTINUE
      RETURN
      END
```

PROGRAM 2 RESFIT

RESFIT takes the onset time residuals for several events from given great circle azimuths and fits these data to a curve of the form $A + B \sin (Az + E)$ by least squares. This is computed for each of ten pits. The observed residuals and the computed best fit curves can be given as output using a graph-plot subroutine. Here the 'GRAPH' program of Mr. P. K. H. Maguire is used and this is available from the Durham Geology Department.

```
C
C    PROGRAM RESFIT
C
C    PROGRAM TO FIT PIT RESIDUALS R(I) TO R(I)=A+B*SIN(AZ(I)+E)
C    OUTPUTS GRAPHS FOR EACH PIT WITH SUPERIMPOSED COMPUTED CURVES
C    ALSO VALUES OF A,B,E FOR EACH PIT
C
C    READ IN ON 5=FILENAME
C
C    CARD 1
C
C    NTOT - TOTAL NO. OF PITS  (10)
C
C    CARD 2
C
C    NPIT - NO. OF PITS WORKING FOR AN EVENT
C    NEVEN - EVENT IDENTIFIER
C
C    CARD 3
C
C    V - VELOCITY COMPUTED FOR EVENT
C    AZ - AZIMUTH COMPUTED FOR EVENT
C    USCGS - NCAA AZIMUTH
C
C    CARD 3 TO CARD NPIT+2
C
C    APIT(J) - PIT IDENTIFIER
C    R(J) - RESIDUAL FOR PIT APIT(J)
C
C    CARD NPIT+3   -----  BACK TO CARD 2
C
C    IF NPIT=0 END OF DATA
C    IF NPIT GT 0 RESIDUALS FOR NEXT EVENT
C
C
      DIMENSION APIT(10),R(10),C(10),LCO(10),RES(10,200),FCC(10,200),
     1SCC(10,200),AC(10),BC(10),E(10),PIT(10),F(200,4),S(3),B(3,4),
     2D(3),DAZ(10,200),ANAL(10),PY(100),LA(100),IIT(4),TA(100),
     3RN(100),ERR(3),THER(10),ERR(10),ERRE(10),ERAN(10),ST(43)
      DATA ST/12.706,4.303,3.182,2.776,2.571,2.447,2.365,2.306,
     12.262,2.228,2.201,2.179,2.160,2.145,2.131,2.120,2.110,2.101,
     22.093,2.086,2.080,2.074,2.069,2.064,2.060,2.056,2.052,
     32.048,2.045,2.042,2.021,2.021,2.021,2.021,2.021,2.021,
     42.021,2.021,2.021,2.021,2.000,2.000,2.000/
      DATA PIT/'R1','R2','R3','R4','R5','Y1','Y2','Y3','Y4','Y5'/
      PI=4.0*ATAN(1.0)
      RTOD=180.0/PI
      READ(5,4)NTOT
    4 FORMAT(1X,I3)
      DO 41 I=1,10
```

```
      LCC(I)=0
   41 CONTINUE
   50 READ(5,1)NPIT,NEVEN
    1 FORMAT(2X,I3,2X,I6)
      IF(NPIT.EQ.0)GO TO 100
      READ(5,2)V,AZ,USCOS
    2 FORMAT(3X,F7.3,2X,F8.3,10X,F8.3)
      READ(5,3)(APIT(J),R(J),J=1,NPIT)
    3 FORMAT(6X,A3,3X,F10.5)
      DO 10 J=1,NPIT
      PPIT=APIT(J)
      RR=R(J)
      DO 11 I=1,NTOT
      IF(APIT(J)-PIT(I))11,13,11
   11 CONTINUE
   13 LCC(I)=LCC(I)+1
      LC=LCC(I)
      CAZ(I,LC)=USCOS
      RES(I,LC)=RR
      FCO(I,LC)=SIN(USCOS/RTOD)
      SCC(I,LC)=COS(USCOS/RTOD)
   10 CONTINUE
      GO TO 50
  100 CONTINUE
      DO 42 I=1,NTOT
      NB=LCC(I)
      WRITE(2,35)I,NB
   35 FORMAT(1X,I3,1X,I3)
      WRITE(2,32)(CAZ(I,LC),RES(I,LC),FCO(I,LC),SCC(I,LC),LC=1,NB)
   32 FORMAT(4(2X,F10.5))
   42 CONTINUE
      N=3
      DO 20 I=1,NTOT
      NE=LCC(I)
      DO 23 K=1,NE
      F(K,1)=0.0
      F(K,2)=0.0
      F(K,3)=0.0
      F(K,4)=0.0
   23 CONTINUE
C
C    SET UP EQUATIONS OF CONDITION
C
      DO 21 K=1,NE
      LC=K
      F(K,1)=FCC(I,LC)
      F(K,2)=SCC(I,LC)
      F(K,3)=1.
      F(K,4)=RES(I,LC)
   21 CONTINUE
```

```
      M=NE
      NC=N+1
C
C   SOLVE EQUATIONS OF CONDITION
C
      CALL NORM(E,S,F,N,M,IMTRX)
      CALL SOLVE(E,S,D,N,M,IMTRX,C)
      RC(I)=SQRT(S(1)*S(1)+S(2)*S(2))
      E(I)=ATAN2(S(2),S(1))
      ANAL(I)=E(I)*RTOD
      IF(ANAL(I).GT.0.0)GO TO 3030
      ANAL(I)=ANAL(I)+360.0
 3030 CONTINUE
      AC(I)=S(3)
C
C   CALCULATE RESIDUALS AND ERRORS ON A,B, AND F
C
      SUMSQ=0.0
      DO 221 K=1,NE
      LC=K
      RN(LC)=RES(I,LC)-(S(3)+RC(I)*SIN((DAZ(I,LC)+ANAL(I))/RTOD))
      SUMSQ=SUMSQ+RN(LC)*RN(LC)
  221 CONTINUE
      DF=FLOAT(NE-3)
      AVSQ=SUMSQ/DF
      T=ST(NE-3)
      ERR(1)=T*SQRT(AVSQ*C(1))
      ERR(2)=T*SQRT(AVSQ*C(2))
      ERR(3)=T*SQRT(AVSQ*C(3))
      THER(I)=ERR(3)
      ERB(I)=SQRT((S(1)*ERR(1))**2+(S(2)*ERR(2))**2)/RC(I)
      ERRR(I)=SQRT((S(2)*ERR(1))**2+(S(1)*ERR(2))**2)/
     1(RC(I)*RC(I))
      ERAN(I)=ERRR(I)*RTOD
   20 CONTINUE
      WRITE(6,2229)(THER(I),ERB(I),ERAN(I),I=1,10)
 2229 FORMAT(3(3X,F10.5))
      WRITE(6,229)
  229 FORMAT(1H1,' RESIDUALS FITTED TO R=A+B*SIN(AZIMUTH+ALP)')
      WRITE(6,29)
   29 FORMAT(//14X,'A',12X,'B',9X,'ALP(RAD)',4X,'ALP(DEG)')
      WRITE(6,30)(PIT(I),AC(I),RC(I),E(I),ANAL(I),I=1,NTOT)
   30 FORMAT(2X,A8,3X,F10.5,3X,F10.5,3X,F10.5,3X,F9.2)
      DO 84 I=1,NTOT
      NP=LOC(I)
      DO 85 LC=1,NP
      UA(LC)=DAZ(I,LC)
      RY(LC)=100.0*RES(I,LC)
   85 CONTINUE
      DO 81 MA=1,12
```

```
      LCC=NB+MA
      UA(LCC)=30.0*FLOAT(MA-1)
      ABV=UA(LCC)+ANAL(I)
      TA(LCC)=LA(LCC)+ANAL(I)
      PY(LCC)=AC(I)+BC(I)*SIN((UA(LCC)+ANAL(I))/PTOD)
      PY(LCC)=100.0*PY(LCC)
   81 CONTINUE
C
C    PLOT RESIDUALS AND OUTPUT GRAPH FOR EACH PIT
C
      NBP=NB+1
      NEND=NB+12
      NM=NB
      NMAX=NB+12
      JJF=1
      IIT(1)=15
      IIT(2)=-15
      IIT(3)=360
      IIT(4)=0
      CALL GRAPH(UA,PY,NMAX,NM,JJF,IIT)
      DO 281 MMA=1,NEND
      PY(MMA)=PY(MMA)/100.0
  281 CONTINUE
      WRITE(6,230)PIT(I)
  230 FORMAT(//10X,' RESIDUALS FOR PIT ',A3)
      WRITE(6,234)PIT(I)
  234 FORMAT(1H1,' CALCULATED CURVE FOR PIT ',A3)
      WRITE(6,232)
  232 FORMAT(//7X,'AZ',8X,'AZ+ALP',4X,' CALC RESDS')
      WRITE(6,233)(UA(LCC),TA(LCC),PY(LCC),LCC=NBB,NEND)
  233 FORMAT(5X,F6.1,5X,F6.1,5X,F10.4)
   84 CONTINUE
      STOP
      END
      SUBROUTINE NORM(Y,X,A,N,M,IMTRX)
      DIMENSION Y(200,4),X(3),A(3,4)
      NC=N+1
      DO 10 I=1,N
      DO 15 J=1,NC
      A(I,J)=0.0
      DO 20 K=1,M
      A(I,J)=A(I,J)+Y(K,I)*Y(K,J)
   20 CONTINUE
      IF(J.EQ.NC)GO TO 15
      A(J,I)=A(I,J)
   15 CONTINUE
   10 CONTINUE
      IF(IMTRX.NE.1)GO TO 668
      WRITE(6,30)
   30 FORMAT(/50X,'COEFFICIENTS FROM NORM')
```

```
      DO 666 I=1,N
      WRITE(6,667)(A(I,J),J=1,NC)
  667 FORMAT(50X,4E10.5)
  666 CONTINUE
  668 RETURN
      END
      SUBROUTINE SOLVE(Y,X,A,M,N,IMTRX,C)
      DIMENSION IND(231),C(231),Y(200,4),X(3),A(3,4)
      DIMENSION B(3),C(3)
  100 AMAX=0.0
      DO 2 I=1,M
      IND(I)=I
      IF(ABS(A(I,1))-AMAX)2,2,3
    3 AMAX=ABS(A(I,1))
      IF=I
    2 CONTINUE
      MM=M-1
      DO 111 J=1,MM
      IF(IF-J)6,6,4
    4 ISTO=IND(J)
      IND(J)=IND(IF)
      IND(IF)=ISTO
      DO 5 K=1,N
      STO=A(IF,K)
      A(IF,K)=A(J,K)
      A(J,K)=STO
    5 CONTINUE
    6 AMAX=0.0
      JC=J+1
      DO 11 I=JC,M
      A(I,J)=A(I,J)/A(J,J)
      DO 10 K=JC,M
      A(I,K)=A(I,K)-A(I,J)*A(J,K)
      IF(K-JC)14,14,10
   14 IF(ABS(A(I,K))-AMAX)10,10,17
   17 AMAX=ABS(A(I,K))
      IF=I
   10 CONTINUE
   11 CONTINUE
  111 CONTINUE
   65 DO 140 IC=1,MM
      I=M+1-IC
      IT=I-1
      DO 41 JC=1,IT
      J=IT+1-JC
      JT=J+1
      WC=-A(I,J)
      IF(IT-JT)141,43,43
   43 DO 42 K=JT,IT
      WC=WC-A(K,J)*C(K)
```

```
 42 CONTINUE
141 C(J)=WC
 41 CONTINUE
    DO 40 K=1,IT
    A(I,K)=C(K)
 40 CONTINUE
140 CONTINUE
    DO 150 IC=1,N
    I=N+1-IC
    IT=I+1
    W=A(I,I)
    DO 56 J=1,N
    IF(I-J)52,53,54
 52 WC=0.0
    GO TO 55
 53 WC=1.0
    GO TO 55
 54 WC=A(I,J)
 55 IF(IC-1)156,156,57
 57 DO 58 K=IT,N
    WC=WC-A(I,K)*A(K,J)
 58 CONTINUE
156 C(J)=WC
 56 CONTINUE
    DO 50 J=1,N
    A(I,J)=C(J)/W
 50 CONTINUE
150 CONTINUE
    DO 60 I=1,N
 63 IF(IND(I)-I)61,60,61
 61 J=IND(I)
    DO 62 K=1,N
    STC=A(K,I)
    A(K,I)=A(K,J)
    A(K,J)=STC
 62 CONTINUE
    ISTC=IND(J)
    IND(J)=J
    IND(I)=ISTC
    GO TO 63
 60 CONTINUE
    DO 90 I=1,N
    B(I)=A(I,N+1)
 90 CONTINUE
    DO 66 J=1,N
    STC=0.0
    DO 67 I=1,N
    STC=STC+A(I,J)*B(I)
 67 CONTINUE
    X(J)=STC
```

```
      C(J)=A(J,J)
   66 CONTINUE
      RETURN
      END
```

PROGRAM 3 SLOWFIT

SLOWFIT fits observed deviations in slowness and azimuth of approach to theoretical deflections for a model of one or two dipping interfaces. Graphs of observed and computed anomalies can be given as output. The final output is a matrix of RMSD values, the minimum of which indicates the best fit to a model with parameters within the specified range of the variables (Appendix A).

```
C
C     PROGRAM SLOFIT
C
C     PROGRAM TO FIT ONE OR TWO DIPPING LAYERS TO REFLECTIONS
C     IN SLOWNESS AND AZIMUTH
C
C     READ IN ON 5=FILENAME   CARD 1
C
C     NC = NO. OF LAYERS
C
C     CARD 2
C
C     VS(I) = EXPECTED APPARENT VELOCITY (REFRIN.FT AL,.960)
C     DV(I) = OBSERVED-EXPECTED APPARENT VELOCITY
C     DA(I) = NCAA AZIMUTH
C     DA(I) = OBSERVED DEVIATION FROM NCAA AZIMUTH
C     DEL(I) = DISTANCE OF EVENT
C
C     READ IN ON 2=FILENAME
C
C     CARD 1
C
C     NL = NO. OF LAYERS - 1 OR 2
C     NX = NO. OF VELOCITY CONTRASTS
C     IGRAPH = =0 FOR GRAPH OF EACH FIT
C     IMT = =0 FOR PRINTOUT OF INTERNALLY REFLECTED RAYS
C     FDEP = DEPTH OF LOWER DIPPING INTERFACE
C     WT = GIVES RATIO OF RMSD'S   RMSD=RMSD(SLOWNESS)+RMSD(AZIMUTH)/WT
C
C     CARD 2
C
C     VI(KK) = VELOCITY BELOW LOWER SLOPE
C     VR(KK) = VELOCITY ABOVE LOWER SLOPE
C     VT(KK) = VELOCITY ABOVE 2ND INTERFACE - OMIT FOR 1 LAYER PROBLEM
C
C     CARD 3
C
C     STAG = INITIAL VALUE OF DIRECTION OF PRINCIPLE PLANE
C     NANG = NO. OF INCREMENTS FOR STAG
C     SANG = SIZE OF INCREMENTS FOR STAG
C
C     CARD 4
C
C     STAD = INITIAL VALUE OF LOWER DIP
C     NDIP = NO. OF INCREMENTS FOR STAD
C     SDIP = SIZE OF INCREMENTS FOR STAD
C
C     CARD 5 - OMIT FOR 1 LAYER PROBLEM
C
C     STAD2 = INITIAL VALUE OF UPPER DIP
```

```
C    NOIP2 - NO. OF INCREMENTS FOR STAG2 - MAKE =1 IF POSSIBLE
C    SOIP2 - SIZE OF INCREMENTS FOR STAG2
C
C    MAP OF PROGS ARE OUTPUTTED - HENCE MINIMUM CAN BE REDUCED
C
C
      DIMENSION VS(50),DV(50),DA(50),UA(100),DEL(50),VI(50),VR(50),
     1SI(50),AI(50),PHI(100),A(100),R(100),DELV(50),F(50),
     2PSM(100,50),VM(100),VA(100),IIT(4),DT(100),ELV(100),SII(100),
     3AII(100),DELV2(100),SR2(50),SI2(50),CIP(50),AL(100),FI(50),
     4AN(50),ANAN(50),PRR(50),DEV(50),ARSM(100,50),VT(50),RCCN(100,50),
     5ARR(50),TRSM(50,50),SLOPN(100),RCSM(30,30),ARCSM(30,30),
     6NSCCN(30,30),TCRSM(30,30)
C
C    READ IN DATA - FIRSTLY EVENT PARAMETERS
C
      READ(5,1)NL
    1 FORMAT(1X,I3)
      READ(5,2)(VS(I),DV(I),UA(I),DA(I),DEL(I),I=1,NL)
    2 FORMAT(5X,F6.1,F6.1,F6.1,F6.1,F6.1)
C
C    READ IN STARTING VALUES FOR MODEL
C
      READ(2,3)NL,NX,ICRAPH,IMT,REEP,MT
    3 FORMAT(4I3,2F6.1)
      READ(2,4)(VI(KK),VP(KK),VT(KK),KK=1,NX)
    4 FORMAT(3F8.0)
      READ(2,5)STAG,NANG,SANG
    5 FORMAT(1X,F7.2,1X,I3,2X,F7.2)
      WRITE(6,5)STAG,NANG,SANG
      READ(2,5)STAG,NOIP,SOIP
      WRITE(6,5)STAG,NOIP,SOIP
      IF(NL.EQ.1)GO TO 200
      READ(2,5)STAG2,NOIP2,SOIP2
      WRITE(6,5)STAG2,NOIP2,SOIP2
  200 CONTINUE
      PI=4.0*ATAN(1.0)
      RTOD=180.0/PI
      DTOK=6371.0/RTOD
      RAD=(6371.0-REEP)/6371.
      DO 12 KK=1,NX
      WRITE(6,39)
   39 FORMAT(1H1)
      DO 54 I=1,ND
      II=I
      SLOPN(I)=DTOK/(DV(I)+VS(I))-DTOK/VS(I)
      VP(II)=SLOPN(I)
      ANAN(II)=DA(I)
      SII(I)=VI(KK)/(RAD*VS(I))
      AII(I)=SQRT(1.0-SI(I)*SI(I))
```

```
      DT(I)=DT(K/VS(I)
   54 CONTINUE
      DO 13 K=1,NANG
      PHI(K)=STAG+SANG*FLOAT(K-1)
      DO 14 L=1,NDIP
      A(L)=STAD+SDIP*FLOAT(L-1)
      ALL=A(L)
      IF(NL.NE.1)GO TO 264
      NDIP2=1
      STAD2=0.0
  264 CONTINUE
      DO 19 M=1,NDIP2
      A2(M)=STAD2+SDIP2*FLOAT(M-1)
      KE=0
C
C    COMPUTE SLOWNESS AND AZIMUTH ANOMALIES FOR EACH EVENT FOR
C    TRIAL MODEL
C
      DO 15 I=1,NS
      IF(UA(I).GT.PHI(K))GO TO 41
      B(I)=360.0+UA(I)-PHI(K)
      GO TO 42
   41 B(I)=UA(I)-PHI(K)
   42 BII=B(I)
      AR=ARSIN(SII(I))*RTOD
      IF(BII.GT.90.0.AND.BII.LT.270.0)GO TO 442
      DAD=AR+ALL
      B(I)=BII
      GO TO 443
  442 DAD=AR-ALL
      A(L)=ALL
      B(I)=+BII
  443 AD=DAD
      SI(I)=SIN(AD/RTOD)
      AI(I)=SQRT(1.0-SI(I)*SI(I))
      F=1.0/(VR(KK)*VR(KK))-(SI(I)*SI(I))/(VI(KK)*VI(KK))
      IF(F.LT.0.0)GO TO 214
      DR=SIN(A(L)/RTOD)
      FA=(SQRT(F)-AI(I)/VI(KK))*SIN(A(L)/RTOD)
      DELV(I)=+FA*LTOK
      IF(NL.EQ.1)GO TO 201
      SR2(I)=VR(KK)*SI(I)/VI(KK)
      PRP=ARSIN(SR2(I))*RTOD
      IF(BII.GT.90.0.AND.BII.LT.270.0)GO TO 167
      BI(I)=PRP-ALL
      SAN=BI(I)+A2(M)
      GO TO 169
  167 BI(I)=ALL+PRP
      SAN=BI(I)-A2(M)
  169 CONTINUE
```

```
      SI2(I)=SIN(SAN/RTOD)
      CI2(I)=SQRT(1.0-SI2(I)*SI2(I))
      R2=1.0/(VT(KK)*VT(KK))-(SI2(I)*SI2(I))/(VP(KK)*VP(KK))
      IF(R2.LT.0.0)GO TO 214
      TAN=(SQRT(R2)-CI2(I)/VP(KK))*SIN(AL(M)/RTOD)
      DELV2(I)=+TAN*DTOK
      GO TO 202
  201 DELV2(I)=0.0
  202 DVEE=DELV(I)+DELV2(I)
      PPRP=SQRT(DT(I)**2+DVEE**2-2.0*ABS(DVEE)*DT(I)*COS(B(I)/RTOD))
      ELV(I)=+(PPRP-DT(I))
      II=I+NP
      VP(II)=ELV(I)
      UA(II)=UA(I)
      R(I)=(SLOWA(I)-ELV(I))**2
      COSA=(DT(I)**2+PPRP**2-DVEE**2)/(2.0*DT(I)*PPRP)
      IF(BII.GT.180.0)GO TO 921
      ANAN(II)=ARCOS(COSA)*RTOD
      GO TO 922
  921 ANAN(II)=-ARCOS(COSA)*RTOD
  922 CONTINUE
      ARR(I)=(DA(I)-ANAN(II))**2
      GO TO 115
  114 IF(INT.NE.0)GO TO 220
      WRITE(6,90)I
   90 FORMAT(' I=',I4,'SQRT -VE')
  220 CONTINUE
      GO TO 15
  115 KL=KL+1
   15 CONTINUE
      IF(KL.NE.0)GO TO 88
      WRITE(6,87)L,M
   87 FORMAT('NO EVENTS PASS AT L=',I4,' AND M=',I4)
      GO TO 12
   88 CONTINUE
      NP=NP
      NMAX=2*NP
      JJP=1
      IIT(1)=5
      IIT(2)=-5
      IIT(3)=360
      IIT(4)=0
      IF(IGRAPH.NE.0)GO TO 90
      CALL GRAPH(UA,VP,NMAX,NP,JJP,IIT)
   90 CONTINUE
      KL=KL
      SR=0.0
      DO 51 I=1,NP
      SR=SR+R(I)
   51 CONTINUE
```

```
      MP=NC
      NMAX=2*NC
      JJF=1
      IIT(1)=15
      IIT(2)=-15
      IIT(3)=360
      IIT(4)=0
      IF(IGRAPH.NE.0)GO TO 281
      CALL GRAPH(DA,ANAM,NMAX,MP,JJF,IIT)
  281 CONTINUE
      SAN=0.0
      DO 251 I=1,NC
      SAN=SAN+APR(I)
  251 CONTINUE
C
C    COMPUTE RMSD FOR ALL EVENTS FOR A TRIAL MODEL
C
      IF(NL.EQ.1)GO TO 205
      ARSM(L,M)=SQRT(SAN/FLOAT(KEE))
      RSM(L,M)=SQRT(SR/FLOAT(KEE))
      NCON(L,M)=KEE
      GO TO 206
  205 RDSM(K,L)=SQRT(SR/FLOAT(KEE))
      ARDSM(K,L)=SQRT(SAN/FLOAT(KEE))
      NCON(K,L)=KEE
  206 CONTINUE
   19 CONTINUE
   14 CONTINUE
      IF(INTRX5.NE.0)GO TO 159
      WRITE(6,157)AR
  157 FORMAT('ANGLE I =',F6.1)
  159 CONTINUE
C
C    IF TWO LAYERS, OUTPUT RMSD MATRICES
C
      IF(NL.EQ.1)GO TO 207
      WRITE(6,33)VI(KK),VR(KK),VT(KK),PHI(K)
   33 FORMAT('1''V1=',F5.2,'   V2=',F5.2,'   V3=',F5.2,5X,
     1'PRINCIPAL PLANE AT ',F6.1,' DEGREES')
      WRITE(6,341)
  341 FORMAT(//3(X,'SLOWNESS RMSD'/)
      WRITE(6,31)(A2(M),M=1,NDIP2)
   31 FORMAT(12X,12F9.2/)
      WRITE(6,30)(A(L),(RSM(L,M),M=1,NDIP2),L=1,NLIP)
   30 FORMAT(F7.2,5X,12F9.4)
      WRITE(6,342)
  342 FORMAT(//30X,'AZIMUTH RMSD'/)
      WRITE(6,31)(A2(M),M=1,NDIP2)
      WRITE(6,234)(A(L),(ARSM(L,M),M=1,NDIP2),L=1,NDIP)
  234 FORMAT(F7.2,5X,12F9.4)
```

```
      WRITE(6,35)
   35 FORMAT(//)
      WRITE(6,343)
  343 FORMAT(//30X,'NO. OF EVENTS USED'/)
      WRITE(6,34)(A(L),(NCCN(L,M),M=1,NDIP2),L=1,NDIP)
   34 FORMAT(F7.2,4X,12I8)
      DO 72 L=1,NDIP
      DO 73 M=1,NDIP2
      TRSM(L,M)=RSM(L,M)+ARSM(L,M)/WT
   73 CONTINUE
   72 CONTINUE
      WRITE(6,344)
  344 FORMAT(//30X,'COMBINED WEIGHTED RMSD'/)
      WRITE(6,31)(A2(M),M=1,NDIP2)
      WRITE(6,75)(A(L),(TRSM(L,M),M=1,NDIP2),L=1,NDIP)
   75 FORMAT(F7.2,5X,12F9.4)
  207 CONTINUE
   13 CONTINUE
C
C    IF ONLY ONE LAYER, OUTPUT RMSD MATRICES
C
      IF(NL.NE.1)GO TO 208
      WRITE(6,633)V1(KK),V2(KK)
  633 FORMAT('V1=',F5.2,'   V2=',F5.2)
      WRITE(6,341)
      WRITE(6,631)(A(L),L=1,NDIP)
  631 FORMAT(12X,12F8.1/)
      WRITE(6,630)(PHI(K),(RCSM(K,L),L=1,NDIP),K=1,NANG)
  630 FORMAT(F7.1,5X,12F9.4)
      WRITE(6,635)
  635 FORMAT(//)
      WRITE(6,342)
      WRITE(6,631)(A(L),L=1,NDIP)
      WRITE(6,6234)(PHI(K),(ARCSM(K,L),L=1,NDIP),K=1,NANG)
 6234 FORMAT(F7.1,5X,12F9.4)
      WRITE(6,343)
      WRITE(6,634)(PHI(K),(NCCCN(K,L),L=1,NDIP),K=1,NANG)
  634 FORMAT(F7.1,4X,12I8)
      DO 672 K=1,NANG
      DO 673 L=1,NDIP
      TCRSM(K,L)=RCSM(K,L)+ARCSM(K,L)/WT
  673 CONTINUE
  672 CONTINUE
      WRITE(6,344)
      WRITE(6,631)(A(L),L=1,NDIP)
      WRITE(6,675)(PHI(K),(TCRSM(K,L),L=1,NDIP),K=1,NANG)
  675 FORMAT(F7.1,5X,12F9.4)
  208 CONTINUE
   12 CONTINUE
      STOP
```